SHRINKAGE BEHAVIOUR OF STEEL-FIBRE-REINFORCED-CONCRETE PAVEMENTS

A thesis submitted for the degree of Doctor of Philosophy

By

Naeimeh Jafarifar

(BSc, MSc)

Department of Civil and Structural Engineering

The University of Sheffield

Sheffield

November, 2012

“To my parents for their everlasting concerns,

To my husband, without his supports it couldn’t have been possible to make such a thing,

And to my little son, for his patience and his motive beautiful smiles”

ACKNOWLEDGEMENTS

I would like to express my deepest gratitude to my supervisor Prof. Kypros Pilakoutas for his continuous support and inspiration. I thank him for his valuable advices, high level of knowledge, and his positive flexibility.

I also would like to appreciate my co-supervisor Dr Terry Bennett for his good collaboration in solving my issues, his valuable advices, and the detailed correction of my thesis.

I acknowledge Ecolanes project, for giving me the chance of working in an important joint group of academic and industrial partners from all over Europe and for its financial support.

I would like to thank the technical staff of the Materials and Structures Laboratory for their high quality help in the experimental phase, especially Chris Todd for his good collaboration, and Kieran Nash for his continuous and accurate care during my experimental measurements.

I appreciate my good friends in the Construction Innovations Group for the happy moments I had with them, and especially I am grateful to Harris Angelakopoulos for his valuable helps.

I thank my parents for their sacrifices and tolerating the distance between us during my studies.

And, last but not least, I specially thank my husband Alireza who stood like a strong column that I could confidently rely on it, and my son Amirreza who suffered for my success but brought loads of happiness to my small family.

ABSTRACT

The use of steel fibres extracted from waste tyres as reinforcement for concrete pavements has been developed at the University of Sheffield. The EU funded EcoLanes Project (Economical and sustainable pavement infrastructure for surface transport) undertook extensive research and developed solutions for Steel-Fibre-Reinforced-Concrete (SFRC) pavements with a particular focus on using recycled steel fibres and roller compacted concrete. The current research project ran alongside the EcoLanes project and aimed at contributing towards the development of design guidelines for pavements reinforced with recycled steel fibres. It was achieved through a study on the restrained shrinkage behaviour of Recycled-Steel-Fibre-Reinforced-Roller-Compacted-Concrete (R-SFR-RCC) pavements, and its consequent effect on the load bearing capacity and fatigue performance of pavements.

The work in this thesis is mainly based on numerical investigations, but experiments were carried out to obtain the material properties (moisture transport, free shrinkage and mechanical). These basic physical properties were extracted from test results, using inverse analysis. The extent of distress induced by drying shrinkage was evaluated using moisture transport analysis coupled with stress analysis. The effect of shrinkage distress on the load bearing capacity of the pavement was investigated in a comparative way with and without shrinkage. Fatigue test results were also used to study the long-term load-bearing capacity.

It was found that the rate of drying and consequent moisture diffusivity in SFRC is higher than for plain concrete and in RCC it is higher than for CC. Moisture diffusivity varies in the range of 0-5 mm^2/day for moisture contents lower than 87-92% and then sharply increases to 30 mm^2/day for saturated concrete. Free shrinkage is lower for SFRC compared with plain concrete, at early ages. RCC free shrinkage develops at a more uniform rate compared to CC.

For the studied SFR-RCC pavement, surface micro-cracks are formed predominantly due to curling (with opening density of 0.69 mm/m) potentially forming micro-cracks (0.014 mm-0.056 mm width) spaced at 20 mm-60 mm. Cracking at the top surface initiates from the beginning of drying, and stabilises after 180 days. Shrinkage cracking penetrates down to around a quarter of the slab thickness, and the tensile strength at the top surface reduces 50% of the maximum strength; whereas based on the Concrete Society TR34, the strength reduces by 30% at the surface and drops linearly to zero at half depth. The current study found that the stress induced by curling is dominant, compared to that induced by external restraints.

Shrinkage induced cracks was found to reduce the ultimate load bearing capacity and the fatigue capacity of the pavement by up to 50%.

TABLE OF CONTENTS

LIST OF FIGURES

LIST OF TABLES

LIST OF ABBREVIATIONS AND SYMBOLS

ABBREVIATIONS

1D	one dimensional
2D	two dimensional
3D	three dimensional
AASHTO	American Association of State Highway and Transportation Officials
ACI	American Concrete Institute
ACPA	American Concrete Pavement Association
ASTM	American Society for Testing and Materials
BS	British Standard
CBR	California Bearing Ratio
CC	Conventional Concrete
CDP	Concrete Damage Plasticity
CMOD	Crack Mouth Opening Displacement
CORD	Catalogue Of Road Defects
CRCP	Continuously Reinforced Concrete Pavement
CSC	Concrete Smeared Cracking
FAA	Federal Aviation Administration
FE	Finite Element
FEA	Finite Element Analysis
FHWA	Federal Highway Administration
ESAL	Equivalent Standard Axle Load
HGV	Heavy Goods Vehicle
I-SFRC	Industrial Steel-Fibre-Reinforced-Concrete
ISO	Internationnal Standarization Organization
JCI	Japaneses Concrete Institute
JPCP	Jointed Plain Concrete Pavement
JRCP	Jointed Reinforced Concrete Pavement
JSCE	Japan Society of Civil Engineers
LOP	Limit Of Proportionality
LVDT	Linear Variable Differential Transformer
NCHRP	National Cooperative Highway Research Program
PC	Plain Concrete
PCA	Portland Cement Association
PCP	Plain Concrete Pavement
RCC	Roller Compacted Concrete
R&D	Research & Development

RILEM	Reunion Internationale des Laboratoires et Experts des Materiaux, Systemes de Construction et Ouvrages (International Union of Laboratories and Experts in Construction Materials, Systems, and Structures)
R-SFRC	Recycled Steel-Fibre-Reinforced-Concrete
R-SFR-CC	Recycled Steel-Fibre-Reinforced Conventional-Concrete
R-SFR-RCC	Recycled Steel-Fibre-Reinforced Roller-Compacted-Concrete
SAL	Standard Axle Load
SFRC	Steel-Fibre-Reinforced-Concrete
SFR-CC	Steel-Fibre-Reinforced Conventional-Concrete
SFR-RCC	Steel-Fibre-Reinforced Roller-Compacted-Concrete
UFC	Unified Facilities Criteria
UoS	University of Sheffield
USFD	Unoversity of Sheffield

SYMBOLS

a	equivalent contact radius of the load
a_1	distance from the load centre to the corner of the slab
$\beta_c(C)$	hygral contraction coefficient
$\beta_{cc}(t)$	coefficient depending on the age of the concrete
b	width of the test specimen (prisms)
C	moisture content
C_0	reference moisture content
C_b	prescribed moisture
C_a	moisture content in the atmosphere
C_s	moisture content at the drying surface
C_T	specific heat capacity
δ_{F_L}	deflection corresponding to load F_L
δ_j	deflection defined in Figure 4.27
$\Delta\varepsilon$	differential strain between top and bottom of the slab
D	stiffness of the slab
ε	strain
ε_{sh}	long-term free shrinkage strain
$(\varepsilon_{sh})_C$	free shrinkage strain
$(\varepsilon_{sh})_u$	ultimate shrinkage strain
E	elastic modulus
E_{cm}	mean elastic modulus of concrete at 28 days
$E_{cm}(t)$	mean elastic modulus of concrete at an age of t days
φ_{ef}	effective creep

f	convective moisture transfer coefficient (film coefficient or surface factor)
f_{cm}	mean compressive strength of concrete at 28 days
$f_{cm}(t)$	mean compressive strength of concrete at an age of t days
$f_{ct,L}^{f}$	flexural tensile strength of concrete (in BS EN 14651, 2005)
$f_{ct,fl}$	flexural tensile strength of concrete
f_{ctm}	mean tensile strength of concrete at 28 days
$f_{ctm}(t)$	mean tensile strength of concrete at an age of t days
f_{cur}	curling-induced stress
F_j	load corresponding to deflection δ_j, ($j = 1, 2, 3, 4$)
F_L	load corresponding to *LOP* (Limit Of Proportionality)
$f_{R,j}$	residual flexural tensile strength
f_{sh}	stress induced by externally restrained shrinkage
$f_{sh,full}$	shrinkage stress for a fully restrained slab
γ	partial material safety factor
γ_{0i}	diffusible moisture per unit volume for specimen *i*
h	slab thickness
h	distance between the tip of the notch and the top of the testing prism, in bending tests
h_i	cutting depth of specimen *i*, in moisture measurement
I	second moment of area of the cross-section
IE_{max}	maximum principal inelastic strain
k	modulus of subgrade reaction
K_C	diffusion coefficient, or moisture diffusivity
K_T	thermal conductivity
l	the radius of relative stiffness
l	length of supported span of the beam, in bending tests
μ	friction coefficient
M_n	negative bending moment capacity
M_p	residual positive bending moment capacity
M_{ti}	moisture loss in the body of specimen *i* up to time *t*
ν	Poisson's ratio
n	unit normal to the boundary surface
N	number of load cycles
Nf	designed number of load cycles at failure
Ψ	dilation angle
p	contact pressure
P	applied load
P_f	punching shear load
$P_{collapse}$	collapse load
P_{cr}	crack initiation load

P_u	ultimate or collapse load
ρ	density
$R_{e,3}$	equivalent flexural strength, based on the definition of JSCE-SF4 (1984)
σ	Stress
s	coefficient depending on the type of cement
S	area of the drying surface
S_0	initial spacing of cracks
τ	shear stress
τ	Boltzman's transformation
τ_{crit}	sliding shear stress
t	age of concrete
t	time, in diffusivity equation
T	temperature
w	crack opening
w_{max}	maximum deflection of the slab
W_{0i}	initial weight of specimen *i*
W_{fi}	dry weight of specimen *i*
x	centre-line spacing of the equivalent contact areas of a dual load
x	variable depth from the drying surface, in moisture measurement

Chapter 1

1 Introduction

Pavements are an essential part of modern surface transport infrastructure and are categorised into flexible and rigid. Concrete is the main substance in the construction of rigid pavements, while asphalt is normally used for flexible pavements. Rigid pavements tend to be thinner than flexible pavements due to reduced foundation layers and their thicknesses, as schematically shown in Figure 1.1.

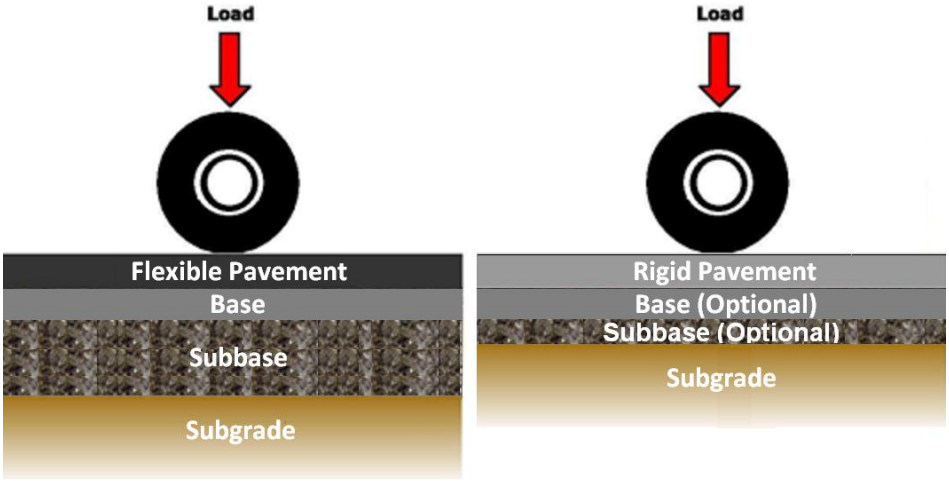

Figure 1.1 (a) Flexible pavement; (b) Rigid pavement

The majority of pavements were previously designed for a 20-year service life, while studies show that a design life of 40 years is more economical (ACPA, 2007; FHWA, 1993). Therefore, recently there has been an increased tendency to design the road pavements for a service life of 40 or more years, particularly for highly trafficked roads (Andrei et al., 2007). The reduction in maintenance is also an important issue since local repairs are usually too disruptive and their performance is not always satisfactory (Mayhew et al., 1987).

Concrete pavements (Figure 1.2) normally have a longer life with less maintenance requirement than asphalt pavements (Embacher et al., 2001). A report by the American Concrete Pavement Association (ACPA, 2000) indicates that concrete pavements provide a

2.1 to 2.5 times longer service life, 13 to 21% lower lifetime cost, and 11 to 21% better benefit/cost ratio. The material cost of reinforced concrete pavements can be generally higher than that of flexible pavements, but low-cost materials (such as steel fibres recycled from post-consumer tyres as reinforcement, and aggregates obtained from construction waste) can be utilised in construction of concrete pavements to bring the cost down.

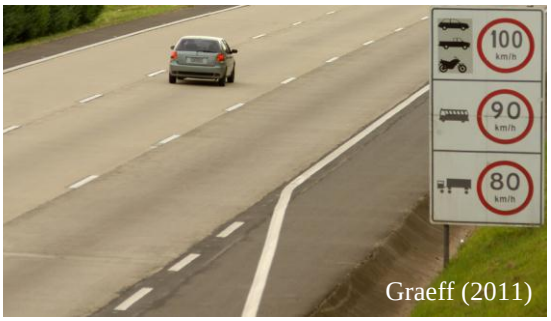

Figure 1.2 Concrete road pavements

Steel fabric mesh is usually used to reinforce concrete pavements to improve structural performance and to decrease the required depth of the pavement. Steel reinforcing bars can be replaced by steel fibres. Steel fibres are mixed with the fresh concrete and facilitate the construction by reducing labour costs and time required for construction. Steel fibre reinforced concrete (SFRC) can also be placed using the roller compaction technology, which is faster compared with conventional concreting techniques. Roller compacted concrete

(RCC) is a zero slump concrete mix which is placed and compacted using modified asphalt pavers and vibratory rollers (PCA, 2006) (Figure 1.3(a) and (b)). The main constituents of RCC are the same as for conventional concrete (CC), but the mix proportions are different resulting in different properties and behaviour of the material. CC is placed using conventional techniques and requires side formwork (Figure 1.4).

Figure 1.3 (a) Placing RCC; (b) Compacting RCC

Figure 1.4 Placing CC for reinforced concrete pavements

The use of industrial steel fibres in concrete road pavement construction is currently limited due to the high cost of these fibres. The use of industrial fibres is only justifiable if the benefits of rapid construction and low labour cost exceeds the extra cost imposed by the higher price of industrial steel fibres than conventional steel bars. Recycled steel fibres (e.g. those extracted from post-consumer tyres) could be replaced with industrial fibres as a cheaper alternative. The use of tyre wire as concrete reinforcement has been demonstrated and patented by the University of Sheffield (USFD, 2001; Tlemat, 2004).

An EU FP6 STREP project, called EcoLanes (2006-2009) and coordinated by the University

of Sheffield aimed to develop long lasting pavement infrastructure for surface transport by using roller-compaction techniques, based on existing asphalt laying equipment, and zero-slump SFRC (EcoLanes, 2006-2009). Ecolanes utilised recycled steel fibres to reduce the energy consumption cost of concrete pavements and developed optimised processes for roller-compacted SFRC.

Utilising new materials in construction is a slow process and follows many years of research and development (R&D) and understanding of the properties of the material in different environments as well as development and approval of appropriate design guidelines.

Concrete pavements are generally categorised into continuously reinforced concrete pavements (CRCP) and jointed concrete pavements. Joints are provided in the concrete pavements either to make breaks in the construction process or as prearranged cracks instead of allowing cracks to develop in an irregular pattern. In this case, the continuity of the slab must be provided by installing load transferring mechanisms such as dowel bars along the joints. Load transferring mechanisms can allow a minimum horizontal displacement to release volumetric movements, while restricting relative vertical movements. Aggregate interlock can also help in load bearing across the restrained movement joints (such as sawn partial-depth joints), but its effectiveness depends on the joint opening and decreases by time (Concrete Society TR34, 2003). Joints are costly to install and provide additional surfaces for deterioration.

Because of their ductile behaviour, SFRC pavements behave similar to conventionally reinforced concrete pavements, although the effective amount of reinforcement is less in SFRC. In RCC pavements there is no need for construction joints and they can be considered as continuous pavements. Due to the compaction process, it is also not easy to install the load transferring dowel bars. Conclusively, steel-fibre-reinforced roller-compacted concrete (SFR-RCC) pavements can be used for CRCPs. In CRCP micro cracks are allowed to occur. However, since the reinforcement keeps the cracks tightly closed, the load transferability across the cracks is maintained as well as the structural integrity of the pavement.

In the design of concrete pavements for given loads, it cannot usually be assumed that the material is ideal, stress-free and sound hardened concrete. The fact is that the slab has passed a strengthening and drying period before reaching its serviceable condition. In this period the slab has been exposed to specific environmental and boundary conditions, which affect

shrinkage. Shrinkage is the effect of losing water from the concrete and occurs when the concrete is exposed to an environment with lower relative humidity. Restraints against volumetric changes may stress the concrete in excess of its early tensile strength, and cause cracking (ACI 360R, 1992). Concrete pavements are practically always restrained and surface cracking is likely to occur. The restraint could be developed by internal resistance of the slab against non-uniform volumetric change across the member, or externally due to resistance of the underlying boundary against shortening (e.g. by friction or bond between the slab and the foundation). Therefore, the effect of drying shrinkage is important in the performance of a concrete pavement since it can cause curling and cracking which can lead to strength loss and loss of support.

Shrinkage-induced cracking in concrete pavements is more critical than other kinds of structural members, because pavements generally have a much larger surface area (Zhang et al., 2001[b]). This kind of early age cracking is one of the most usual types of cracking for slabs and pavements (ACI 544.1R, 1996; Kwon et al., 2008).

In the past decades, shrinkage of concrete has received considerable research attention. Many studies have been conducted over the years to investigate the restrained shrinkage in concrete pavements. Studies have shown that the use of steel fibres in concrete pavements is beneficial to reduce the adverse effects of shrinkage (Meda et al., 2004[b]; ACI 544.1R, 1996; Swamy et al., 1979; Chern et al., 1989). However, the methods proposed so far for restrained volumetric changes of SFRC are still few and are not directly applicable to practice.

Furthermore, laboratory investigations on the drying shrinkage of RCC are very few. The performance of recycled steel fibres on the behaviour of RCC or CC pavements under restrained conditions is not well understood. The published research work on the shrinkage properties of SFR-RCC is limited to the studies performed by Graeff (2011), which shows significantly higher free shrinkage for SFR-RCC than plain RCC and SFR-CC mixes when reinforced with recycled fibres.

The available design guidelines (e.g. Concrete Society TR34, 2003) specify methods to estimate the load carrying capacity of SFRC pavements, while the evaluation of distress resulting from restrained shrinkage is only based on very simple rules of thumb. For instance, TR34 indicates that the interaction between shrinkage induced stresses and those due to loading is not well understood, and roughly suggests deducting a value around 1.5 N/mm^2

from the flexural tensile strength of the concrete as the effect of restrained shrinkage.

In achieving long-term performance, appropriate structural design is a major factor. For obtaining long life in pavements, early age distress must also be taken into account to reduce the potential for cracking (Andrei et al., 2007). Therefore, significant research effort is required in the above mentioned field, in order to contribute to the development of cost-effective and reliable guidelines to predict the performance of SFRC pavements, and facilitate the use of recycled fibres and roller-compaction technology in pavement construction.

1.1 Aims and objectives of the study

This study aims to quantify distress induced by drying shrinkage in SFRC pavements, and its consequent effect on the long-term load bearing capacity.

The research objectives are:

(1) To determine appropriate material data for computational modelling:

- Moisture diffusivity as a function of moisture content
- Convective moisture transfer coefficient (surface factor)
- Relation between moisture loss and free shrinkage ("hygral contraction coefficient")
- The compressive strength, elastic modulus, and the tension stiffening behaviour.

(2) To investigate by computational modelling the effect of restrained shrinkage on SFRC pavements

(3) To compare the restrained shrinkage behaviour of SFR-RCC and SFR-CC pavements

(4) To quantify using computational analysis the effect of shrinkage distress on the load bearing capacity and the long-term performance of SFRC pavements

(5) To make comparisons with existing guidelines and to give suggestions for future development of design guidelines

1.2 Research method

The research methodology involves a combination of experimental measurements and numerical investigations employing Finite Element Analysis (FEA). The experimental studies are carried out to determine the material properties. Data processing analysis is performed on the experimental results to obtain the appropriate material data for FEA of pavements. Figure 1.5 illustrates the main stages of this research.

1.2.1 Experimental study

Two SFRC mixes are developed for CC and RCC using the optimum practical amount of recycled fibres proved by Ecolanes. Two plain CC and RCC mixes are also developed as reference mixes for comparison with SFRC.

- Moisture measurement test

A moisture measurement test is developed to determine the moisture transport parameters such as moisture diffusivity inside the concrete and moisture conductivity at the drying surface. A gravimetric method is used for moisture measurement.

- Free drying shrinkage test

A free drying shrinkage test is developed to evaluate the mapping function from the moisture space to the strain space, so-called “hygral contraction coefficient”. This function is a material property applicable for any shape of the concrete member with any type of restraint.

- Flexural toughness test

Flexural toughness tests are developed to derive stress-strain (σ-ε) constitutive models to be used in FEA as the tensile properties of the SFRC. For flexural toughness, bending prisms are tested using the four-point load arrangement.

- Compressive strength and elastic modulus tests

The compressive strength and elastic modulus are measured on cylinder specimens and cubes.

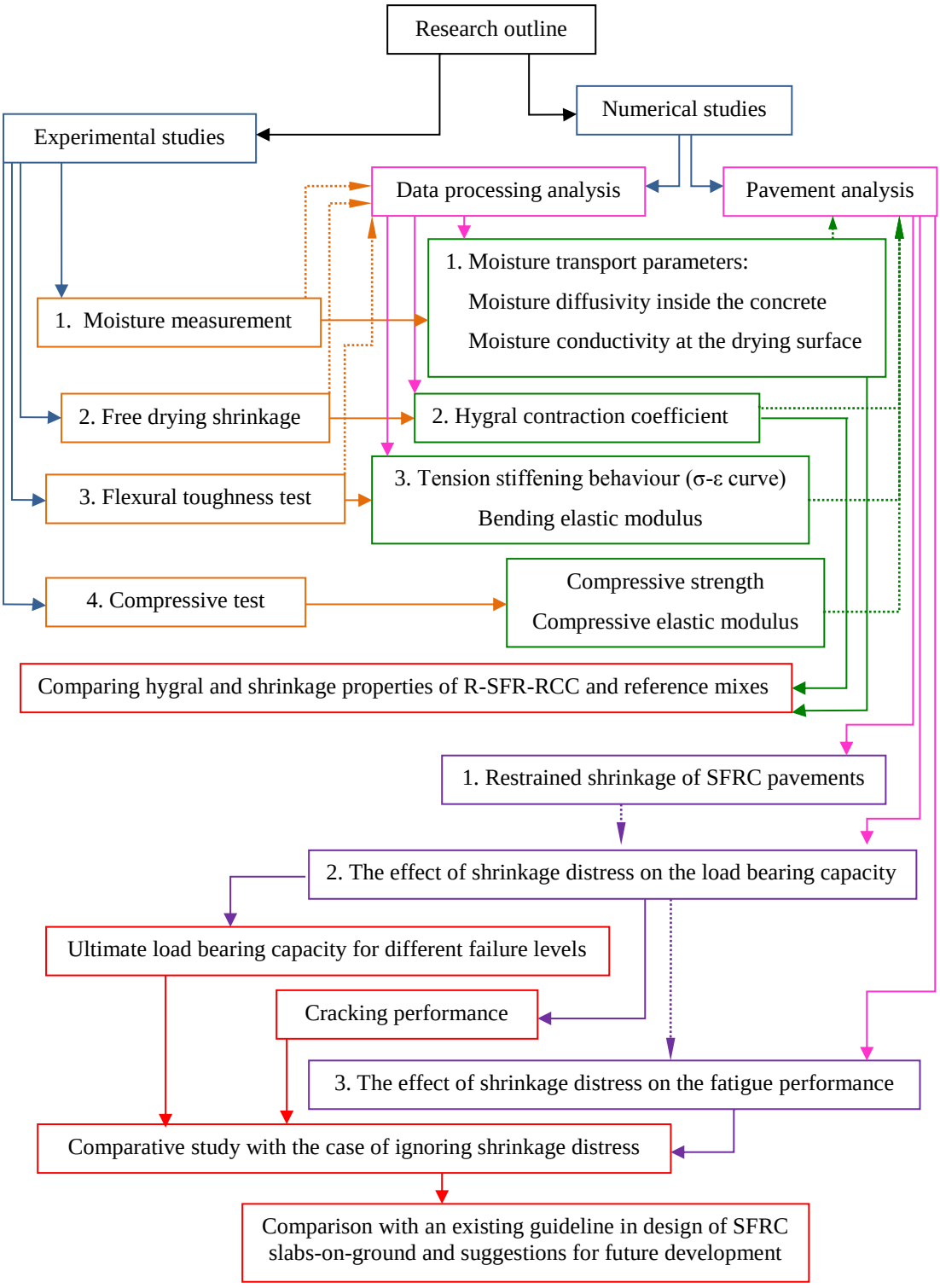

Figure 1.5 Diagram of the research outline and the main expected output results

1.2.2 Numerical study

Two types of analyses are performed. The first type deals with data processing to obtain the material properties from experimental data and relies on inverse analysis. The second type of analysis, which is the main body of the current research, focuses on pavement analysis.

1.2.2.1 Data processing analysis

FE models are developed and using the inverse analysis technique the following properties are back-calculated from the test results.

- Moisture diffusivity and surface factor
- Hygral contraction coefficient
- Tension stiffening properties of SFRC (σ-ε models)

1.2.2.2 Pavement analysis

The pavement structure including the concrete slab and a multi-layered foundation is simulated using the FE technique. The contact surface of the slab and the foundation is simulated so as to allow for uplift and movement of the slab against the foundation.

- The restrained shrinkage of SFRC pavements

The moisture transport analysis is carried out and the time history of the spatial moisture profiles is calculated. The moisture transport analysis is then coupled with a stress analysis to calculate shrinkage stresses and cracks. The history of the stresses and cracks are saved in the memory of the slab as the pre-loading distress.

- The effect of shrinkage distress on the load bearing capacity of SFRC pavements and the long-term performance

As the second stage, the slab under pre-loading distress is analysed for various wheel load configurations. The performance of the slab is analysed in terms of the ultimate load bearing capacity, and cracking performance under monotonic loading. The comparative study is

performed ignoring the pre-loading effects. The effect of early-age distress on the fatigue performance of the pavement is also evaluated, using the fatigue test results obtained by Graeff (2011) as a part of the Ecolanes project for the same R-SFR-RCC mix.

1.3 Layout of the thesis

Chapter 2 presents the review of the state-of-the art in research on environmental effects on fibre-reinforced rigid pavements restrained against volumetric movements as well as previous attempts to study restrained shrinkage in concrete pavements. Chapter 3 explains the moisture transport mechanism and drying shrinkage properties in concrete and the theoretical and experimental methods to quantify them. Chapter 4 describes the experimental work carried out to obtain the material properties required to be fed in the numerical modelling after processing. Chapter 5 deals with data processing to obtain the material properties from experimental data based on inverse analysis. The numerical studies based on a FE model predicting the behaviour of rigid road pavements are presented in Chapter 6. Long-term fatigue analysis is performed in Chapter 7. Discussions, conclusions and suggestions for the future work based on this research are presented in Chapter 8 (Figure 1.6).

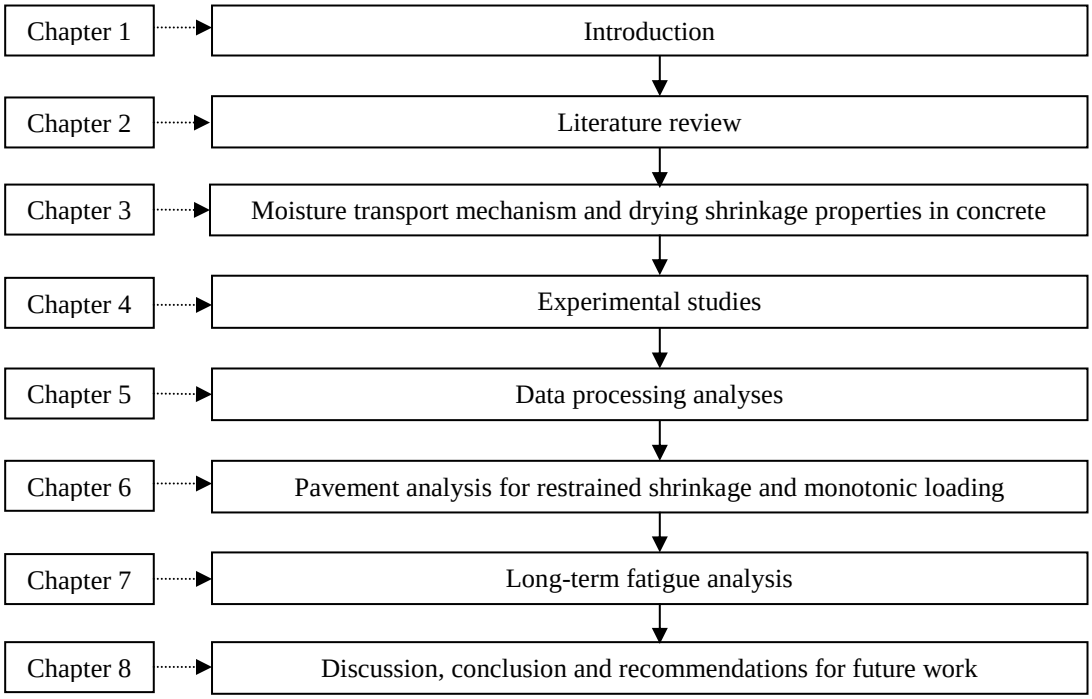

Figure 1.6 Layout of the thesis

Chapter 2

2 Literature review

The chapter begins with an introduction on various types of concrete pavements. The early-age behaviour of concrete pavements is reviewed followed by an investigation in the effect of early-age distress caused by drying shrinkage on the long-term performance of concrete pavements. Previous studies on restrained shrinkage in different types of concrete pavements are reviewed and finally the pertinent findings are discussed and conclusions are made.

2.1 Rigid pavements

Pavements are structural systems that should provide a uniform riding surface for a given period of time, requiring only low maintenance. Unlike flexible pavements, rigid pavements do not deflect much locally under traffic load (Figure 2.1).

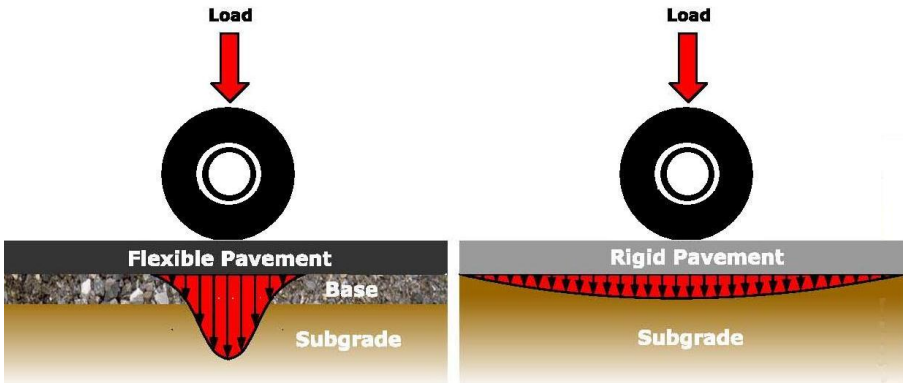

(a) (b)

Figure 2.1 Stress distribution (a) Flexible pavement; (b) Rigid pavement

Rigid pavements tend to distribute the load over a relatively wide area of the subgrade preventing concentrated pressure in the foundation. Excessive foundation pressure may increase irrecoverable deformation and cause differential settlement. Stresses in rigid pavements arise from two sources:

- Imposed loads
- Volume changes (thermal expansion, shrinkage or swelling)

There are various types of concrete pavements based on the concrete type, construction technique and structural design. Improved concrete technology and construction techniques have brought new possibilities such as SFRC and RCC pavements.

2.1.1 Conventional Concrete (CC) pavements

CC pavements are constructed using normal concrete, placed with side formworks and compacted using vibrators. CC pavements are practically grouped in two major types, based on their continuity and reinforcement; Jointed Plain Concrete Pavements (JPCP) and Continuously Reinforced Concrete Pavements (CRCP). Other possible types such as Jointed Reinforced Concrete Pavements (JRCP) or Palin Concrete Pavements (PCP) (without tie bars or dowels) are not commonly used. JRCPs are laborious due to the combined need for joints and reinforcement, and PCPs are only efficient for small concrete slabs (Graeff, 2011).

2.1.1.1 Jointed Plain Concrete Pavements (JPCP)

Due to considerable differences between the strength of concrete in tension and compression, the tensile strength usually dominates the pavement design. Therefore, in plain concrete pavements the compressive capacity of the slab remains largely unused. In flexure, for short-term loading the material in general remains in the elastic domain until cracking takes place (Figure 2.2). Hence, the structural behaviour of JPCP can be predicted by elastic analysis.

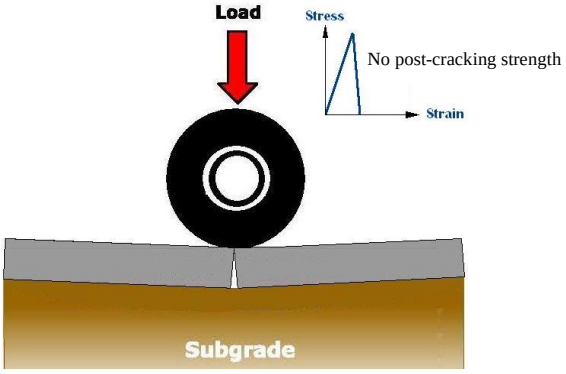

Figure 2.2 Brittle cracking, plain concrete

Since no control on the crack opening is provided in plain concrete pavements, design of transversal and longitudinal joints, as "prearranged" cracks, are of utmost importance (Figure 2.3).

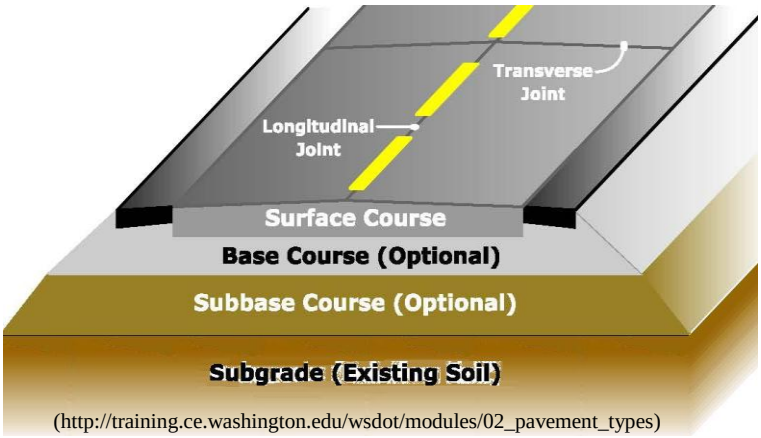

(http://training.ce.washington.edu/wsdot/modules/02_pavement_types)

Figure 2.3 Longitudinal and transversal joints

Joints release volumetric changes by allowing controlled horizontal movement. The relative vertical movements across the joints are restricted by installing load transferring devices and the vertical continuity of the slab is ensured (Figure 2.4).

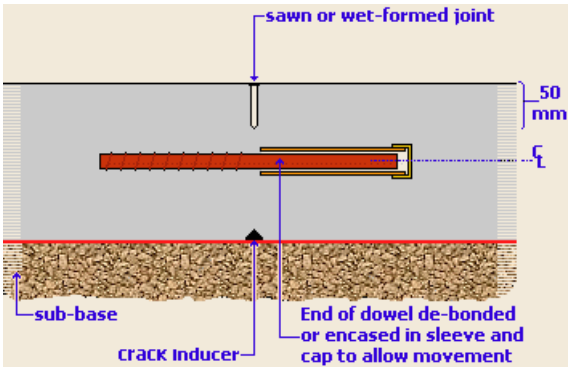

(http://www.pavingexpert.com/concjnt1.htm)

Figure 2.4 Dowel bars in a crack control joint

If the vertical movement is not restricted, the joint acts as a free edge with a load bearing capacity less than 50% of the interior areas (Concrete Society TR34, 2003). To restrict vertical movements dowel bars or reinforcing bars must be provided across the joints. Dowel bars are installed for free-movement joints, and for restrained-movement joints reinforcing bars pass across the joints (Concrete Society TR34, 2003). Aggregate interlock can also help

to improve the load transfer capacity across sawn (or wet-formed) restrained-movement joints. However, the effectiveness of the aggregate interlock is limited and depends on the width of the joint opening. When the opening becomes wider than 0.5 mm, some aggregate interlock is expected to be lost (Rogers, 2003; Mayhew et al., 1987), and when the width exceeds 1.3 mm, a complete loss of aggregate interlock is predicted (Mayhew et al., 1987).

Other than movement releasing joints, the other reason for the provision of joints in concrete pavements is to make breaks in the construction process (Concrete Society TR34, 2003).

Joints provide additional surfaces for deterioration (Walker, 2002) and are costly to install. In addition, they may cause faulting and affect the riding quality (Walker, 2002).

2.1.1.2 Continuously Reinforced Concrete Pavements (CRCP)

Jointed pavements require more maintenance than CRCP (Rogers, 2003). To avoid using many joints structural reinforcement is required (Figure 2.5).

Although cracks are likely to occur in CRCPs, if they are neither too wide nor too close, they do not give rise for concern. Reinforcement keeps the cracks tightly closed, maintaining a high load transfer via aggregate interlock across the cracks and improves the structural integrity of the pavement. Thinner slab thickness and superior long-term performance can justify the initial cost of CRCPs and make them cost effective over the life time of the pavement (Hassan et al., 2005).

Figure 2.5 Reinforcement for CRCPs

For reinforced concrete pavements a significant part of the load bearing capacity is developed after cracking and mobilization of the force in the reinforcement (Figure 2.6). Therefore, the slab enters the non-elastic domain of structural behaviour and using elastic assumptions may

lead to a significant underestimation of the slab capacity.

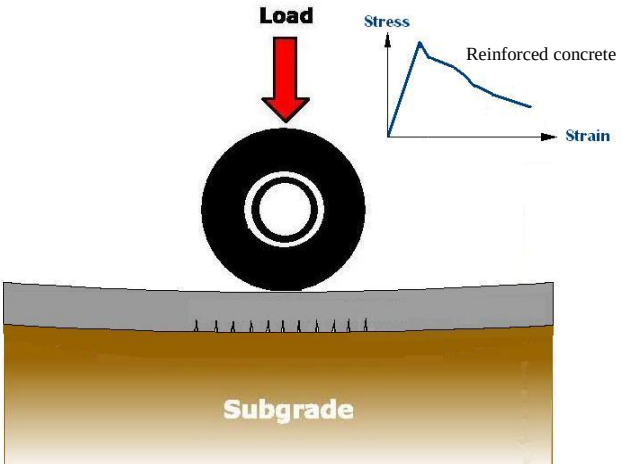

Figure 2.6 Distributed cracking in reinforced concrete pavements

Usually, volume changes produce large stresses in CRCPs resulting in extensive transversal cracking. Typical crack spacing in CRCPs ranges from 0.9 to 2.4 m (Darter, 1977).

2.1.2 SFRC pavements

SFRC pavements behave similar to conventionally reinforced (with rebar) concrete pavements, because of their ductile behaviour. However, randomly positioned steel fibres do not act as efficiently as appropriately placed reinforcing bars. Therefore, the effective amount of reinforcement is much less in SFRC. As an example, Barros et al. (1999) reported that 40 kg/m^3 of hooked-end steel fibres can provide a maximum resistance under positive and negative moments at least equivalent to slabs conventionally reinforced with 19 kg/m^3 of wire mesh (284 mm² / m in both faces). More information on use of fibres in concrete, various types of steel fibres and structural benefits of steel fibres particularly in ground supported slab is given bellow.

2.1.2.1 Fibre reinforced concrete

The idea of improving crack resistance of concrete, by reinforcing it with closely spaced fibres, was first explored in the early 1960s (Romualdi et al., 1963 cited in Yin et al., 1989).

Many different types of fibres have been historically used in concrete consisting of natural fibres (without industrial treatment, such as horse hair, asbestos and sisal bamboo), synthetic

fibres with organic origin (such as cotton, polypropylene, acrylic, polyethylene), and synthetic fibres with inorganic origin (such as carbon, ceramic, glass, and steel) (Graeff, 2011).

Steel fibre is the most commonly used fibre type in construction (Graeff, 2011). The practical use of steel fibres in pavement construction has been mainly focused on industrially produced steel fibres, so far. Industrial steel fibres are expensive, and considering their lower reinforcing efficiency compared to steel bars (due the random dispersion of fibres) their use may be only justifiable in rapid construction. Using recycled steel fibres (Section 2.1.2.3) is a cheaper and more environmentally friendly alternative.

2.1.2.2 Industrially produced steel fibres

Industrial steel fibres are produced in different shapes. The most common geometries are straight, crimped, crimped-end (or hoked), and coned-end (Figure 2.7). Typical lengths of steel fibres range from 6.4 to 76 mm, and their typical aspect ratios (length/diameter) range from 20 to 100. The ability of fibres to bond with the concrete depends on the aspect ratio of the fibres and the surface characteristics. Hence, the deformed shapes of fibres improve bond.

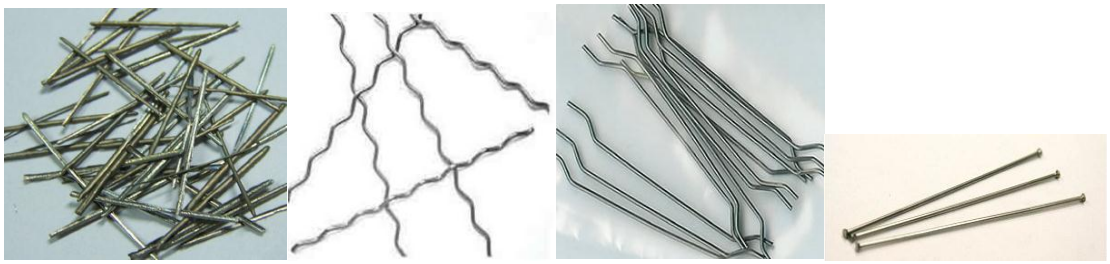

(a) (b) (c) (d)

Figure 2.7 Industrial steel fibres; (a) straight; (b) crimped; (c) crimped-end; (d) coned-end

2.1.2.3 Recycled steel fibres from post-consumer tyres

The use of recycled tyre wire as concrete reinforcement (Figure 2.8) has been demonstrated and patented by the University of Sheffield (USFD, 2001; Tlemat, 2004). Several studies have been performed since at the University of Sheffield investigating the mechanical properties of concrete reinforced with recycled steel fibres from post-consumer tyres (Pilakoutas et al., 2001; Pilakoutas et al., 2004; Tlemat, 2004; Tlemat et al., 2003[a]; Tlemat et al., 2003[b] ; Tlemat et al., 2006; Neocleous et al., 2006; Graeff, 2011; Graeff et al., 2012), in addition to further studies performed by the Ecolanes project. These studies showed comparable behaviour of R-

SFRC with SFRC reinforced with industrial fibres (I-SFRC).

Figure 2.8 Recycled steel fibres from post-consumer tyres

To maximise the improvement in the mechanical properties of concrete by adding recycled steel fibres fibres characteristics (length, diameter, aspect ratio, and fibre content) must be optimised. This issue has been investigated by the Ecolanes project. Obtaining recycled fibres from post-consumer tyres, of appropriate geometry and quality, needs special processes. These processes were also investigated and improved by the Ecolanes project.

2.1.2.4 The procedure of extracting steel fibres from post-consumer tyres

The most economical and environmentally friendly process to extract fibres from tyres is mechanical treatment by shredding (Figure 2.9). There are other alternatives such as pyrolysis and cryogenics. As a first stage in shredding process the bead wires are normally removed mechanically from truck tyres due to their high strength and size (beads are structural components that frame the edges to anchor the tyre to the metal wheel rim to keep it in place during driving actions). Tyres (car or truck tyres) are then passed through a series of cutting and crushing equipment to be cut in progressively smaller pieces.

Shredding and crumbing is normally repeated several times and with different settings to produce granulated rubber of various sizes useful for various applications. During the cutting stages, steel fibres are detached from rubber and collected by magnets (Musacchi et al., 2007). Polymeric fibres and extra particles are removed from steel fibres by blowing or by vacuum.

(a) (b)

(c) (d)

Figure 2.9 Mechanical treatment to extract recycled steel fibres (a) Tyre granulator (Musacchi et al., 2007); (b) Shredded tyres; (c) Collected granulated rubbers; (d) Collected steel fibres

A sieving process is then performed on fibres to obtain fibres with the optimum length (Musacchi et al., 2008). Earlier research at the University of Sheffield has revealed that the benefits of steel tyre-cord in concrete is best utilised, if the length of the steel tyre-cord fibres is in the range of 15 to 25 mm and the diameter is around 0.2 mm (USFD, 2001). The optimum length of fibres has been obtained based on improvements in the mechanical behaviour of concrete and in avoidance of balling during mixing of concrete. Steel fibres shorter than the optimum range are not efficient, since they cannot be properly anchored to the concrete. Longer fibres than the optimum range are prone to balling, since they may get

interlocked among themselves due to their irregular shape (Figure 2.10).

Workability of concrete is also influenced by the aspect ratio of fibres and the volume content of fibres added to concrete. Higher volume contents of steel fibres are not desirable due to increasing the possibility of balling and reduction in workability. The optimum practical amount of recycled fibres, determined by the Ecolanes project, is 50-60 kg per each cubic metre of concrete.

Figure 2.10 Fibre balling in concrete

2.1.2.5 Structural use of steel fibres

SFRC has two main applications: (1) ground-supported slabs; and (2) reinforcement of tunnels by shotcrete. This material is used, to a lesser extent, for precast segments, bored piles, and for non-load bearing irregular shape elements. The ductility of SFRC makes it effective under dynamic and cyclic loads and suitable for use in blast-resistant construction and highway pavements (Paskova et al., 1997).

Using fibres in concrete leads to increased strain capacity as well as energy absorption capacity (ACI 544.4R, 1999; Concrete Society TR34, 2003). Therefore, the resultant composite concrete can have considerable ductility or "toughness" (Meda et al., 2004[a]; Altoubat et al. 2008).

Displacement control tension, compression and bending tests reveal the high-energy absorption capacity of SFRC (Barros et al., 2001), but as the result of adding steel fibres the flexural strength of concrete is enhanced much more than direct tension and compression (ACI 544.1R, 1996). This is attributed to stress and strain redistribution along the specimen depth after cracking.

Under static loading, the area under the load-deflection curve in flexure represents the total energy absorbed up to a specific deformation. Two values usually define the flexural strength characteristics of SFRC. One of these values termed first-crack flexural strength represents the load at which the load-deformation curve departs from linearity (point A in the typical curve shown in Figure 2.11). The other value, which is usually called modulus of rupture or the ultimate flexural strength, corresponds to the maximum load achieved (point C in Figure 2.11) (ACI 544.4R, 1999). Different amounts and types of fibres used in a similar mix can result in a range of flexural load-deflection curves.

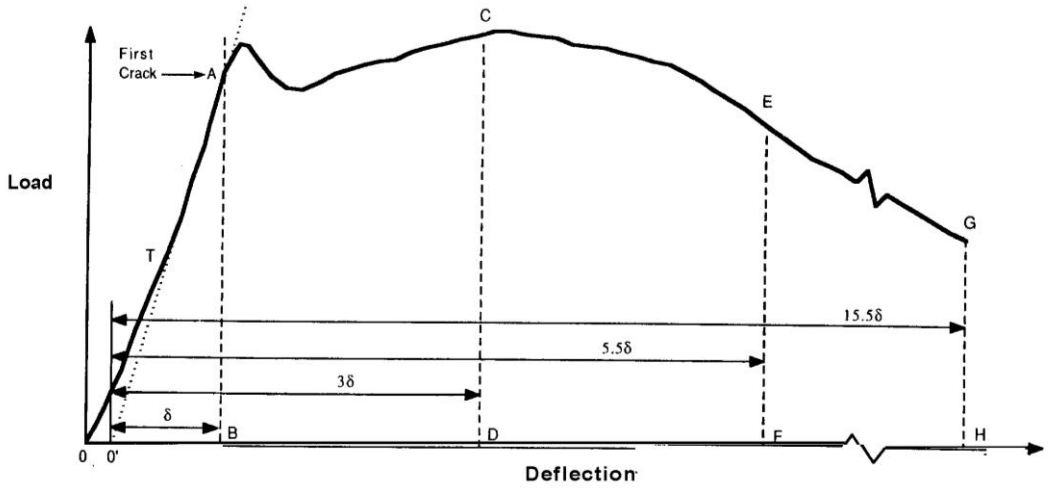

Figure 2.11 Flexural characteristics of SFRC (ACI 544.4R, 1999)

Until recently, in structural members such as beams, columns, or elevated slabs (such as roofs and suspended floors), where flexural or tensile loads occur, reinforcing bars had to be used to resist the tensile stresses. This is because of the variability of fibre distribution which could cause low fibre content in critical areas, and unacceptable reduction in strength (ACI 544.4R, 1999). In applications such as floors on ground and pavements, where the presence of continuous reinforcement is not essential to the safety and integrity of the structure, steel fibres can be used alone (Sorelli et al., 2006; Chen, 2004; ACI 544.4R, 1999).

2.1.2.6 Use of steel fibres in ground supported slabs

Fibres in concrete slabs in ground applications have been used for over 40 years (Roesler et al., 2004; Altoubat et al. 2008). For ground slabs use of steel fibre reinforcement could be beneficial and economically competitive, compared with plain concrete and conventionally reinforced concrete slabs (Barros, 1999; Chen, 2004; Nanni et al., 1989; Tatnall et al., 1992

cited in Barros et al., 2001). SFRC slabs can be 30%-40% thinner than plain concrete slabs (Barros et al., 1997). In addition, when compared with conventional reinforced concrete pavements, SFRC pavements are simpler and faster to construct and reduce trip hazards. Slip forming or roller compaction concreting also becomes a lot easier.

The improved toughness of SFRC (as explained in Section 2.1.2.5) is particularly important in the case of statically indeterminate structures like pavements as it allows for redistribution of forces after cracking (Meda et al., 2004[a]). As a result of moment redistribution, the addition of fibres increases the failure load of slabs and also assists in crack propagation resistance and crack bridging (Roesler et al., 2004; Altoubat et al., 2008). Sorelli et al. (2006), after extensive experimental investigations, showed that steel fibres, even at relatively low volume fractions (<1%), significantly enhance the bearing capacity and ductility of slabs on ground. This enhanced load-bearing capacity can be considered in optimising floor thickness design (Concrete Society TR34, 2003). Steel fibres can also improve resistance to material deterioration as a result of fatigue, impact (Sorelli et al., 2006), shrinkage, or thermal stresses (Vondran, 1991 cited in Meda et al., 2004[a]).

Despite the extensive experience in the use of SFRC in ground slabs, SFRC pavements are not widely used in surface transport infrastructures. The reason for this is that steel fibres do not act in the same manner as reinforcing bars in conventionally reinforced concrete pavements. Therefore, the well-developed design methods used for conventionally reinforced concrete pavements cannot be used for SFRC pavements. Furthermore, using the design criteria developed for plain concrete pavements incorporation of steel fibres is not sufficiently rewarded. Design guidelines specifically developed for SFRC (Concrete Society TR34, 2003; ACI 544.1R, 1996; ACI 544.4R, 1999) are normally aimed at ground slabs rather than road pavements, and do not cover all aspects of their behaviour. For instance, early-age distress and long-term behaviour are not well addressed by the existing design guidelines for SFRC.

2.1.3 RCC pavements

Roller compacted concrete (RCC) is a zero slump concrete mix which is placed and compacted using modified asphalt pavers and vibratory rollers (PCA, 2006). It is drier than CC, since it should be stiff enough to be compacted with rollers. Since RCC is placed in the same manner as paving, it is mainly suitable for dam and pavement applications.

RCC generally has time and cost benefit over CC. Since RCC needs lower water content, for the same water to cement ratio (w/c) lower cement content is required for RCC compared to CC (w/c is an index for representing strength of concrete). Another advantage of RCC is its lower hydration heat due to lower cement content, which makes it suitable for mass concreting. This advantage is more highlighted for gravity dams in which the cement content can be reduced further or be partially replaced by fly ash (since not too much strength is required), leading to much lower heat generation and lower cost.

In pavement applications, RCC is typically constructed without joints, dowels or steel rebar. RCC does not need forms or finishing. These characteristics make RCC fast, simple, and economical for any type of heavy-duty pavement. In fact, RCC has the strength and performance of CC with the economy and simplicity of asphalt, in addition to long service life and minimal maintenance (PCA, 2006).

2.1.3.1 Elimination or reduction of joints in RCC pavements

In concrete pavements, joints should be possibly avoided, because they increase the potential source of problems by adding more edges to the surface (Concrete Society TR34, 2003).

In RCC pavements, due to compaction of the zero-slump mix with heavy duty rollers, it is not practically viable to install load transferring devices such as dowel bars. Therefore, RCC pavements are generally not jointed but are allowed to crack naturally. Spacing between these cracks is usually irregular, ranging from 1.2 to 2m for plain RCC (although much greater and much lower crack spacing has also been reported) (UFC, 2004). In some cases, saw cuts of one-fourth to one-third of the pavement depth have been made to initiate cracks (or fresh cuts which are created before compaction and filled with bitumen). In these cases, the U.S. Army Corps of Engineers (UFC, 2004) recommends the distance of the artificially-made cracks in the range of 1.5 to 2.25m.

Although, aggregate interlock can provide some load transfer capacity across sawn/freshly-cut partial-depth joints for small joint openings, its effectiveness depends on the joint opening and decreases with time (Concrete Society TR34, 2003). Hence the efficiency of load transferability through aggregate interlock cannot be assured for the whole life of the pavement. Pittman (1996) showed that load transferability across RCC joints may decrease to 22%, and the U.S. Army Corps of Engineers design procedures for plain RCC pavements

(UFC, 2004) conservatively assumes no load transferability at RCC pavement joints.

Previous studies (Nanni et al., 1989, Thom et al., 2000) have shown that using fibres in RCC can improve the load transfer across sawn (/freshly-cut) joints or natural joints (cracks) and help to control crack opening. Furthermore, use of steel fibres in RCC helps to reduce the number of potential contraction joints to a minimum. Since conventional reinforcement is not viable in RCC, steel fibres can also act as reinforcement. Conclusively, SFR-RCC pavements can be treated as CRCPs.

However, studies focusing on reinforcement of RCC with steel fibres are very few in the literature (Nanni et al., 1989; Thom et al., 2000; Graeff, 2011; EcoLanes, 2006-2009). Use of recycled steel fibres in RCC has only been examined for the first time in the EcoLanes project.

2.2 Early-age and early-life distress in pavements

Slab distress in pavements is caused not only by external loading but also by environmental factors that affect thermal and moisture variations particularly at early ages (ACI 360R, 1992). Early age distress in concrete arises from volume changes such as restrained drying shrinkage, autogenous shrinkage and thermal deformations, which can cause tensile stresses when strength is relatively low (Altoubat et al., 2001).

There is no universally accepted definition of early-age in the literature (Liu et al., 2005). Ruiz et al. (2005[b]) defined the early age as the first 72 hours after pavement construction, whilst they assumed the "early life" as approximately one year after construction.

Ruiz et al. (2005[b]) reported that, based on previous experience, during the few days after construction there is significant potential for damage to the pavement structure due to excessive environmental related stresses. However, the cracking behaviour of CRCPs continues to change during the first year after construction (Ruiz et al., 2005[b]). In the first days after construction, volume changes usually initiate in concrete as a result of environmental factors. During the first year, stresses begin to build up due to the existing restraints against slab deformation (Ruiz et al., 2005[a]).

In CRCPs it has been reported that, during the first year after construction, the crack spacing

decreases rapidly, then remains nearly constant during the service life, and at the end of the fatigue life decreases again (McCullough et al., 2000 cited in Ruiz et al., 2005[b]) (Figure 2.12).

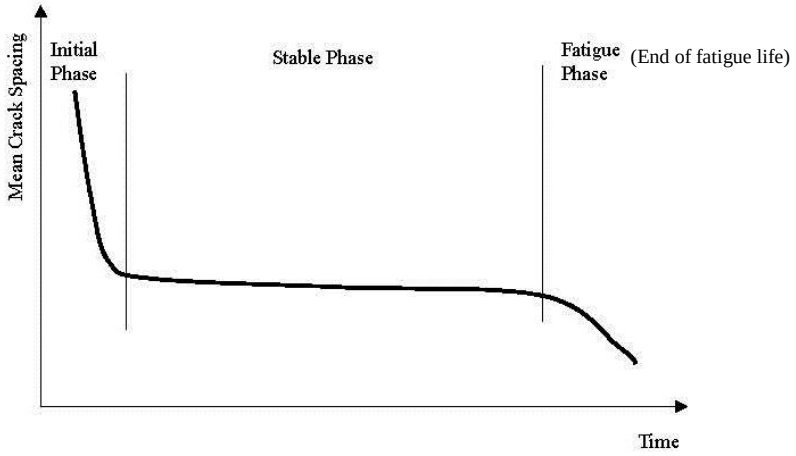

Figure 2.12 Conceptual reduction of the mean crack spacing over time for CRCPs (McCullough et al., 2000 cited in Ruiz et al., 2005[b])

In the current research, for more clarity "early-age" refers to the whole first year after construction of the pavement in which the initial moisture (and temperature) in the concrete can be considered to have stabilised with the environment.

Based on the above definition, the "early-age" behaviour of concrete pavements is generally influenced by the following factors:

- Thermal variations inside the pavement, as the result of heat generation caused by hydration and being exposed to daily and seasonal environmental conditions; these variations gradually reach the final mean stable temperature with smaller amplitude. The final mean stable temperature is the mean annual air temperature. Concrete placing temperature can also affect the thermal variations inside the concrete pavement.

- Shrinkage of the concrete slab, mainly as a result of drying and autogenous water loss; this phenomena will be described further in Section 2.2.1.

- Curling of the concrete slab as a result of non-uniform volumetric changes.

- Internal restraint from the concrete slab against curling.

- External restraint from the slab-foundation interface against the volumetric

movements.

- Creep / relaxation phenomena under restrained volumetric movements which is a delayed response to a built up of stresses and strains.

Since the main focus of this research is the "early-age" drying shrinkage and its consequent effects on the long-term performance of the pavement, this issue is discussed further in the following sections.

2.2.1 Shrinkage

Shrinkage is volumetric changes due to loss of water from the concrete (either to internal chemical reactions or to the environment). Concrete members are affected by four main types of shrinkage (Gribniak et al., 2008):

- Plastic shrinkage, which is loss of moisture from freshly poured concrete to its surroundings.
- Autogenous shrinkage, which is caused in the early age of concrete by loss of water from capillary pores as a result of hydration of cement without migration of moisture to the surrounding environment.
- Carbonation shrinkage, which is caused by the chemical reaction of carbon dioxide in the air with various products of cement hydration.
- Drying shrinkage, which is the volumetric change in the concrete as a result of movement of water from hardened concrete into the surrounding environment.

The two components of shrinkage, usually taken into account in structural analysis, are drying shrinkage and autogenous shrinkage (Gribniak et al., 2008). If the pavement is cured properly, plastic shrinkage can be eliminated (Ruiz et al., 2006). Autogenous shrinkage is more important for high-strength concrete where the water to cement ratio (w/c) is low (Ruiz et al., 2005[b], Ruiz et al., 2006; Fernandez et al., 2007). For normal strength concrete autogenous shrinkage has been observed to be less significant (Ruiz et al., 2005[b]), varying between 20 and 110 micro-strains which is about 10 to 20 % of the long-term shrinkage (Silliman et al., 2006 cited in Gribniak et al., 2008; Fernandez et al., 2007). Therefore, autogenous shrinkage

is usually neglected in comparison with drying shrinkage in the case of normal strength concrete (Figure 2.13).

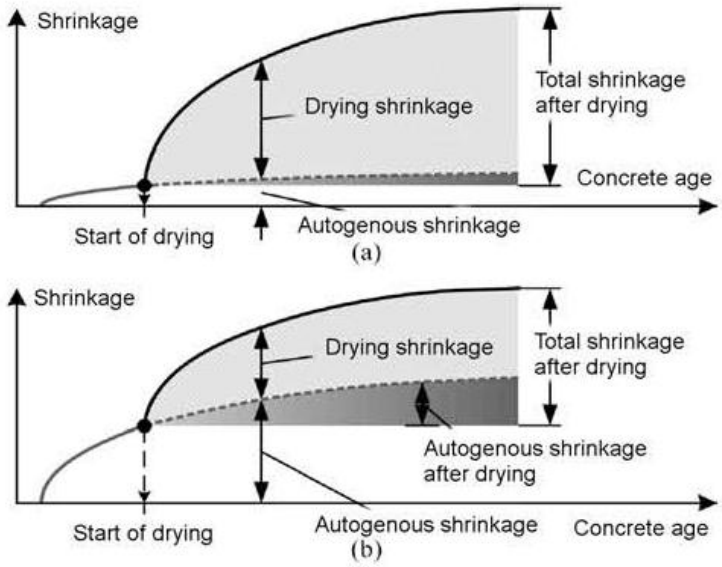

Figure 2.13 Shrinkage strain components in (a) normal; and (b) high strength concrete (Sakata et al., 2004 cited in Gribniak et al., 2008)

2.2.1.1 Drying shrinkage

Drying shrinkage occurs when concrete is exposed to a drying environment, and is known as the most widely recognized source of volume change in concrete (Liu et al., 2005). In pavements, water evaporation from the exposed top surface creates moisture gradients between the top and bottom surface. Moist subgrades can also magnify the moisture gradients. Therefore the upper half of the slab shrinks more than the lower half, although some shrinkage occurs in all three dimensions (ACI 360R, 1992). It should be noted that the distribution of moisture during the drying time is highly nonlinear (Kwon et al., 2008).

Factors affecting the extent of drying shrinkage are: material properties, age of concrete when exposed to drying environment, volume to surface ratio of the concrete mass, relative humidity and temperature of the drying environment (ACI 544.1R, 1996).

When concrete dries for the first time, the extent of shrinkage strains are much bigger than when it is rewetted and dries for the second time. In fact a large amount of the first time drying shrinkage cannot be recovered upon rewetting (Bisschop, 2002). Pioneer investigations

(Pickett, 1956; Helmuth et al., 1967) have shown that irreversible shrinkage can be as large as 60% of the ultimate first drying shrinkage (cited in Bisschop, 2002).

2.2.1.2 Drying shrinkage of SFRC

Early-age drying shrinkage of SFRC has received considerable attention in the literature. One of the primary benefits of fibre reinforcement is to reduce the adverse effects of shrinkage (Li et al., 2006; Altoubat et al., 2003, Meda et al., 2004[b]; ACI 544.1R, 1996; Swamy et al., 1979; Chern et al., 1989). Fibres can reduce shrinkage strains and/or its associated potential for crack growth.

In some studies, the improvement in the shrinkage behaviour of SFRC has been attributed to the reduction of free shrinkage strain, due to mobilising the bond strength between the fibres and the concrete matrix which contributes to physically restraining shrinkage (Chern et al., 1989; Mangat et al., 1984, Li et al., 2006; Tan et al., 1994; Zhang et al., 2001[b]). As reported by Tan et al. (1994) and Zhang et al. (2001[b]), the higher the steel-fibre content, the lower is the free shrinkage strain. While other studies say that cracking control is the most significant effect of fibres in shrinkage of concrete (Swamy et al., 1979; ACI 544.1R, 1996; Grzybowski et al., 1990). Some studies have also reported that addition of fibres leads to higher free drying shrinkage due to increasing the porosity of concrete (Wang et al., 2001; Aly et al. 2008 cited in Graeff, 2011; Graeff, 2011).

Li et al. (2006), in a study of non-uniform drying of SFRC, reported that the presence of fibres reduces the overall drying shrinkage, although for a low volume fraction of fibres the degree of shrinkage reduction may not be great.

Balaguru et al. (1988) experimentally investigated shrinkage and creep behaviour of SFRC mixes containing 44 kg/m^3 hooked fibres with a length of 50 mm. They reported that shrinkage strains were generally less for SFRC as compared to plain concrete (Figure 2.14), and creep strains were consistently higher for SFRC (Figure 2.15).

Grzybowski et al. (1990) reported that addition of around 1% by volume steel fibres does not alter greatly the drying shrinkage of concrete. However, fibres bridge cracks and significantly reduce the width of cracks resulting from restrained drying shrinkage, even with a small amount of fibres, as small as 0.25% by volume (Grzybowski et al., 1990).

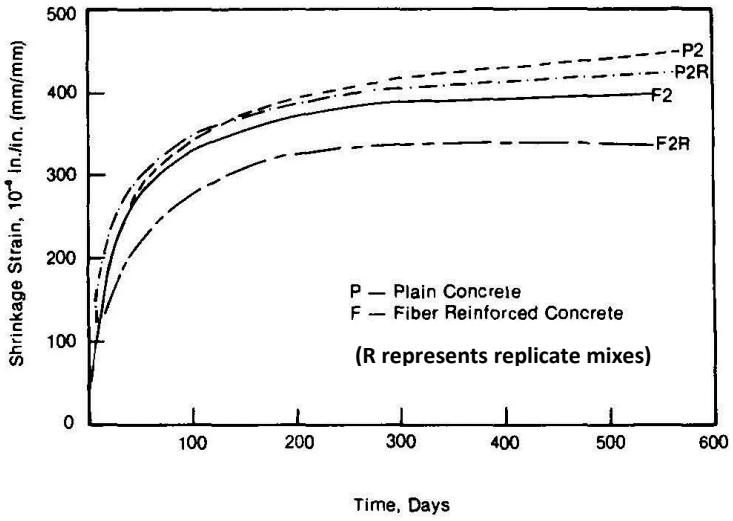

Figure 2.14 Comparison of shrinkage strains for PC and SFRC (Balaguru et al., 1988)

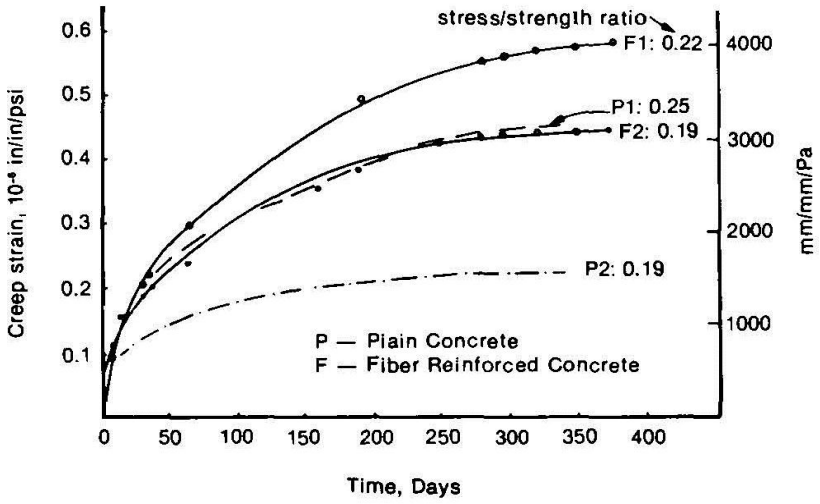

Figure 2.15 Comparison of creep strains PC and SFRC (Balaguru et al., 1988)

Zhang et al. (2001[b]) analytically compared the effect of fibre content in the range of 0.5% to 5% by volume on free shrinkage strains (Figure 2.16). They reported that although the presence of fibres reduce the overall drying shrinkage, the reduction is not great for the low volume fraction of fibres. This study stated that the restraining effects of fibres prior to cracking are generally beneficial, but of secondary importance, while their restricting effect on crack opening after matrix fracture is of primary importance. Steel fibres play three roles in this case: (1) increasing the tendency for multiple cracking, (2) transferring tensile stresses across cracks (by maintaining the residual tensile strength even after cracking), (3) avoiding micro-crack propagation by maintaining the stress transfer for a long time allowing for

healing / sealing of cracks in long-term (Hoff, 1987 cited in ACI 544.1R, 1996).

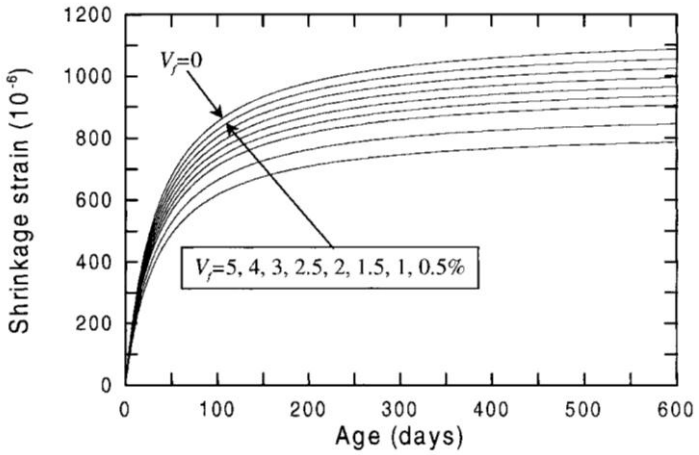

Figure 2.16 Influence of fibre content on free shrinkage behaviour (Zhang et al., 2001[b])

Kwon et al. (2008) revealed that steel fibres reduce crack widening. In SFRC several micro-cracks are formed and propagated as a result of drying shrinkage, while in plain concrete the weakest among the micro-cracks develops into a macro-crack (Kwon et al., 2008).

Graeff (2011) studied shrinkage of SFRC reinforced with industrial and recycled fibres, and showed that for various amounts of fibre contents (ranges between 2-6% by weight) the free shrinkage of concrete is slightly increased by adding fibres. This effect was attributed to higher porosity of SFRC compared to plain concrete.

The level of developed stresses due to restrained shrinkage can also be a function of the creep-relaxation properties of concrete (Ruiz et al., 2005[b]). Altoubat et al. (2001) studied the early age effect of fibre reinforcement on tensile creep and restrained shrinkage behaviour of concrete. In that study it was reported that low volume fraction of steel fibres (in the range of 0.5% by volume) delay shrinkage cracking. This was attributed to the ability of the fibres to improve stress relaxation by the creep mechanism and by engaging a greater volume of the matrix in stress transfer and reducing damage at the micro level. That study revealed that tensile creep can relax shrinkage by 50%.

Afterward, Altoubat et al. (2003), in a study of tensile creep of fibre reinforced concrete, divided creep mechanisms into beneficial aspects associated with intrinsic creep mechanisms and detrimental aspects associated with apparent creep mechanisms (microcracking). In that study the effect of steel fibres in improving the overall creep performance of concrete was

attributed to the tendency of steel fibres to enhance beneficial creep aspects and reducing the detrimental creep mechanisms as a result of microcracking. They concluded that steel fibres enhance desirable creep mechanisms and suppress undesirable ones.

The literature reviewed in this section revealed that adding steel fibres can alter free drying shrinkage of concrete, but in different ways (there is not a general agreement on the effect of steel fibres on free drying shrinkage of concrete). However, in the practical range of under 1% (by volume) drying shrinkage properties do not alter significantly. On the contrary, the restricting effect of fibres on crack opening after matrix fracture is significant. It can also be argued that the effect of creep deformation during the drying period might be considerable. These results are mostly based on incorporating industrial fibres in concrete. For concrete reinforced with recycled fibres only one study by Graeff (2011) has been reported so far.

2.2.1.3 Drying shrinkage of RCC

The early age shrinkage behaviour of RCC has been reported to be quite different to that of CC (Shaw, 2010).

Pittman et al. (1998) reported that the drying shrinkage of RCC pavement is relatively low compared to CC pavements, resulting in a crack spacing much greater for RCC than what is expected for CC pavements. Pitman et al. (1998) concluded that the greater crack spacing for RCC is possibly due to the lower moisture content. Delatte (2004) also pointed out that shrinkage and differential shrinkage of RCC pavements should be less than CC due to the lower paste content of RCC. Luhr (2004) revealed that the crack openings are usually small in RCC pavements due to generally less shrinkage and good interlock provided by crushed aggregates.

The drying shrinkage of concrete depends not only on the water content of the mixture, but also on the porosity of concrete. Although less paste content in RCC may have a positive effect on reducing the volumetric changes induced by drying, the more voids and pores existing in RCC will have adverse effects on the moisture transport properties. Higher porosity of RCC, which is caused globally by lower paste content and locally by insufficient compaction, increases the moisture diffusivity in concrete pavements. Therefore, drying and differential drying of the pavement may be accelerated. In the case of SFR-RCC even higher porosity is expected as the result of incorporating fibres.

Studies performed during the Ecolanes project (Graeff, 2011) investigating free shrinkage of RCC showed that RCC mixes have higher free shrinkage strains than CC mixes (for both fibre reinforced and plain mixes). Graeff (2011) showed that adding fibres increases the free shrinkage strain of RCC, when reinforced with recycled fibres. R-SFR-RCC presented around 30% higher free shrinkage strain than RCC with industrial fibres and plain RCC mixes. However, no conclusion on the performance of recycled steel fibres on the behaviour of RCC pavements under restrained conditions can be made, since the improvement in the shrinkage resistance of SFRC is mainly observed in a restrained situation.

The published research work on the shrinkage properties of R-SFR-RCC is limited to the studies performed by Graeff (2011).

2.2.2 Restraint and distress

Shrinkage of concrete pavements is resisted by external resistance of the underlying boundary against shortening, or by internal restraint against non-uniform volumetric change (Kwon et al., 2008). The restrained shortening at early age may stress the concrete in excess of its early tensile strength (ACI 360R, 1992), and it is well recognised that shrinkage movements can cause serious cracking (micro-cracks and macro-cracks) in concrete pavements (Hughes, 2003, Grasley et al., 2004).

2.2.2.1 External restraints

External restraints are mainly imposed due to the frictional resistance between the slab and the foundation. These stresses are created even if there is a uniform temperature or moisture drop in the entire member, and causes tensile stresses to build up at locations of restraint (slab/base interface) (Delatte, 2008). These stresses may cause cracks to start from the bottom face of the slab and develop towards the top face (Figure 2.17).

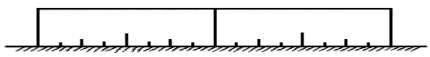

Figure 2.17 Initiation and propagation of cracks at the bottom face as the result of external restraint against slippage

If drying shrinkage in a concrete pavement was distributed uniformly through the depth it would be of less concern. In that case, it would be possible to accommodate the movement

by reducing the frictional resistance between the slab and the foundation. The differential shrinkage through the depth is a major issue (Jeong et al., 2005).

2.2.2.2 Internal restraints

The internal restraint acts when there is a non-uniform moisture (or temperature) distribution. The deformed shape of the member in this condition (e.g. the curled shape of the slab) causes stresses to be developed. Curling is the distortion of an originally planar slab into a curved shape due to moisture (or temperature) gradient (ACI 360R, 1992). When there is no external force and external restraint, the internal forces should be self-equilibrated. Therefore, both tensile and compressive stresses are developed through the section (Sa et al., 2008). The moisture gradient causing the top surface of the slab to shrink is called a negative gradient. Negative gradient causes the slab corners to curl upwards creating tensile stresses on the top surface and compressive stresses on the bottom surface (Figure 2.18(a)). Positive gradient (usually temperature gradient when the sun warms the top of the slab) causes the slab edges to curl downward creating compressive stress at the top surface of the concrete slab, while the bottom is in tension (Figure 2.18(b)).

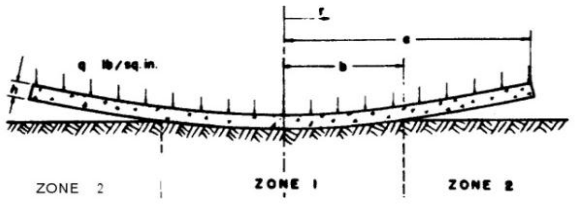

(a)

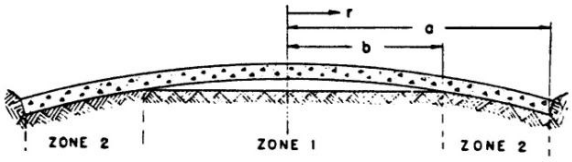

(b)

Figure 2.18 (a) Curling upward; (b) Curling downward (ACI 360R, 1992)

Curling also increases the flexural stresses due to a reduction in the subgrade support (ACI 360R, 1992). The slab dimensions and the stiffness of the support affect the stress induced by curling. Thin sections are more likely to exhibit curling. The stiffer the support and the larger

the slab, the higher the stresses induced in a curled slab (Jeong et al., 2005).

Poblete et al. (1989) monitored twenty pavements and observed a permanent upward curling of slabs in all pavements. Cracks induced due to curling were reported to start from the surface downward and from the edges inward (NCHRP 372, 1995) (Figure 2.19). This kind of cracking is one of the most usual types of cracking for slabs and pavements which is often overlooked by designers (ACI 544.1R, 1996; ACI 360R, 1992 & Kwon et al., 2008).

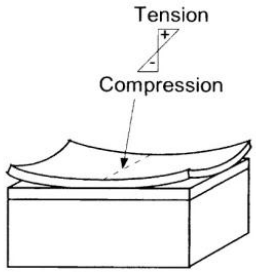

Figure 2.19 Initiation of cracks at the top face as the result of internal restraint against curling

2.3 The effect of early-age distress on the long-term performance of concrete pavements

Premature deterioration in concrete pavements generally influences durability, integrity and long-term service life (Altoubat et al., 2001). The effect of early-age volumetric changes, specifically drying shrinkage, on the performance and the lifetime of concrete pavements can be quite significant (Ye et al., 2007; McCullough et al., 1975 (cited in Ruiz et al., 2005[b]); Kwon et al., 2008; Kim et al. (1998); Zhang et al., 2001[b]; Nam et al., 2006).

Kwon et al. (2008) reported that cracks in highway pavements are often due to drying shrinkage. NCHRP 372 (1995) has reported that differential shrinkage in concrete slabs have produced increased slab stresses and deformations under loads. The stresses induced at the early age of concrete may immediately cause cracking or remain in the pavement as residual stresses. Theses residual stresses limit the capacity of concrete and influence its fatigue life, even if the pavement can resist crack formation at early ages and against the combined effect of traffic and environmental loading (Altoubat et al., 2001; Ruiz et al., 2005[b]). Smith et al. (1990) believe that the combined effect of traffic and early-age environmental loading is the most significant factor affecting long-term fatigue (cited in Ruiz et al., 2005[b]).

Repetitive loading causes existing flaws in the concrete to worsen (Ruiz et al., 2005[b]). As an example Figure 2.20 shows the performance of Jointed Plain Concrete Pavements (JPCP) versus time (Smith et al., 1990 cited in Ruiz et al., 2005[b]). This figure shows that after sustaining a critical number of loads the number of cracked slabs in JPCPs increases significantly following an S-shaped curve. The comparison of the curve considering the early-age cracking with the curve without early-age cracking in Figure 2.20 highlights that the percentage of cracks is significantly higher for the former case. Early-age cracks might be initially tight, but they can extend to full depth and affect the structural integrity of the pavement after traffic loading (Ruiz et al., 2005[b]).

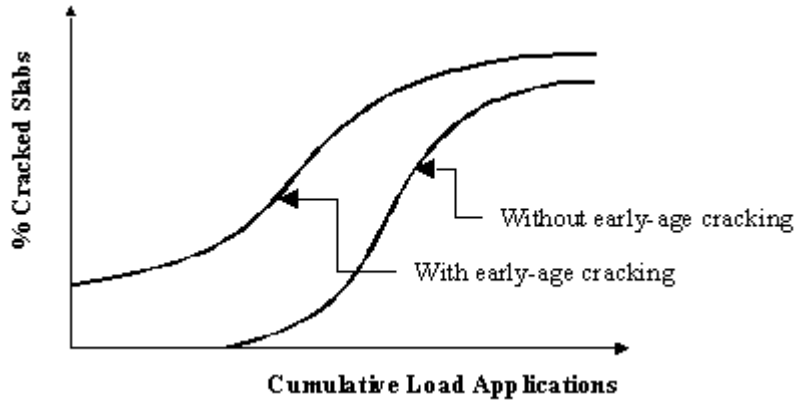

Figure 2.20 Schematic of long-term performance of JPCPs versus time (Smith et al. 1990)

2.3.1 Mode of failure in JPCPs

The long-term failure modes of concrete pavements under the influence of early-age distress have been addressed in several researches (Ruiz et al., 2005[b]; McCullough et al., 1975; and Suh et al., 1992 (cited in Ruiz et al., 2005[b])). Curling of JPCPs has been defined as an early-age indicator of their future performance (Ruiz et al., 2005[b]). Upward curling, as a direct result of non-uniform drying shrinkage, in combination with the self-weight of the slab, induces a high stress region near the drying surface (Lee et al., 2010). It may become more severe considering the fact that curling will affect further the support conditions when the slab lifts off the foundation (Ruiz et al., 2005[b]; Titus-Golver et al., 1998 cited in Ruiz et al., 2005[b]; Delatte, 2008; Lee et al., 2010). Bending stresses resulting from curled shapes and traffic loads when combined with poor subgrade support, cumulatively damage the pavement structure (Ruiz et al., 2005[b]; Jiang et al., 1998).

Partially supported upward curled slabs lead to corner cracking (Delatte, 2008; Ruiz et al., 2005[b]) or edge cracking (ACI 544.4R 1999) (Figure 2.21). Initially developed microcracks, though not visible to the naked eye, will get longer and wider to form a visible crack over time as a result of fatigue loading. Top-down corner break is the mode of failure in this condition (Ruiz et al., 2005[b]).

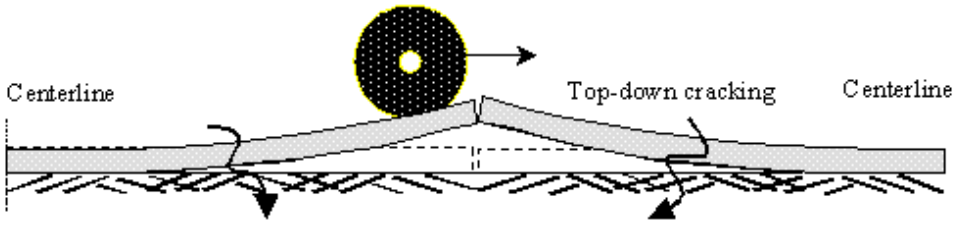

Figure 2.21 Schematic of top-down corner cracking in pavements with upward curling as the result of loss of support and wheel loading (Ruiz et al., 2005[b])

Figure 2.22 shows an enhanced photograph of two corner breaks (Ruiz et al., 2005[b]).

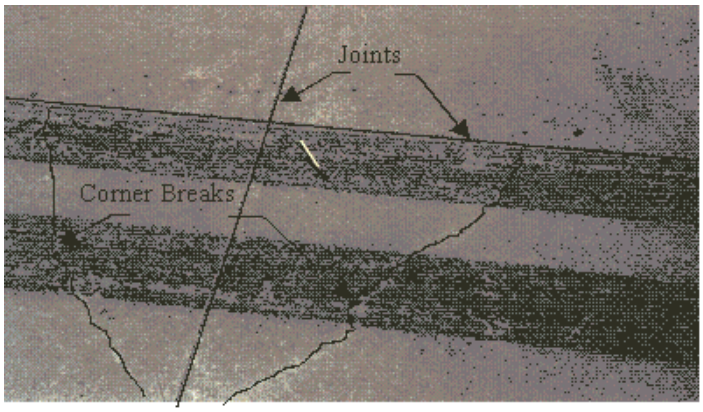

Figure 2.22 Photograph of corner breaks (Ruiz et al., 2005[b])

Ruiz et al. (2005[b]) introduced two criteria for a crack to be classified as a corner break. The first criterion is that the crack must extend vertically through the thickness of the slab. The other one is that the crack must intersect both the longitudinal and transversal joints or edges at less than 1.8 m from the slab corner (Figure 2.23) (Huang, 1993 cited in Ruiz et al., 2005[b]).

The percentage of corner breaks is relatively small in the first load cycles, but it goes up sharply by increasing the load cycles and then levels off (Ruiz et al., 2005[b]).

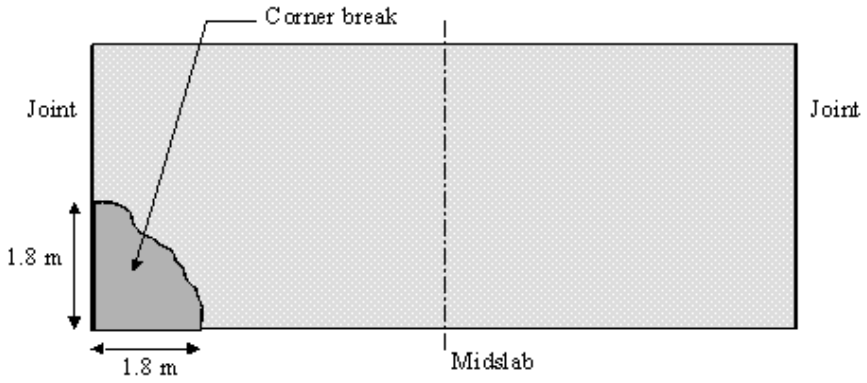

Figure 2.23 Plan view of a corner break (Ruiz et al., 2005[b])

While erodible subbases are not desirable as water infiltrates at a faster rate, the use of cement-treated bases can also lead to problems (Titus-Golver et al., 1998 cited in Ruiz et al., 2005[b]). The cement-treated bases can increase the potential for corner breaks and transverse cracking due to lack of flexibility (Titus-Golver et al., 1998 cited in Ruiz et al., 2005[b]).

2.3.2 Modes of failure in CRCPs

CRCPs have less vulnerability to corner breaks compared to JPCPs due to less free edges. However, the continuity acts as a type of end restraint. This extra restraint increases the overall risk of cracking by decreasing the potential for releasing volumetric movements. Regularly spaced transversal cracking is an expected mode of failure for CRCPs other than corner breaks. Crack spacing, crack width, and stresses were reported as the early-age indicators of the long term performance of CRCPs by U.S Department of Transportation (FHWA) (Ruiz et al., 2005[b]).

2.3.3 Performance of SFRC pavements

There is significant research on the literature to evaluate the influence of early-age environmental factors on the long-term behaviour of CC pavements. However, there remains a lack of knowledge of the effect of early age distress on long term performance of SFRC and RCC pavements.

In fact, the benefits of using fibres in concrete pavements have not been fully quantified yet (Delatte, 2008). For instance, use of steel fibres in concrete pavements can result in reducing

the slab thickness and increasing the joint spacing. Excessive reduction in thickness, larger panel sizes and disregard of environmental effects has led to premature failures (Delatte, 2008; Bordelon et al., 2009; Rollings 1993). Rollings (2005) reported the construction of several SFRC airfield pavements during the 1980s which tended to be as thin as only 100 to 150 mm thick and as large as 15 or even 30 m between contraction joints. Widespread corner breaks were soon reported at these airfields. Due to the large surface area relative to the thin cross section dimensions of these slabs, even low differential shrinkage between the top and bottom caused curling. Consequently, widespread corner breaks developed once the pavements opened to traffic (cited in Delatte, 2008). As a learned lesson from the previous failures in SFRC pavements, there are clear indications that the effects of curling cannot be ignored (Bordelon et al., 2009).

2.4 Previous attempts to study restrained shrinkage in concrete pavements

The restrained shrinkage of concrete pavements has been studied numerically, analytically or experimentally in the literature. Furthermore, the shrinkage behaviour of SFRC overlays has been investigated by many researchers. The main difference between concrete pavements and concrete overlays is that the performance of a concrete overlay depends significantly on the degree to which the overlay is bonded to the substrate (Carlswärd, 2006; Granju, 1996), while for concrete slabs it is possible to separate the slab from the foundation by applying a slippery membrane (Carlswärd, 2006). For concrete overlays the bond strength is essential, because loss of bond between the overlay and the underlying layer will cause progressive damage. However, there are many similarities in simulating the moisture transport and shrinkage behaviour of the concrete pavements and overlays. The following is a brief survey of the literature on the shrinkage behaviour of concrete pavements and overlays. The works cited are considered the most relevant to this study.

2.4.1 Shrinkage behaviour of JPCPs

As a historical background, one of the earliest studies documented in the literature on shrinkage behaviour of concrete pavements was carried out by Hveen (1957). He investigated the factors influencing shrinkage of concrete pavements and concluded that much damage

incurred in concrete pavements would not occur if upward curling could be prevented.

In the more recent studies, Zhang et al. (2001[a]) and Zhang et al. (2004) analytically studied the influence of base characteristics on shrinkage stresses in concrete pavements. The purpose of these studies was to determine transverse crack spacing or the maximum slab length that can survive shrinkage cracking. In these studies, the friction resistance between the slab and the base was assumed to be the main mechanism of restraint when concrete shrinks. A one-dimensional model with a linear elastic behaviour for concrete was assumed in this study. All shrinkage deformation was assumed to be uniformly distributed throughout the concrete slab, and friction was assumed as a bilinear function of slab slippage.

Zhang et al. (2001[a]) calculated that shrinkage stresses increase with slab length and the frictional resistance under the slab. Zhang et al. (2004) found a lower limit for pavement crack spacing. For slab lengths shorter than the limit value no shrinkage crack is developed regardless of how high the shrinkage strain in the slab is. However, this study was highly simplified, since the differential shrinkage through the depth and curling of the slab resisted by internal restraints were ignored and the stresses were averaged over the slab thickness.

Liu et al. (2005) numerically investigated the early-age drying shrinkage behaviour of concrete pavements relative to material-related moisture properties. It was concluded that through the early age of concrete delamination would occur at the saw-cut locations instead of other locations in the pavement. It was also revealed that, in terms of relieving delamination in concrete pavements, the best performance is provided by a cutting depth of ¼ of the whole slab thickness. The traffic loading phase was not considered in this study.

Jeong et al. (2005) investigated the behaviour of concrete pavements under early-age curling induced by shrinkage and creep through a fully instrumented JPCP test-slab. Weather conditions, displacement, strain and moisture distribution was monitored through the depth of the slab. It was found that the early-age behaviour is more related to moisture than temperature change. In this research drying shrinkage produced a high level of tensile strain on the top of the slab increasing the upward movement, and creep strain made a shift in strain cycles with respect to time. Creep strain apparently diminished some days after construction, while increase of tensile strain due to drying shrinkage at the top surface continued over a 2 year period. Tensile strain at the top of the slab was induced at the time of final setting (around 5hrs after placement) due to upward curling and internal restraints. It was finally

concluded that drying shrinkage significantly affects the long-term curling behaviour of the slab. No external load was applied on the slab.

In one of the most recent studies, Lee et al. (2010) numerically investigated the moisture curling of JPCPs. In that study the predominant stress field as a result of the long-term shrinkage curling, the self-weight and the inverse effect of creep in a plain single concrete slab was evaluated. It was recommended that this predominant stress field, that may accelerate cracks when the external wheel load is applied, shall be incorporated into the design process. Aging (evolution of the elastic modulus), creep, drying shrinkage, and daily thermal variations of concrete were considered in that research, while cracking phase was not developed in the adopted model. The authors concluded that the creep effect can play an important role in moisture curling of concrete slabs.

2.4.2 Shrinkage behaviour of CRCPs

It is well-known that in CRCPs shrinkage cracks are usually uniformly distributed (Zhang et al., 2004). However, since the pavement is more restrained at the centre, the crack spacing is typically greater near the ends; the longitudinal movements occur mostly at the ends and higher stresses occur at the centre (Ruiz et al., 2005[b]).

Nam et al. (2006) experimentally investigated the behaviour of CRCP exposed to drying shrinkage, creep and daily thermal variations. The crack width profiles along the slab depth were obtained at a very early age (24h). Cracks were wider near the top surface, narrower at the bottom surface and much narrower near the middle of the slab.

Kim et al. (1998) investigated numerically the early-age behaviour of CRCP due to drying shrinkage, temperature variations and the creep effect. In this study an FE model was built up in between two assumed adjacent transverse cracks. It was concluded that considering the creep effect reduces stresses by about 20% and decreases the cracks width by about 10%.

The U.S. Department of Transportation (FHWA) issued a set of guidelines to minimise early-age damage to JPCPs and CRCPs based on the study of Ruiz et al. (2005[b]). HIPERPAVII software was developed as a result of that study. The main objective of that study was to evaluate the effect of early-age behaviour factors on the long-term performance. A mechanistic approach was used to describe the existing link between early-age behaviour and

long-term performance. Cement hydration, thermal gradients, moisture, shrinkage, creep, subbase restraint were predicted and considered in HIPERPAVII. Both autogenous and drying shrinkage were considered. However, the long-term performance of only JPCPs was included in this guideline and the authors could not validate the results obtained for the early-age behaviour of CRCPs for crack spacing and crack widths.

2.4.3 Shrinkage behaviour of SFRC pavements and overlays

2.4.3.1 SFRC pavements

A review of literature on the benefits of using steel fibres in concrete to reduce the adverse effects of shrinkage was performed in Section 2.2.1.2. Slab curling resulting from drying shrinkage is a common cause of SFRC slab failures. This has been recognized and investigated by a few researchers. For more information refer to Section 2.3.3.

2.4.3.2 SFRC overlays

Shrinkage induced distress in concrete overlays has received more attention than pavements. A remarkable research in this field was performed by Carlswärd (2006). In this research, test methods and theoretical analyses were used to assess the cracking response of thin concrete overlays due to restrained shrinkage. Curling and the effect of bond strength (uplift resisting strength) on shrinkage cracks of an overlay was examined (Figure 2.24).

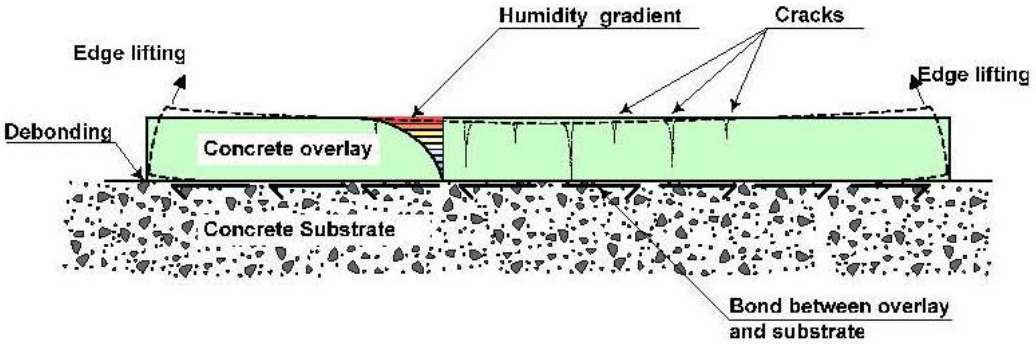

Figure 2.24 Cracking and edge lifting of a bonded overlay due to shrinkage (Carlswärd, 2006)

The results showed that steel fibres may provide a significant contribution to crack width limitation. Carlswärd (2006) studied the bond strength in three categories of (1) fully bonded, (2) partially bonded and, (3) un-bonded overlay. In the third case, interaction was excluded

which is similar to the case of ground-slabs. Frictional resistance of the interface was not considered. It was concluded that, higher bond strength distributes cracks over the entire length of the overlay and finer cracks will be formed. Lower bond strength causes wider and concentrated cracks in fewer localities. Subsequently, fibres do not particularly influence the crack distribution or crack widths for bonded overlays. However steel fibres reduced crack widths for debonded overlays.

Material properties, such as extent of free shrinkage and toughness characteristics of SFRC, were obtained experimentally. Carlswärd (2006) developed a free shrinkage test in which a strip specimen of the concrete layer was cast and the sides and the bottom face were covered with air-tight plastic foil. In this manner, drying was only permitted through the upper face and real moisture migration was simulated. Then, the shrinkage strain at the top and bottom faces, excluding the effect of base-restraint, was monitored as a function of time (Figure 2.25). However, this configuration cannot simulate a truly free shrinkage test, as the effect of internal restraints against non-uniform drying is not excluded.

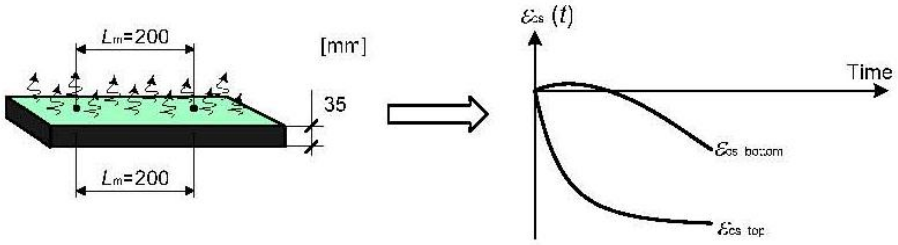

(a) (b)

Figure 2.25 (a) Free shrinkage test proposed by Carlswärd; (b) The principle response on the top and bottom faces due to one-sided drying (Carlswärd, 2006)

Beushausen et al. (2006) experimentally studied the differential shrinkage of bonded concrete overlays, and concluded that the mode of failure as the result of restrained shrinkage of overlays is either cracking or debonding.

Numerical modelling of shrinkage induced cracking and debonding in cement composite overlays were performed by Bolander et al. (2004). That study showed that for a weak interface as the shrinkage load increases propagation of debonding occurs without any vertical cracks through the overlay, whilst for strong interfaces numerous vertical cracks develop and additional drying results in localisation of some of the cracks.

2.4.4 Shrinkage behaviour of RCC pavements

There is not a general agreement on the shrinkage behaviour of RCC (especially SFR-RCC) in the literature compared to CC (refer to Section 2.2.1.3). Research and investigation on shrinkage and curling behaviour of RCC pavements is also not sufficient. As a remarkable research, Pittman et al. (1998) studied drying shrinkage of RCC for pavement applications by laboratory investigations. In that study drying shrinkage for different RCC mixes were measured according to the procedures described in ASTM C 157 (2008). More information is given in Section 2.2.1.3.

There is no field measurement on curling of RCC pavements.

2.5 Discussion and conclusion

- Long-lasting pavements, lower construction cost and less maintenance

Steel fabric mesh, that has been traditionally used to reinforce concrete pavements, can be replaced by steel fibres. Steel fibres, which are mixed with the fresh concrete, reduce labour costs and time required for construction. SFRC can also be placed using the roller compaction technology to reduce construction time. To decrease the construction cost further, industrial steel fibres can be replaced by recycled steel fibres extracted from post-consumer tyres. The incorporation of recycled steel fibres in roller-compacted concrete has been investigated by the EcoLanes project (conducted between 2006-2009) targeting development of the long lasting pavements.

- Need for development of standard design guidelines for SFRC pavements

The adoption of SFRC pavements for surface transport infrastructures has been curtailed due to the slow development and acceptance of standard design guidelines. Design guidelines specifically developed for SFRC are normally aimed at industrial ground slabs and some aspects such as early-age distress and its interaction with the service load and long-term behaviour are not well addressed by them.

- Shrinkage-induced distress and long-term performance

Drying shrinkage significantly affect the performance and the lifetime of concrete pavements. Curling resulting from drying shrinkage is a common cause of slabs failure. A high stress region is induced near the drying surface as the result of the curling. It also affects the support conditions under the pavement. Curling when combined subsequently with traffic load increase the level of stresses developed in the slab and may cumulatively damage the pavement. Top-down corner breaks is the mode of failure in this condition. CRCP pavements although less vulnerable to corner breaks, their continuity acts as a type of end restraint and may increases the overall risk of early age cracking by decreasing the potential of releasing volumetric movements. Regularly spaced transversal cracking is the other expected mode of failure for CRCPs other than corner breaks.

In SFRC pavements even little differential shrinkage can result in curling, due to the large plan relative to thin cross section dimensions. Therefore, the effects of curling cannot be ignored for them.

- The lack of knowledge for SFRC and RCC pavements

Studies show that the use of steel fibres in concrete pavements is beneficial in reducing the adverse effects of shrinkage. There is not a general agreement on the effect of steel fibres on free drying shrinkage of concrete in the literature, although in the practical range of under 1% (by volume) free drying shrinkage properties do not alter significantly. But in terms of restrained shrinkage, the restricting effect of fibres on crack opening and distribution is significant. The methods proposed so far for restrained volumetric changes of SFRC are still few and are not directly applicable to practice.

The early shrinkage behaviour of RCC has been reported quite different to that of CC. Few laboratory investigations have shown that drying shrinkage of different RCC mixes is relatively low compared to that of CC mixes. This effect has been attributed to its lower moisture content or lower paste content. On the contrary, studies performed during the Ecolanes project (Graeff, 2011) investigating free shrinkage of RCC, showed that RCC mixes have higher free shrinkage strains than CC mixes due to higher porosity (especially when reinforced with recycled fibres).

Research and investigation on shrinkage and curling behaviour of RCC and SFR-RCC pavements is not sufficient in the literature to make definitive conclusions. There is no field measurement on curling of RCC pavements. The published research works on shrinkage properties of SFR-RCC, are very few and in the case of R-SFR-RCC is limited to a single research (performed by Graeff, 2011). Even using the existing information on the free shrinkage behaviour of SFR-RCC no conclusion can be made on the restrained performance, since the improvement in the shrinkage resistance of fibre reinforced concrete pavement is mainly observed in a restrained situation.

- Significance of research on the effect of shrinkage-induced distress on the long-term performance of SFR-RCC

The improvements in structural properties of SFRC, which are documented in the literature, have not been all considered in existing design guidelines for concrete pavements and slabs. However, there are some design guidelines that specify methods to estimate the load carrying capacity of SFRC slabs (e.g. Concrete Society TR34, 2003), but the evaluation of distress resulting from restrained shrinkage in those references is only based on very simple rules of thumb. Designers may ignore these early-age distress caused by shrinkage, or use roughly estimated rules which are the same as for conventional concrete. Ignoring pre-loading distress will not lead to a long-lasting pavement design, besides affecting the structural integrity and lowering the riding quality. To encourage the use of SFRC in pavement construction and to benefit from its advantages, specific design guidelines must be developed for SFRC considering all possible sources of distress in these pavements.

In order to contribute to the development of cost-effective and reliable guidelines to predict the performance of SFRC pavements, and to facilitate the use of recycled fibres and roller-compaction technology, significant research effort is required in this field.

Chapter 3

3 Moisture transport mechanism and drying shrinkage properties in concrete

In studying drying shrinkage of concrete it is important to understand the behaviour of moisture in concrete when drying occurs. Therefore, predicting the moisture transport properties is essential. Drying is a phenomenon which occurs when concrete is placed in an environment with relative humidity lower than its internal humidity. Therefore, pore water moves towards the drying surface resulting variable moisture content in space and time.

Moisture transport occurs through the pore network of the material. As there is a wide variety of pore structures in concrete and the pore structure changes with age of concrete, the moisture transport in concrete can be more complex than in other media (Xin et al., 1995).

Modelling of moisture movement in porous materials has always been a matter of interest, and has received significant research attention in soil science, concrete technology and geotechnology (Kodikara et al., 2005). In porous media, moisture can flow partly as liquid in capillaries and partly as vapour. In soil science, the water movement happens distinguishably under both mechanisms of bulk water flux and vapour flux. The bulk water flux is controlled by the pore water suction and elevation potential (capillary action). The vapour flux is governed by the vapour diffusion in unsaturated pore space (Kodikara et al., 2005). Although, the above mechanisms can more-or-less couple through the moisture transport in concrete, when the pore relative humidity is in the range of 15 to 95%, the moisture movement in the form of vapour flux is dominant (like a predominantly unsaturated soil) (Bazant et al., 1972). Therefore, the flow of moisture in concrete subjected to drying has been mostly assumed to obey the diffusion equation (Carlson, 1937; Pickett, 1946; Bazant et al., 1971; Sakata, 1983; Asad et al., 1997; Wittmann et al., 1989; Kodikara et al., 2005; Wong et al., 2001; Li et al., 2008; Rahman et al., 1999), especially when the moisture content decreases below 70 to 80% of initial saturation (Selih et al., 1996).

The first application of diffusion principles in a study of moisture distribution in concrete has been reported in 1937 by Carlson (Carlson, 1937). In 1946, Pickett studied shrinkage stresses in concrete and stated that if the flow of water is entirely by vapour diffusion, if the vapour pressure of the water in the concrete is proportional to the moisture content, and if permeability is independent of the moisture content, then the flow of water would be described by the diffusion equation which is equivalent to the equation of heat conduction. However, the order of magnitude of corresponding coefficients in diffusion of heat and diffusion of moisture are entirely different (Pickett, 1946). This approach was since been adopted for moisture transport in concrete drying. In this approach only a material property, diffusivity, and the coefficient of convective moisture transfer to the environment are involved in characterising the moisture movement within concrete which makes it very convenient for numerical calculations.

3.1 Factors involved in moisture transport and drying shrinkage of concrete

3.1.1 Diffusion coefficient

Assuming that the diffusion theory applies, the transport of moisture in concrete is governed by Fick's second law (Rahman et al., 1999; Asad et al., 1997), given in the following equation:

$$\frac{\partial C}{\partial t} = div(K_C(C)grad(C)) \qquad \text{(Eq. 3.1)}$$

Where, C is the moisture content which is a function of spatial components and the time from the beginning of diffusion process, and $K_C(C)$ is the diffusion coefficient. This coefficient is a property of the material and is defined as the rate of moisture flow within the concrete while the moisture gradient is equal to unity. The above equation is strongly nonlinear and its nonlinearity is due to the high dependency of K_C on moisture content (Bazant et al., 1972).

For any particular geometry, applying boundary and initial conditions, Eq. 3.1 can be solved for C. For a boundary with surface evaporation Eq. 3.2 applies. With prescribed moisture, Eq. 3.3, and for a no flow boundary Eq. 3.4 applies (Asad et al., 1997).

$$K_C(C)\frac{\partial C}{\partial n} = f(C_s - C_a) \qquad \text{(Eq. 3.2)}$$

$$C = C_b \qquad \text{(Eq. 3.3)}$$

$$\frac{\partial C}{\partial n} = 0 \qquad \text{(Eq. 3.4)}$$

Where, f is the convective moisture transfer coefficient (also called surface factor or film factor). C_s is the moisture content at the drying surface, C_a is the moisture content in the atmosphere, C_b is the prescribed moisture, and n is the unit normal to the boundary surface.

To determine the moisture diffusivity as a material property, moisture measurements should be taken from a drying specimen as a function of time and depth. Based on experimental moisture profiles, the diffusivity equation can be solved to obtain the relevant moisture diffusivity.

Different forms of analytically or empirically estimated closed-form functions defining the dependency of K_C on C have been introduced in the literature (Bazant et al., 1971 also adopted in CEB-FIP ('90) model code, 1993; Penev et al., 1991; Pihlajavaara, 1965; Pihlajavaara et al., 1965 cited in Wittmann et al., 1989; Xi et al., 1994 cited in Kwon, 2008; Li et al., 2006; Mensi et al.,1988 cited in Wittmann et al., 1989; Ayano et al., 2002; and Rahman et al., 2000) (refer to Appendix A).

In an approach proposed by Sakata (1983) and followed by other researchers (Asad et al., 1997; Penev et al., 1991; Wong et al., 2001; Kodikara et al., 2005), assuming one-dimensional moisture transport, the diffusion equation can be analytically solved using Boltzman's transformation (1974), $\tau(x,t) = x/\sqrt{t}$, (Eq. 3.5).

$$K_C]_{C=C_1} = \left(-\frac{1}{2}\int_1^{C_1}\tau.dC\right)/\left(\frac{dC}{d\tau}\right]_{C=C_1}) \qquad \text{(Eq. 3.5)}$$

Initial condition: $C = 1$ for $x > 0$, $t = 0$

Boundary condition: $C = C_1$ for $x = 0$, $t > 0$

Some typical functions for $C(\tau)$ are given in Appendix A. Since the slope of the curve $C(\tau)$ is very sharp at the start of drying, small inaccuracies in estimating the function $C(\tau)$ from

experimental data can make a big difference in the resulting derivative, $\frac{dC}{d\tau}$, which is applied in Eq. 3.5. This significantly influences the calculated K_c at the beginning of drying. Therefore, this method is not generally satisfactory and some scholars have suggested adopting numerical inverse analysis instead (Xin et al., 1995; Wittmann et al., 1989). For numerical inverse analysis, a numerical model (e.g. Finite Element model) is used in which the moisture diffusivity function is assumed iteratively to cause the same moisture profiles as the test results.

Vapour transfer in the air occurs with a diffusion coefficient of about 218 mm^2/day at 20ºC, that is nearly 50 to 100 times faster than in concrete (Ayano et al., 2002). This upper limit has not been regarded in analytically calculated values proposed by some researchers such as Asad et al. (1997) and Kodikara et al. (2005), who have proposed values varying up to 10000 mm^2/day for the diffusion coefficient in concrete. Based on the values proposed by other researchers (Ayano et al., 2002; Yuan et al., 2002; Sakata, 1983; Bazant et al., 1971), the diffusion coefficient in concrete varies in the range of 0.0 to 5 mm^2/day for moisture contents lower than 80% and then increases sharply to reach to maximum values between 20 to 100 mm^2/day at 100% moisture content. In some studies a constant value has also been attributed to the diffusion coefficient of concrete. For instance Carlson (1937) suggested the constant value of 9.29 mm^2/day; Pickett (1946) adopted the value of 23 mm^2/day and Sakata (1983) applied the value of 30 mm^2/day. These differences in the values proposed in the literature can be big enough to change significantly the drying pattern in concrete. Hence, for the particular concrete mixes studied in this research, the diffusion coefficient will be determined from experimental measurements combined with inverse analysis.

3.1.2 Convective moisture transfer coefficient, f

Convective moisture transfer is the moisture exchange between the concrete surface and the atmosphere. Convective moisture transfer coefficient, f, somewhat depends on the water to cement ratio, w/c (Sakata, 1983). The rate of moisture transfer is also controlled by the moisture gradient as well as the surface texture and the speed of air flow. However, the effect of the environment on f is negligible (Ayano et al., 2002). For normal concrete, f was found by Sakata (1983) to be in the range of 0.75 mm/day to 7.0 mm/day, which is a wide range of values. Therefore, for the particular concrete mixes studied in this research f can be

calculated by inverse analysis.

3.1.3 The relationship between free shrinkage strain and moisture loss ("Hygral contraction coefficient")

This relationship is a material property applicable for any shape of the concrete member with any type of restraint. Free shrinkage strain is normally given as a nonlinear function of drying time and ultimate shrinkage (e.g. in ACI 209R, 1992; CEB-FIP ('90) model code, 1993). Ultimate shrinkage strain is usually a function of ambient relative humidity, initial curing condition, volume to surface ratio, concrete composition, air content and percentage of fine aggregates. These factors indirectly alter ultimate shrinkage strain by affecting the moisture movement in the concrete member and the resultant moisture content at any time t. Therefore, it is relatively straightforward to directly relate the free shrinkage strain to relative moisture content.

It was initially thought (Picket, 1946) that the shrinkage strain in concrete is a linear function of moisture loss. More recently, It is accepted that the relationship between moisture loss and free shrinkage strain is nonlinear (Rahman et al., 1999). Ayano et al. (2002) proposed a power function for this relationship.

In this study inverse analysis is adopted to calculate the relationship between free shrinkage strain and the moisture content for given mixes from the experimental measurements on free shrinkage specimens.

3.2 Moisture measurement in concrete

There are two methods to measure the depth distribution of moisture as a function of time in an experimental specimen;

- Use of small probe-type sensors placed in measurement holes or embedded in the concrete member at different distances from an exposed surface

- Conventional gravimetric method

Using probe-type sensors, it usually takes long time for the measurement to stabilise,

particularly in high internal humidity conditions. Therefore, for early days that moisture content drops sharply, this type of measurement may be unsuitable.

The gravimetric method has been used by many researchers (Selih et al., 1996; Wittmann et al., 1989; Wong et al., 2001; Asad et al., 1997; Sakata, 1983). The gravimetric method, as conventionally used, relies on the assumption that for a one-dimensional moisture transport, the moisture content at any given depth from the drying surface is independent of the total height of the specimen. Therefore, instead of embedding a moisture meter at any given depth, a specimen with a height equal to that given depth is cast. The weight changes of the various height specimens are measured in frequent time steps (Figure 3.1), and then using a simple formulation (Section 3.2.2) the moisture profiles are calculated as a function of depth and time.

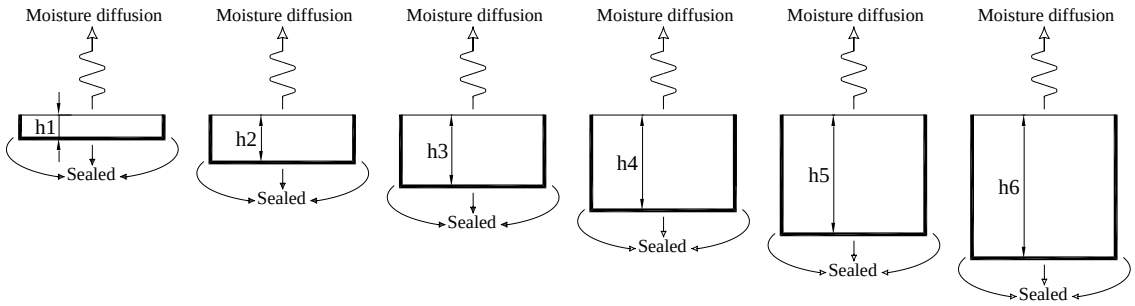

Figure 3.1 Specimens in traditional gravimetric method for moisture measurement

However, this assumption is not accurate. In practice, the moisture under any given depth passes through the cross section of that depth to reach the drying surface. Numerical analysis also shows that, the moisture content at any given depth from the drying surface, besides many other factors, depends also on the total height of the specimen. This deficiency in the gravimetric method can be modified as explained in section 3.2.1.

3.2.1 Modifying the gravimetric method for moisture measurement

The gravimetric method can be modified by casting all specimens at the same height and then cutting each of them at a given depth (*h1, h2, h3*, …) (Figure 3.2). Therefore, the boundary condition from the underlying depth of the concrete specimens is maintained by keeping both

segments in contact for the duration of measurements.

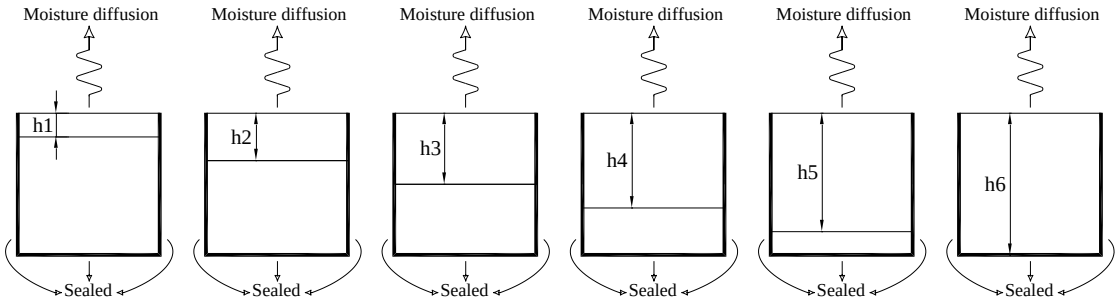

Figure 3.2 Specimens in the modified gravimetric method for moisture measurement

The relevant surfaces of the top and bottom segments will be sealed separately (Figure 3.3(a)) (surfaces 1 to 4 in the top segment and surfaces 1 to 5 in the bottom segment). After each weight measurement, the top segment is gently placed back on the bottom segment (Figure 3.3(b)) and a wide plastic tape is used to keep them together and to seal the joint (Figure 3.3(c)).

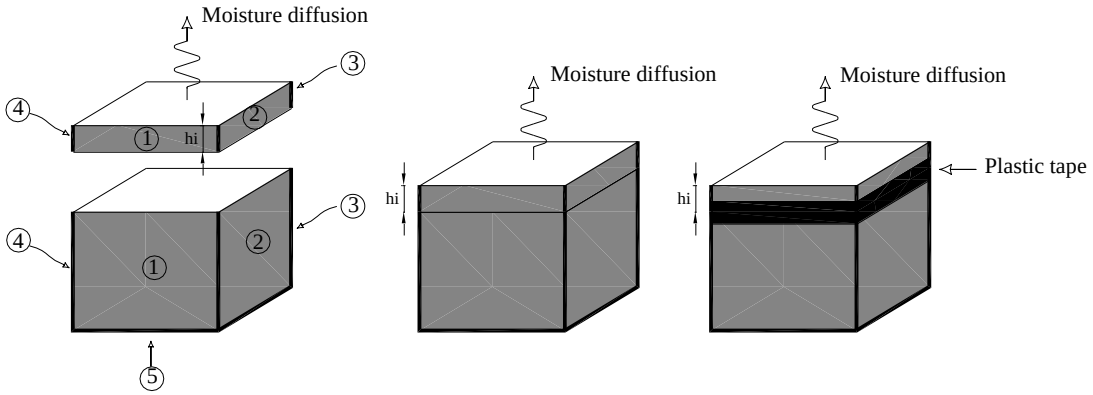

Figure 3.3 Sealing specimens in the modified gravimetric method

The only issue in this modification is the effect of the gap between two segments on moisture transfer. Ayano et al. (2002) investigated the effect of gaps on moisture transfer in a sliced specimen. They compared the moisture diffusion coefficient of a pile of sliced specimens with that of a solid specimen, and found that the effect of gap can be considered to be small.

3.2.2 Calculation of moisture content in the gravimetric method

The moisture content, $C(x,t)$, as the percentage of initial diffusible moisture (initial weight minus final dry weight, $W_{0i} - W_{fi}$), at any depth x_i Figure 3.4(b) and at time t can be calculated from Eq. 3.6 and 3.7 (Asad et al., 1997).

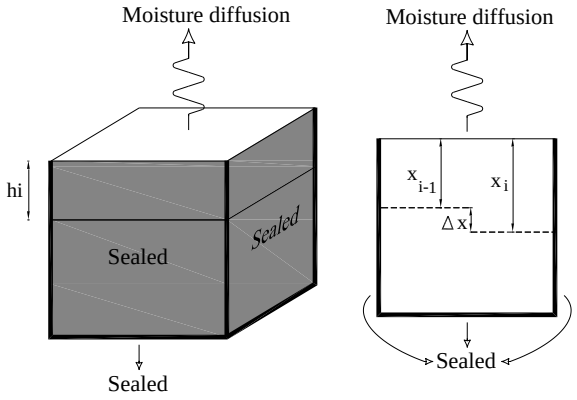

(a) (b)

Figure 3.4 (a) Specimen *i* in formulation of the moisture content; (b) Full height Concrete element in formulation of the moisture content

$$C(x_i,t) = [1 - \frac{(M_{ti} - M_{t(i-1)})}{\gamma_0 . S . \ (h_i - h_{i-1})}] \times 100 \qquad \text{(Eq. 3.6)}$$

$$\gamma_{0i} = \frac{W_{0i} - W_{fi}}{h_i . S} \qquad \text{(Eq. 3.7)}$$

Where h_i is the height of the specimen (Figure 3.4(a)); M_{ti} is the moisture loss in the body of specimen *i* up to time *t*, S is the area of the drying surface; γ_0 is diffusible moisture per unit volume for specimen *i*; W_{0i} is the initial weight of specimen *i* before drying; W_{fi} is the dry weight of specimen *i* finally after drying in the oven. More details on the derivation of Eq. 3.6 and 3.7 are given in Appendix B.

Using the above formulation and measuring the weights of the various length specimens at frequent time steps it is possible to extract the time history of moisture profiles.

Chapter 4

4 Experimental studies

Experimental studies are needed to obtain material properties required for modelling the restrained shrinkage behaviour of SFRC pavements. The required material properties consist of mechanical properties as well as moisture movement and shrinkage properties.

The required mechanical properties are:

- Compressive strength
- Elastic modulus
- Peak tensile strength, and the tension stiffening curve

The required moisture movement and shrinkage properties are:

- Moisture diffusivity, $K_C(C)$
- Convective moisture transfer coefficient (also called surface factor or film factor), f
- Relation between free shrinkage and moisture loss ("Hygral contraction coefficient")

In this chapter the experimental work to obtain the above properties for SFRC mixes (SFR-RCC and SFR-CC) is explained and the results are presented. Plain CC and RCC mixes are also tested as reference mixes for comparison with SFRC.

To ensure that only drying shrinkage is monitored and there is no significant effect of autogenous and plastic shrinkage, the drying shrinkage and moisture measurement in experimental specimens were delayed until full maturity in concrete was attained. Autogenous and plastic shrinkage, which occur in immature concrete, are strongly dependent on the curing conditions. Plastic shrinkage can be fully eliminated by curing in 100% humidity and autogenous water absorption may be replaced by damping the concrete member during the

curing time. Drying shrinkage is the dominant component of hygral volume change in normal strength concrete (by more than 80%) and is inevitable under normal service conditions. In the early ages of concrete, when hydration is still in progress, some micro-cracks can also be healed at the same time as strength increasing (autogenic healing). By delaying the measurements the effect of autogenic healing (which acts inverse to the autogenous shrinkage) could also be ignored, simplifying the interpretation of the results. Thus the specimens were cured in water for 90 days and drying began after that period. Consequently, the moisture content, free shrinkage strains and mechanical properties were measured after that period, apart from an extra measurement for compressive strength at 28 days.

4.1 Mix proportions and casting preparations

Plain and fibre reinforced CC and RCC mixes were cast. River aggregates and sand were used for CC mixes (Figure 4.1(a) and (b)), while graded crushed granite (Porphyritic Andesite) was used for RCC mixes to increase the bond between the paste and aggregates (Figure 4.1(c)).

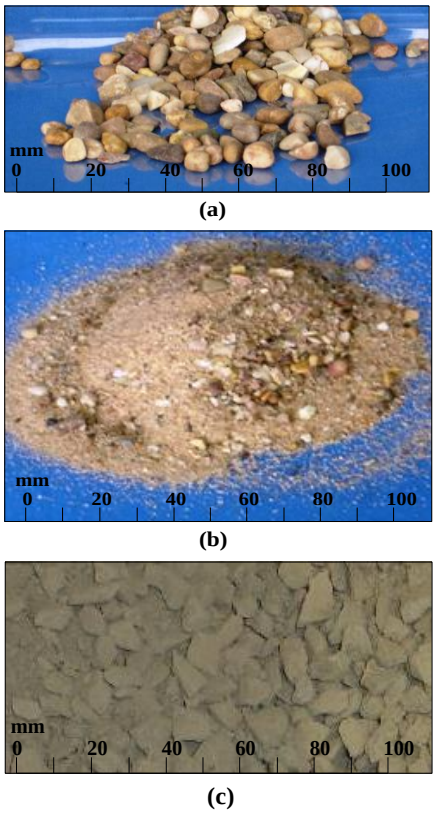

Figure 4.1 (a) Coarse aggregates for CC mixes (river aggregates); (b) Fine aggregate for CC mixes (sand); (c) Blended crushed graded aggregates for RCC mixes

An electric vibrating hammer (Figure 4.2(a) and (b)) was used to compact the RCC concrete specimens to simulate roller compaction, using a circular tamper for cylinders and a rectangular tamper for prisms. This electric vibrating hammer consumed 1600W and its operating frequency ranged from 16 to 32.5 Hz. As seen in Figure 4.2(c), the vibrating hammer was attached to a metal frame, developed by Ecolanes (Angelakopoulos, 2012), to apply a constant compaction effort.

(a)

(b)

(c)

Figure 4.2 (a) Electric vibrating hammer to compact RCC; (b) Operating the hammer manually; (c) Operating the hammer using the metal frame

The mix proportions for CC and RCC are given in Table 4.1 and 4.2, respectively. The cement type used was a sulfo-aluminate low energy cement and the fibre content used for SFRC mixes was the optimum practical amount for recycled fibres determined by the Ecolanes project (60 kg per each cubic meter of concrete or around 2.5% by weight). The water content in RCC was determined as the optimum that yielded the maximum dry density of the compacted mix.

Table 4.1 Proportions used for CC mixes

Cement (kg / m^3)	(w/c)	River agg. (kg / m^3)	Sand (kg / m^3)	Superplasticizer*	Air-entrainer*
380	0.35	1004	833	0.85%	0.135%

* % by cement mass

Table 4.2 Proportions used for RCC mixes

Cement (kg / m^3)	(w/c)	Crushed graded agg. (kg / m^3)
300	0.54	2084

The steel fibre used was recycled form tyre-cord that has been processed to remove rubber particles and minimise the geometrical irregularities. Earlier research at the University of Sheffield has revealed that steel tyre-cord in concrete is best utilised, if the length of the fibres is in the range of 15 - 25 mm and the diameter is around 0.2 mm (USFD, 2001). According to a classification determined at the University of Sheffield, Class A recycled tyre steel fibres (RTSF) should be treated to fulfil the following criteria:

- Rubber content (by mass of the steel tyre-cord fibres) less than 2%.
- At least 50% of the steel fibres having length in the range of 15-25 mm, and no more than 20% of the steel fibres being longer than 25 mm.

Satisfying the above criteria, the statistical length distribution of recycled fibres used in this study is shown in Figure 4.3 (85% of the fibres had length in the range of 10-25 mm, and 50% of them in the optimum range of 15-25 mm).

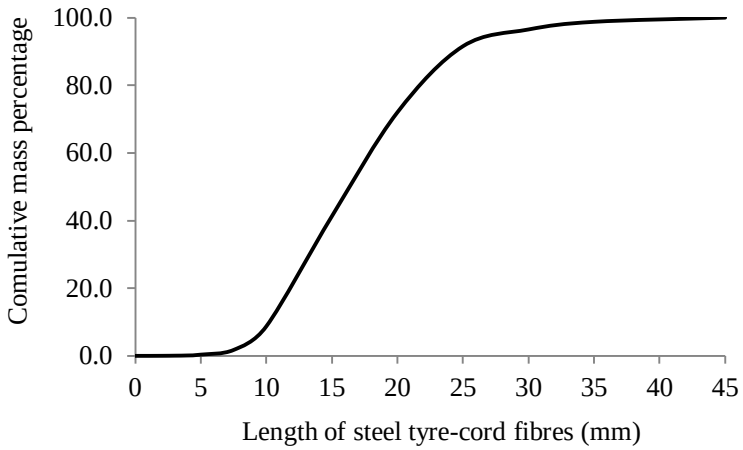

Figure 4.3 Statistical length distribution of steel tyre-cord steel fibres used in SFRC mixes

This curve has been calculated by statistical analysis of the fibre length via image analysis (Neocleous et al., 2007). In this method after selecting a random sample of fibres, a conventional desktop scanner is used to acquire images of the fibre sample. After enhancing the contrast of the images, they are analysed and the length distribution is obtained using Digimizer™ software (or similar tools).

To avoid balling and to optimise the use of fibres in concrete, it is recommended that the nominal maximum size of coarse aggregate is less than 2/3 of the dominant fibre length (JSCE-SF1, 1984). To allow the use of the relatively short tyre-cord fibres and to achieve a good surface texture and reduce the potential for segregation, the nominal maximum size of course aggregates in this study is limited to around 14 mm. This is also the predominant maximum size used in RCC applications in UK. The aggregate gradations used for RCC and CC mixes are presented in Table 4.3.

Table 4.3 Gradation of aggregates used for CC and RCC mixes

gradation (mm)	CC mixes		RCC mixes
	Sand (%)	Coarse agg. (%)	Crushed agg. (%)
>14	-	-	2.5
9.5-14	-	10	19
4.75-9.5	2	80	21
1.18-4.75	26	10	19.5
0.5-1.18	32	-	10.5
0.15-0.5	37	-	14
.075-0.15	2	-	7
< 0.075	1	-	6.5

The measured air content of the CC mixes was 5%, determined in accordance with (BS EN 12350-7, 2000) using pressure gauge method apparatus (Figure 4.4).

Figure 4.4 Pressure gauge method apparatus

The target slump for CC mixes was 70 mm. The slump was measured (Figure 4.5) in accordance with BS EN 12350-2 (2009). Whenever the concrete slump was not within the range of 60 to 80 mm the mix was modified by adjusting the superplasticizer content.

Figure 4.5 Slump test apparatus

For RCC mixes, the graded crushed aggregate were weighted and mixed one day before casting. Then the whole amount of water was manually added to the mixed aggregates in a container. The container was then covered by an airtight lid to allow the aggregates to absorb the water for 24 hours without evaporation of moisture. On the casting day, only the cement (and fibres for SFRC) was needed to be incrementally added to the mix in a concrete mixer.

4.2 Experimental studies to obtain mechanical properties

4.2.1 Compressive strength and compressive elastic modulus

4.2.1.1 Cubes

Cubes of 150 mm side dimensions were cast in steel moulds (Figure 4.6(a)). RCC cube specimens were cast in three layers. For the first layer, the RCC mix was placed in the mould up to the half the depth and then compacted for 60 seconds with a vibrating hammer. The surface of the compacted layer was then scratched by a sharp object to provide a better bond between layers. The second and third layers were filled and compacted in a similar manner. A day after casting, the specimens were demoulded and then placed in water till the day of testing. After 28 days the compressive tests were carried out in accordance with BS EN 12390-3 (2009). Figure 4.6(b) shows a cube specimen crushed in compression.

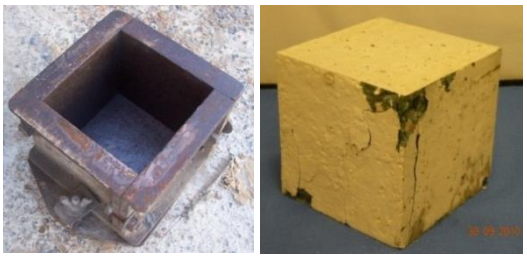

(a) (b)

Figure 4.6 (a) Steel moulds for cube specimens; (b) Cube specimen after crushing

The 28 days-mean compressive strength of cubic specimens and their standard deviations are given in Table 4.4 for all the mixes.

Table 4.4 Mean 28-days compressive strength (Cubes)

	SFR-RCC	SFRC-CC	Plain RCC	Plain CC
No. of specimens	3	2	3	3
Average compressive strength, MPa	51.7	60.6	48.9	58.1
Standard deviation	1.0	0.0	1.7	1.6

4.2.1.2 Cylinders

Cylinders of 150 mm diameter and 300 mm height were cast in steel moulds (Figure 4.7(a)). RCC cylinder specimens were cast in 5 layers in a similar way to the cube specimens. The specimens were de-moulded after one day and were cured in water for more than 90 days to gain full maturity. Compressive testing was carried out in accordance with BS EN 12390-3 (2009). Figure 4.7(b) shows a cylindrical specimen in the testing machine.

(a) (b)

Figure 4.7 (a) Steel moulds for casting cylinders; (b) Compressive test of a concrete cylinder

The elastic modulus was determined in accordance with BS ISO 1920-10 (2009).

The mean compressive strength of cylindrical specimens (after 90 days) for all the mixes is given in Figure 4.8 and Table 4.5. The compressive elastic modulus is also given in Table 4.5.

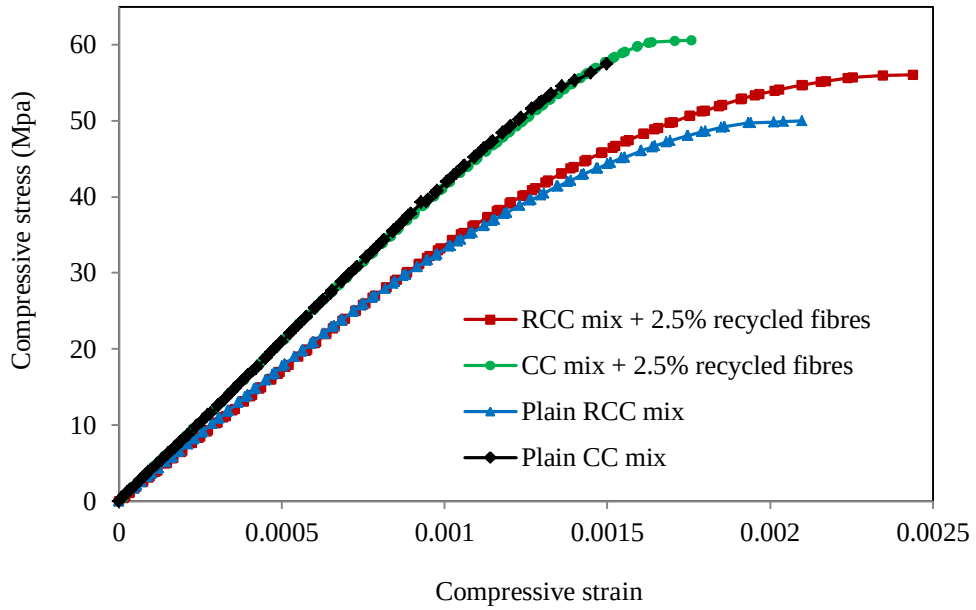

Figure 4.8 Mean compressive stress-strain curves

Table 4.5 Mean compressive strength and elastic modulus (Cylinders)

	SFR-RCC	SFR-CC	Plain RCC	Plain CC
No. of specimens	3	3	3	2
Average compressive strength, MPa	56.0	60.6	50.0	56.3
Standard deviation	3.9	4.8	0.5	0.5
Elastic modulus, GPa	34.3	41.2	34.8	41.6
Standard deviation	1.0	0.9	1.5	0.0

4.2.1.3 Discussion on the compressive test results

28-day mean compressive strengths obtained from cubes and 90-day mean compressive strengths obtained from cylinders are shown in Figure 4.9. The results show that the compressive strength of CC mixes is slightly higher than that of RCC mixes, and the compressive strength of SFRC mixes is marginally higher than that of plain mixes.

It is usually expected that, at the same age, the compressive strength of cylinder specimens is 80% of that of cube specimens (BS EN 1992-1-1, 2004). In this study, cylindrical specimens

were tested at an age of more than 90 days to represent the long-term compressive strength, while cubes were tested at 28 days.

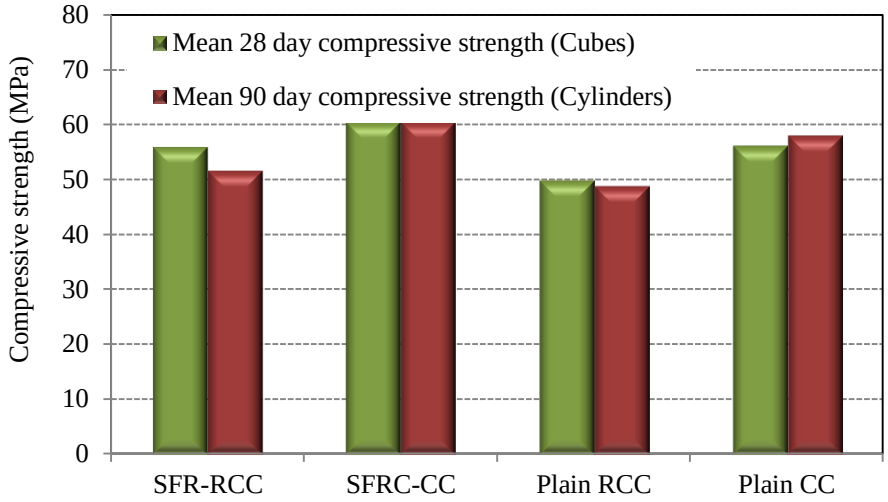

Figure 4.9 Comparison of compressive strength from cube and cylinders

The elastic modulus obtained for the RCC mixes is considerably lower than that of CC mixes. This difference is considerably less for the elastic modulus obtained from bending tests (see Section 4.2.2.3). This bigger difference may be attributed to the effect of boundaries on the compaction of RCC cylinders. Due to the relatively small cross section of the cylinders, the compaction of RCC results in lower quality concrete in the boundaries, which could affect the elastic modulus and strength of RCC specimens.

4.2.2 Flexural behaviour, and bending elastic modulus

Peak tensile strength, tension stiffening behaviour, and bending elastic modulus can be obtained from flexural tests on standard prisms.

There is no standard test to determine the stress-strain curve of fibre reinforced concrete in direct tension, because uniaxial tension tests on concrete are extremely difficult to perform (ACI 544.4R, 1999). Using numerical techniques (inverse analysis), it is possible to extract the tension softening behaviour of SFRC from the results of the flexural tests on prisms.

The prism specimens are commonly tested under three or four point loading. The use of four-point load arrangement in bending tests creates a region of constant moment at the middle of

the beam, hence, the overestimation of bending resistance caused by the load-spreading effect at the point of load application (Timoshenko et al., 1970) is minimised. Therefore, in this study bending tests on prisms carried out adopting the four-point load arrangement.

In flexural test of prisms, RILEM TC 162-TDF (2002), JSCE-SF4 (1984), BS EN 14651 (2005) and JCI-S-001 (2003) recommend to make a notch at the middle of the prism, in order to concentrate the cracking at the centre of the prism. ASTM C 1018 (1997) and JCI-S-003 (2007) do not necessitate a notch. In the un-notched prisms, cracking may form at any section in the middle one-third of the prism, where the moment is maximum and constant. When the test aims to study the fracture energy behaviour of concrete through a load versus crack mouth opening curve, it is more appropriate to follow the notched-prism test procedures. Whereas to obtain the bending moment versus curvature curve (or to obtain σ-ε curve), unnotched-prism testing can also be used.

To study the fracture energy behaviour of concrete a discrete crack model approach is usually adopted in FE programs which uses the stress-crack opening (σ-w) relationship as the softening law of the concrete in tension. The location of the crack should be predefined in this approach (necessitating the use of the notched specimen test results). With this approach the behaviour of concrete in tension is characterized by a stress-displacement response rather than a stress-strain response. The implementation of this stress-displacement concept in a FE model requires the definition of a characteristic length, which is based on the element geometry and formulation. For a first-order solid element the characteristic length is the average element dimension. Therefore, elements with large aspect ratios will have rather different behaviour depending on the direction in which they crack, and some mesh sensitivity remains because of this effect. The displacement corresponding to each integration point is calculated by multiplying the strain by the characteristic length.

In the current study the softening law is described with the stress-strain (σ-ε) relationship, in which it is assumed that the cracking is smeared over the characteristic length representing the crack band width. In this case the unnotched specimens test result can also be used for determination of the stress-strain (σ-ε) relationship, and the characteristic length does not directly affect the calculation of the softening law.

In this study both notched and unnotched tests were undertaken and the results were processed in a comparative way. The notched specimens were studied to benefit from the

more accurate behaviour of them in testing. The unnotched specimens were also examined to avoid uncertainties caused by limitations in FE modelling of the notched prisms (Section 5.3.2).

4.2.2.1 Prisms for bending tests

The prisms were 150 mm deep, 150 mm wide and 550 mm long and were cast in steel-plate moulds to avoid deformation of the moulds due to compaction of the RCC specimens (Figure 4.10(a)). RCC specimens were cast in three layers in a similar way to cubes (Figure 4.10(b)).

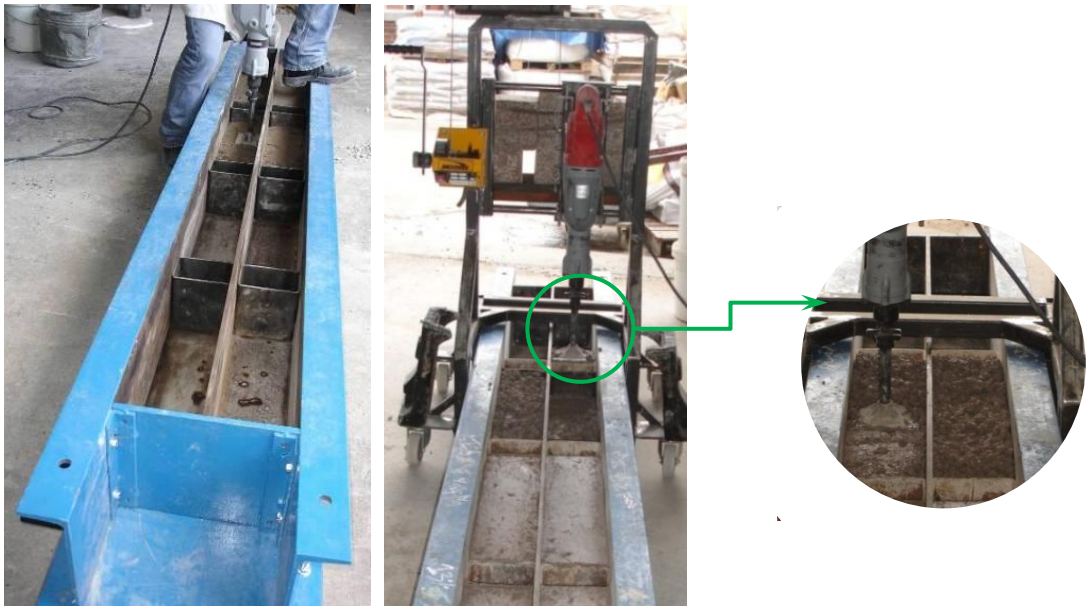

(a) (b)

Figure 4.10 (a) Steel-plate prismatic moulds; (b) Casting RCC prisms using electric hammer

The recommendations of BS EN 14651 (2005) were followed, apart from the loading arrangement which is four-point loading instead of three-point loading. The specimens were de-moulded after one day and were cured in water for more than 90 days to gain full maturity.

For the notched prisms, a notch (25 mm height and 5 mm width) was sawn on the tensile face of the mid-span, using a rotating diamond blade (Figure 4.11). For the RCC specimens the notch was perpendicular to the compacted layers, and for CC mixes it was sawn on a side with an angle of 90º to the top casting surface (BS EN 14651, 2005).

Figure 4.11 Notching prisms using rotating diamond blade

To ensure accurate deflection measurements and ignore the effect of any possible torsion, a yoke was used as specified by the Japan Society of Civil Engineers (JSCE-SF4, 1984). The specimens were tested in a 1000 kN servo-hydraulic machine, as seen in Figures 4.12(a) and 4.13(a), under displacement control. Two bearing rollers (free to rotate out of plane) were used to impose the load on the specimen.

The average mid-span beam deflections were measured on both sides of the prisms versus the applied load using two transducers fixed to the yoke. For the notched prisms, the rate of displacement was controlled by the crack mouth opening, while for the un-notched prisms the rate of displacement was controlled by the mid-span deflection. Initially the displacement was applied at the very slow rate of 0.02 mm/min and then the rate was increased to 0.2 mm/min. The arrangements of the LVDTs for the notched and un-notched specimens are shown in Figure 4.12(b) and 4.13(b), respectively. To obtain extra information on crack propagation, some additional LVDTs were also installed at different locations, but their results will not be used directly in the analysis.

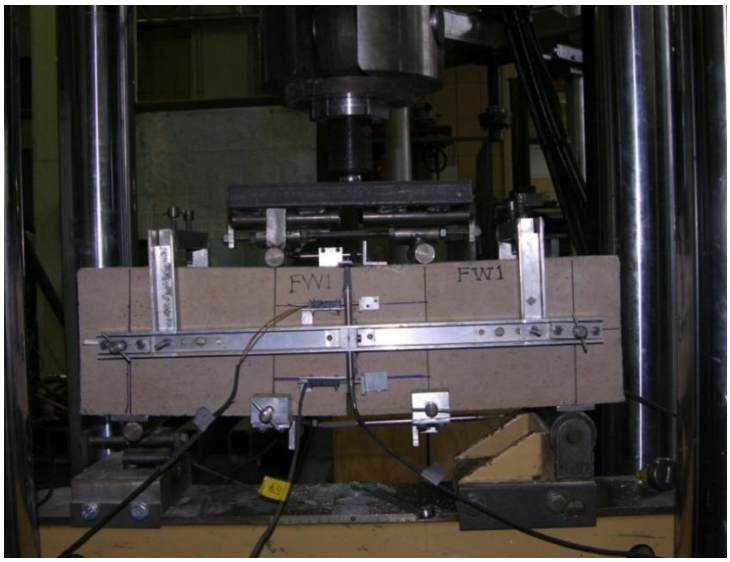

(a)

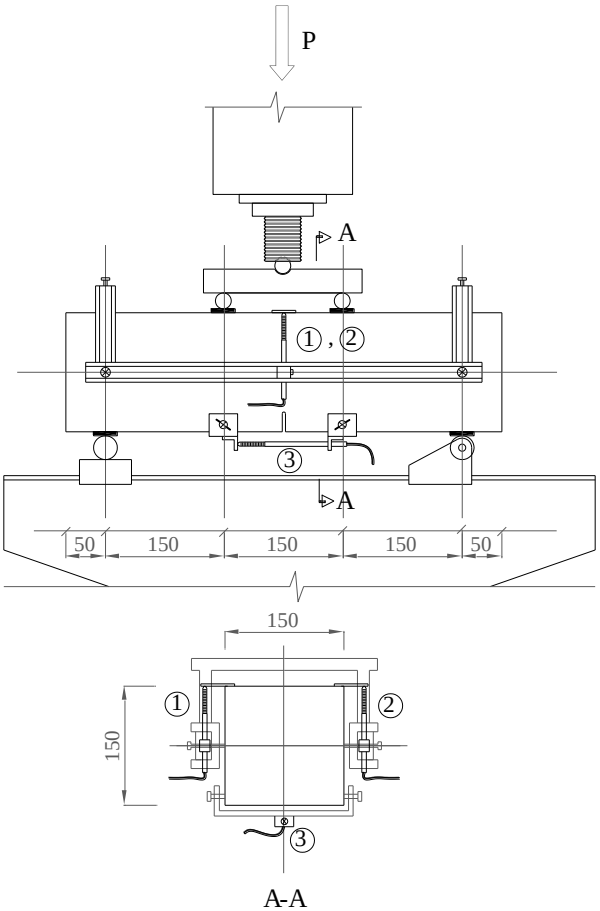

(b)

Figure 4.12 (a) Set up of bending test; (b) Arrangement of LVDTs, for the notched prisms

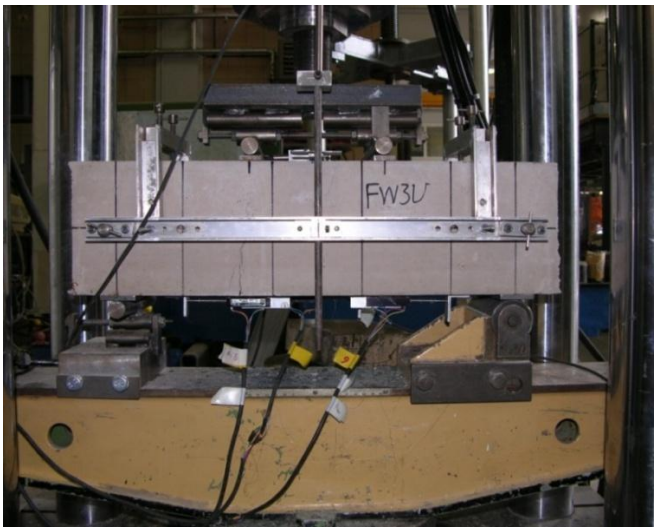

(a)

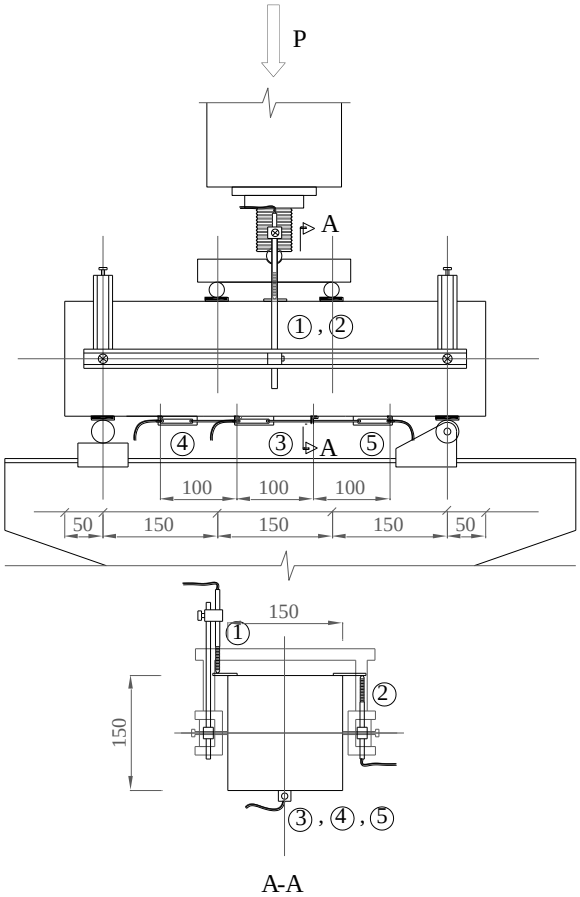

(b)

Figure 4.13 (a) Set up of bending test; (b) Arrangement of LVDTs, for the un-notched prisms

4.2.2.2 Estimation of the bending elastic modulus

The elastic modulus of concrete can be estimated using the results of bending tests. The formula derived by Alexander (1982) (cited in Elshaigh, 2007) is adopted for this purpose (Equation 4.1).

$$E\ (MPa) = \frac{23}{1296}.\frac{P}{\delta}.\frac{l^3}{I}[1 + \frac{216}{115}.(\frac{h}{l})^2.(1+\nu)].10^3 \qquad \text{(Eq. 4.1)}$$

Where, $\frac{P}{\delta}$ is the slope of the linear elastic part of the load-deflection curve (N/mm^2); l is the supported span of the beam (mm); I is the second moment of area of the cross-section $\frac{bh^3}{12}$ (mm^4); b is the width of the cross-section (mm); h is the height of the cross-section (mm); and ν is the Poisson's ratio.

The above formula is based on the elastic beam theory which ignores the load distribution or the load-spreading effect through the depth of the specimen (Timoshenko et al., 1970). Due to the effect of load-spreading in deep elements, the concentrated forces may transform into distributed pressure (Figure 4.14), leading to lower displacement compared to the elastic beam theory (Graeff, 2011).

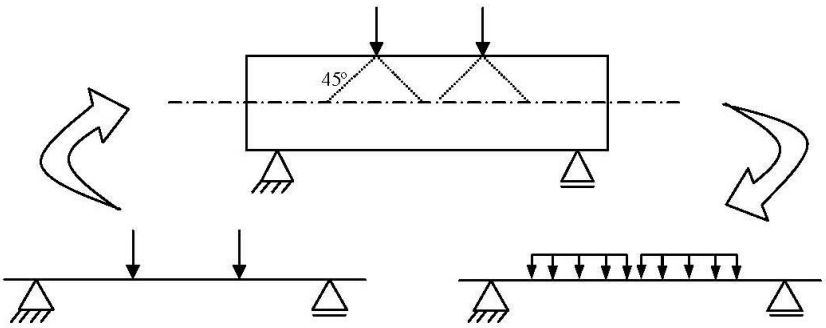

Figure 4.14 Load spreading effect (Graeff, 2011)

Graeff (2011) assessed the effect of load-spreading in reducing the vertical displacement induced in FEA models of the same size and the same material as tested in the current research. The results of FEA showed that the reduction in vertical displacement caused by the effect of load-spreading is approximately 2%, which cannot be significant in calculation of the elastic modulus based on Eq. 4.1.

4.2.2.3 Bending tests results

Plotted in Figure 4.15 are the averaged load-deflection curves of the notched (dashed lines) and un-notched (solid lines) prisms for different mixes. The flexural elastic modulus is also averaged for different mixes and summarised in Table 4.6. More details on the results obtained for various specimens and mixes are given in Appendix C. For the notched prisms, the crack was initiated from the notch for all prisms. For the un-notched prisms, the crack had variable locations between the loading points. Pictures showing these positions are given in Appendix C.

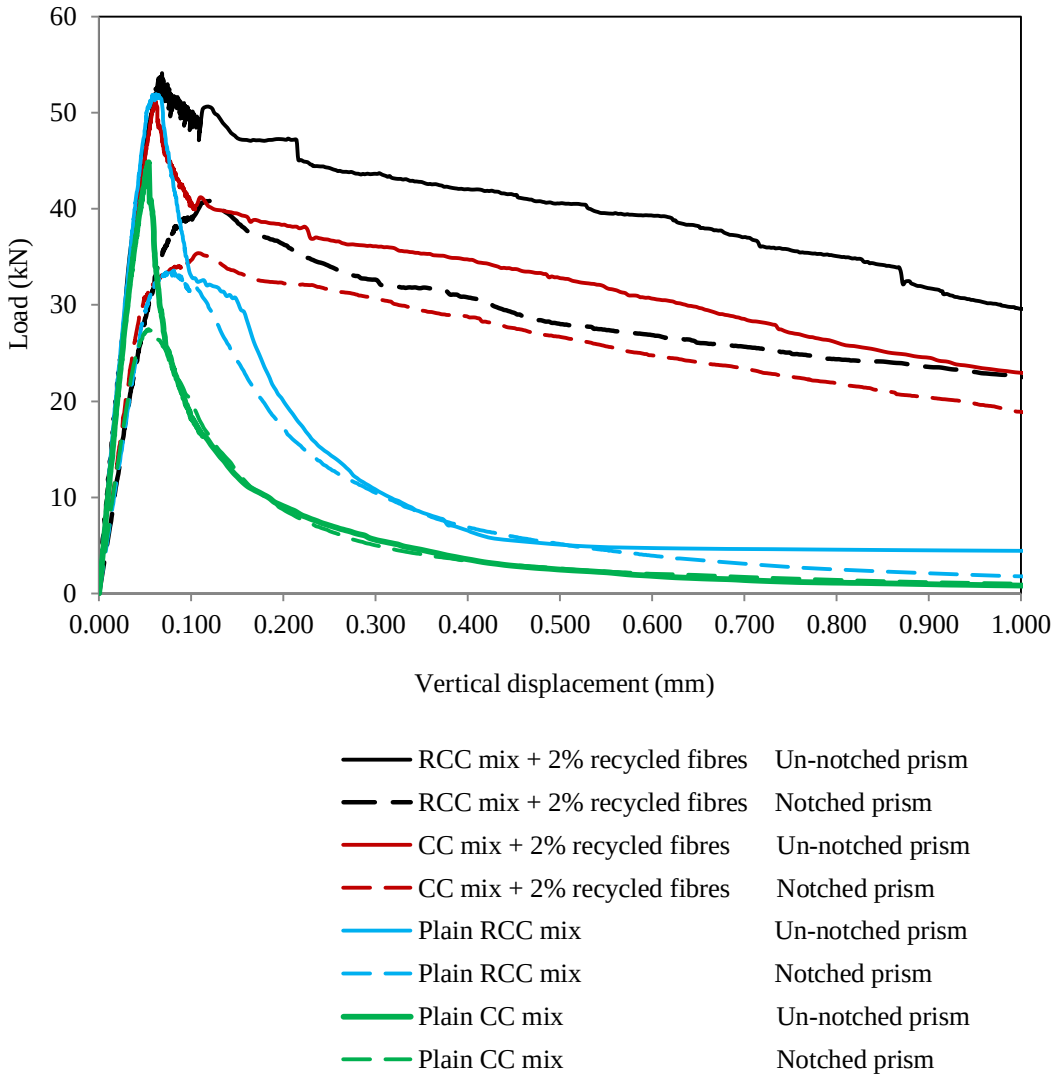

Figure 4.15 Averaged load-deflection curves for various mixes of notched and un-notched prisms

Table 4.6 Elastic modulus obtained from bending tests

			SFR-RCC	SFRC-CC	Plain RCC	Plain CC
E modulus (GPa)	Notched prisms	Specimen 1	40.0	47.1	42.9	46.4
		Specimen 2	39.9	41.9	43.1	44.0
		Specimen 3	38.2	48.3	41.9	46.5
		Average	**39.4**	**45.8**	**42.6**	**45.6**
		St. deviation	0.8	2.8	0.5	1.2
	Un-notched prisms	Specimen 1	42.5	35.6	46.1	39.5
		Specimen 2	-	45.2	36.7	39.6
		Specimen 3	-	-	40.8	39.1
		Average	**42.5**	**40.4**	**41.2**	**39.4**
		St. deviation	-	4.8	3.8	0.2
	Average		**41.0**	**43.1**	**41.9**	**42.5**
	St. deviation		1.6	2.7	0.7	3.1

4.2.2.4 Discussion on the bending test results

Limit of proportionality (LOP), $f_{ct,L}^{f}$ (also called flexural tensile strength), and residual flexural tensile strength, $f_{R,j}$, have been calculated for experimental prisms (BS EN 14651, 2005; modified for four-point load arrangement).

(LOP), $f_{ct,L}^{f}$, is defined as stress at the tip of the notch (or at the constant moment zone of an un-notched prism, at the bottom surface) with linear stress distribution, which is assumed to act in an uncracked mid-span section of a prism subjected to the load F_L as defined in Figure 4.16 (BS EN 14651, 2005). The figure shows the force versus displacement rather than CMOD in the standard. Equation 4.2 has been modified to account for 4-point loading.

$$f_{ct,L}^{f} = \frac{F_L\, l}{b\, h^2} \qquad \text{(Eq. 4.2)}$$

Where, F_L is the load corresponding to LOP; l is the span length; b is width of the test specimen; and h is the distance between the tip of the notch and the top of the test specimen (of the total depth of the test specimen for an un-notched prism).

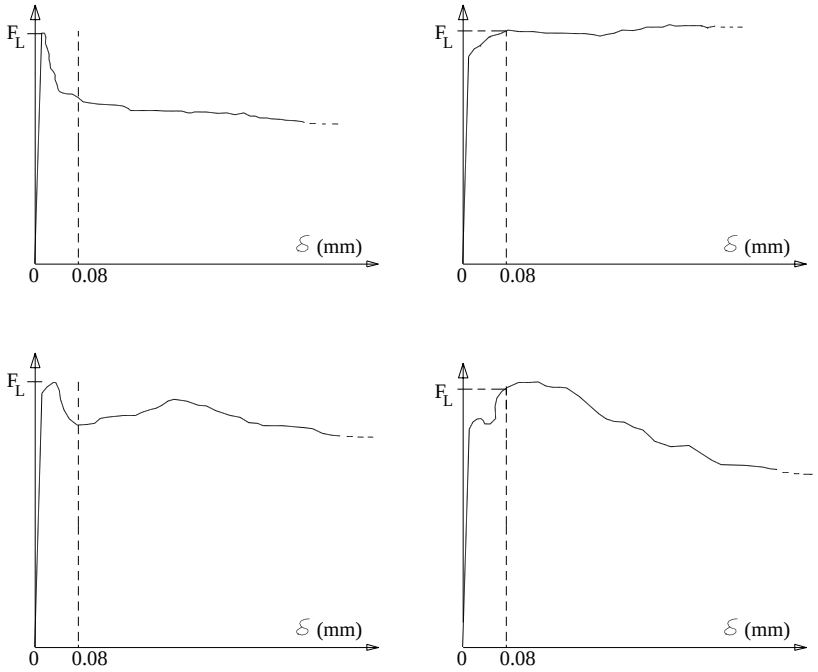

Figure 4.16 Definition of F_L (after BS EN 14651, 2005)

Residual flexural tensile strength, $f_{R,j}$, as given in Equation 4.3 is defined as a fictitious stress at the tip of the notch (or at the bottom surface of the constant moment zone of an un-notched prism) with linear stress distribution, which is assumed to act in an uncracked mid-span section of a prism subjected to a load F_j corresponding to deflection δ_j, where $\delta_j > \delta_{F_L}$ $(j = 1, 2, 3, 4)$. The load F_j corresponding to deflection δ_j is defined in Figure 4.17 (modified from CMOD in BS EN 14651, 2005).

$$f_{R,j} = \frac{F_j\, l}{b\, h^2} \qquad \text{(Eq. 4.3)}$$

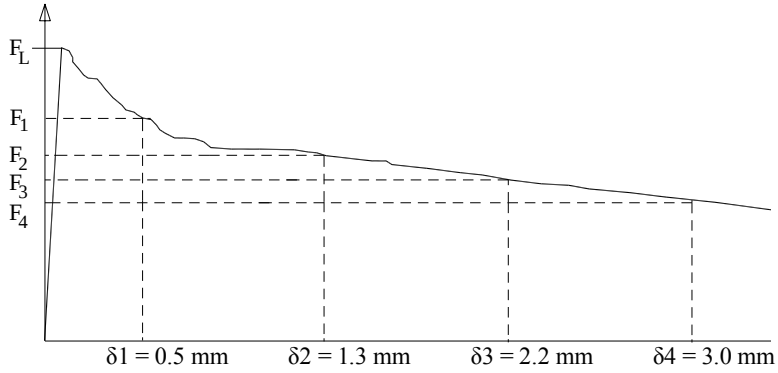

Figure 4.17 Load-deflection diagram and F_j (j = 1, 2, 3, 4)

Figure 4.18(a) and 4.18(b) show the experimental load levels obtained for the notched and the un-notched prisms, respectively, based on the definition given in Figure 4.16 and 4.17. The calculated values for the LOP, $f_{ct,L}^{f}$, and residual flexural tensile strengths, $f_{R,j}$, are given in Table 4.7.

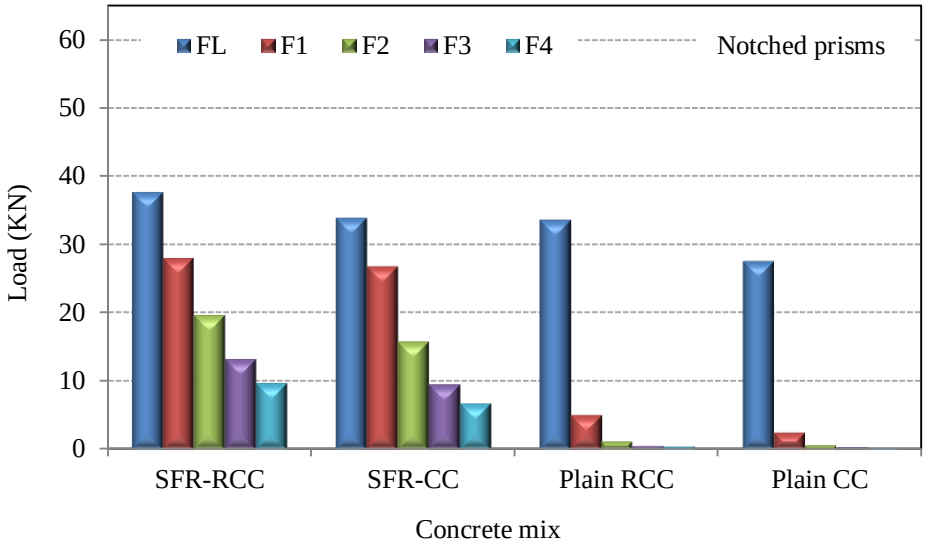

(a)

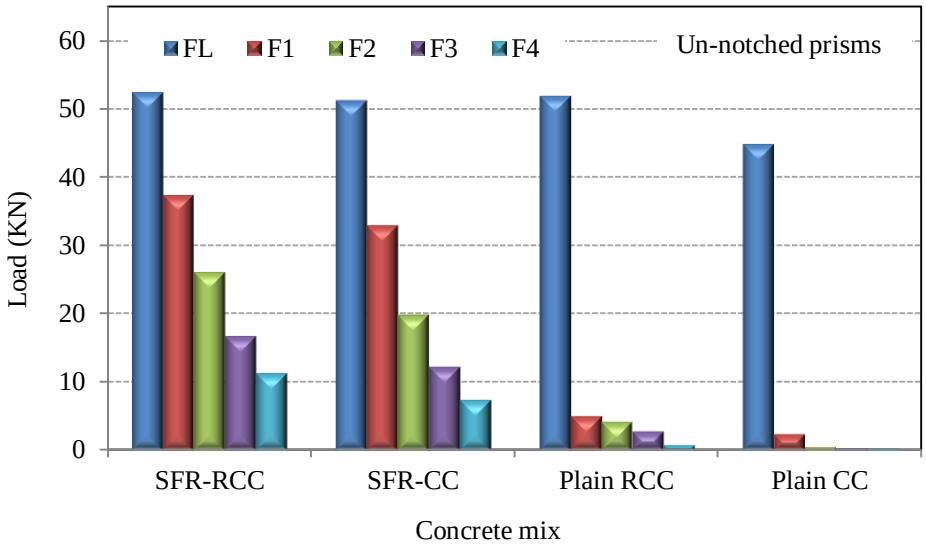

(b)

Figure 4.18 Experimental load levels, (a) notched prisms; (b) un-notched prisms

Table 4.7 Values for the LOP, $f^{f}_{ct,L}$, and residual flexural tensile strengths, $f_{R,j}$

		SFR-RCC	SFRC-CC	Plain RCC	Plain CC
Notched prisms	$f^{f}_{ct,L}$ $(\frac{N}{m^2})$	7.2	6.5	6.4	5.3
	$f_{R,1}$ $(\frac{N}{m^2})$	5.4	5.1	1.0	0.5
	$f_{R,2}$ $(\frac{N}{m^2})$	3.8	3.0	0.2	0.1
	$f_{R,3}$ $(\frac{N}{m^2})$	2.5	1.8	0.1	0.1
	$f_{R,4}$ $(\frac{N}{m^2})$	1.8	1.3	0.1	0.1
Un-notched prisms	$f^{f}_{ct,L}$ $(\frac{N}{m^2})$	7.0	6.8	6.9	6.0
	$f_{R,1}$ $(\frac{N}{m^2})$	5.0	4.4	0.7	0.3
	$f_{R,2}$ $(\frac{N}{m^2})$	3.5	2.6	0.6	0.1
	$f_{R,3}$ $(\frac{N}{m^2})$	2.2	1.6	0.4	0.1
	$f_{R,4}$ $(\frac{N}{m^2})$	1.5	1.0	0.1	0.1

The LOP, for SFR-RCC specimens is slightly higher than for SFR-CC specimens (by less than10%). The LOP, for plain RCC specimens is also higher than for plain CC specimens by 15-20%. The LOP, for SFRC specimens, is slightly higher than for plain specimens. The increase of the LOP by adding fibres is bigger for CC mixes compared to RCC mixes.

Although LOP, $f^{f}_{ct,L}$, is defined as the stress with a fictitious linear distribution corresponding to the load F_L, it does not represent the first-crack flexural strength of concrete. The first-crack flexural strength corresponds to the load at which the load-deformation curve departs from linearity. The first-cracking load in SFRC is smaller than F_L or the maximum load achieved.

It is also observed that, as expected, the residual flexural strengths are considerably higher for SFRC mixes compared to plain mixes. This is due to the increased energy absorption and strain capacity of SFRC called toughness. The area under the load-deflection curve represents the total energy absorbed up to any specific deformation. The flexural strength and toughness

in SFRC is enhanced due to the stress redistribution along the specimen depth after cracking.

The residual flexural strength of SFR-RCC specimens is also higher than that for SFR-CC specimens.

The elastic modulus obtained from the bending tests is compared in Figure 4.19 for the notched and the un-notched prisms. This figure shows that the average bending elastic modulus is nearly the same for SFRC and plain mixes. The average elastic modulus of RCC mixes, from the bending tests, is slightly lower than CC mixes.

The elastic modulus obtained from the bending tests for CC mixes are very close to the values obtained from the compressive tests on cylinders. However, the compressive elastic modulus of RCC mixes is considerably lower than the bending elastic modulus. As stated earlier in Section 4.2.1.3, this difference is attributed to the effect of boundaries on the compaction of RCC cylinders. Therefore, the FE analyses presented in the following chapters will be based on the elastic modulus obtained from the bending tests.

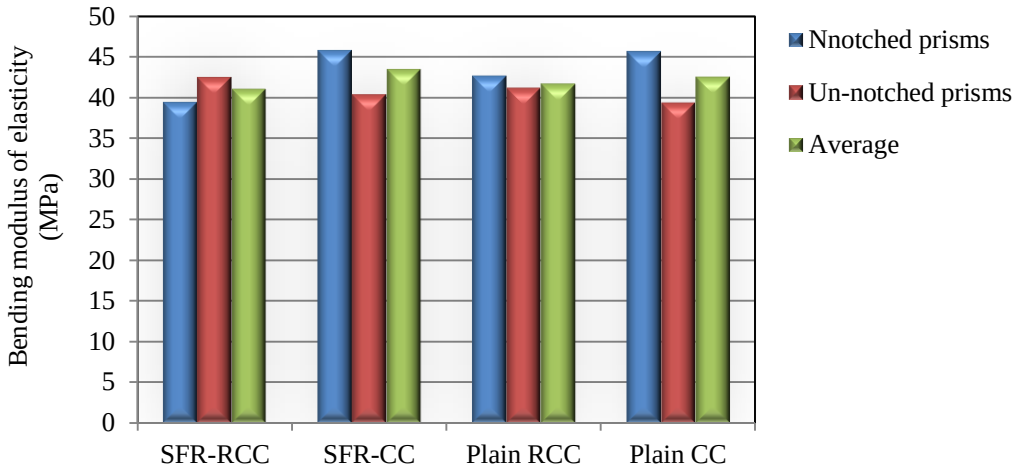

Figure 4.19 Comparison of the bending modulus of elasticity

The obtained results are valid for the specific compositions of RCC and CC mixes as given above reinforced with 2.5% recycled steel fibres of the mentioned characteristics. These concrete compositions, fibre content and characteristics have been chosen based on the optimisation studies carried out during the Ecolanes project. For other concrete compositions, different fibre contents and fibre types (such as for industrially produced fibres) different results are anticipated.

4.3 Experimental studies to obtain moisture movement and shrinkage properties

To obtain moisture transport and free shrinkage properties of concrete mixes, two sets of specimens were cast; one set to obtain moisture profiles in one-dimensional drying and another set for free shrinkage measurements.

4.3.1 Specimens for moisture measurement

The modified gravimetric method (described in Section 3.2.1) was used for moisture measurement. For determination of moisture profiles, specimens with a size of 180 × 150 × 150 mm were cast. Different heights were prepared by cutting each specimen into two and maintaining the integrity by placing the two pieces on top of each other during the drying period to preserve the original boundary conditions (Figure 4.20(a) and 4.20(b)). Cutting was performed in wet conditions, and there was no possibility of drying before the specimens were sealed on the sides and bottom surface. Sealing was designed to provide one-dimensional drying conditions. The relevant surfaces of the top and bottom segments were sealed permanently using a high-performance 5 ply laminated aluminium foil tape (as explained in Section 3.2.1). To prevent moisture escape from the cut surface, after each measurement, the joint between the top and bottom segments was sealed by a layer of plastic tape which could be easily unwound for the next measurement (Figure 4.20(c)). This piece of tape was discarded after each use. Based on the study carried out by Ayano et al. (2002), the effect of these joints on moisture transfer can be considered to be small. In that study the moisture diffusion coefficient of a pile of sliced specimens with that of a solid specimen was compared and the effect of sealed cut surfaces was found small.

(a) (b) (c)

Figure 4.20 Specimens used for moisture measurement

The casting and cutting dimensions are illustrated in Figure 4.21.

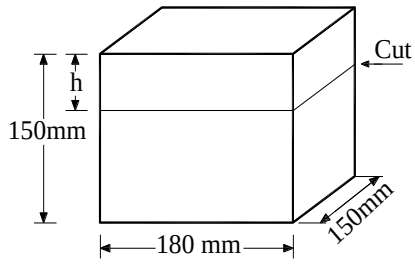

Specimen No.	Cutting depth (h)
1	10 mm
2	20 mm
3	35 mm
4	60 mm
5	100 mm

Figure 4.21 Cutting depths in moisture measurement

The standard experimental humidity condition is usually around 55%-60%. Drying is a very slow phenomenon. The rate of drying is highly affected by the difference between the environmental humidity and the specimen's humidity. Due to time limitations and in order to accelerate drying of the specimens, in this research the specimens were placed in a chamber with relative humidity of 40±3% and temperature of 25±3ºC.

After 90 days of water curing, drying in the experimental conditions began. At 1, 3, 5, 7, 14, 28, 42, 56, 70 and 84 days after the start of drying the weight changes of the top pieces were measured in order to obtain the spatial distribution of moisture content over time.

To obtain dry density, after 84 days of measurement, the specimens were unsealed and put in the oven for a period of seven days at 120ºC. This duration was not long enough to dry the core of the thick specimens. Figure 4.22 shows the penetration depth of drying for a broken CC specimen, after one week drying in the oven.

Based on the visual observations the wet core had a dimension of 100 mm in CC specimens (and slightly less than 100 mm in RCC specimens). The drying rate for the specimens thinner than 35 mm also approached zero after a week of drying in the oven. It means that the specimens with a thickness less than 35 mm were fully dried in that condition. Therefore, the dry density of each mix was determined based on the dry weight of the top segments having thickness less than 35 mm.

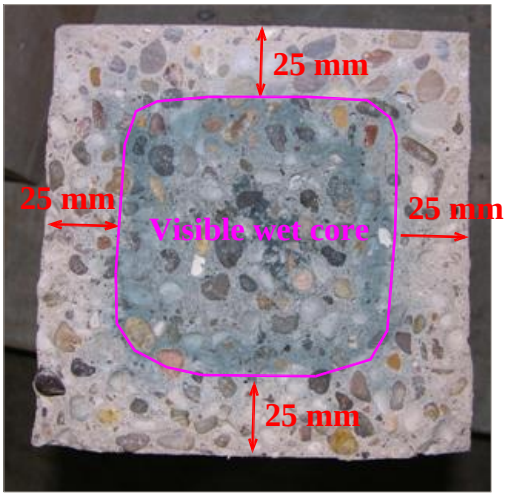

Figure 4.22 Penetration depth of drying after one week drying in the oven in addition to 90 days drying in the experimental conditions, for a broken CC specimen

4.3.2 Free shrinkage specimens

To measure free shrinkage, the use of a long prismatic specimen is recommended by most standards (ASTM C 157, 2008; and BS EN 12617-4, 2002). The length change of this specimen versus drying represents one dimensional free shrinkage provided that the length of the specimen is assumed much larger than the cross sectional dimension. The specimen size recommended by ASTM is 76 × 76 × 286 mm, and the specimen size specified by BS EN is 40 × 40 × 160 mm. In this study, to eliminate the effect of boundary conditions on fibre distribution and due to limitations in compaction of RCC, the size of specimens was increased to 150 ×150 × 550 mm. The two end sides of the specimen were sealed and moisture transport was allowed only from the sides which were all exposed to drying (Figure 4.23).

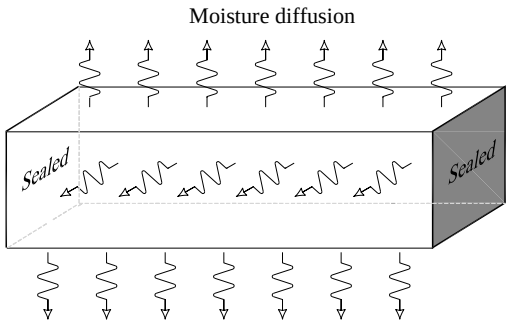

Figure 4.23 Prismatic specimen for free shrinkage measurement

There were three samples from each mix. Unrestrained conditions were provided by laying the specimens on two sharp edges (Figure 4.24(a)). The environmental conditions and the measurement plan were exactly the same as for moisture measurement. The measurements were made on the length changes of the specimens using the device shown in Figure 4.24(b) and according to BS EN 12617-4 (2002).

(a)

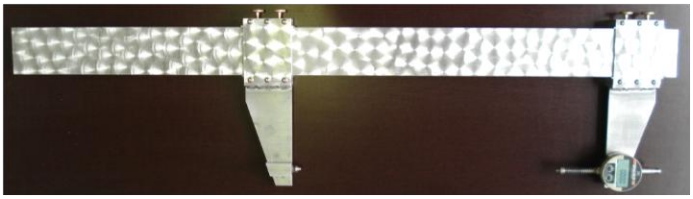

(b)

Figure 4.24 (a) Free shrinkage specimens; (b) Free shrinkage measurement device

4.3.3 Results and discussion on experimental moisture movement and shrinkage properties

Plotted in Figure 4.25 are the results obtained from moisture measurements. The results are presented in the form of moisture content profiles for a period of 84 days drying in the specific experimental conditions, as explained in Section 4.3.1. More details on how to calculate moisture profiles, from experimental data in gravimetric moisture measurement, are given in Appendix B.

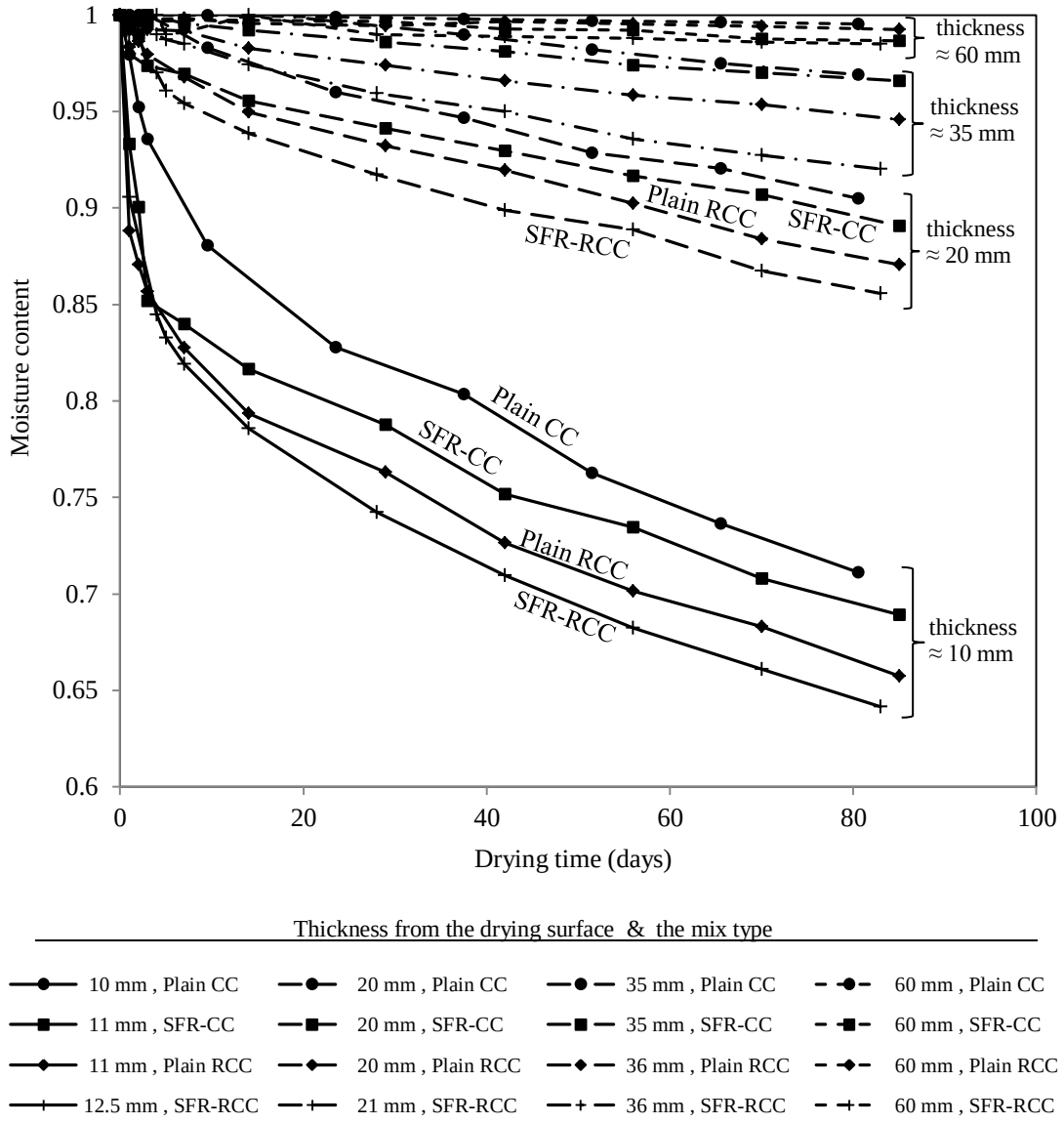

Figure 4.25 Experimental moisture profiles, all mixes

As it is seen in Figure 4.25, after around 84 days, at a depth of 10 mm from the drying surface, the moisture content dropped to the range of 65% to 70% for all the mixes, while at a depth of 60 mm it only dropped to around 99%, at the same time. This shows that penetration of drying front into the depth occurs at a very slow rate. This can be attributed to the dense pore system of concrete (also stated by Bisschop (2002)).

As expected, drying in RCC mixes is faster than CC mixes. The reason can be the higher porosity of RCC mixes. For the same reason, drying of SFRC mixes is also faster than plain

mixes. The rate of drying is faster at early ages and then decreases with concrete aging.

Figure 4.26 shows the results obtained for free shrinkage. Shrinkage of CC mixes at early ages occurred in a faster rate and then the rate considerably decreased, while for RCC mixes shrinkage occurred at a more uniform rate. This could be the reason for the lower short-term shrinkage of RCC compared with CC mixes reported by some researchers (Pittman et al., 1998; Delatte, 2004) (Section 2.2.1.3). Figure 4.26 shows that at the end of the experimental time period shrinkage of the RCC mixes meet the value of shrinkage obtained for CC mixes and it is predicted to exceed it afterwards.

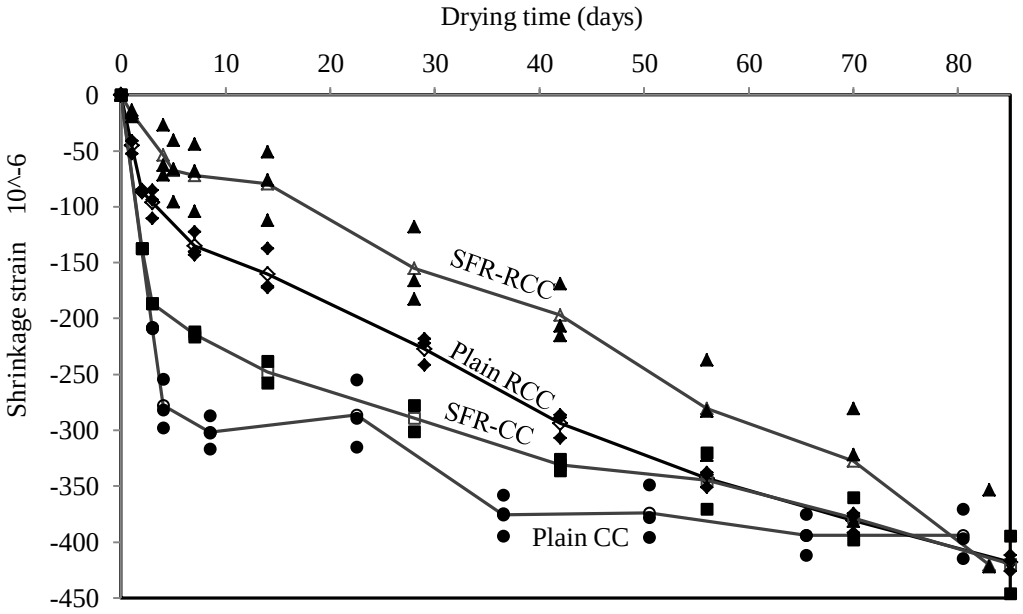

Figure 4.26 Strain history curves for free shrinkage specimens

Shrinkage values were higher for plain mixes compared with SFRC mixes, at any given time during the experimental measurements. This behaviour was observed by some researchers (Chern et al., 1989; Li et al., 2006), and was attributed to the restraining effect of the fibres (Section 2.2.1.2). This difference approaches to zero at the end of the experimental time period.

In the shrinkage curves of plain CC mix, a relative expansion is seen around the age of 15-22 days. This cannot be due to the un-controlled variation in the test conditions, since measurements were taken on other mixes, at the same date. This issue will be examined in

comparison with analytical models in Chapter 5, Section 5.2.1.

The obtained results are valid for the specific compositions given, and under the experimental environmental conditions (40% relative humidity and 25°C). For other concrete compositions, with various fibre contents and types, and under different environmental conditions different results are expectable. For example lower environmental relative humidity can accelerate drying of the specimens. Consequently, the amounts of moisture contents and shrinkage strains presented in Figure 4.25 and 4.26 may be obtained during a shorter period of time. Higher environmental relative humidity may also affect the results inversely (by delaying drying and shrinkage of the specimens). The environmental relative humidity examined in this research (40%) is relatively a low value for outdoor conditions and has been chosen to accelerate drying of the experimental specimens due to the short time available for experimental studies. However, the material properties such as diffusivity and hygral contraction coefficient of concrete mixes, which will be obtained in the next chapter based on the above mentioned results, would be independent of the environmental conditions. The role of keeping a constant temperature nearly the same as the curing temperature is also important in avoiding the effect of thermal volumetric movements to interfere with the drying shrinkage test results.

Chapter 5

5 Data processing analyses

This chapter deals with data processing to obtain the material properties from experimental data and relies on inverse analysis. The material properties derived from the experimental data, are as follow:

- Moisture diffusivity, $K_C(C)$, and Convective moisture transfer coefficient (also called surface factor or film factor), f, by inverse analysis of moisture profiles (Figure 4.25)

- Relationship between free shrinkage strain and moisture loss ("hygral contraction coefficient"), by inverse analysis of shrinkage strain time histories (Figure 4.26)

- Peak tensile strength and the tension stiffening curve, by inverse analysis of bending test on prisms.

The inverse analyses are performed via FE modelling. ABAQUS (2010) is adopted for FE modelling, because of its availability and its good capabilities for modelling non-linear behaviour of concrete and SFRC.

5.1 Moisture diffusivity, $K_C(C)$, and surface factor, f

It is assumed that the flow of moisture in concrete subjected to drying obeys the diffusion equation (Chapter 3). An FE model of the tested specimens is developed for the moisture transport analysis. This model is verified using some existing experimental and analytical moisture transport models (Asad, 1995). Then using inverse analysis technique the moisture diffusivities are back-calculated from the test results of moisture measurement specimens for the concrete mixes, as non-linear functions of moisture content. Similarly, the convective moisture transport coefficients or the surface factors are back-calculated from moisture measurements.

Since the diffusion equations governing heat transmission and moisture migration are analogous, moisture transport is simulated using a heat transfer analysis in ABAQUS in which:

- Free moisture content maps to the temperature as the main field variable;
- Moisture diffusivity maps to the thermal conductivity as the transport property;
- The "hygral contraction coefficient" maps to the thermal expansion coefficient in stress calculation.
- To avoid the effect of extra multipliers which are needed in the heat transfer equation but not in the moisture transport equation (specific heat and density), these relevant properties are taken equal to unity.

Therefore, moisture transport physical parameters should be defined in the form of heat transfer physical parameters considering unit consistency in the equations. To have a comparison between these equations, the governing equations for heat transfer and for moisture transport are presented below:

For hardened concrete the heat transfer is governed by the following equation:

$$div[K_T\ grad(T)] = \rho C_T \frac{\partial T}{\partial t} \qquad \text{(Eq. 5.1)}$$

Where K_T is thermal conductivity $(W/m°C)$, T is temperature (°C), ρ is density (kg/m^3), C_T is the specific heat capacity $(J/kg°C)$ and t is time (s).

The moisture diffusion in concrete is governed by the following equation:

$$div[K_C\ grad(C)] = \frac{\partial C}{\partial t} \qquad \text{(Eq. 5.2)}$$

Where K_C is moisture diffusivity (m^2/s), C is free moisture content (m^3/m^3) and t is time (s).

For unit consistency in simulation of moisture tranport equation with heat transfer equation in ABAQUS, ρ (density) and C_T (specific heat capacity) should be entered equal to unity. Therefore, K_C is entered instead of $\frac{K_T}{\rho C_T}$.

5.1.1 Verifying the FE model for moisture transport analysis

For verifying the model developed for moisture transport analysis, a comparison is made with the results of the research carried out by Asad (1995). The geometry and the boundary conditions of the experimental sample tested by Asad are illustrated in Figure 5.1.

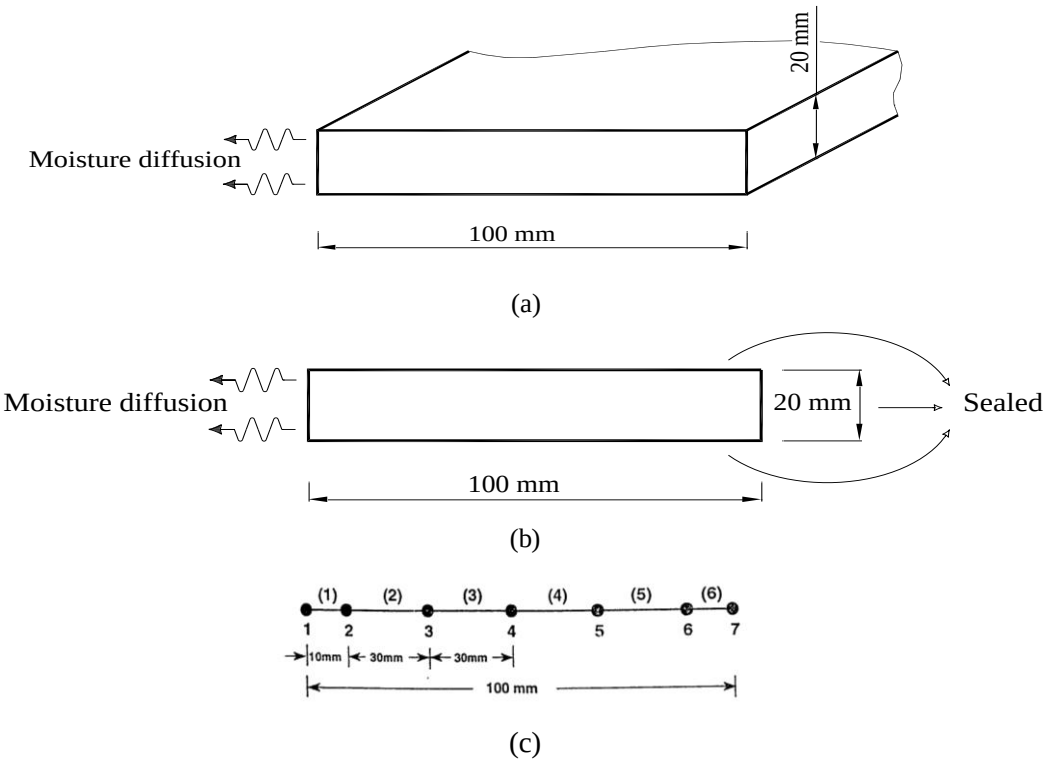

Figure 5.1 Asad's (1995): (a) The physical model; (b) 2-D FE simplification of the physical model; (c) 1-D FE discretisation of the physical model

The initial moisture content of this sample is equal to 1.0 or 100%. The surface factor has been assumed 3 mm/day, and diffusivity, k_c, has been considered to be the following function of the moisture content by Asad (1995):

$$k_c(mm^2/day) = 11.75 + 5(\frac{c}{1-c})^{1.878} \qquad \text{(Eq. 5.3)}$$

In the current study, the above sample is modelled in 3D as shown in Figure 5.2.

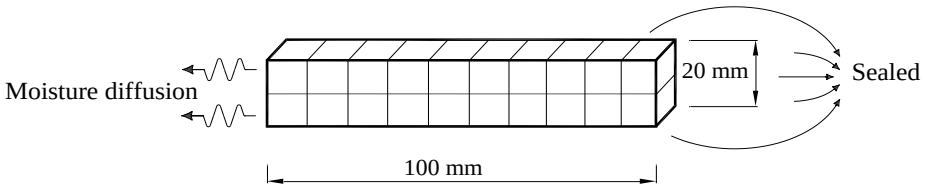

Figure 5.2 3D FE model of Asad's sample in the current study

A comparison between the results of the experimental and analytical work carried out by Asad (1995) with the 3D model developed in the current research is shown in Figure 5.3.

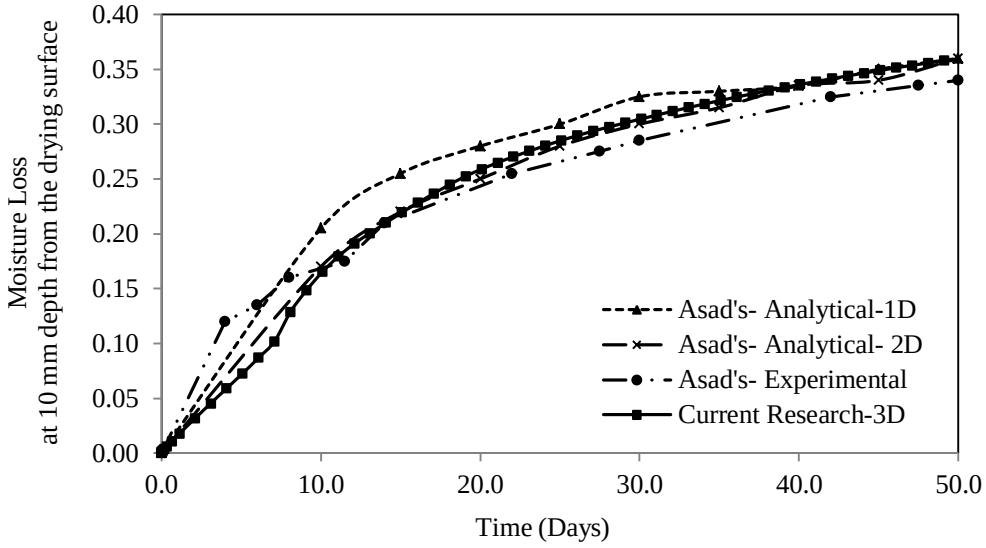

Figure 5.3 Moisture transport FE analysis in the current research and in the literature

A good agreement is observed in this comparison between the moisture transfer from the FE analysis and the case study. The difference at the initial stages between the experimental curve and the FE result (2D and 3D) will be discussed later.

5.1.2 Inverse analysis for moisture diffusivity and surface factor

The moisture movement is modelled for the 180×150×150 mm experimental specimens. Since the experimental specimens are sealed on the sides and bottom surface, those surfaces are assumed not to have any moisture interaction with the surrounding environment in the model. A constant ambient humidity of 40% is assumed (same as experimental conditions), and moisture convection from the top surface, occurs via a surface convection factor. As the initial condition, the moisture content is set equal to 1.0 (saturation condition).

The element used for moisture transport analysis is the ABAQUS 3D 8-noded solid element called DC3D8 (originally for heat transfer analysis). Since the FE model of the experimental moisture measurement specimens is a small model without computationally-costly features, the element sizes are taken small enough to easily capture the non-uniform moisture distribution. Figure 5.4 shows the FE model for moisture diffusivity analysis.

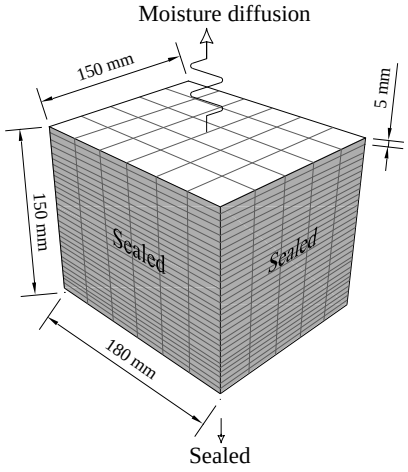

Figure 5.4 FE model for moisture diffusivity analysis

The moisture diffusivity, $K_C(C)$, as a function of moisture content, C, is back-calculated for mixes to obtain the best fit to the experimental curves. The resulted moisture diffusivity curves for the concrete mixes are shown in Figure 5.5.

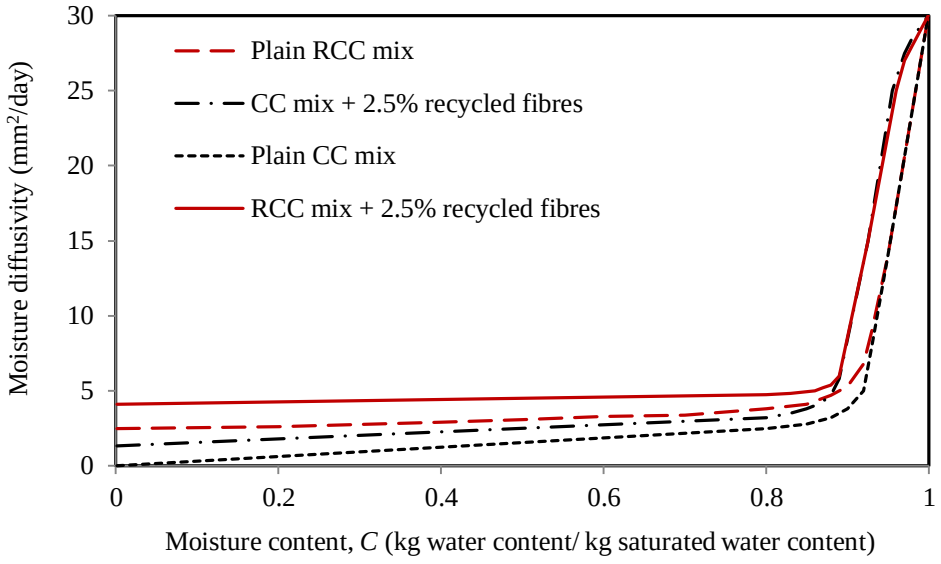

Figure 5.5 Moisture diffusivity, $\boldsymbol{K_C(C)}$, versus moisture content, C

As shown in Figure 5.5, moisture diffusivity curves are similar for all mixes and contain a near-horizontal branch followed by a near-vertical branch. Moisture diffusivity varies in the range of 0-5 mm^2/day for moisture content lower than 87-92% and then increases sharply. The moisture diffusivity of RCC mixes is slightly higher than for CC mixes, and for SFRC mixes slightly higher than plain mixes. This may be due to the higher porous nature of RCC and the air entrapped around fibres for SFRC.

The surface factors were also back-calculated as given in Table 5.1.

Table 5.1 Surface factors back-calculated by FE analysis

	CC mixes	RCC mixes
Surface factor (mm/day)	3-10 mm/day	5-10 mm/day

The surface factor can significantly affect the moisture profiles near the drying surface. Away from the drying surface, the effect of the surface factor on the moisture profiles quickly diminishes as shown in Figure 5.6. Therefore, to obtain *f* more accurately by inverse analysis the experimental values of moisture content at very close distance from the drying surface must be known, which are not always possible to measure. However, the accuracy of the surface factor, in the calculated range, does not have a significant effect on the final results especially at the end of the drying period.

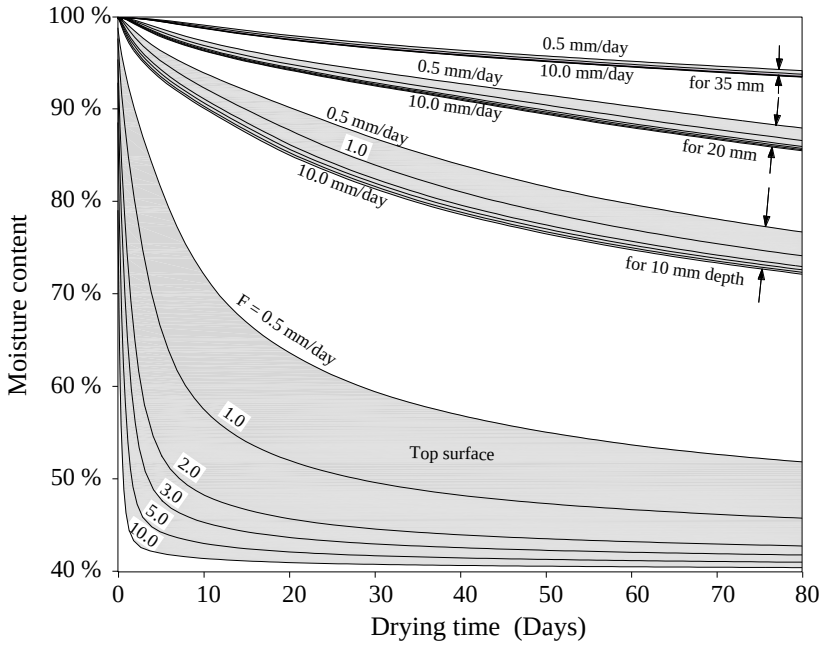

Figure 5.6 Effect of surface factor variations on the moisture profiles at different depths

Assuming the back-calculated moisture diffusivity functions shown in Figure 5.5 and the lower limit of the estimated ranges for the surface factors, the numerically calculated and experimental moisture profiles are shown in Figure 5.7. The curves presented in this figure are best fit curves to the experimental results, determined by changing moisture diffusivity and surface factors.

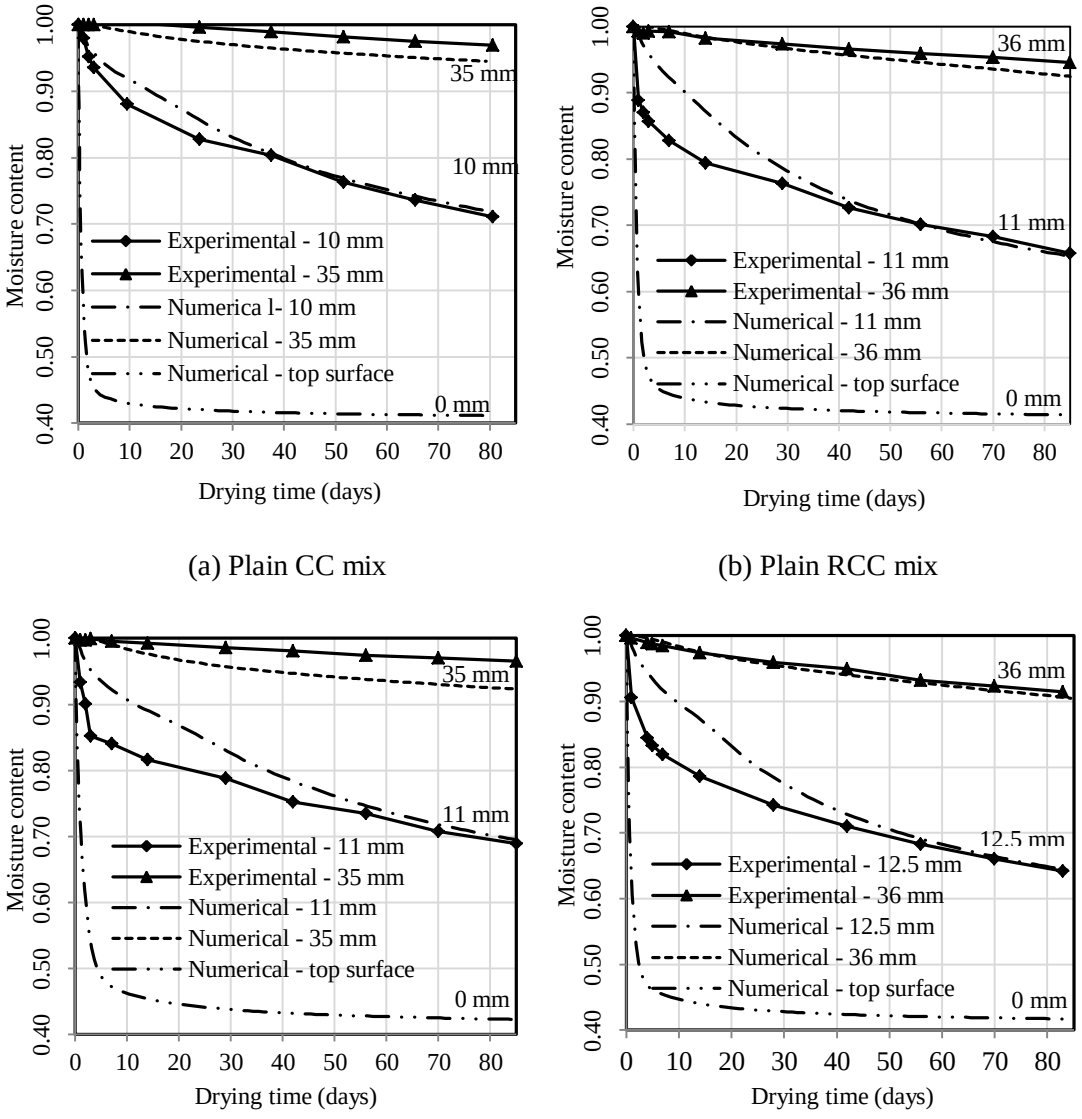

(a) Plain CC mix

(b) Plain RCC mix

(c) SFR-CC mix (2.5%)

(d) SFR-RCC mix (2.5%)

Figure 5.7 Numerical moisture profiles compared with the experimental: (a) Plain CC mix; (b) Plain RCC mix; (c) SFR-CC mix (2.5%); (d) SFR-RCC mix (2.5%)

As shown in Figure 5.7, the use of the diffusion theory as the single moisture transport mechanism in concrete gives good accuracy at moisture contents lower than 75-80%. This

indicates that for nearly saturated conditions bulk water flux also participates in moisture transport in the form of pore water suction and elevation, although diffusion in the form of vapour flux is the governing mechanism in unsaturated concrete.

5.2 "Hygral contraction coefficient"

"Hygral contraction coefficient" is determined based on the inverse analysis of free shrinkage test results. Due to the very slow process of drying in concrete, concrete members typically dry non-uniformly which means a moisture gradient develops across the member. Reaching a drying equilibrium may take months or years depending on the specimen size (Bisschop, 2002). Due to that moisture gradient, a shrinkage gradient is developed across the specimen.

Measuring true free shrinkage strain in concrete is not straightforward for two reasons: 1) drying rate through the section of the specimen is not constant, hence the measured drying shrinkage is some kind of average shrinkage, depending on where on the specimen shrinkage is measured; 2) an internal restraint is developed in the specimen to resist non-uniform shrinkage, such that tensile stresses are developed on the surface areas and compression in the core of the specimen. The tensile stresses restrain free shrinkage at the surface and the compressive stresses impose larger strains than the corresponding free shrinkage strain at the core (Figure 5.8).

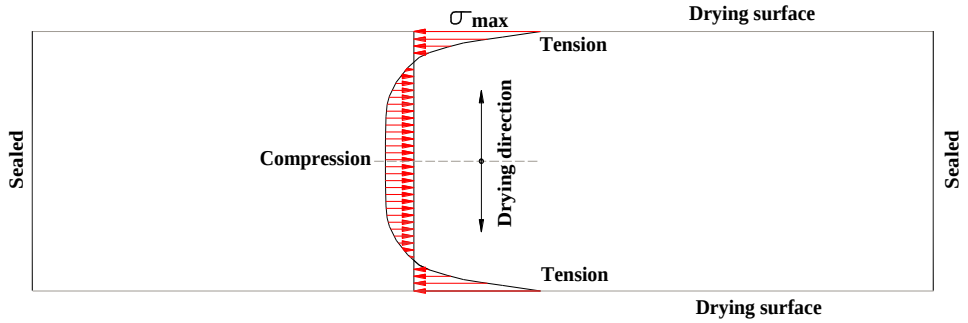

Figure 5.8 Stress distribution through the section of specimens in the free shrinkage test

The degree of the developed internal restraint depends on the specimen size, and consequently the measured drying shrinkage is larger for smaller size specimens (Wittmann, 2001). For bigger volume to surface ratios the tensile stresses on the surface can be big enough to develop severe micro-cracking, particularly for plain concrete specimens (Bisschop, 2002). These micro-cracks are visible via microscope and tend to close as the moisture distribution in

the concrete specimen approaches the equilibrium state. Bazant et al. (1982) reported that the largest shrinkage stresses are developed near the drying surface right at the start of drying.

Hwang et al. (1984) have described drying shrinkage micro-cracking in five stages. In stage I, a sudden drying at the surface results in extreme contraction and causes surface microcracks. In stage II and III, surface cracks open further and propagate up to a depth where the internal tensile stresses are less than the concrete strength. In stage IV, internal stresses decrease because the moisture gradient flattens, and therefore cracks close again (cited in Bisschop, 2002). After the internal moisture content reaches an equilibrium with the ambient conditions, at the ultimate drying state, the moisture and shrinkage gradient disappear and the shrinkage will be unrestrained (Bisschop, 2002).

Therefore, measurement of drying shrinkage, by recording length changes upon drying (of prismatic elements), includes the effect of free drying shrinkage, internal restraint, cracking, and possibly creep deformation (if the duration of measurement is long enough for creep to develop). To quantify shrinkage as a material property for modelling purposes, shrinkage measurements should be stress-free or unrestrained. Unrestrained drying shrinkage can only be measured on miniature specimens with a thickness of few millimetres (Bisschop, 2002). Small specimen sizes are possible for cement-paste materials, but for concrete and particularly for RCC there is a limitation in the minimum specimen size possible to be cast.

Another alternative for concrete specimens (instead of direct determination of free shrinkage properties by experiments) is to use inverse analysis. If the model used for the inverse analysis is able to develop internal restraint, cracking, and creep deformation, then it is possible to extract free shrinkage properties even from the experimental results of an internally restrained specimen. In the current research, since the duration of experimental measurements is relatively short (shrinkage strains are accumulated during 90 days of measurement) and induced stresses do not sustain long enough to produce considerable creep deformation, the viscous behaviour of concrete under sustained stresses is ignored.

5.2.1 Inverse analysis to obtain “hygral contraction coefficient”

FE models of free shrinkage test specimens are developed and by using the calculated moisture transport parameters for each given concrete mix, the moisture transport analysis is performed. The same 3D 8-noded solid element DC3D8 is used for moisture transport

analysis. This analysis is linked to a structural analysis to calculate shrinkage deformations. The element type used for the structural analysis is called C3D8. The element size is 10×10×25 mm. The "hygral contraction coefficient" is then back-calculated from the free shrinkage test results for each concrete mix.

Since the experimental specimens are sealed on the end sides to model uniform deformation through the length, those surfaces are assumed not to have any moisture interaction with the surrounding environment in the model. Half of prisms are modelled due to symmetry (Figure 5.9). A constant ambient humidity of 40% is assumed and moisture convection from the exposed surfaces is assumed to occur via a surface convection factor. The initial moisture content is set equal to 1.0 (saturation condition).

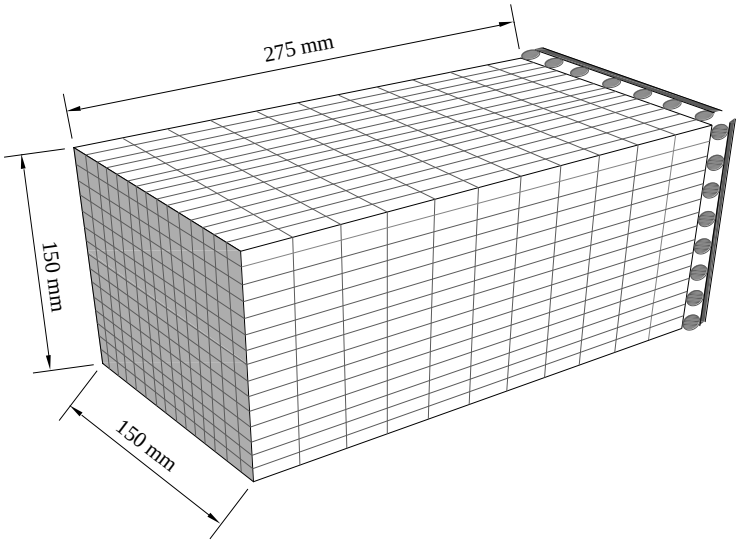

Figure 5.9 FE model for free shrinkage prisms

As discussed in Chapter 3, free shrinkage strain can be expressed as a nonlinear function of moisture content. In the literature two types of functions are seen for relating shrinkage strain to the moisture content. These functions are (references given in Chapter 3, Section 3.1.1):

$$(\varepsilon_{sh})_C = \frac{(C_0 - C)^a}{b + (C_0 - C)^a}(\varepsilon_{sh})_u \qquad \text{(Eq. 5.4)}$$

$$(\varepsilon_{sh})_C = a * (C_0 - C)^b \qquad \text{(Eq. 5.5)}$$

Where, $(\varepsilon_{sh})_C$ is free shrinkage (a function of C), $(\varepsilon_{sh})_u$ is the ultimate shrinkage strain, C is the variable moisture content during drying, C_0 is the reference moisture content (1.0 for

initial saturation), and *a* and *b* are constant parameters.

Eq. 5.4 relates the free shrinkage strain to the moisture content and the ultimate shrinkage strain. Ultimate shrinkage is a function of initial curing conditions, ambient relative humidity, concrete composition, air content, percentage of fine aggregates and volume to surface ratio. These factors alter ultimate shrinkage strain by affecting the moisture movement in the concrete member and the resultant moisture content at any time *t*. It is desirable to directly relate the free shrinkage strain to relative moisture content to bypass the indirectly affecting factors. Therefore, Eq.5.5 is adopted which assumes the free shrinkage strain is a power function of the moisture content. The dependency is then predicted, for each mix, by determining the constant parameters (*a* and *b*) through inverse analysis.

The "hygral contraction coefficient", $\beta_C(C)$, induces free shrinkage strain, $(\varepsilon_{sh})_C$, in the specimen based on Eq. 5.6.

$$(\varepsilon_{sh})_C = -\beta_C(C) \times (C_0 - C) \qquad \text{(Eq. 5.6)}$$

Where C_0 is the reference moisture content, 1.0.

Therefore, the "hygral contraction coefficient", $\beta_C(C)$, is back-calculated as a function of moisture content, C, based on the Eq. 5.7. The constant parameters, *a* and *b*, are given in Table 5.2 for the experimental concrete mixes.

$$\beta_C(C) = -a * (C_0 - C)^{b-1} \qquad \text{(Eq. 5.7)}$$

Table 5.2 Back-calculated constant parameters, *a* and *b*

	a	*b*
Plain CC	1100E-6	0.35
SFR-CC	900E-6	0.4
Plain RCC	2500E-6	0.8
SFR-RCC	2000E-6	0.9

The calculated "hygral contraction coefficient" as a function of moisture content for various concrete mixes are shown in Figure 5.10.

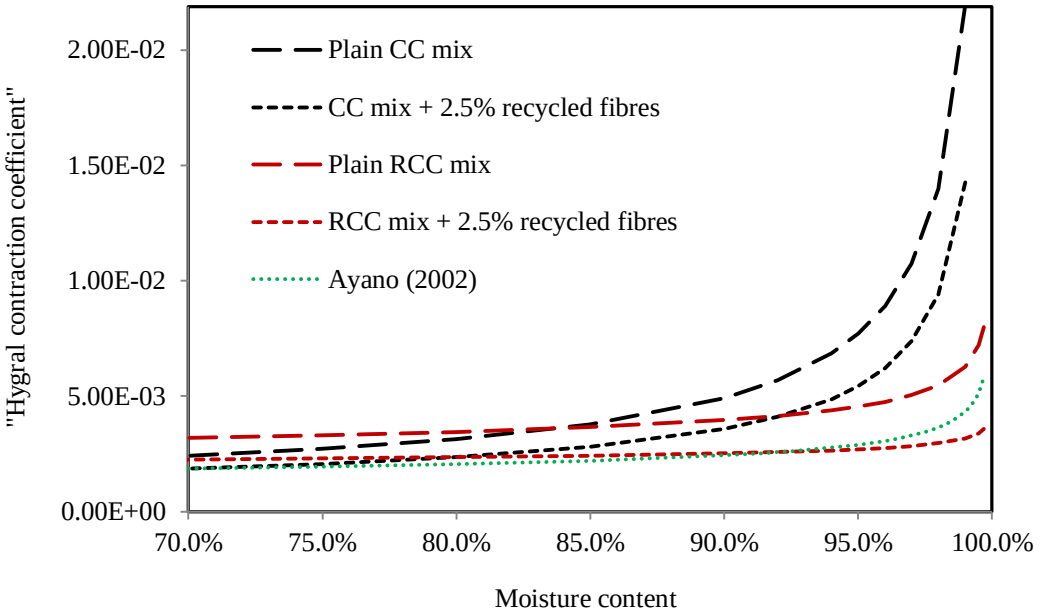

Figure 5.10 "Hygral contraction coefficients" versus moisture content

Figure 5.10 shows that the "hygral contraction coefficient" of CC mixes is higher than for RCC mixes for moisture contents higher than 80%. This can be attributed to the higher restraining effect of crushed aggregates in RCC mixes and the higher percentage of aggregate used. For moisture contents lower than 80%, the hygral contraction coefficient of CC reaches that of RCC and gets slightly lower. This can be justified by the fact that the total amount of shrinkage is limited overall. As CC mixes showed a sharper initial rate of contraction, smaller rate and slower contraction was left at the end. The "hygral contraction coefficient" of SFRC mixes is generally lower than for plain mixes (RCC and CC). This can be attributed to the restraining effect of the fibres. The difference between SFRC and plain concrete curves is less and more uniform than the difference between RCC and CC curves. It must be pointed out that these curves are determined for a maximum experimental moisture loss of 30% and extrapolation can be used to obtain higher shrinkage values.

Based on the calculated parameters, the variation of shrinkage strain versus drying time for free shrinkage specimens is presented in Figure 5.11 for different mixes, in comparison with experimental values. The comparison shows that there is good agreement between experimental and numerical curves.

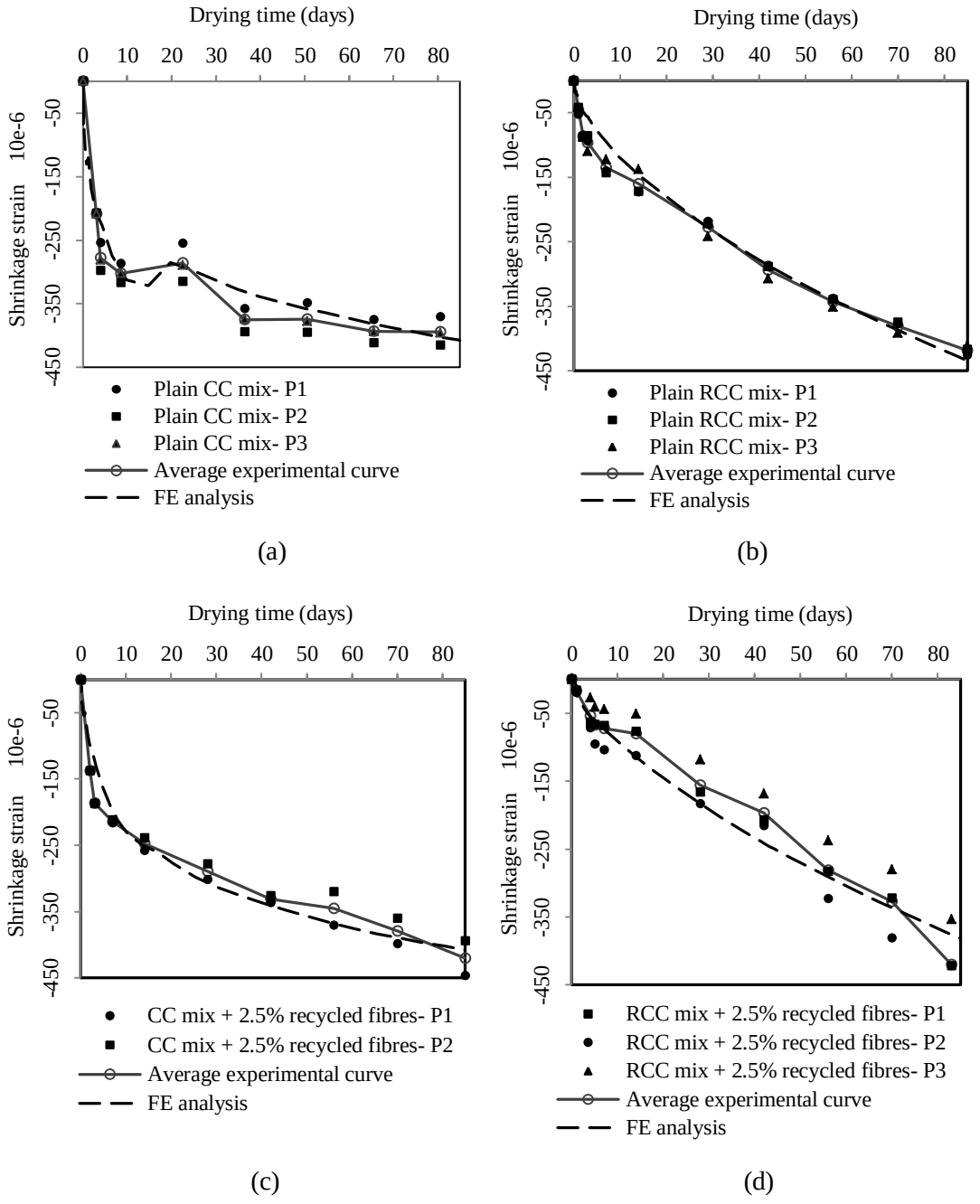

Figure 5.11 Numerical free shrinkage strain curve compared with experimental: (a) Plain CC mix; (b) Plain RCC mix; (c) SFR-CC mix (2.5%); (c) SFR-RCC mix (2.5%)

The "hygral contraction coefficient" of the plain CC mix shows a sharp declining slope at higher moisture contents, compared to the other mixes with higher porosities. In the shrinkage curves of plain CC mix (Figure 5.11 (a)), an unexpected relative expansion is seen around 15-22 days. In the analytical model this relative transient expansion can arise because the

calculated "hygral contraction coefficient" rises sharply after 99.9% moisture content. If the "hygral contraction coefficient" is limited to the value corresponding to 99.9% moisture content (Figure 5.12(a)), the expansion does not develop (Figure 5.12(b)).

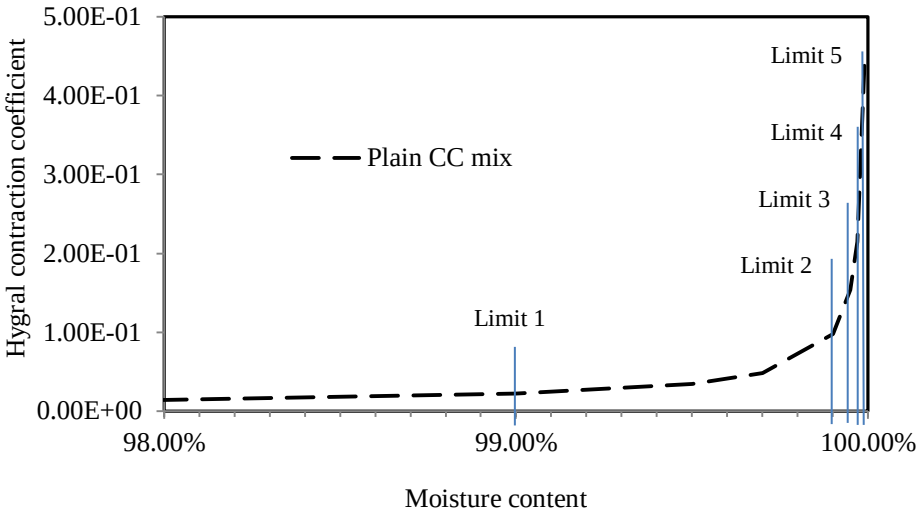

(a)

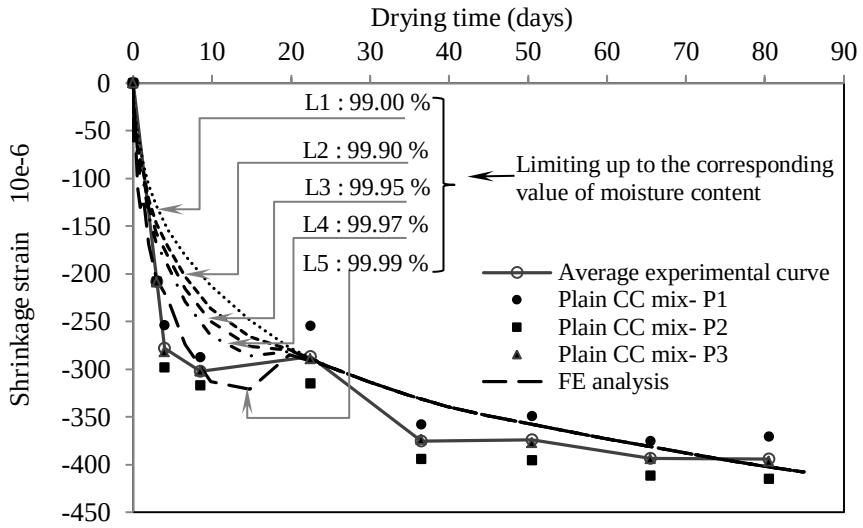

(b)

Figure 5.12 Effect of considering upper limit for β_c (C) for plain CC mix; (a) Limits, (b) Free shrinkage time histories

If the "hygral contraction coefficient" predicted for plain CC mix is applied without an upper limit for moisture contents higher than 99.9%, a transient tensile wave is formed in the model moving from the surface into the core (Figure 5.13). This tensile wave resists the internal restraints and results in a relative small expansion in the specimen between of 15-20 days

(Figure 5.12 (b)). For thinner specimens the effect of internal restraint is less significant. Since the above mentioned tensile wave is a transient effect, it could be considered as a temporary numerical peculiarity. However, expansion during the period of 15-22 days was also found in the experiment, hence this topic requires further investigation in the future.

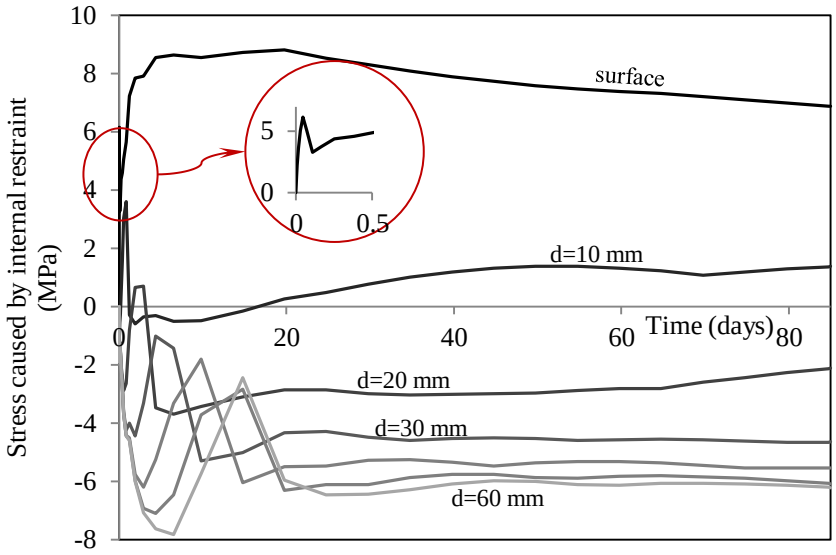

Figure 5.13 Tensile wave, moving from the surface inward

5.3 Tension stiffening properties of SFRC (σ-ε models)

SFRC is a composite material whose mechanical properties depend on the properties of the fibres and concrete and the properties of the interface between fibres and the matrix. After cracking, stress is transferred from the matrix to the fibre by interfacial shear or by interlock between the fibre and matrix. The tensile stress is shared by the fibres and matrix until the cracks open significantly, and then the total stress is resisted by the fibres. The enhanced post-cracking tensile behaviour of SFRC can increase the load bearing capacity of structural members.

The post-cracking behaviour of concrete against crack development, under direct tension across cracks, can be simulated by tension stiffening. A tension stiffening model can be used to define the tension softening diagram, which represents the relationship between tensile stress and tensile strain (or the crack mouth opening) in the fracture zone (ABAQUS, 2010). The tension softening diagram can be obtained by inverse analysis of flexural loading test results. Inverse analysis can be performed using multi-linear approximation (Figure 5.14)

combined with finite element (FE) or cross-sectional analysis. The extended part of the tension softening diagram (Figure 5.14 (a)) is iteratively chosen so that the analytical load-displacement curve (Figure 5.14 (b)) matches the experimental curve. The tension softening diagram (σ-ε curve) is the main property of the SFRC material that increases the load bearing capacity of the structural member. However, the increase in load bearing capacity is not only dependent on the material properties but also depends on the geometry of the structure, boundary conditions and loading. The tension softening depends on factors such as geometry and strength of fibres, fibre content and distribution, and fibre-concrete interaction.

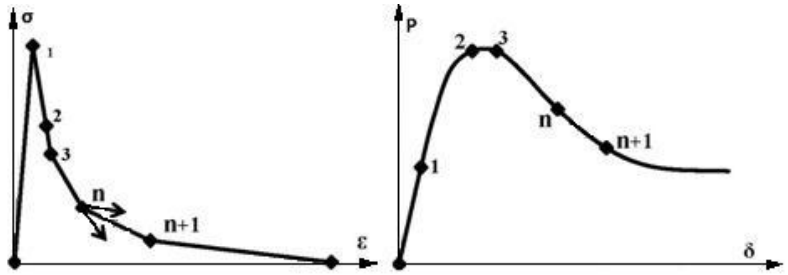

(a) (b)

Figure 5.14 Multi-linear approximation; (a) tension softening; (b) load-displacement curves

Alternatively RILEM proposed, instead of numerical back-analysis, empirical estimations to be used to characterise the tension softening diagram of SFRC. RILEM TC 162-TDF (2000) proposes the use of the experimental load-deflection curve directly to predict the σ-ε model, for design purposes and to facilitate section analysis. However, the accuracy of this method is in some doubt (Tlemat et al, 2006). CEB-FIP Model Code (2010) also suggests a simplified model to compute the constitutive law in uniaxial tension by means of the residual nominal bending strength values considering a linear constitutive law, but emphasises that for numerical analyses more advanced constitutive laws are recommended.

The most basic method of inverse analysis of SFRC sections is the traditional section analysis (Appendix D). The cross-sectional analysis is an iterative procedure in which an individual section is analysed using tensile and compressive stress blocks assumed for the section. The main output of the section analysis is the moment-strain curve of the individual section disregarding the entire geometry of the prism and boundary conditions. The moment-strain curve resulting from section analysis is reliable enough and can be used as a benchmark to verify the accuracy of other theoretical and numerical methods. The moment-strain curve should be transformed into a load-deflection curve considering the geometry and boundary

conditions. This transformation is not straightforward, because after cracking the middle length of the prism behaves nonlinearly while the two ends are in the linear-elastic domain.

The other method apart from section analysis, which can be adopted for inverse analysis, is FE modelling. The cracking process can be described via two approaches in FE programs. The first approach is the discrete crack model which uses the stress-crack opening (σ-w) relationship as the softening law of the concrete in tension. The location of the crack should be predefined in this approach. Cohesive elements usually are used in the position of the predefined cracks. This approach is computationally more expensive and less useful in dealing with practical applications (Tlemat, 2004) compared to the second approach. In the second approach it is assumed that the cracking is smeared over a characteristic length representing the crack band width, and the stress-strain (σ-ε) relationship is used to describe the softening law. The characteristic length is usually assumed as the average element length. The main disadvantage of the smeared crack approach is usually known as its sensitivity to mesh refinement, particularly for small amounts of post-cracking tension stiffening. This issue is also investigated in this chapter.

In this research both section analysis and FE method are used comparatively to obtain the post-cracking tension stiffening behaviour of SFRC materials made of RCC and CC mixes. FE models are verified with section analysis for some existing experimental results.

5.3.1 FE modelling of the flexural SFRC prisms

In this research, the σ-ε softening relationship is used for simulating the post-cracking behaviour of SFRC. This approach does not track individual "macro" cracks. The presence of cracks enters into the calculations by the way in which the cracks affect the stress and material stiffness. This approach can be followed via two different constitutive material models in ABAQUS. These material models are called "Concrete Smeared Cracking" (CSC), and "Concrete Damaged Plasticity" (CDP). In CSC, representation of anisotropic behaviour of cracking dominates the modelling, while CDP uses the concept of isotropic damaged elasticity in combination with tensile and compressive plasticity to represent the inelastic behaviour of concrete. Therefore, the crack opening smeared over the element length in CSC is analogous to the inelastic deformation over the element length in CDP. More details on CSC and CDP material models are given in Appendix E. The required parameters for stress analysis based on these models are listed in Table 5.3.

Table 5.3 Required parameters to be adopted in CSC and CDP models

Constitutive material model	Required input parameter		How to obtain the parameter
CSC	Uniaxial tension		Experimentally
	Uniaxial compression		Experimentally
	Multi-axial failure ratios (as explained in Appendix E)	FR1	Using a typical value (modified for SFRC)
		FR2	Experimentally
		FR3	Using a typical value
		FR4	Using a typical value
	Shear retention factors		Typical values
CDP	Uniaxial tension		Experimentally
	Uniaxial compression		Experimentally
	Damage factors in tension		Applied in the same rate as tension softening
	Damage factors in compression*		Ignored
	Multi-axial yield and flow parameters (as explained in Appendix E)	Dilation angle, ψ	The best value from a survey in the literature
		Eccentricity, ε	Using a typical value
		FR1	Using a typical value (modified for SFRC)
		K_c	Using a typical value

* Compressive damage is applicable for compressive strain-softening regime, which will never be suffered by the structure in the current research, since the compressive stresses are not dominant.

5.3.1.1 Element choice for FE modelling of prisms

A variety of elements can be used with the mentioned concrete models, such as beam, shell, plane stress, plane strain and three-dimensional elements. In the current research, shell elements are used to model flexural prisms (Figure 5.15). Using shell elements, the total number of degrees of freedom is much less than when solid elements are used (since several element layers are required through the thickness of the prism when solid elements are used). Therefore, the model made of shell elements runs much faster, and is less prone to numerical instabilities (as the author's experience shows). However, the inverse analysis of prisms in this chapter is basically relied on section analysis, and the use of FE models is just for a mutual confirmation of the results obtained from section analysis and the material models used for FE modelling. Therefore, using shell elements can be appropriate to meet this

purpose, besides of reducing the computational time.

The element size shown in Figure 5.15(b) is a typical element size. To address the mesh sensitivity issue, other element sizes are also examined in the model.

The element used is 8-noded reduced integration shell element called S8R. To model progressive failure of the concrete through the thickness with acceptable accuracy, the number of integration points through the thickness of the shell must not be less than nine (ABAQUS, 2010). Although, to obtain a continuously increasing compressive and tensile strain through the control section, a larger number of integration points is required most of the time depending on the level of tension stiffening assigned to the material. This is because there is still the potential of an unexpected drop in the compressive or tensile strains caused by numerical peculiarities, due to insufficient integration points through the section.

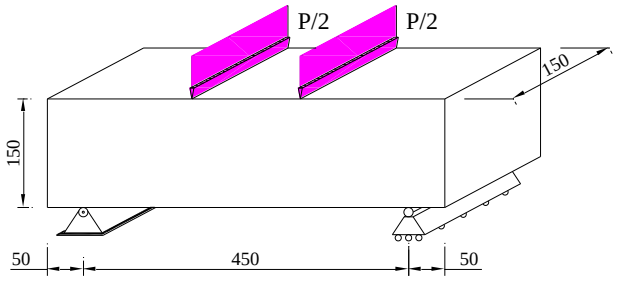

(a)

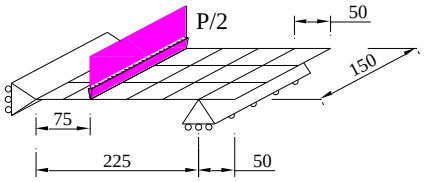

(b)

Figure 5.15 Four-point loaded prism (a) Physical model (b) FE model

5.3.1.2 Comparing alternative material models

Each of the mentioned material models provided for concrete in ABAQUS has its own advantages and disadvantages.

The advantage of CSC model is its ability to model orthotropic damage, while it is prone to a virtual numerical stiffening and consequent instabilities in multi cracked conditions.

In the CSC concept, cracks can be formulated as single-fixed, multiple-fixed or rotating cracks. In the fixed crack formulation the orientation of cracks is kept constant, while in the rotating formulation (Cope et al., 1980 cited in Elshaigh, 2007) orientation is updated continuously. In the fixed crack formulation, the orientation of the crack coincides with the orientation of the maximum principal stress at crack initiation and remains fixed throughout the loading time. However, the orientation of principal stresses can change. Therefore, in the single-fixed formulation virtual numerical stiffening is seen in the response which is not observed in the experiments (Rots, 1988 cited in Elshaigh, 2007). In the multiple-fixed formulation (de Borst et al., 1985 cited in Elshaigh, 2007) the formation of secondary cracks is allowed, but once they have been initiated the orientation of all existing cracks remain fixed. The secondary cracks are initiated when the change in the orientation of principal stress, with respect to the previously formed crack, exceeds a threshold angle. In the multiple-fixed formulation the numerical stiffening response is released after formation of each secondary crack (Elshaigh, 2007) (Figure 5.16).

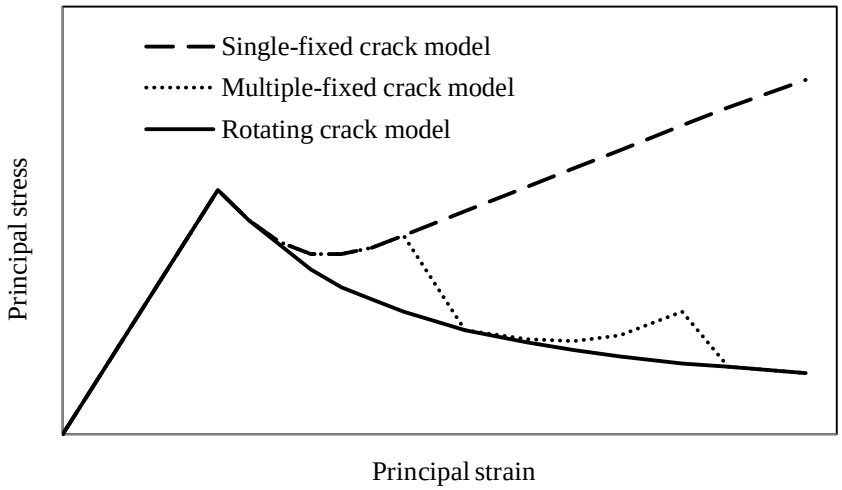

Figure 5.16 Virtual stiffening in the multiple-fixed cracking formulation in CSC models

CSC in ABAQUS is formulated as a multiple-fixed model. In the current study, virtual hardening is observed in CSC models in ABAQUS, when the principal stress axes rotate significantly from the initial crack. Therefore, in 3D CSC models (developed for slabs) the analysis solution cannot continue much further after the formation of primary cracks and numerical instabilities stop the analysis from proceeding.

The disadvantage of CDP model is that the damaged elasticity is applied isotropically, while it has the advantage of more stable solutions and the capability of graphical visualisation of

the crack patterns in ABAQUS. Since the inelastic deformations represent the crack development in CDP model, the direction of maximum principal plastic strain can be viewed as the normal vectors of the cracked planes.

In the next section, the FE model developed via CSC material model is verified with section analysis, for different SFRC mixes used in four-point bending tests in the literature. Both the above mentioned material models are adopted, for modelling flexural prisms tested in the current research, to assess their suitability.

5.3.1.3 Verifying the FE model for the flexural inverse analysis

For verifying the FE model developed for flexural inverse analysis, the results of FE (CSC model) and section analysis are compared for experimental works performed for three SFRC mixes developed by Task 2.2 of the Ecolanes (2006-2009) deliverables "Concrete optimisation" (Angelakopoulos et al., 2008[a,b]). The average results of the bending tests, carried out as part of Task 2.3 "SFRC experimental characterisation" (Angelakopoulos et al., 2008[c]), are utilised in the analyses. The specimen sizes and loading configurations are the same as the specimens tested in the current research (Figure 5.15(a)).

The SFRC mixes consist of a CC mix reinforced with 2% industrial fibres (by mass of concrete), a RCC mix reinforced with 2% industrial fibres, and a RCC mix reinforced with 3% recycled fibres. The uniaxial σ-ε curves derived for the mixes are shown in Figure 5.17.

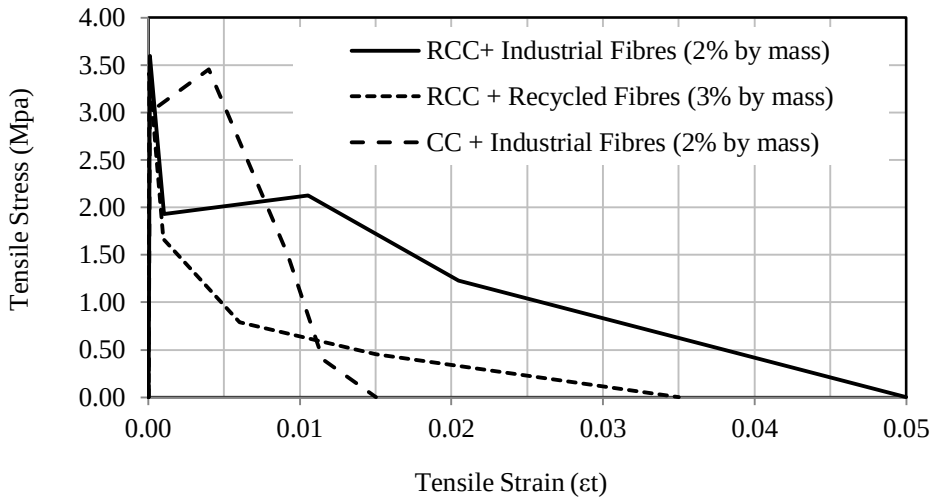

Figure 5.17 σ-ε curves for various concrete mixes (Angelakopoulos et al., 2008[a,b])

Figure 5.18 shows the load-displacement curves resulted from FE analysis verified by the curves resulted from numerical section analysis and compared with experimental curves, for the RCC mix reinforced with 2% industrial steel fibres.

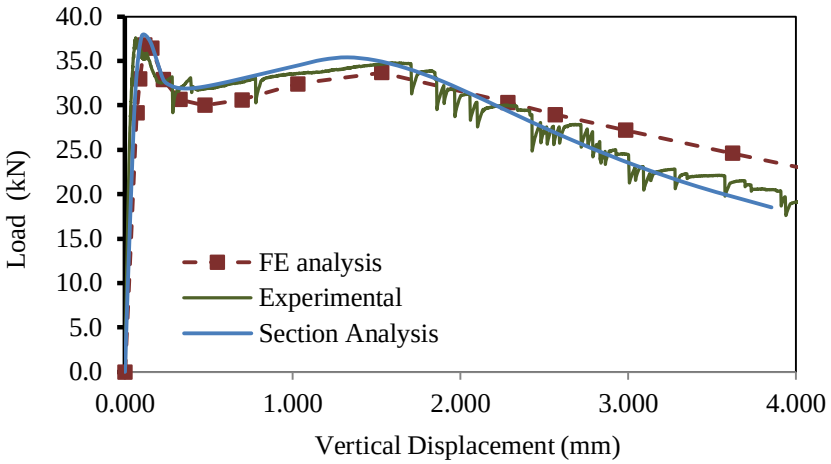

Figure 5.18 Load-displacement curves for the RCC mix + 2% industrial fibres

The direct output in the numerical section analysis is the moment-strain curve of the individual section. Analytical formulas are then used to calculate the load-vertical displacement curve (Appendix D). To check that FE and section analysis results match irrespective of the accuracy of the formula adopted to calculate the vertical displacement, the load-strain curves are also compared in Figure 5.19.

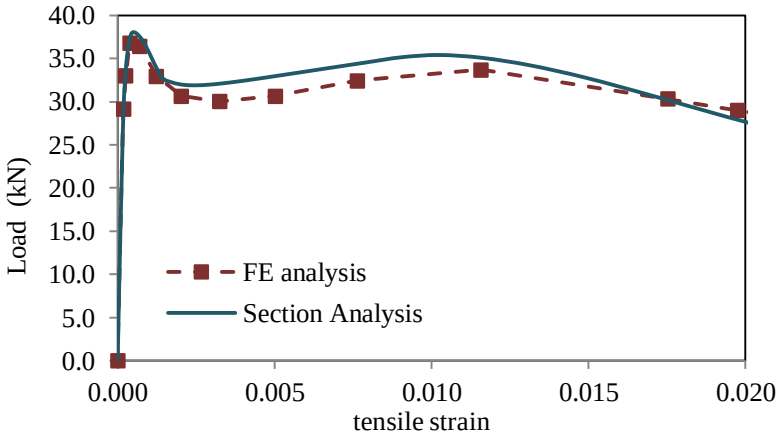

Figure 5.19 Load-tensile strain curves for the RCC mix + 2% industrial fibres

The comparison for RCC reinforced with 3% recycled fibres is made in Figure 5.20 and 5.21.

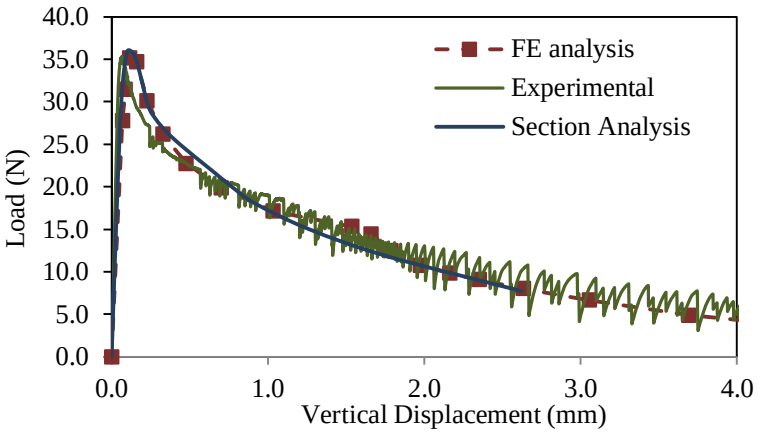

Figure 5.20 Load-displacement curves for the RCC mix + 3% recycled fibres

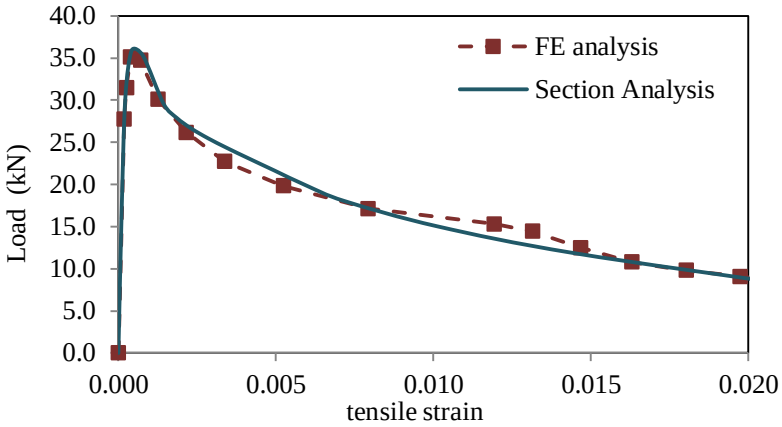

Figure 5.21 Load-tensile strain curves for the RCC mix + 3% recycled fibres

To study the effect of element size in smeared cracking analysis of the concrete beams, for the last mix (CC mix reinforced with 2% industrial fibres) the effect of the element size is also investigated. For this purpose, three element sizes are tried as shown in Figure 5.22.

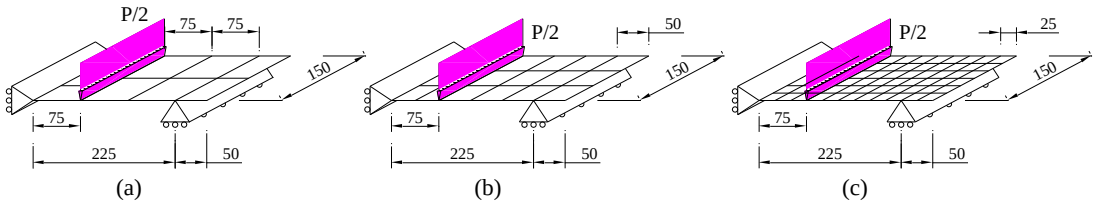

Figure 5.22 FE models with (a) coarse, (b) medium and (c) fine meshes

Figures 5.23 and 5.24 show the load-displacement and the load-strain curves, respectively, obtained from FE analysis for different element sizes verified by section analysis and compared with experimental curves, for the CC mix reinforced with 2% industrial steel fibres.

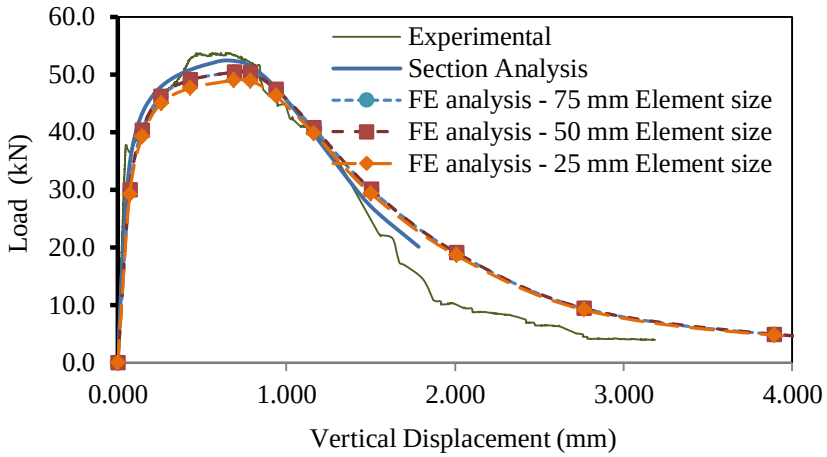

Figure 5.23 Load-displacement curves for the CC mix + 2% industrial fibres

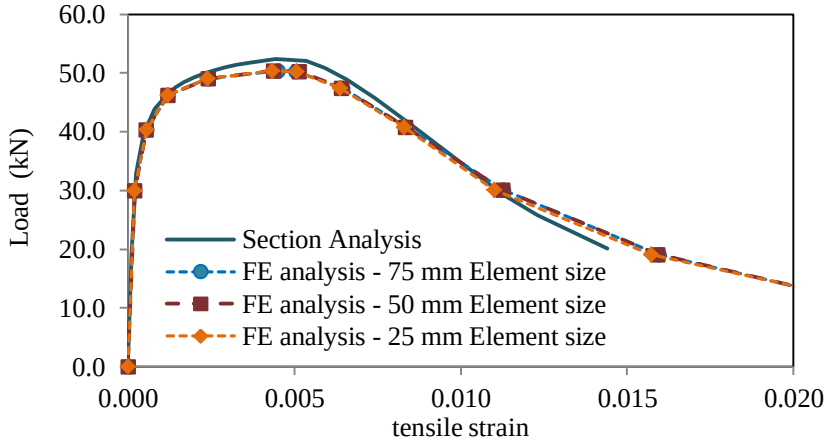

Figure 5.24 Load-tensile strain curves for the CC mix + 2% industrial fibres

The comparison made in this section shows that the results from FE analysis and section analysis match well. The variety of selected materials (Figure 5.17) implies that the developed FE models are valid for a wide range of different post-cracking behaviours. Figure 5.23 and 5.24 also show that for element sizes less than 75 mm no mesh sensitivity is seen.

Mesh sensitivity generally occurs in cases with little or no reinforcement, and it means that the FE predictions do not converge to a unique solution when the mesh is refined, because mesh refinement leads to narrower crack bands. In those cases, cracking occurs in the form of localised (or non-distributed) cracks (Figure 5.25).

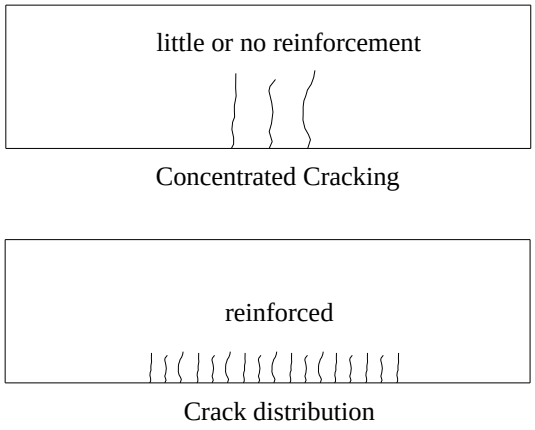

Figure 5.25 The effect of reinforcement on crack distribution in bending prisms

If cracks are regularly distributed (due to the effect of reinforcement) mesh sensitivity is less of a concern (ABAQUS, 2010). More description is given in Appendix F.

As a conclusion of this section the FE model used for the inverse analysis was verified by the section analysis method and it was shown that the mesh sensitivity issue can be resolved by choosing element sizes less than the length of the cracking zone. After verifying the FE model developed for the flexural inverse analysis, it is used in the next section to derive the uniaxial tensile stress-strain characteristics of the experimental mixes developed for the current study.

5.3.2 Inverse analysis of the tested prisms and results

In FE modelling of the notched prisms, the presence of the notch creates a singularity point in the model. Singularities often appear where geometry or loading conditions change abruptly. In FE modelling, results are normally stabilised or converged upon mesh refinement, but in the presence of singular points no convergence is obtained upon mesh refinement. Although there are some modelling tricks to bypass singularities, FE modelling of the notched prisms to get appropriate results is somewhat complicated.

Since the flexural test has been done for both the notched and un-notched prisms in the current study, the inverse analysis is initially performed for the un-notched prisms adopting comparative section analysis and FE analysis (using both CSC and CDP material models). The resulting σ-ε curve is then fed into a section analysis for the notched prisms to compare the consequent load-deflection curve with the experimental one. This extra control is performed to catch any possible mismatch caused by moving the cracking position throughout

the middle one-third of the prism in the un-notched specimens (refer to Section 4.2.2).

The tension stiffening behaviour is back-calculated for each mix to obtain the best fit to the experimental average load-deflection curve. The tensile σ-ε curves for concrete mixes are obtained as shown in Figure 5.26.

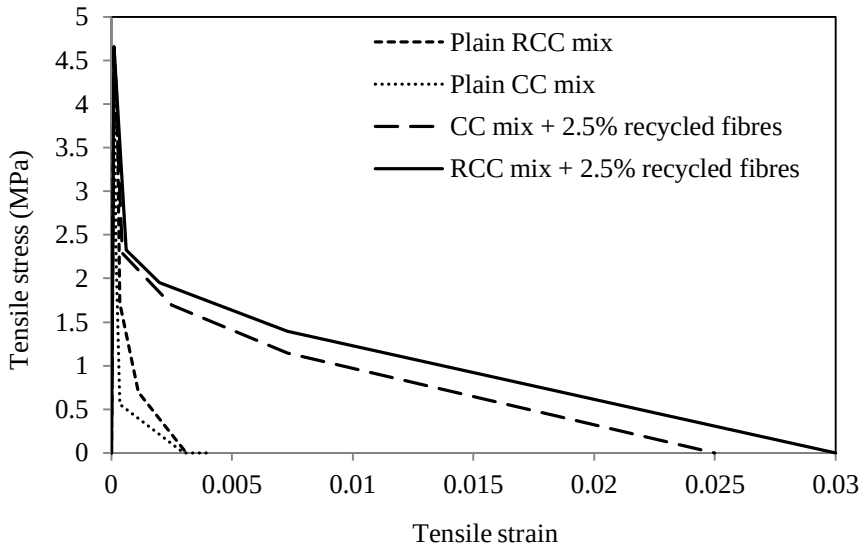

Figure 5.26 Tension stiffening curves obtained for the experimental concrete mixes

Assuming these back-calculated σ-ε curves, the numerical and experimental load-deflection curves are as shown in Figure 5.27 to 5.38.

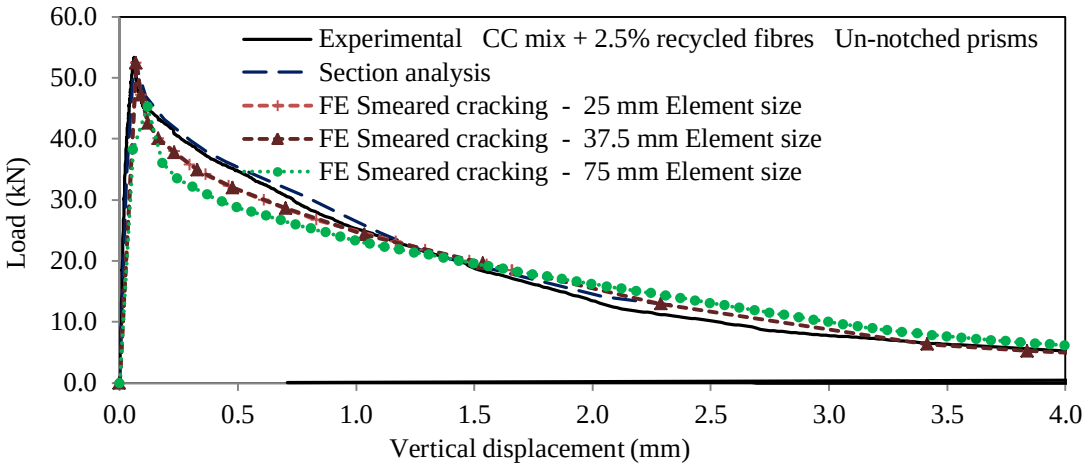

Figure 5.27 Load-deflections for **un-notched** prisms, **CC** + 2.5% recycled fibres and **CSC**

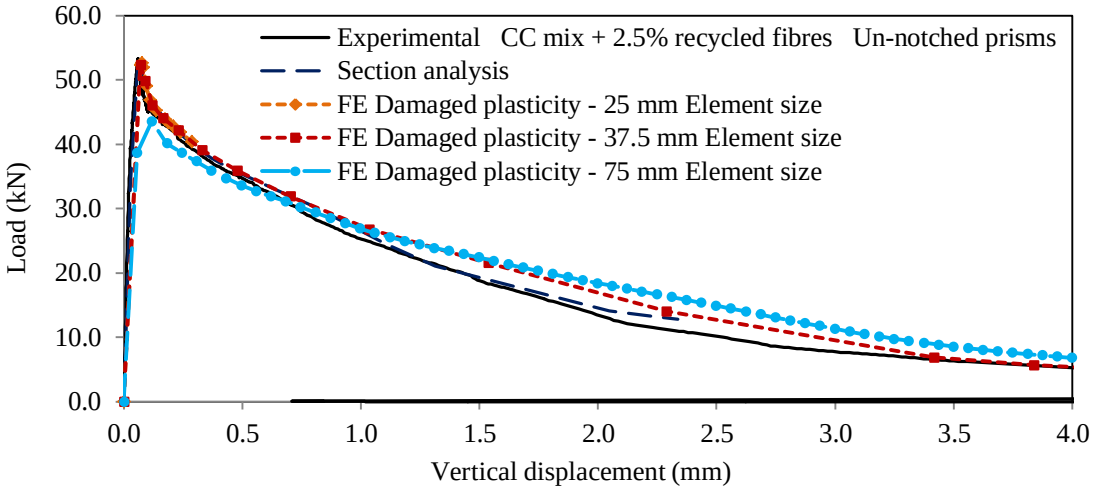

Figure 5.28 Load-deflections for **un-notched** prisms, **CC** + 2.5% recycled fibres and **CDP**

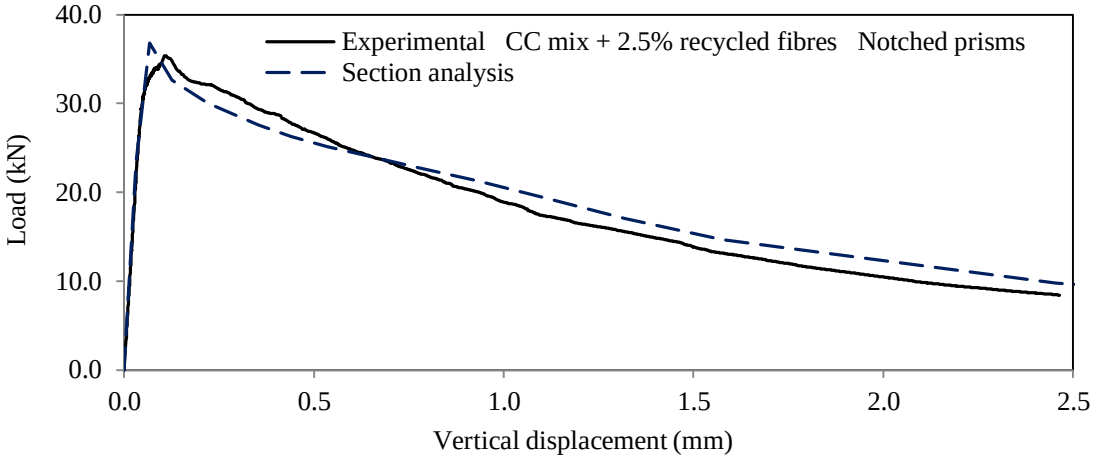

Figure 5.29 Load-deflections for **notched** prisms, **CC** +2.5% recycled fibres

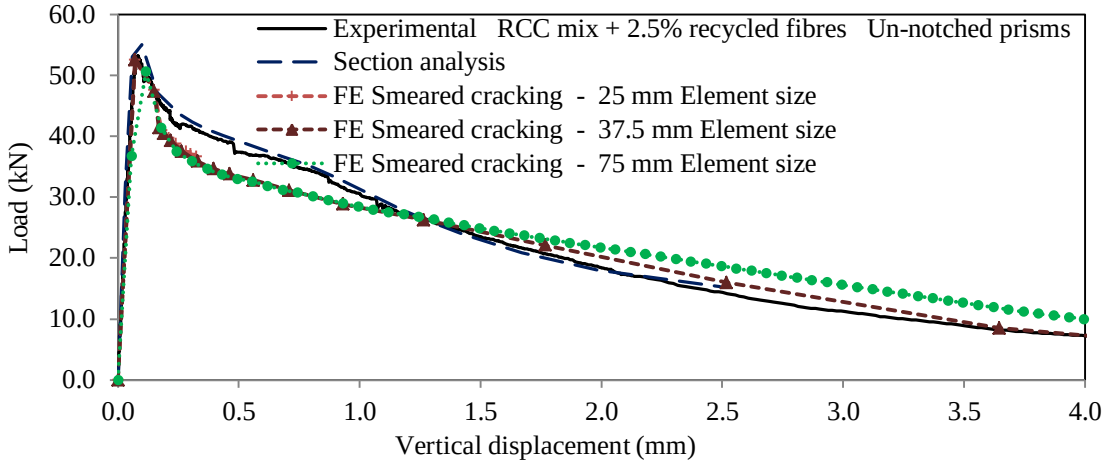

Figure 5.30 Load-deflections for **un-notched** prisms, **RCC**+2.5% recycled fibres and **CSC**

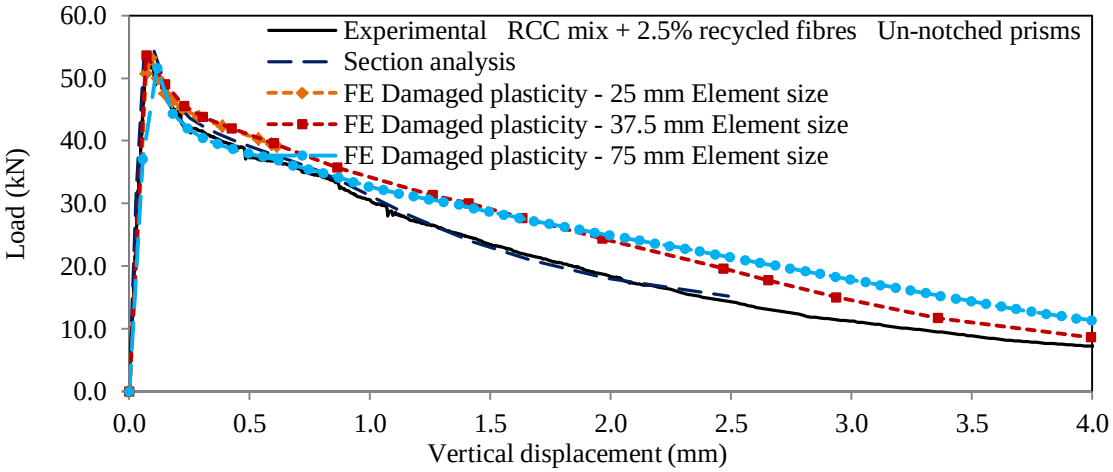

Figure 5.31 Load-deflections for **un-notched** prisms, **RCC** +2.5% recycled fibres and **CDP**

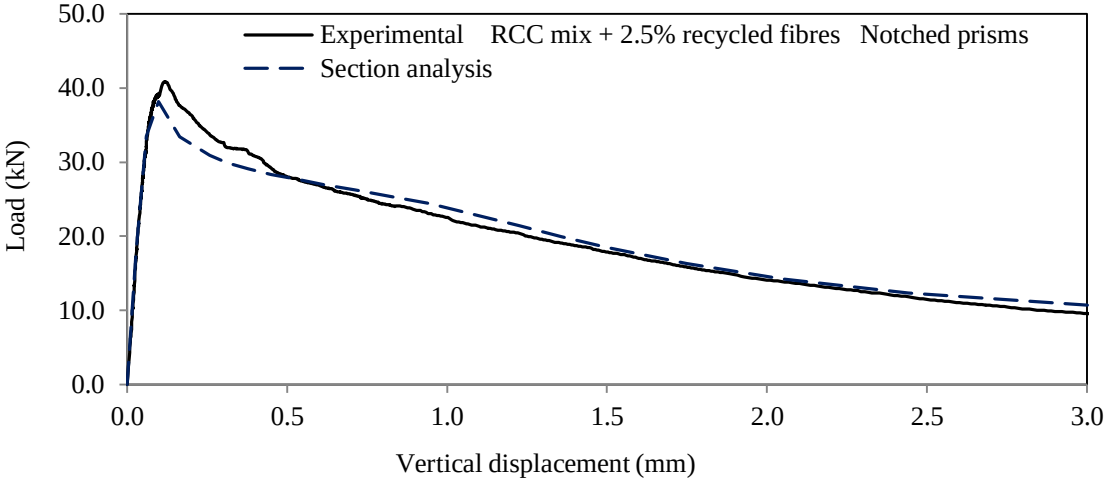

Figure 5.32 Load-deflections for the **notched** prisms, **RCC** mix +2.5% recycled fibres

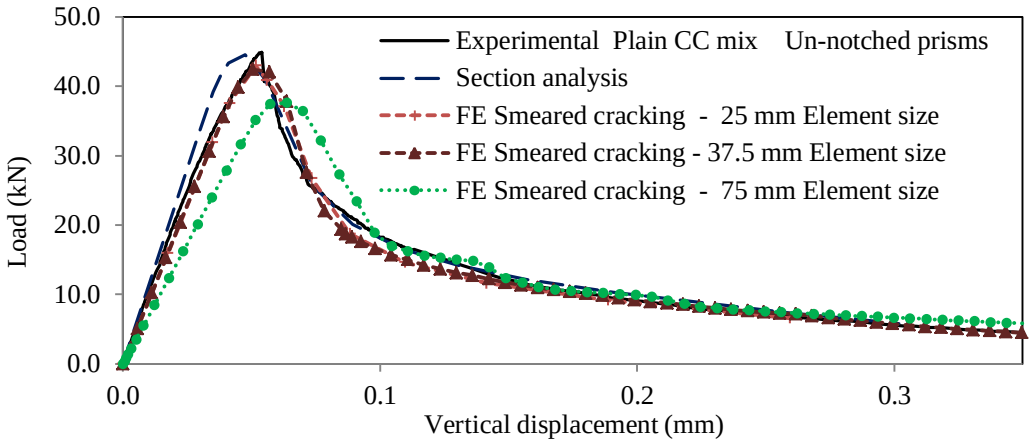

Figure 5.33 Load-deflections for the **un-notched** prisms, plain **CC**, **CSC** model

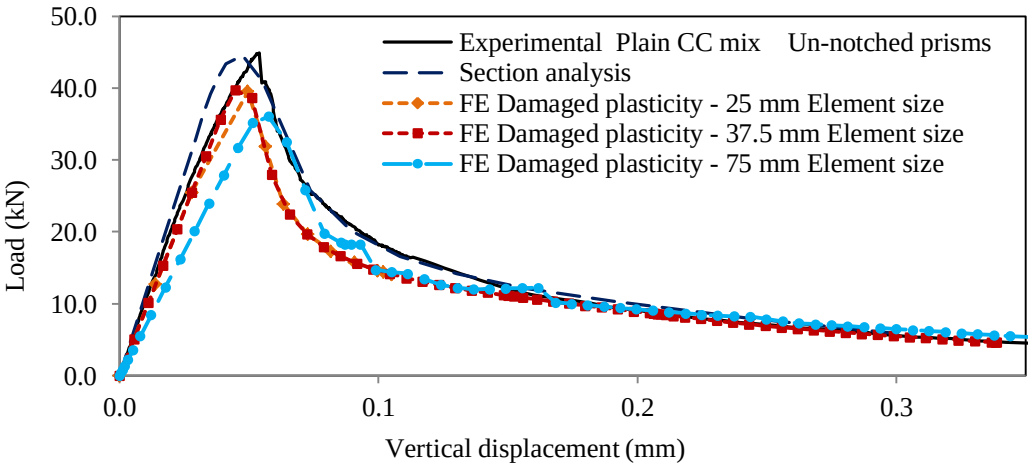

Figure 5.34 Load-deflections for the **un-notched** prisms, plain **CC**, **CDP** model

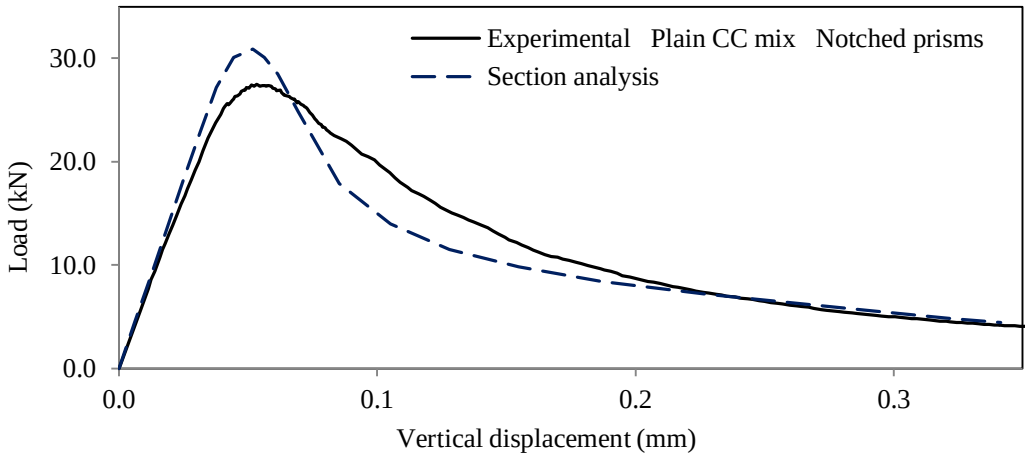

Figure 5.35 Load-deflections for the **notched** prisms, plain **CC**

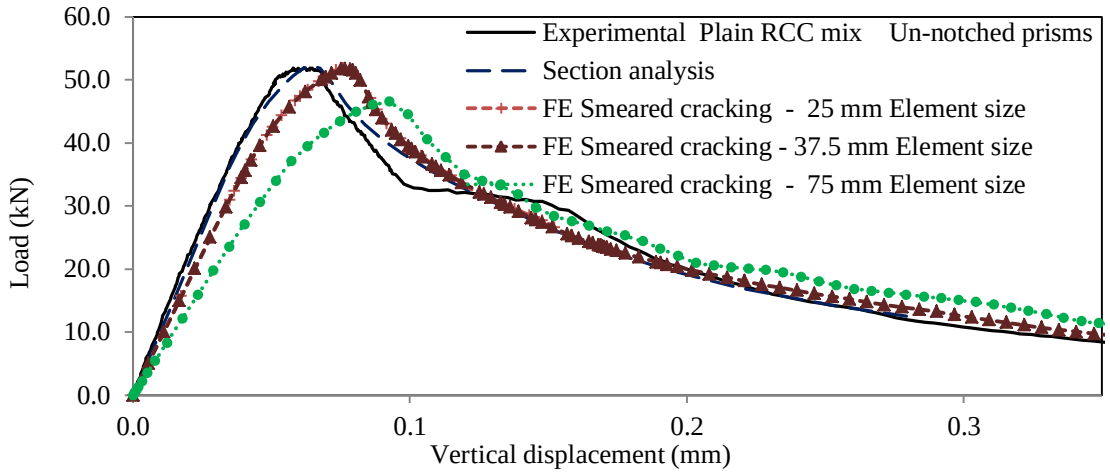

Figure 5.36 Load-deflections for the **un-notched** prisms, plain **RCC**, **CSC** model

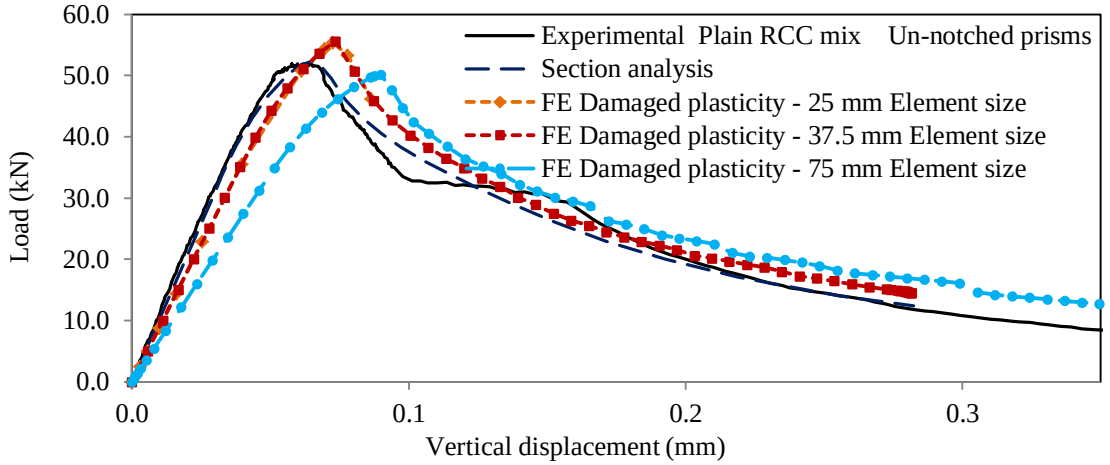

Figure 5.37 Load-deflections for the **un-notched** prisms, plain **RCC**, **CDP** model

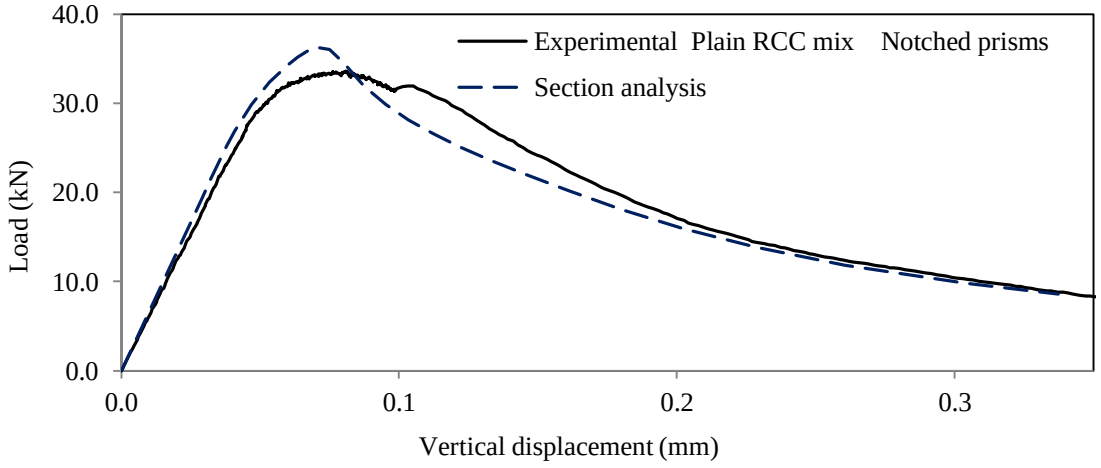

Figure 5.38 Load-deflections for the **notched** prisms, plain **RCC**

5.3.3 Discussion on the inverse analysis of prisms

Inverse analysis was performed via three numerical approaches (section analysis, FE analysis using CSC material model, and FE analysis using CDP material model) for the un-notched prisms. The average experimental curve was used, for each concrete mix, in the inverse analysis.

Three element sizes were adopted in FE analyses (25 mm, 37.5 mm, and 75 mm). For all concrete mixes, the load-deflection curves resulting from the 25 mm and 37.5 mm element sizes match exactly. This means that for all concrete mixes a crack band width bigger than 75 mm (2 × 37.5 mm) is formed at the middle of the prism, irrespective of the element size. For SFRC mixes the load-deflection curves from the 75 mm element size are slightly different from the other element sizes. Therefore, for SFRC mixes, mesh refinement does not result in a crack band width much smaller than the middle one-third of the prism. It can be concluded that, for SFRC mixes, cracking is approximately smeared over a high percentage of the constant-moment zone, in the FE models. For plain mixes, there is a mismatch between the load-deflection curves from the 75mm element size and smaller element sizes. Hence, for plain mixes the length of crack smearing in the FE models is much less than for SFRC mixes.

The results show that there is a very good agreement between the three numerical approaches, after enough mesh refinement in the FE models.

The results of the section analysis performed for the notched prisms, using the σ-ε curve obtained for the un-notched prisms, also fit the experimental curves. It should be noted that the experimental load-deflection curves relevant to the notched prisms are significantly different from the un-notched prisms. Therefore, this good match can lead to some conclusions: 1) The location of the crack through the constant-moment zone of the un-notched prisms does not alter significantly the result of the inverse analysis; 2) In the section analysis, the extra height of the prism corresponding to the depth of the notch has been ignored in the calculation of displacement using the closed-form formula. Therefore the height corresponding to the notch does not contribute much to the reduction of deflection.

The results of the inverse analyses carried out in this section will be used for pavements analyses.

The results obtained in this chapter are all properties of the given materials with the specified compositions. The concrete mixes proportioning, fibre content and fibre characteristics have been chosen based on the optimisation studies carried out during the Ecolanes project. For other concrete compositions, different fibre contents and fibre types (such as for industrially produced fibres) different results are anticipated. However, the material properties are independent of the environmental and boundary conditions.

Chapter 6

6 Pavement analysis for restrained shrinkage and monotonic loading

This chapter investigates numerically the effect of drying shrinkage on the short term behaviour of SFRC pavements (the effect of load repetition in long-term is studied in Chapter 7). The analytical studies performed in this chapter consist of the following steps:

- Moisture transport analysis, to obtain the time history of moisture profiles for SFRC pavements, for given environmental and boundary conditions.
- Drying shrinkage analysis, to obtain the time history of shrinkage strains induced by moisture variation under the given restraints imposed on SFRC pavements.
- Stress analysis to obtain the time history of stress distribution and distress resulting from restrained shrinkage (the effect of drying creep is also discussed).
- Stress analysis under monotonic loading, to take into account the applied external loads on a pavement initially distressed by restrained shrinkage.

A good numerical tool for research purposes is the finite element (FE) method. Versatility is one of the important advantages of the FE method, as any type of material model, geometrical configuration or boundary condition is possible to adopt in this method. Another attractive capability of FE is its ability to provide the complete history of deformations up to the collapse of the structure. Considering the increased tendency in codes of practice to move from working-stress to ultimate-strength philosophies, the resultant load-deflection curves can be useful in the development of design guidelines under ultimate limit state conditions. However, simulating the pavements behaviour considering all kinds of nonlinearities in the slab and foundation, combined with the effect of environmental factors such as shrinkage, is a big challenge.

For FE modelling of pavements, ABAQUS (2010) is adopted, because of its availability, its good capabilities for modelling non-linear behaviour of concrete and SFRC, and its facilitating option for modelling the elastic foundation by easily applying a modulus of reaction on the interacting surface.

FE modelling in this research is performed in 3D. In spite of the higher computational cost, there are still many advantages in modelling in 3D rather than 2D. Differential drying shrinkage causes a 3D deformed shape in the curled slab, which cannot be simulated in 2D modelling. The rectangular footprint and different configurations of the wheel load could also be simulated in 3D analysis. In 2D analysis the load shape is restricted to an infinite strip load in plane strain conditions or circular shape in axisymmetric conditions.

6.1 Simulation of SFRC road pavements (applied approaches and assumptions)

Numerical simulation is the most precise method to predict the response of concrete exposed to restrained shrinkage, since it allows the cracking response of SFRC to be accurately simulated considering the complete softening behaviour as well as the moisture transport and shrinkage profiles at different ages of the slab (Carlswärd, 2006).

Numerical simulation of SFRC slabs-on-ground is a serious challenge in computational mechanics (Barros, 1999), due to different kinds of nonlinearities in the structural system of pavements. Major nonlinearities in the response of a concrete pavement arise from material nonlinearities, geometrical nonlinearities, and nonlinear boundary conditions.

Material nonlinearities are caused by cracking of concrete in tension, crushing in compression and the nonlinear response of the foundation. The geometrical nonlinearities are due to curling of the slab under temperature or moisture gradients and partial loss of support or removal of supporting material for other reasons such as pumping. The other source of nonlinearity in ground slabs is due to nonlinear response in the slab-foundation interaction (e.g. friction at the interface).

In this section, the complete pavement including the concrete slab and a multi-layered foundation is simulated using the FE technique. The contact surface of the slab and the

foundation is simulated so as to allow for uplift and movement of the slab against the foundation. The moisture transport analysis is first carried out and spatial moisture profiles are calculated as functions of time. The moisture transport analysis is then coupled with a structural analysis during which the time history of moisture profiles are used to calculate shrinkage strains by applying the "hygral contraction coefficient". The time history of shrinkage strains are then used to predict stresses and cracks in the restrained conditions. The self-weight of the slab is also applied simultaneously. The history of the stresses and cracks are saved as pre-loading distress. Then the slab is analysed for the desired wheel load in terms of magnitude and position. The performance of the slab is analysed and compared with the case of ignoring the pre-loading effects.

6.1.1 Modelling approaches for FE analysis of pavements

The existing approaches for modelling the cracking behaviour of concrete in a stress analysis (discrete and smeared crack approaches) were explained in Section 5.3. Both of these approaches have been used in the literature in FE modelling of concrete pavements (Barros et al., 2001; Barros, 1999, Barros et al., 2005; Meda et al, 2004[a]; Meda et al, 2004[b]; Sorelli et al., 2006; Channakeshava et al., 1993).

In the discrete crack approach, the linear elastic subdomains are connected by interface elements representing the predefined cracks (Figure 6.1). Therefore, the position of cracks should be known before creating the model.

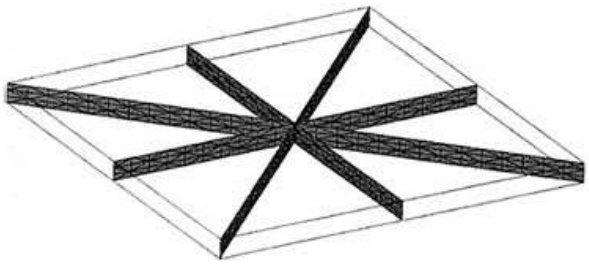

Figure 6.1 Discrete crack approach, elastic subdomains connected by interface elements (Meda et al., 2004[a])

The smeared crack approach does not need a-priori knowledge of the cracking pattern. Therefore, it could be used to study different loading positions and geometries. In the current study the smeared crack approach is used for stress analysis of concrete pavements.

In the smeared crack approach, as explained in detail in Appendix E and Section 5.3.1, two material models can be used; CSC and CDP material models. The advantages and disadvantages of these material models were discussed in Section 5.3.1.2. The results of adopting these two material models were compared in Section 5.3.2, for inverse analysis of flexural prisms and verified with section analysis. However, in 3-D CSC models of concrete pavements, the analysis solution cannot continue much beyond the formation of primary cracks and numerical instabilities terminate the analysis. This problem can be attributed to the multiple-fixed cracking approach which is used for the CSC model in ABAQUS (Section 5.3.1.2). Therefore, the CDP material model is chosen for stress analysis of concrete pavements. The detailed description of the CDP material model has been given in Section 5.3.1 and Appendix E.

6.1.2 Assumptions of modelling

This sub-section explains the assumptions made for modelling a typical pavement.

6.1.2.1 Design load and service life

The primary cause of structural damage to road pavements are commercial vehicles with an unladen weight over 15 kN. The damage caused by private cars is negligible compared to that of the commercial vehicles (Rogers, 2003). Based on a common historical approach, the traffic load (from wheel loads of various magnitudes, configurations and repetitions) is converted to an equivalent number of standard axles, in terms of the damage imposed to the pavement. As an example, the effect of 5000 repetitions of a 9 kN axle load equates to one passage of an 80 kN axle load (ACI 215R, 1992). Therefore, the equivalent standard axle load is a combination of a load magnitude and a number of repetitions. Definition of the equivalent number of standard axles is only useful for fatigue analysis, since it is not necessarily the maximum load which would be applied to the pavement.

The range of standard axles used in design in European countries is from 80 kN to 130 kN, and concrete roads are designed for a twenty year life in the majority of those countries. In the UK concrete roads are designed for 40 years, and the standard axle is an 80 kN single axle with dual tyres (two tyres at either side of the axle). For the highest traffic flows in the UK, a maximum value of 300 million standard axles (msa) is suggested for design purposes, as the maximum 40 year cumulative traffic loading. The maximum permissible axle load in the UK

is 10.5 tonnes (Hassan et al., 2005).

In this study the standard axle load of 80 kN is assumed, with a service life of 300 msa. Considering a tread width of 240 mm for each tyre and a tyre pressure of 700 kPa, the footprint of each tyre is estimated as a rectangular shape in the size of 240 × 120 mm (The contact area of a single tyre is approximated by dividing the tyre load by the tyre pressure). Assuming a distance of 240 mm between the footprint of tyres, the contact area of the dual tyres for the standard axle is considered as Figure 6.2 (a) and (b). The track width relevant to the standard axle load is considered as 2.4 m as shown in Figure 6.2 (c).

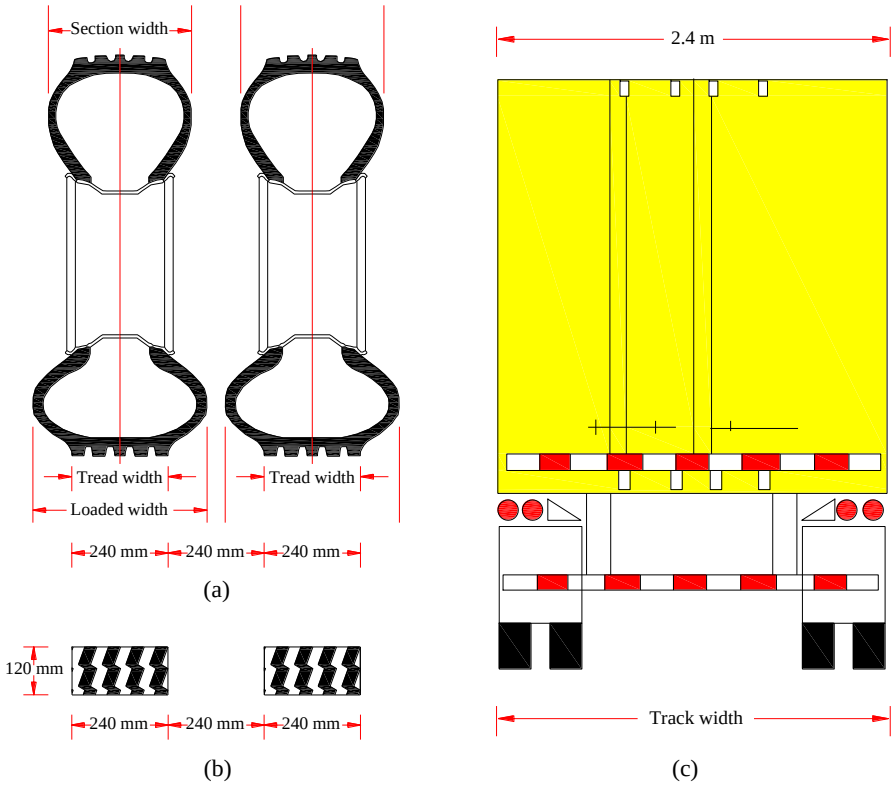

Figure 6.2 (a) The cross section of the dual tyre at one end of a loaded axle; (b) The footprint of the dual tyre; (c) The track width of the commercial vehicle

6.1.2.2 Geometry of the pavement

The geometry of the pavement is initially chosen based on the assumed traffic, the design life, and design criteria proposed in guidelines.

In US, the standard lane width is between 3.4 m to 3.7 m, depending on the traffic and

location of the lane. In European countries, lane width varies between 2.5 m to 3.25 m. In the UK, lanes for HGVs must be at least 3.0 m wide; and if there is only one lane per direction, it should be at least 3.25 m wide. In this study, a lane width of 3.4 m is considered in the analysis.

Edge strips and hard shoulders are usually designed for CRCPs to reduce the thickness requirement and provide a safety zone. Usually the edge strips are provided by widening the pavement slab beyond the traffic lane edges. Previous studies have shown that nearside widening of 0.4 m should keep heavy vehicle tyres away from the slab edge (Hassan et al., 2005). Since the studied lane can be a middle lane, no edge strip has been considered in the current study.

The thickness of the concrete slab can be estimated from the thickness design curves provided in the guidelines. In Highway Agency report TRL630 (Hassan et al., 2005) the minimum specified thickness for CRCPs is 200 mm, and for the cumulative traffic of 300 msa the slab thickness is between 200 to 270 mm, depending on the stiffness of the foundation and flexural strength of the concrete. For the stiffness of the assumed foundation in this study (Section 6.1.3.1) and the experimental flexural strength of the concrete mixes (Chapter 4, Section 4.2.2.4), a thickness of 200 mm is initially chosen for the concrete slab.

The length of the concrete slab, in modelling, must be big enough to take into account the continuity of the pavement. In this study to model the realistic conditions, the length is taken as three times the width and by applying the end constraint the continuity is simulated at one end (Figure 6.3).

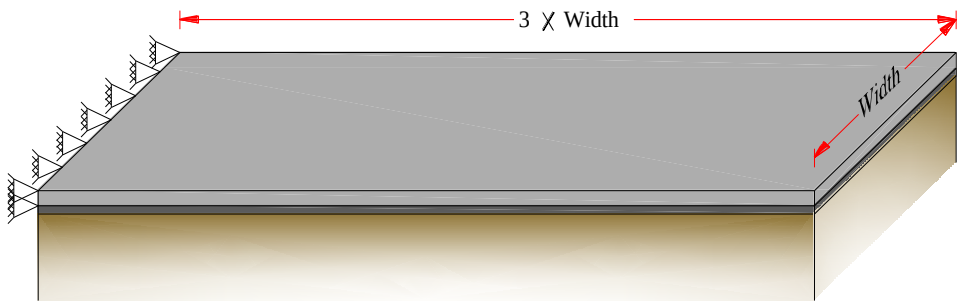

Figure 6.3 Continuity of the pavement in modelling

6.1.3 Modelling of the Foundation

Appropriate modelling of the foundation is an important issue in numerical modelling of pavements. The foundation usually includes the original subgrade soil, sometimes a layer of ballast as the subbase, and usually a layer of cement bound material as the base (Figure 6.4).

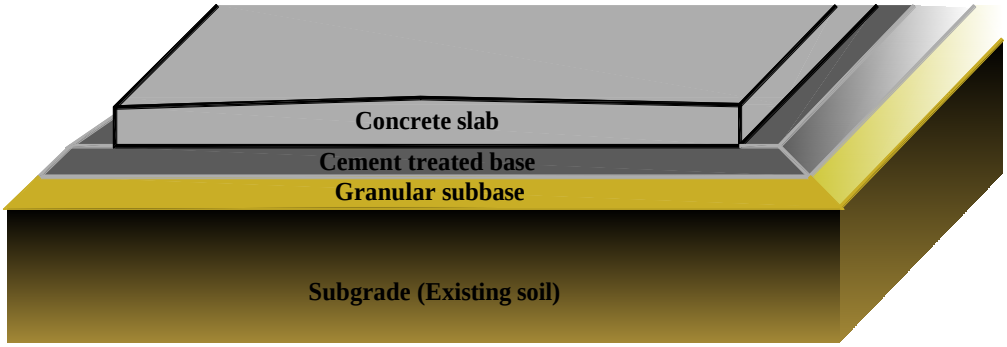

Figure 6.4 Layers constituting the foundation

When the subgrade is soft, adopting a treated base instead of an aggregate base can increase the load-carrying capacity. For flexible pavements, granular or cement-treated bases are permitted, while for rigid pavements only cemented bases are recommended (Rogers, 2003). The purpose of a cement-treated base layer for rigid pavements is to reduce weakness of the base as a result of water penetration from joints and cracks (Rogers, 2003). In the UK, only cement-treated bases are permitted under rigid pavements (Hassan et al., 2005).

The performance of the pavement support is a function of the stiffness of the supporting layers, the way of interaction between the slab and the foundation, and loss of support as the result of environmental effects. These issues are addressed below.

6.1.3.1 Stiffness and strength of the supporting layers

In design of concrete pavements, the foundation is mostly characterised by a *k*-value (modulus of subgrade reaction), representing elastic springs (NCHRP Report 372, 1995). This model is attributed to Winkler (1867) and assumes that the foundation deflects under an applied vertical force in direct proportion to the force without shear transmission to adjacent areas. This model is also called a dense liquid foundation in the sense that the modulus of subgrade reaction is equal to the unit weight of a virtual liquid support (Eyre, 2006).

The modulus of subgrade reaction is defined as the load per unit area causing unit deflection. Values of *k* are usually determined from a plate-loading test. The standard plate load test is conceptually based on the volumetric method of calculating *k*. In this method the total applied load is divided by the volume of the deflection basin.

Another model that sometimes is adopted to simulate the foundation is the elastic solid model, in which the applied load to the surface of the foundation is assumed to produce a continuous basin (Figure 6.5).

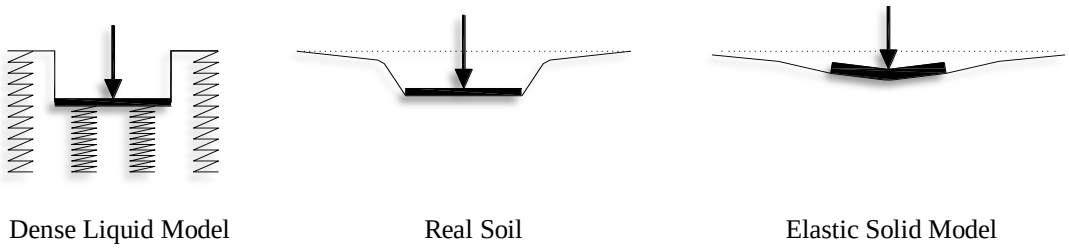

Figure 6.5 Dense liquid and elastic solid extremes of the elastic soil response

The elastic response of real subgrades is located between the elastic solid and dense liquid idealisations. Granular and fine-grained unbound soils with lower shear strength are more similar to the dense liquid model than the elastic solid model. In contrast, bonded or stabilised materials exhibit more similarity to the elastic solid model.

One approach, which is usually used to consider the stiffness of multi-layered foundations, is to assume an integrated foundation and to evaluate a "top-of-base" or "composite" *k*-value. Studies show that measuring the "composite" *k*-values, by performing the plate bearing test on the top of the base layer, misleadingly overestimates the stiffness of the foundation, particularly for treated base layers (NCHRP Report 372, 1995). In fact, including such a stiff treated base in a stiffness measurement approach, which is defined for granular and unbound soils, is totally unrealistic.

A more realistic approach to define the support under the concrete pavement is to determine the *k*-values for the subgrade and the granular subbase, and then consider the base course as a structural layer (NCHRP Report 372, 1995).

According to PCA manual (1966), among the two approaches explained above, the latter approach (considering the base as a structural layer) is more appropriate, particularly for stiff bases, thick pavements, and large load sizes (NCHRP Report 372, 1995). Considering the

base course as a structural layer in modelling, is also beneficial to take into account the relative movement between the slab and the base. These movements include out-of-plane up-lift as a result of temperature and moisture influences, and in-plane displacement as a result of imperfect frictional resistance between the slab and the base.

In this research, to achieve both accuracy and computational saving, the base is modelled as a structural layer interacting with the slab and the rest of the foundation (the granular subbase & the subgrade) is simulated as a Winkler foundation characterised by a *k*-value (Winkler, 1867). In this manner, it is possible to model up-lift due to environmental variations, frictional behaviour and loss of support due to curling. For this purpose, the contact surface between the slab and the base layer is modelled comprehensively (Figure 6.6). The base layer is considered as an isotropic, homogeneous, and linear elastic material.

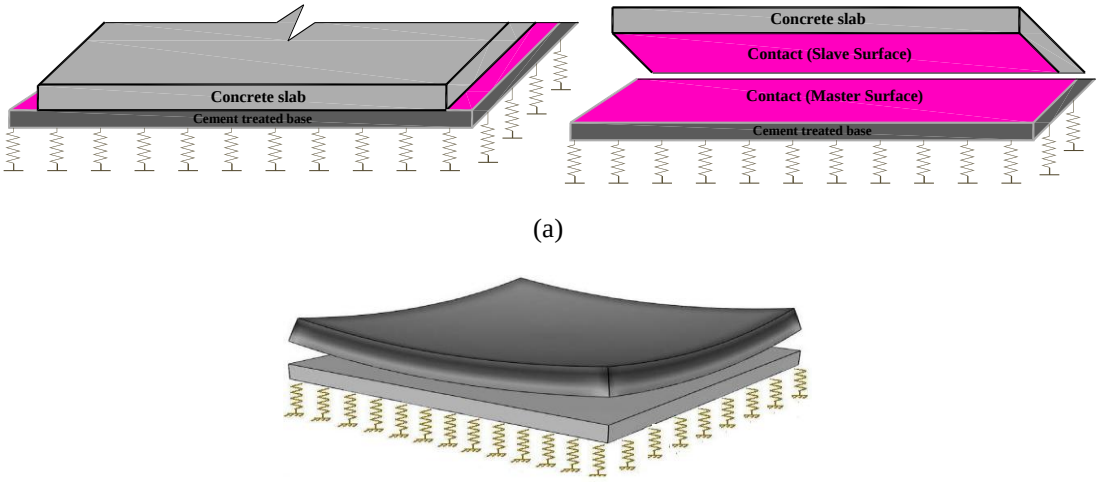

(a)

(b)

Figure 6.6 (a) Modelling of the foundation layers; (b) Capability of relative movement between the slab and the foundation

In the literature, the modulus of subgrade reaction is correlated to the California Bearing Ratio (CBR: is a test representing the resistance of the subgrade soil to penetration) (Concrete Society TR34, 2003). *k* value ranges between 0.01 N/mm^3 to 0.1 N/mm^3 for a wide variety of soil types (Concrete Society TR34, 2003). The effect of a layer of granular subbase on improving the modulus of reaction has been evaluated by US Army corps of engineers (EM 1110-3-142, 1984). Based on this evaluation, a thickness of 150 mm of a granular subbase increases the *k* value by 20% and 75% for the subgrade *k* values of 0.1 N/mm^3 and 0.01

N/mm^3, respectively.

Therefore, considering a moderate value of 0.04 N/mm^3 as the subgrade *k* value and increasing it by 50% as the effect of a thin layer of granular material to improve the stiffness of the soil, the modulus of reaction (k) at the top of the subbase is assumed to be 0.06 N/mm^3.

It is believed that the *k* value has a minor effect on the thickness design of the slab, and no great accuracy is required in estimating it (NCHRP Report 372 cited in Concrete Society TR34, 2003).

The thickness of the cement bound base in most of European countries is specified as 150 mm. In the UK a 150 mm thickness cement-treated base with a strength of 10 MPa at 7 days is required (Hassan et al., 2005). In the UK, the compressive strength requirement for the cement bound base is considerably higher than other countries. However, stronger does not always mean better, and a more economic construction can be obtained using a weaker material (Hassan et al., 2005). Stabilised bases induce higher curling stresses in pavements; the stiffer the base, the more curling stress is induced in the slab (ACPA, 2002). AASHTO recommends an upper limit of 10.3 MPa for the compressive strength of lean concrete bases to prevent the increased risk of cracking in the concrete pavement (ACPA, 2002). The Federal Aviation Administration (FAA) guide recommends an upper limit of 8.3 MPa for the compressive strength of the base (ACPA, 2002). Therefore, a 7 days strength of 7 MPa, a long-term strength of 10 MPa, a long-term elastic modulus of 8 GPa, and a Poisson's ratio of 0.3 have been assumed for the cement bound base.

6.1.3.2 Interaction between the slab and the foundation

The interface between the concrete slab and the base is modelled by surface-based contact (the contact properties are assigned to the existing surfaces of the structural members and no contact element is defined). Surface-to-surface contact discretization is used in the overall contact formulation. The master surface is defined as the top surface of the base and the slave surface is assigned to the bottom surface of the concrete slab. The finite-sliding approach is chosen which is the most general tracking approach allowing for arbitrary relative separation, sliding, and rotation of the contacting surfaces (ABAQUS, 2010).

The normal constraint enforcement method is the direct enforced hard contact. In the hard

contact relationship, any pressure can be transmitted between the surfaces when they are in contact. If the pressure reduces to zero, the surfaces separate. To allow for a particular tensile resistance between the surfaces, in arbitrary cases, the "modified" hard contact relationship should be used. With this modification, the surfaces are allowed to transmit tensile contact pressures (cohesion) up to a particular value, before they separate (ABAQUS, 2010).

The frictional constraint enforcement method is the penalty method, and an isotropic frictional resistance is applied. The concept of Coulomb friction model is used to relate the frictional stress to the contact pressure. Based on the Coulomb model, in the sticking state the surfaces carry shear stresses, τ, proportional to the contact pressure, p ($\tau = \mu p$), up to a certain magnitude, τ_{crit}, before they start sliding. After reaching τ_{crit}, the transition from sticking to sliding occurs. The multiplier μ is known as the friction coefficient, which is assumed to be the same in all directions in isotropic friction.

In this manner the effect of friction, sliding and bonding is taken into account. By defining zero bond strength between surfaces, unrestrained separation of the concrete slab and base can be allowed when tensile strains arise between surfaces.

ACPA (2002) specifies the value of coefficient of friction between the concrete pavement and the cement-stabilised base as high as 10.0 and strongly recommends to apply a bond-breaking medium between these two layers. Based on BS EN 12812 (2008), the coefficient of friction between concrete surfaces has a minimum value of 0.5 and a maximum value of 1.0. The minimum value of 0.5 is assumed for analysis in this research, assuming that the cement stabilised base frictionally behaves like a lean concrete.

The maximum friction stress between the concrete slab and the cement stabilised base is given as 100 kPa by FHWA (McCullough et al., 1998), and is adopted in the current research.

In most of the cases, there is no bond between the concrete slab and the foundation, and only the self-weight of the pavement resists up-lift. In some cases, shrinkage curling overcomes the self-weight and up-lift occurs (Channakeshava et al., 1993). The bond strength between concrete surfaces, measured by pull-off test, was evaluated in the range of 0 to 2 MPa by Carlswärd (2006), depending on the level of wetness and priming applied on the substrate layer.

6.1.3.3 Loss of support

Loss of support is defined as any gap or clearance occurring between the slab and the base, or between the stabilized base and the underneath foundation.

There are three basic causes for loss of support (NCHRP Report 372, 1995):

- Moisture and temperature curling of the slab.
- Erosion of the base or the sub-grade
- Settlement or consolidation of the base or the sub-grade

An unsafe failure load will be estimated if the loss of contact between the slab and the foundation is not taken into account (Barros, 1999).

In the first kind of loss of support, the slab lifts up under variable environmental conditions. The loss of support caused by curling due to non-uniform drying shrinkage is considered in this research. This negative curling causes the corners and edges of the slab to displace upward.

6.1.4 Drying creep

Creep is deformation of concrete under sustained stress conditions. Since tensile stresses are dominant in the design of concrete pavements, the term “creep” in this thesis refers to tensile creep.

Total tensile creep in concrete is composed of basic creep and drying creep. Basic creep is defined as creep of concrete under any given stress domain, considering constant moisture content in the concrete. Drying creep is observed when concrete is exposed to drying under restrained conditions. This behaviour is also known as the Pickett effect (Pickett, 1942). Drying creep has two components; intrinsic creep, and microcracking. Microcracking can be considered as the apparent component of creep, since it is not associated with deformation of the solid body of the concrete member, but it is relevant to the microstructural damage (Altoubat et al., 2003). The intrinsic component of drying creep is the beneficial aspect of creep to the structure, while microcracking has detrimental effects.

Different methods have been proposed to estimate the effect of basic creep on the behaviour

of concrete structures. As an instance, in BS EN 1992-1-1 (2004) creep is taken into account, at ultimate limit states only, by dividing the elastic modulus by a factor $1 + \varphi_{ef}$, where the φ_{ef} is the effective creep. FHWA (McCullough et al., 1998) also follows the same approach to consider the effect of creep for concrete pavements, but the effective creep coefficient is taken as a function of time. Since the aim of this research is to investigate the drying shrinkage behaviour of concrete pavement, the effect of drying creep will be considered distinctly.

Altoubat et al. (2001) comprehensively studied the drying creep behaviour of SFRC at the early age. In that study the effect of fibre reinforcement on tensile creep and restrained shrinkage behaviour of concrete was investigated. It was reported that the tensile creep induced by the drying stresses is proportional to the free shrinkage strain. It means that by applying a reduction factor to the "hygral contraction coefficient", obtained from free shrinkage test, the effect of creep can be considered as a material property. In restrained tests, Altoubat et a. (2001) defined a creep/shrinkage ratio as an index reflecting the degree of stress relaxation. The creep/shrinkage ratio is increased by time at early days of exposure and then decreases to reach a stable value after the first week of exposure. The results of that study indicated that the creep/shrinkage ratio at the time of cracking for concrete in restrained conditions is ultimately in the order of 0.5 to 0.6, for all mixtures.

The microcracking component of drying creep is automatically taken into account in the current research, since a cracking model is used. The intrinsic creep mainly occurs in the pre-cracking stage, since in the post-cracking stage tensile stresses are dominantly released by crack opening. In the damage plasticity model that is used in the current study, inelastic tensile strains are developed in the post-cracking stage, while in the pre-cracking stage the tensile behaviour of concrete is in the elastic domain. Therefore, intrinsic creep mainly releases elastic strains. Shrinkage analysis performed in the current study shows that the elastic strains, developed in critical zones (e.g. drying surface with high magnitude of shrinkage strains), are in the order of 14% of the total strain (on average) (Section 6.3.2.1, Figure 6.21). Based on the estimation made by Altoubat et al. (2001), intrinsic creep relaxes the elastic strains by 50%. Therefore, intrinsic creep can reduce the total strain in the highly distressed areas, only by the order of 7%. This is comparable with the results obtained by Kim et al. (1998), who predicted drying creep between two adjacent transverse cracks and reported 10% deformation release between the adjacent cracks (Chapter 2, Section 2.4.2).

In the current study, the intrinsic component of drying creep is ignored. This seems reasonable for highly distressed zones on the surface, since the tensile strain sustained by concrete during the pre-cracking phase is too small compared to the strain developed in the post-cracking phase. However in deeper zones in the concrete slab thickness, intrinsic creep forms a bigger proportion of the total creep, and it is suggested to be considered in further development of this research.

6.1.5 Maturity

Curing of concrete may be stopped before complete hardening and drying shrinkage may be allowed to occur when hydration is in progress. In such cases, to consider the maturity of concrete in the duration of the shrinkage analysis, the mechanical properties of concrete should be defined as a function of time. For this purpose in ABAQUS, the unixial compressive strength and the elastic modulus of concrete can be defined to be time dependent by specifying them at several different times. In this way, other concrete material properties which are defined proportional to the uniaxial compressive strength will also be affected by this time variation (such as ultimate biaxial compressive stress).

Based on BS EN 1992-1-1 (2004), for a mean temperature of 20ºC, the compressive strength of concrete at various ages is estimated from the following expressions:

$$f_{cm}(t) = \beta_{cc}(t)\ f_{cm} \qquad \text{(Eq. 6.1)}$$

$$\beta_{cc}(t) = \exp\{s[1 - (\frac{28}{t})^{0.5}]\} \qquad \text{(Eq. 6.2)}$$

Where, f_{cm} is the mean compressive strength at 28 days; $\beta_{cc}(t)$ is a coefficient which depends on the age of the concrete; t is the age of concrete in days; $f_{cm}(t)$ is the mean compressive strength at an age of t days; s is a coefficient which depends on the type of cement.

In BS EN 1992-1 (2004), s is specified as 0.2, 0.25 and 0.38 for different cement types, but for the concrete mixes developed in the current research the values of $s = 0.15$ for CC mixes and $s = 0.38$ for RCC mixes matches the experimental maturity curves obtained by Ecolanes (Angelakopoulos et al., 2008[a,b]). The compressive strength of concrete mixes has been

measured for cubes at 28 days and for cylinders at 90 days.

The elastic modulus and the tensile strength of concrete at various ages are also estimated from Equation 6.3 and 6.4, respectively.

$$E_{cm}(t) = (f_{cm}(t)/f_{cm})^{0.3}\, E_{cm} \qquad \text{(Eq. 6.3)}$$

$$f_{ctm}(t) = (\beta_{cc}(t))^{\alpha}\ \ f_{ctm} \qquad \text{(Eq. 6.4)}$$

Where, f_{ctm} is the mean tensile strength at 28 days; $f_{ctm}\ t$ is the mean tensile strength at an age of t days; E_{cm} is the mean elastic modulus at 28 days; $E_{cm}(t)$ is the mean elastic modulus at an age of t days; $\alpha = 1$ for $t < 28$ and $\alpha = 2/3$ for $t \geq 28$.

It must be noted that fresh RCC mix is stiffer than what is predicted based on Eq. 6.3, since it supports the compaction equipment.

Figure 6.7 shows the tensile strength development for RCC mix reinforced with 2.5% recycled steel fibres.

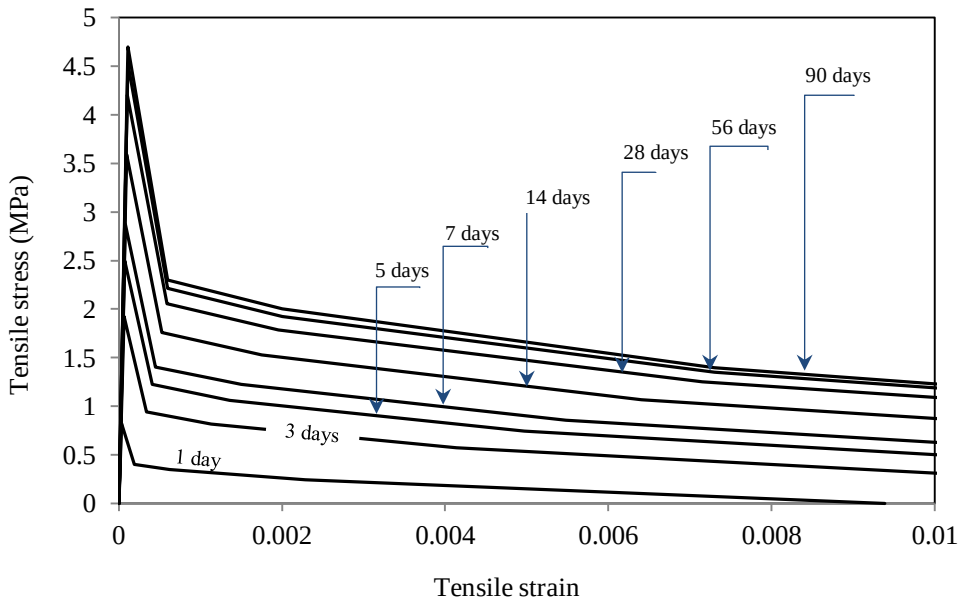

Figure 6.7 Tensile strength development for SFR-RCC mix

The variation of tensile strength versus tensile strain (σ-ε curve) at the age of 90 days has been obtained by inverse analysis of flexural test results (Section 5.3.2). The elastic modulus and the peak tensile strength for various ages are estimated by Equation 6.3 and 6.4

respectively. The elastic strain at the cracking point for various ages is calculated by dividing the corresponding tensile strength by the elastic modulus. To obtain the post-cracking behaviour of concrete at early ages, the post-cracking behaviour at 90 days is scaled proportionally to the stress and strain ratios at the peak points. This assumption needs to be verified experimentally, in the future.

Applying a maturity approach to concrete shrinkage is difficult. In fact, there is not a predictable change in shrinkage as concrete strength increases (Clarke, 2009). It has been reported that accelerating the rate of concrete strengthening by curing the specimens at high temperatures does not significantly change the shrinkage properties (Clarke, 2009). Therefore, The effect of concrete age, apart from the moisture content, on shrinkage properties, such as "hygral contraction coefficient", is considered less important (same as the effect of age on coefficient of thermal expansion, as mentioned in ACI 209R (1992)).

6.1.6 Failure criteria and load bearing capacity

To evaluate the load carrying capacity of pavements, a criterion representing the failure of the slab is usually required. According to the ultimate limit state criteria, the structure must not collapse under the maximum design load. Therefore, in the ultimate limit state the collapse condition limits the load carrying capacity of the pavement, and all stresses and material properties should be factored.

In the serviceability limit state, the pavement must remain functional under routine conditions, and this is not satisfied unless the pavement does not deflect by more than certain limits. An example of serviceability limit requirement includes crack width, which must be kept below a specified amount.

Owners and designers of slabs are much more concerned about the serviceability limit state of cracking at the top surface rather than the 'ultimate limit state' (Eyre, 2006), but in many cases, the serviceability limits depend on the finish materials. Therefore, these limits are sometimes descriptive and the choice is left to the designer. Here a description of both serviceability and ultimate limit states criteria for pavement design is given.

6.1.6.1 Failure based on the collapse condition

The first cracking point, which is conventionally assumed as the loss of linearity in the behaviour of the slab, can be estimated by Westergaard's theory (1925, 1926, 1948). However, the bearing capacity of a pavement is greatly underestimated using the first crack criterion, particularly when reinforced with steel fibres (Meda et al., 2004[b]).

SFRC pavements do not exhibit a sudden or catastrophic failure (Sorelli et al., 2006). This means that even after a collapse mechanism develops, the slab is able to carry further load (see Figure 6.8). The ultimate load corresponding to the formation of a collapse mechanism is conventionally defined as the point when a sudden change in the monitored displacement occurs (Sorelli et al., 2006). This considerable change in the monitored displacement could be associated with the diagonal or median cracks reaching the edges of the slab (Meda et al., 2004[b]), and depends on the geometry of the slab and the ratio of stiffness between the slab and foundation.

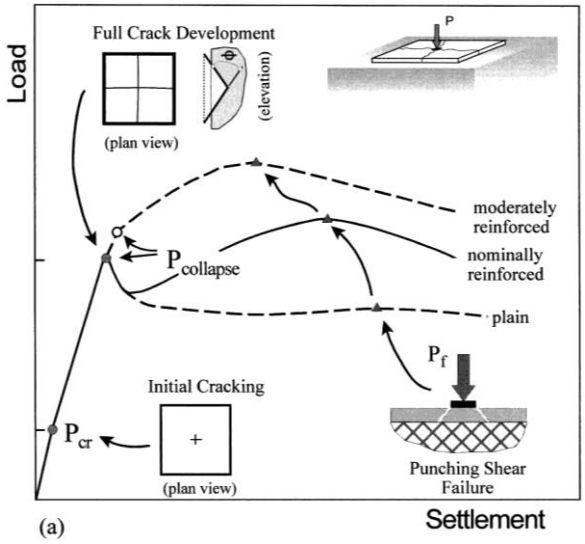

Figure 6.8 Idealised model slab response (Bischoff et al., 2003)

In the slabs response, as shown in Figure 6.8, the load-deflection curve behaves linearly up to crack initiation at a load P_{cr}. After cracking, the curve deviates only slightly from linearity, and the slab continues to carry higher amounts of load until the cracks extend to the edges and a collapse mechanism is formed at a load $P_{collapse}$, which is typically 3 to 5 times greater than the first cracking load (Bischoff et al., 1996 & 1998 cited in Bischoff et al., 2003;

Beckett, 1999; Roa et al.,1986). Once the collapse load is reached, a distinct change in the behaviour is observed. Failure is eventually reached as the result of punching shear at a load P_f (Bischoff et al., 2003).

Chen (2004) reported full-scale tests on SFRC ground slabs. For all slabs in that experimental research, the load-deflection curves exhibited linear behaviour even after initiation of cracks at the bottom along the medians. After the upward development of cracks, as the cracks reached the top surface, the curves exhibited a non-linear behaviour. The results showed that the onset of initial cracks is not delayed by the reinforcement, but the post-cracking capacity of the SFRC slabs increases the overall load-carrying capacity to the slab.

Concrete Society guideline TR34 (2003) for the design of industrial SFRC ground floors recommends a less conservative method to predict the load bearing capacity, compared to linear approaches. However, there is still confusion in this method arising from the limit state definition (Eyre, 2006), because the ultimate limit state in TR34 has been defined as the criterion of cracking in the slab top surface, and factored loading is used to check this criterion, in addition to partial safety factors which are applied to reduce the strength of materials. This differs from other structural design guidelines in which the use of load safety factors is kept for those limit states which threaten human safety (Eyre, 2006).

Chen (2004) compared his test results with the formula presented by the Concrete Society TR34 (2003) for calculating the ultimate loading capacity of the slab, and concluded that TR34 provides a conservative prediction (Chen, 2004).

However, Concrete Society TR34 (2003) is still the most up-to-date method in predicting the ultimate load bearing capacity of SFRC ground slabs, and will be used in Section 6.4.4.3 to compare with the FE result in the current research.

6.1.6.2 Failure based on cracking criteria

Cracks are classified as hair, fine, medium and wide cracks. The average crack width value usually assigned to each category is 0.1 mm (hair), 0.25 mm (fine), 1.0 mm (medium) and 2.0 mm (wide) (Hassan et al., 2005).

Load transfer efficiency across the cracks can be provided by the aggregate interlock, if the crack is kept tightly closed (Hassan et al., 2005). The long-term performance of pavements is

mainly influenced by the medium and wide cracks, since these cracks increase loss of aggregate interlock, decrease structural integrity, increase the risk of corrosion in the slab and deterioration of the foundation (Hassan et al., 2005; Mayhew et al., 1987).

The maximum allowable crack width suggested by AASHTO (1986) is 1mm to hold the load transfer efficiency (Hassan et al., 2005). Other studies showed that to prevent loss of aggregate interlock and to prevent water penetration through the crack, the maximum crack width should be in the order of 0.5 mm (Hassan et al., 2005).

In the FE models developed in this research, the equivalent crack openings are calculated versus the applied monotonic load (Section 6.4). This parameter is used to evaluate the effect of shrinkage distress on the crack width induced by loading.

6.2 Moisture transport analysis of SFRC pavements

The basis of the FE model developed for the moisture transport analysis was explained and verified in Section 5.1.

There is no need to model all the layers forming the pavement (foundation and slab) in the moisture migration analysis. The concrete slab is the main layer which is required to be modelled, assuming that it is the only active domain in the drying procedure. However, the geometry of the slab and its elements are directly transmitted to the stress analysis where the geometry of other layers and the foundation are added.

The back-calculated moisture diffusivities (Figure 5.5) and the lower limit of the calculated surface factors for the experimental concrete mixes (Section 5.1.2) are adopted in the analysis.

6.2.1 Boundary and initial conditions

Although it is possible to consider any possible variation in the environmental relative humidity, to ignore unnecessary variables the surrounding environment is assumed to have a constant relative humidity. The top surface of the slab is exposed to the environment and other surfaces are assumed to not have any moisture interaction with the neighbouring domains. The moisture convection from the top surface occurs via a surface convection factor (Section 3.1.2 and Section 5.1). An ambient humidity of 40% is assumed and as the

initial condition, the moisture content is set equal to 1.0 (saturation condition).

6.2.2 Element type for moisture transport FE analysis of pavements

Generally, for 3D modelling of a ground slab, shell elements and three-dimensional solid elements can be used. Although shell elements are capable of capturing the moisture variations through the thickness, differential shrinkage strains cannot be calculated through the thickness of the slab using shell elements. The element type used for the moisture transport analysis must be consistent with the stress analysis in the next stage. The same mesh of elements must also be used for moisture transport and stress analysis. ABAQUS 3D 8-noded solid elements called DC3D8 are used for moisture transport analysis of the pavement. Since moisture movement occurs through the depth of the pavement, alternatives given in Table 6.1 were investigated for one of the mixes (SFR-RCC) to choose the optimum element size through the thickness. The number of elements through the thickness should be such that, besides good accuracy, the computational cost remains reasonable. Details on how to select the horizontal dimensions of elements are explained in Section 6.3.2.1.

Table 6.1 Alternatives for mesh refinement in moisture transport FE analysis

		Horizontal element size (mm)
		60
Vertical element size (mm)	12.5	Alt 1
	25	Alt 2
	50	Alt 3

Figure 6.9 shows the results of mesh sensitivity analysis for different element sizes through the thickness, as the time history of moisture contents at various depths.

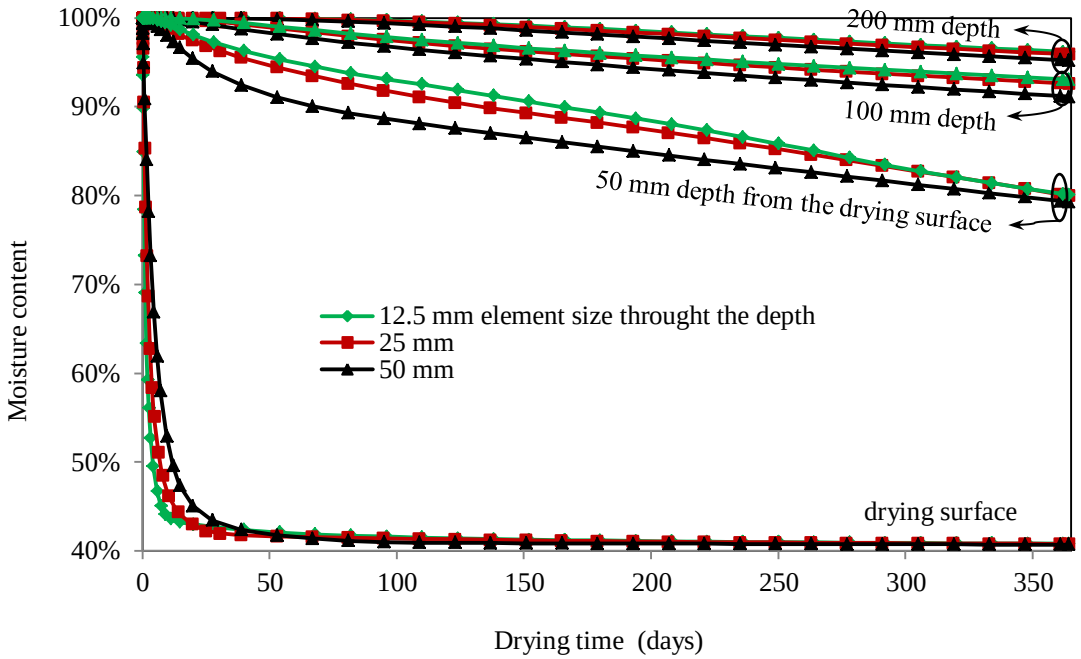

Figure 6.9 Mesh sensitivity analysis through the thickness (SFR-RRC mix)

6.2.3 Results of the moisture transport analysis

The numerically calculated time history of moisture profiles are as given in Figure 6.10.

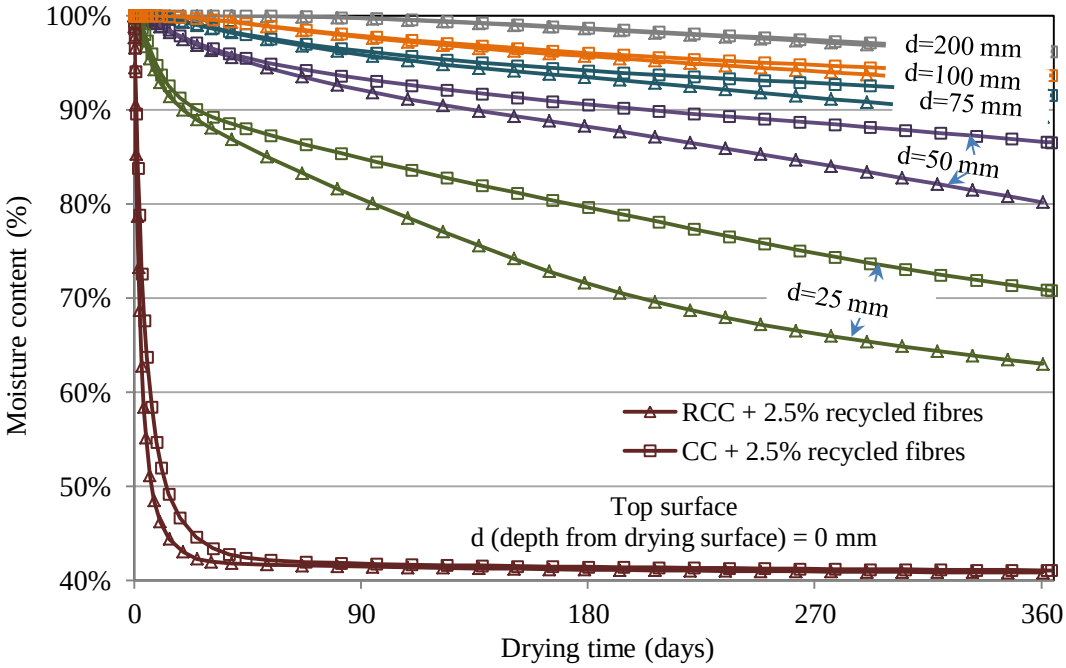

Figure 6.10 Time history of the moisture profiles

Figure 6.11 (a) and (b) shows the moisture contours after 1 year of drying for SFR-RCC and SFR-CC, respectively. The moisture content at the drying surface sharply approaches the environmental relative humidity, while penetration of drying into the depth occurs at a very slow rate. At a depth of 25 mm from the drying surface, after one year of drying, the moisture content only reaches 63% and 71% for SFRC-RCC and SFR-CC mixes, respectively. The RCC mix dries faster than the CC mix for the reason given in Chapter 4, Section 4.3.3.

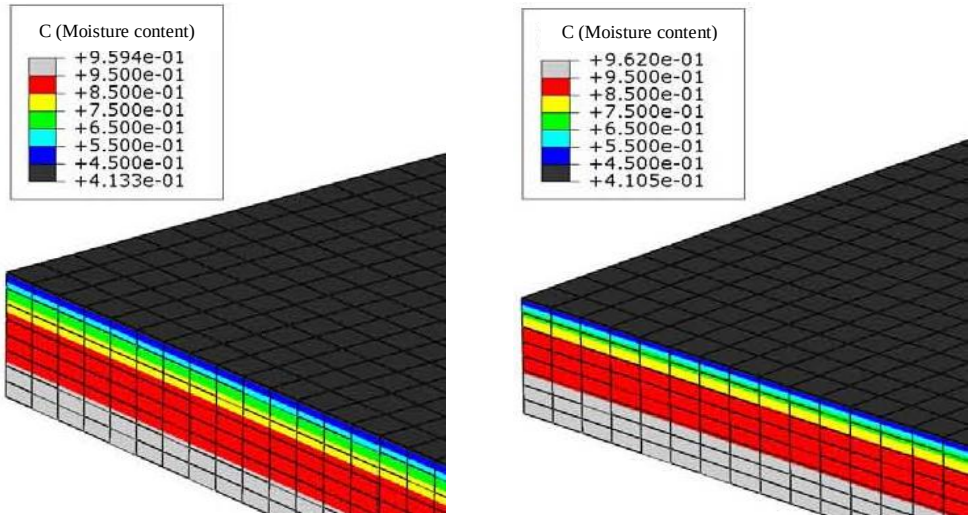

(a) (b)

Figure 6.11 Moisture content contour after 1 year drying; (a) SFR-RCC mix; (b) SFR-CC mix

6.3 Stress analysis of SFRC pavements at early age

The results of the moisture transport analysis are transferred to the stress analysis. The "hygral contraction coefficient", back-calculated from experiments (Figure 5.10), is applied to obtain the time history of shrinkage strains induced by moisture variations under the given restraints imposed on the pavement. The time history of stress distribution and cracking resulted from restrained shrinkage are also obtained in the stress analysis. The experimental mechanical properties, consisting of compressive strength (Figure 4.8), elastic modulus (Table 4.6), and the back-calculated tension stiffening curves (Figure 5.26), are used for stress analysis. For unavailable experimental properties, such as biaxial behaviour, typical values have been adopted (Section 5.3.1 and Appendix E).

6.3.1 Element type for FE stress analysis of pavements

Shell elements are not capable of dealing with differential shrinkage strains through the thickness of the slab. Therefore 3D solid elements are used for stress analysis of concrete pavements. In pavement slabs, the surface dimensions are very big compared to the thickness. For numerical accuracy in FE modelling, the aspect ratio of elements must be as close to unity as possible (since the characteristic length of the 3D elements is calculated as the average of the element sizes in three dimensions). Therefore, to avoid a huge number of elements, there is limitation in element size refinement through the thickness. In Section 6.2.2, the element size through the thickness was chosen 25 mm based on a mesh sensitivity analysis for moisture transport. This size is small enough to capture the strain variations through the thickness. Therefore, the concrete slab is modelled in a set of 8 layers of 8-noded elements, called C3D8. The effect of mesh refinement on the accuracy of the solution is also investigated through alternatives presented in Table 6.2. The result of the mesh sensitivity analysis, for these alternatives, is presented in Section 6.3.2.1.

Table 6.2 Alternatives for mesh refinement in FE stress analysis

		Horizontal element size (mm)		
		120	60	40
Vertical element size (mm)	25	Alt 1	Alt 2	Alt 3

The FE model developed based on the issues given above is shown in Figure 6.12 for Alt. 1 of element sizes assumed in Table 6.2. Due to symmetry, half of the slab has been modelled (in transversal direction), for shrinkage analysis.

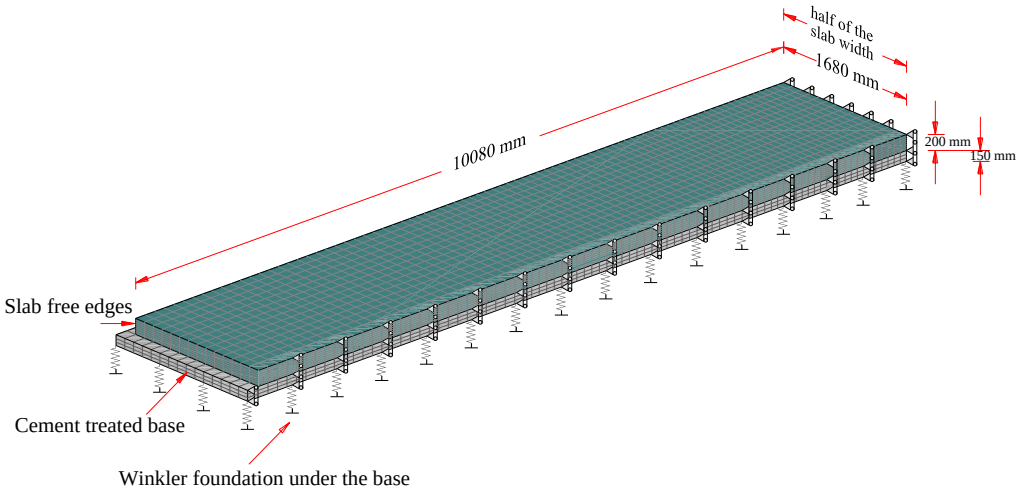

Figure 6.12 FE model developed for stress analysis of the SFRC pavement

6.3.2 Shrinkage of the SFRC pavement at early-age

Two conditions are analysed for this load case:

- For the first condition it is assumed that there is no cohesion between the concrete slab and the cement treated base. Therefore, the slab lifts up freely under non-uniform drying shrinkage. This condition is common in real pavements, since in most of the cases there is no bond between the concrete slab and the foundation, and only the self-weight of the pavement resists against up-lift (Channakeshava et al., 1993). Applying a bond-breaking medium between the concrete slab and the foundation is also recommended (ACPA, 2002).
- In the second condition, as an extreme case, it is assumed that there is enough cohesion between the concrete slab and the cement treated base causing the slab to be fully bonded to the base.

Maturity of concrete during the first 90 days of its life is considered. The weight of the concrete slab is loaded initially. The results for this load case are presented in the following subsection. The analysis was initially performed for SFR-RCC mix and then for the chosen condition the analysis is repeated for SFR-CC mix.

6.3.2.1 SFR-RCC mix, Condition 1: no cohesion between slab and base

In this condition a continuous SFR-RCC pavement deforms under drying shrinkage as shown in Figure 6.13. Contact opening occurs over a large area under the slab, and only a small fraction of the contact surface remains in touch to transfer the weight of the slab to the foundation.

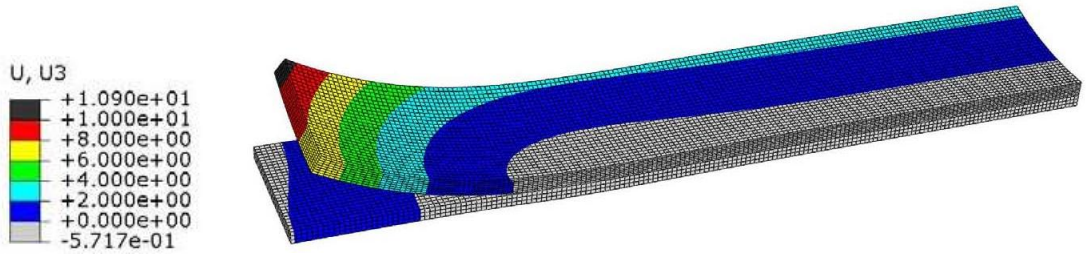

Figure 6.13 Deformed shape of SFR-RCC pavement, due to drying shrinkage (values in mm)

Mesh sensitivity analysis is performed for this case, to choose the appropriate element size. The chosen element size is adopted for the rest of the analyses performed in this chapter. For

mesh sensitivity analysis, the time history of maximum cracking strains and tensile stresses were compared for the alternatives given in Section 6.3.1 (Figure 6.14 (a) and (b)). Maximum stresses and strains occur in the interior areas of the slab forming surface microcracks.

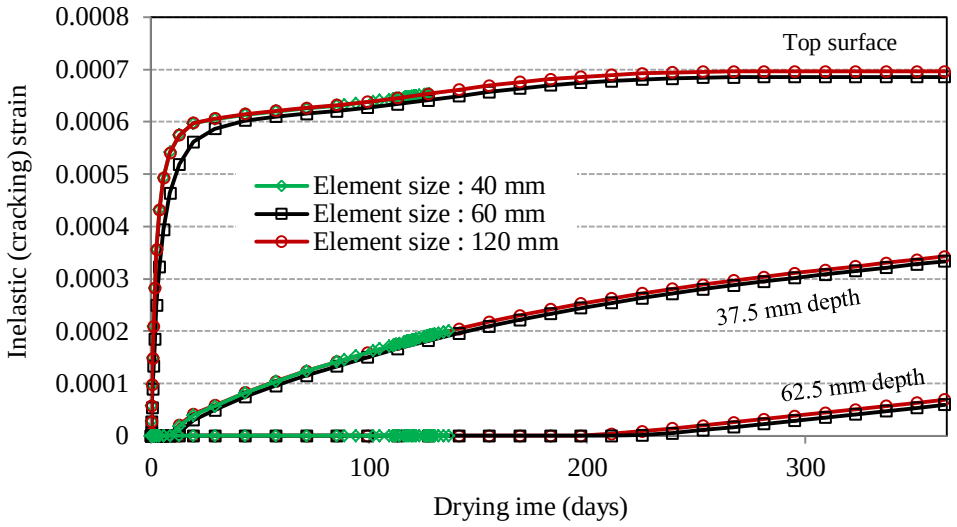

(a)

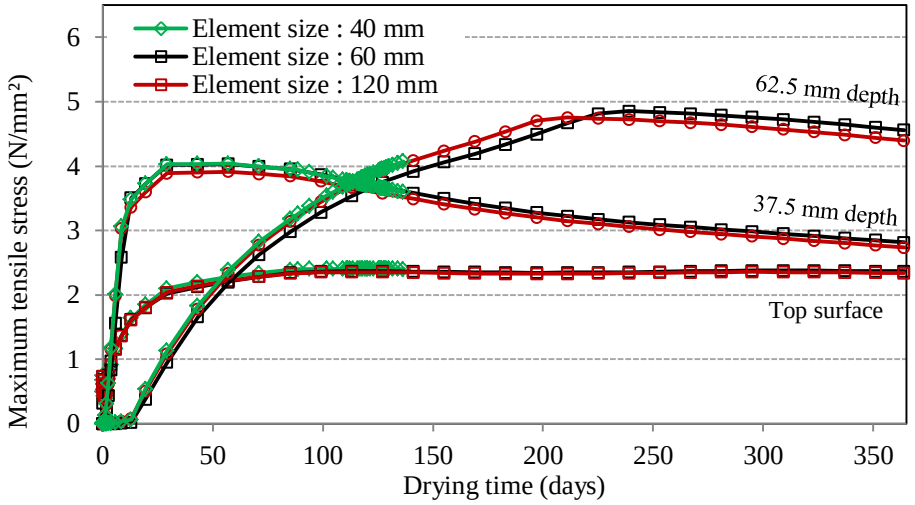

(b)

Figure 6.14 Time history of (a) maximum cracking strains; (b) maximum tensile stresses, for SFR-RCC pavement and various element sizes

As seen in Figure 6.14 the results are not mesh-sensitive for element sizes equal and smaller than Alternative 1 (120 mm horizontal size, 25 mm vertical size). Therefore, any horizontal element size equal or smaller than 120 mm can be adopted. To analyse the SFRC pavements under restrained shrinkage, the 60 mm element size is used to obtain a better contour plot

(since half of the slab is modelled due to symmetry, and the computational cost allows the use of a finer mesh). To analyse the SFRC pavements under traffic load, 120 mm element size is used to save the computational cost, since the full slab should be modelled (due to asymmetric loading).

Due to the curled shape of the slab (Figure 6.13), surface cracks are formed. In the damage plasticity model, "Inelastic Strain", IE, also called cracking strain, can be interpreted as crack width over the length. As shown in Figure 6.15 (a), a nearly uniform cracking strain has been produced in the middle part (along the length) of the slab decreasing towards the transversal free edge. The orientation of these cracking strains, which can be interpreted as the direction of crack opening, is shown in Figure 6.15 (b).

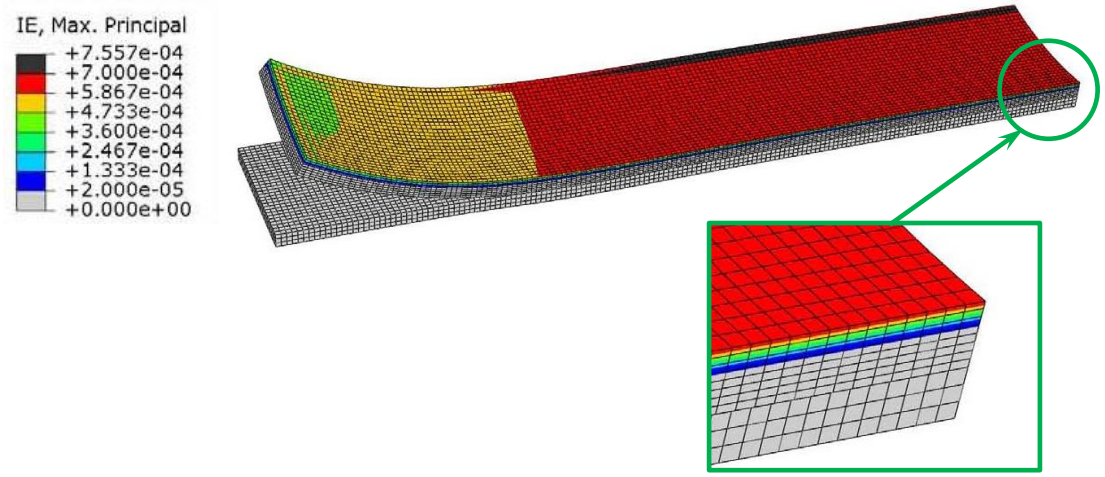

(a)

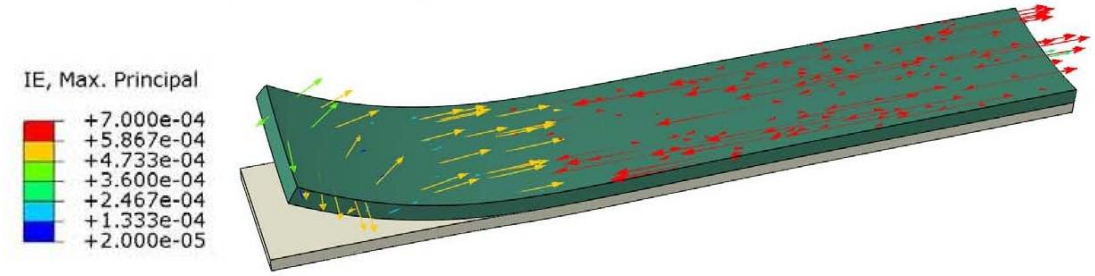

(b)

Figure 6.15 Maximum principal component of inelastic (cracking) strains, IE_{max}, for SFR-RCC pavement, under drying shrinkage; (a) strain contour; (b) strain orientations

Based on the field studies reported in the literature, shrinkage cracks are initially short and tiny micro-cracks, shallow in depth and spaced closely (CORD, 1992) (see Figure 6.16).

Although the summation of these micro-crack openings over a unit length creates a considerable cracking strain, each individual micro-crack is rarely eye visible.

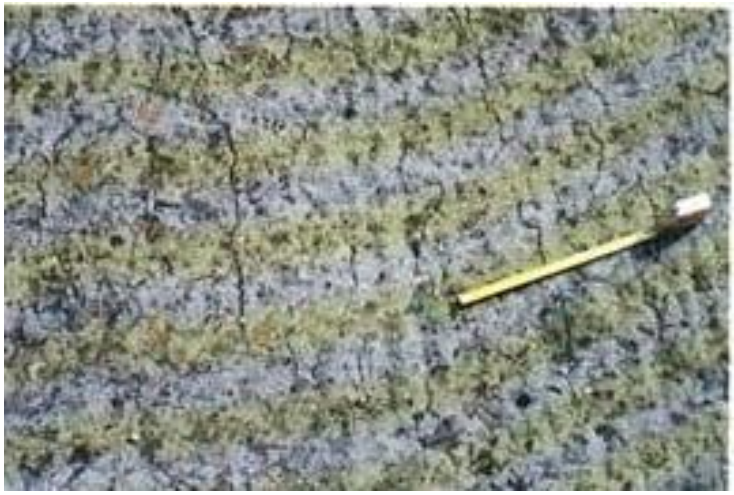

Figure 6.16 Shrinkage cracks (CORD, 1992)

From Figure 6.15 (a) and (b), it can be concluded that, the primary cracks include transversal surface cracks formed all over the slab (with lower density near the transversal edge), diagonal surface cracks near to the corner and longitudinal surface cracks near the middle of the transversal edge (Figure 6.17). Longitudinal surface cracks spread along the slab length as secondary cracks.

Figure 6.17 Cracking pattern for SFR-RCC pavement, under drying shrinkage

The shortly-spaced transversal micro-cracks of the middle part of the slab have an average opening density of 0.69 mm/m at the surface (Figure 6.18), which decreases to 0.5 mm/m at a depth of 25 mm and 0.19 mm/m at a depth of 50mm from the surface. These cracking strains diminish gradually at bigger depths. The secondary longitudinal micro-cracks also have an average opening density of 0.5 mm/m at the surface.

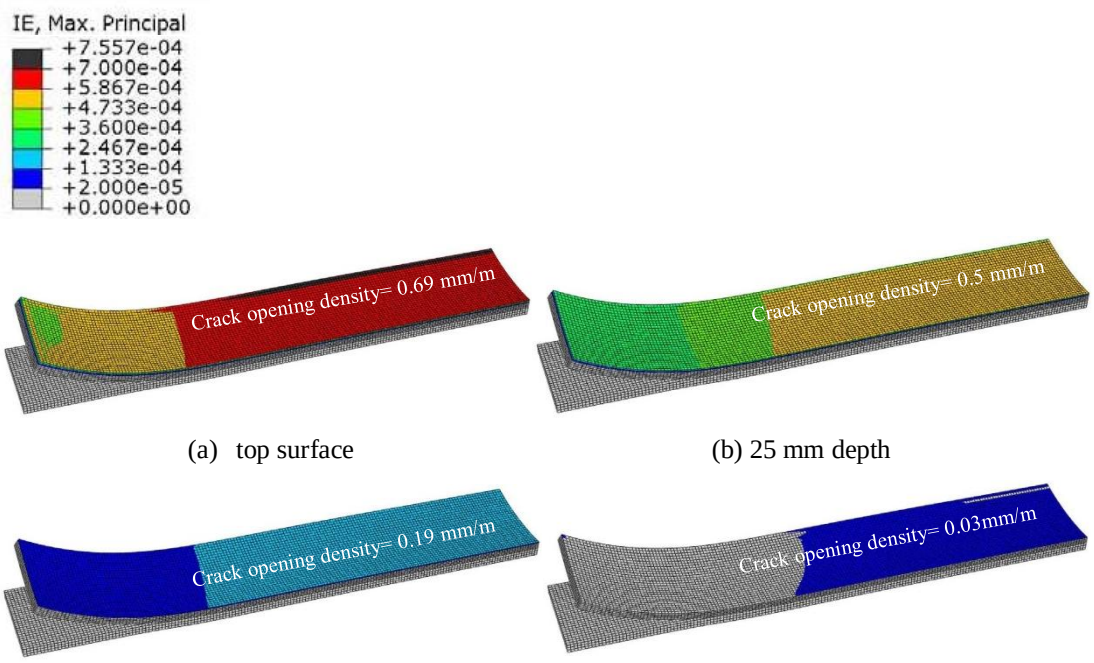

(a) top surface (b) 25 mm depth

(c) 50 mm depth (d) 75 mm depth

Figure 6.18 Cracking strains contour in depth, SFR-RCC pavement, under drying shrinkage

The time history of the maximum cracking strain at the top surface of the slab and two other depths from the top surface is shown in Figure 6.19.

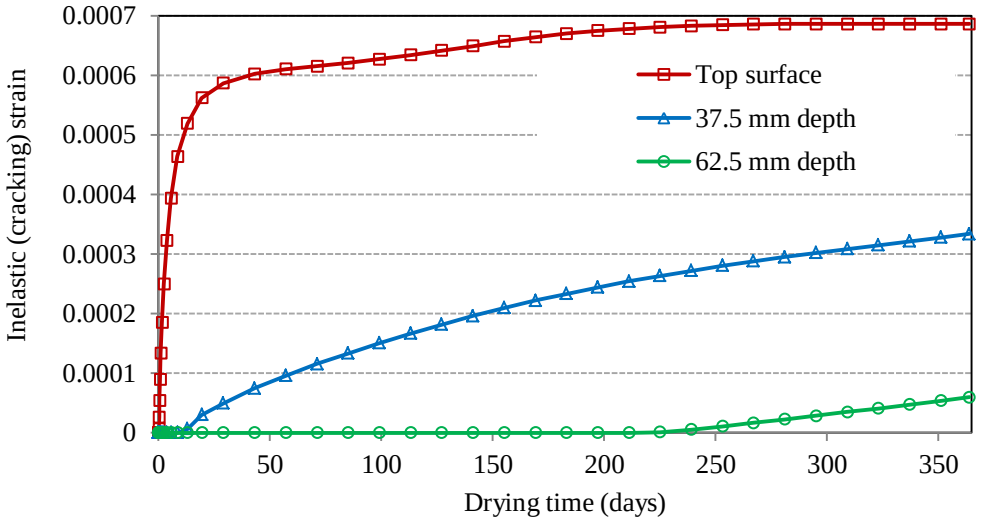

Figure 6.19 Time history of maximum cracking strain at various depths

This figure shows that cracking, at the top surface, initiates from the beginning of drying, while at a depth of 37.5 mm, crack initiation occurs after 7 days of drying. The crack

penetration reaches a depth of 62.5 mm after 225 days of drying. From the time history of cracking strains, it is also observed that the cracking strain at the top surface approaches a constant value after 180 days of drying. This means that the shrinkage cracks at the surface stabilise after that time period.

Figure 6.20 shows the time history of the maximum tensile stress relevant to the curves shown in Figure 6.19.

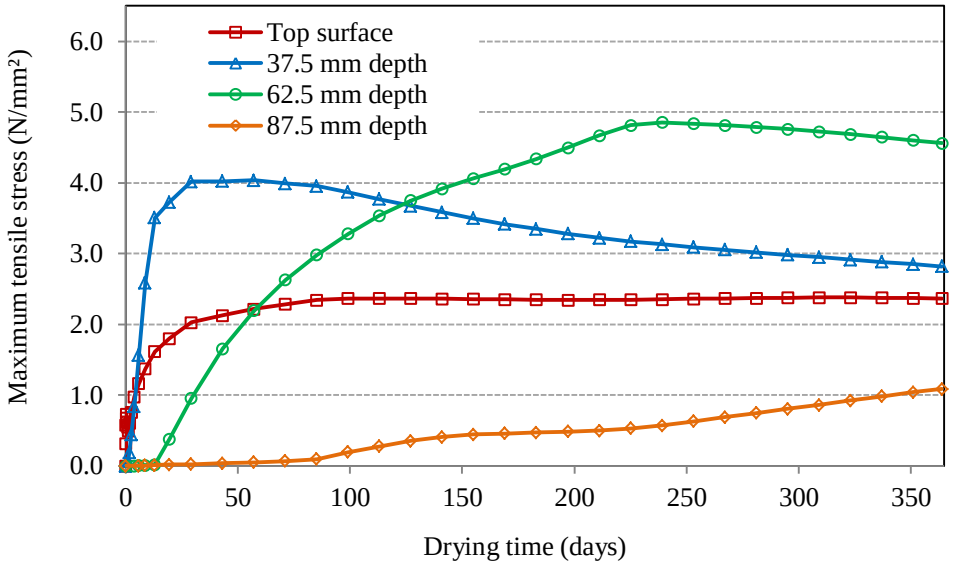

Figure 6.20 Time history of maximum tensile stress at various depths

Although the maximum crack opening occurs at the top surface, it doesn't mean that the maximum tensile stress is developed at that location. As shown in Figure 6.20, the maximum tensile stress at the top surface is significantly lower than at a depth of 37.5 mm. That is because shrinkage cracking at the top surface occurs at a very early age, when the strength of concrete is still low. Therefore, a low maximum tensile stress can be resisted by the concrete and then the concrete cracks. At the depth of 37.5 mm, shrinkage cracking occurs after 7days when the strength of concrete is much higher. Therefore, a higher tensile stress induced by shrinkage is resisted by the concrete slab at that depth. The maximum tensile strength is developed at the depth of 62.5 mm, since the drying front reaches to that depth when the concrete is completely matured. After cracking, SFRC shows a softening behaviour in tension and the strength drops. At the bottom of the slab compressive stresses are developed initially to balance the stress profile through the section.

In Figure 6.21, the magnitude of cracking strain is compared to the elastic strain. This comparison is beneficial to estimate the order of neglected intrinsic creep (see Section 6.1.4). Elastic strain at the end of the time period is around 14% of the total strain. Therefore, assuming a 50% creep/shrinkage ratio (Section 6.1.4), the neglected component of creep does not affect the strain results by more than 7%.

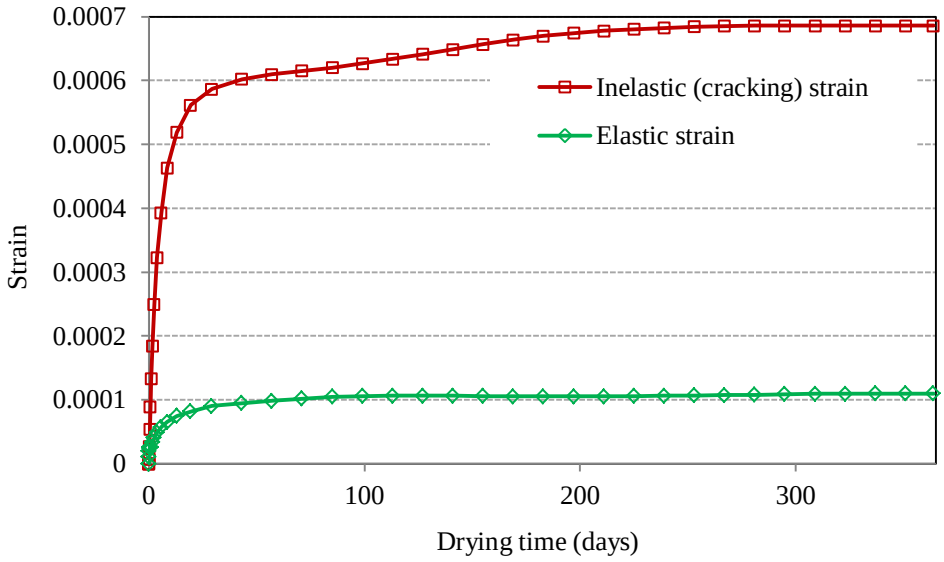

Figure 6.21 Comparison between the magnitude of the elastic and inelastic strains

As it is generally expected (Bisschop, 2002), concrete shrinks as soon as water is lost to the environment. Bazant et al. (1982, 1979) studied crack evolution in terms of spacing, penetration and width of cracks due to development of non-uniform shrinkage (or moisture gradient) in a homogenous concrete domain. A system of parallel cracks was predicted based on that study with initial spacing, S_0, width w and length a_1 (Figure 6.22(a)). With further penetration of the drying front, secondary and tertiary cracks are formed with spacings of $2S_0$ and $4S_0$, respectively, and some of the initially formed cracks are closed (Figure 6.22(b) and 6.22(c)). In that study, for cement paste material, a lower bound of 3mm spacing and 4µm width were calculated for $a_1 \geq 10$ mm. Formation of primary, secondary and tertiary microcracks, due to differential shrinkage, was confirmed later in a numerical study performed by Granger (1997) (cited in Bisschop, 2002).

For the crack spacing and width calculated by Bazant et al. (1979) for cement paste, a primary drying shrinkage strain density of 1.3 mm/m can be estimated.

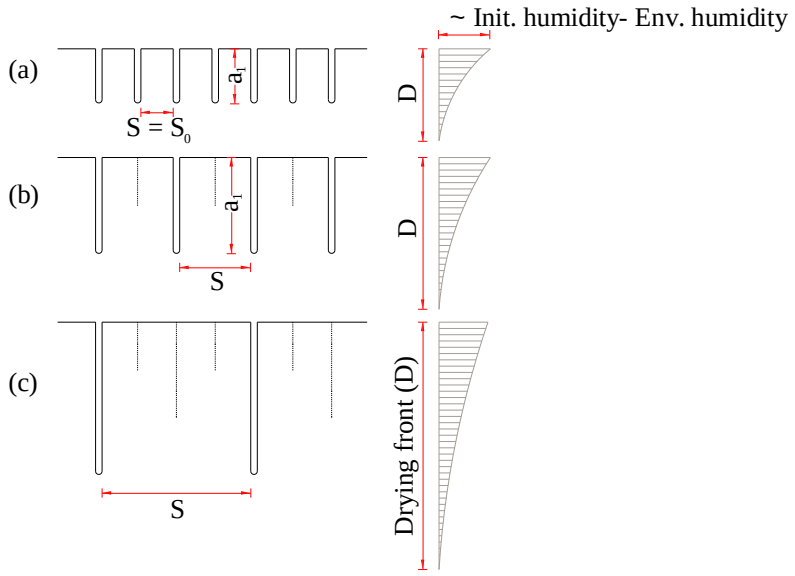

Figure 6.22 Crack development due to drying shrinkage; (a) primary cracks; (b) secondary cracks; (c) tertiary cracks

In comparison with the above mentioned estimation (Bazant et al., 1979), in the current study a maximum shrinkage strain density of 0.69 mm/m has been obtained for SFR-RCC, with a propagation depth equal to around 65 mm. Based on these values and assuming a minimum primary micro-crack spacing in the order of the maximum aggregate size (say 14 mm) for SFR-RCC pavements, and considering the secondary and tertiary state of micro-cracking (Figure 6.22), the spacing can be estimated in the range of 14 mm-56 mm, with an opening in the range of 0.01 mm-0.04 mm at the stabilised state of drying.

6.3.2.2 SFR-RCC mix, Condition 2: full bond between slab and base

The deformed shape of a continuous SFR-RCC pavement under this condition is shown in Figure 6.23. Contact opening does not occur under the slab.

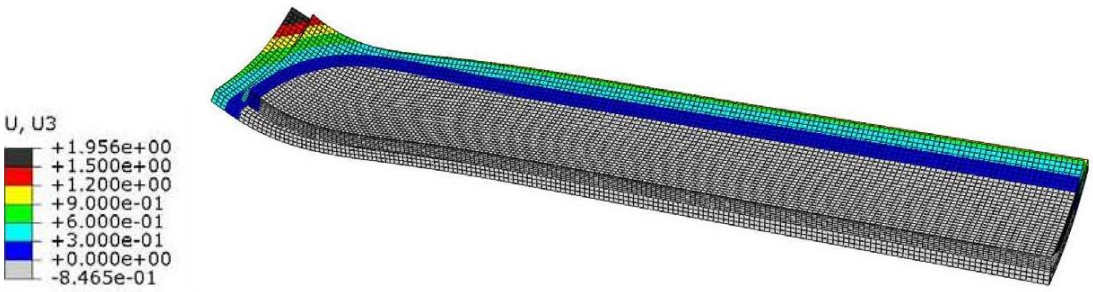

Figure 6.23 Deformed shape of fully bonded SFR-RCC pavement, due to drying shrinkage

Surface cracks are formed for the fully bonded slab in the same manner as for the unbonded slab. As shown in Figure 6.24 (a), a uniform cracking strain has been produced in the interior part of the slab. The orientation of these cracking strains is shown in Figure 6.24 (b).

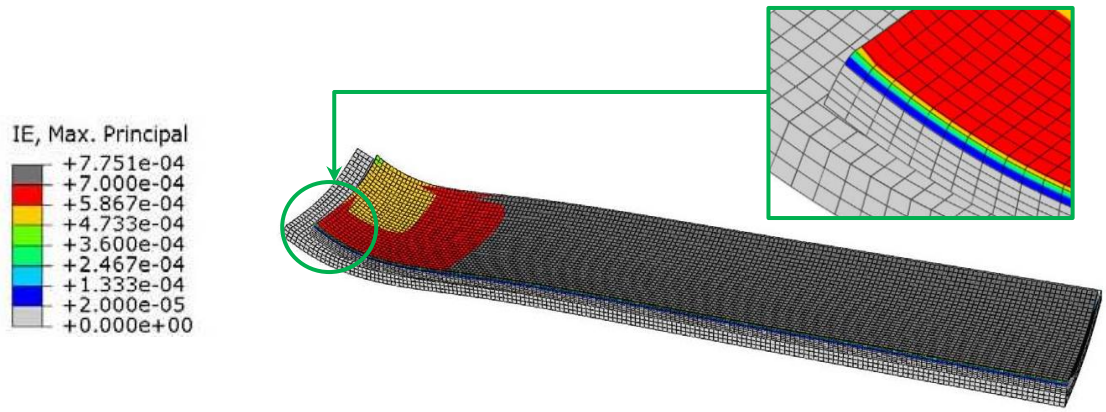

(a)

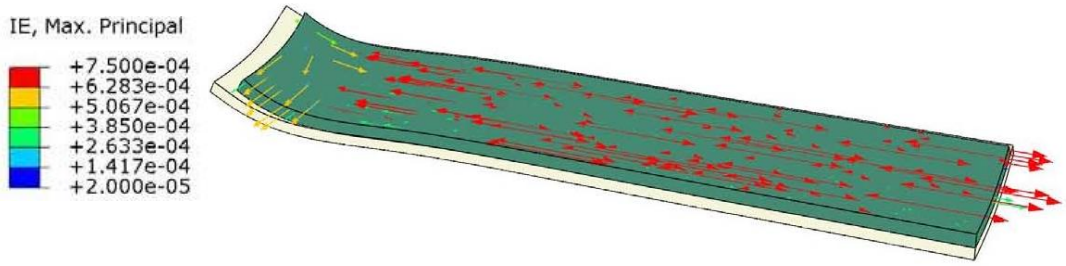

(b)

Figure 6.24 Maximum principal inelastic (cracking) strains, IE_{max}, for fully bonded SFR-RCC pavement, under drying shrinkage; (a) strain contour; (b) strain orientations

Figure 6.24(a) shows that, for a fully bonded slab, surface micro-cracks are distributed more uniformly compared to the unbonded slab, with an average opening density of 0.73 mm/m (slightly bigger than for the unbonded slab). The strain corresponding to the secondary longitudinal micro-cracks has also increased by around 22% (0.61 mm/m) compared to the unbonded slab.

Since continuity by itself acts as a type of external restraint, which prevents the slab from free movement, bonding to the base does not make a big difference in cracking induced by this load case (shrinkage only). The condition of a slab fully bonded to the foundation is an extreme condition, and its worse effect, before applying the traffic load, is not significant. Therefore, only condition 1 (unbonded slab) is considered for the remaining analyses.

6.3.2.3 SFR-CC mix

The time history of cracking strains for SFR-CC mix is compared with SFR-RCC mix in Figure 6.25.

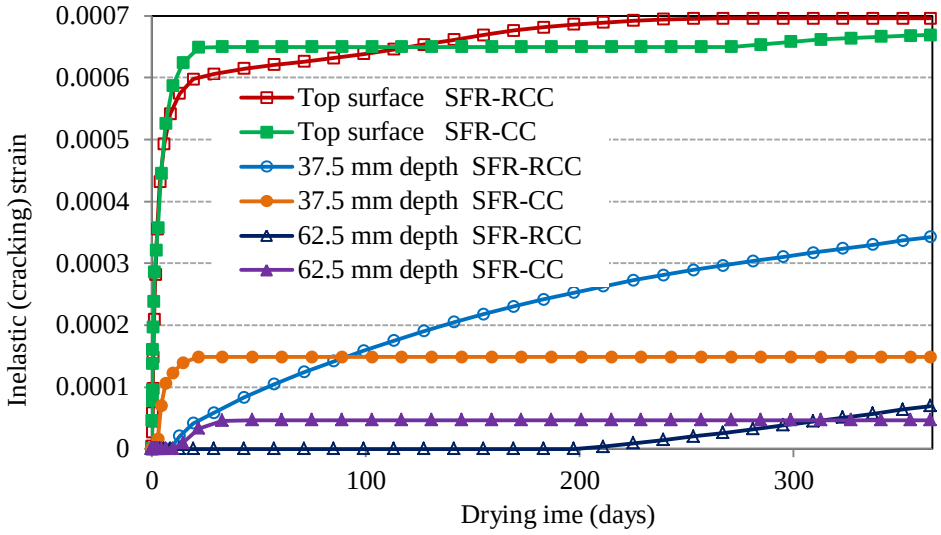

Figure 6.25 Maximum inelastic (cracking) strains, IE, for SFR-RCC compared with SFR-CC

The comparison shows that shrinkage cracking in SFR-RCC is less than for SFR-CC at early days, but it gets worse after a couple of months. The stabilised amount of cracking strain for SFR-RCC is bigger than that of SFR-CC. Therefore, the rest of the study will be continued with SFR-RCC, as the more critical mix.

6.3.3 Comparing the FE results with the evaluations given in the Concrete Society TR34

The residual tensile strength of the SFR-RCC slab after the effect of drying shrinkage has been normalised by dividing the curves to the cracking strength of SFR-RCC (Figure 6.26).

As this figure shows, the tensile strength at the top surface after stabilising reaches around 50% of the maximum tensile strength capacity of concrete. This value is 60% at the depth of 0.2h from the drying surface and 95% at the depth of 0.3h. These values are compared with the estimation given in Concrete Society TR34 (2003), in the following.

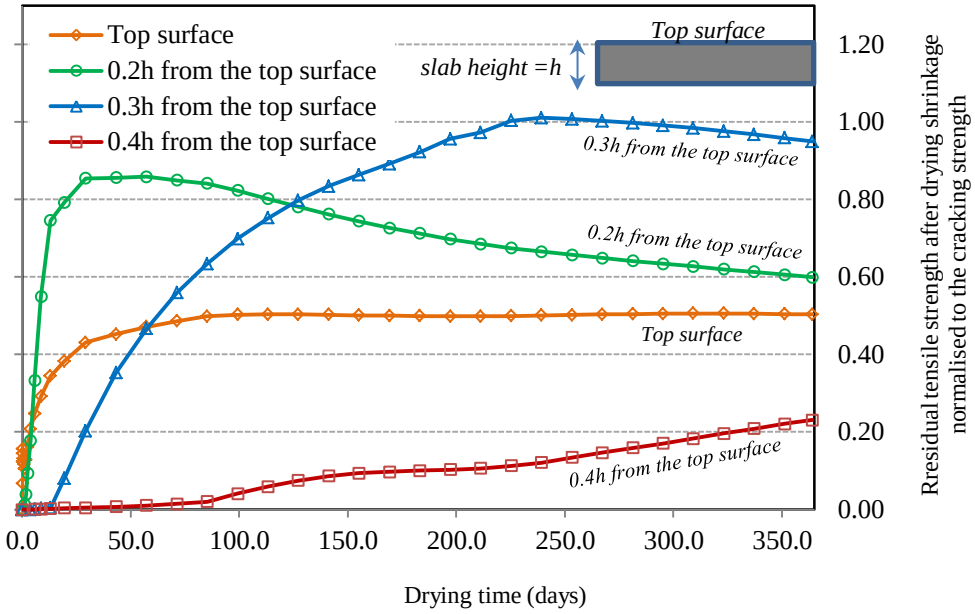

Figure 6.26 Residual tensile strength of the SFR-RCC slab after the effect of drying shrinkage, normalised to the cracking strength

In Concrete Society TR34 (2003) three sources for inherent movement are defined for concrete slabs, consisting: plastic shrinkage, thermal movements, and long-term drying shrinkage. It has been mentioned that long-term moisture loss from hardened concrete may last many years, depending on the environment and the properties of the concrete. TR34 implies that, although the interaction between the shrinkage stresses and loading is not well understood, shrinkage-induced stresses should be considered in design, particularly when considerable negative moments occur due to imposed loads.

Two simple calculations have been proposed to evaluate shrinkage stresses in concrete ground-slabs induced by external restraints and internal restraints (curling):

- Stress induced by external restraints

For a fully restrained slab, the shrinkage stress has been expressed by the following equation:

$$f_{sh,full} = E_{cm}\varepsilon_{sh} \qquad \text{(Eq. 6.5)}$$

Where, $f_{sh,full}$ is the shrinkage stress for a fully restrained slab, ε_{sh} is the long-term free shrinkage strain, and E_{cm} is secant modulus of elasticity of the concrete.

To consider the effect of creep, the elastic modulus is then reduced to $E_{cm}/3$. However, the fully restrained condition does not usually occur in practice, through provision of some means of restraint reducers such as slip membranes. TR34 recommends the use of a restraint factor of 0.2 (where full restraint is taken as 1.0). Therefore, the estimated stress in the slab induced by external restraints to shrinkage is given by Eq. 6.6.

$$f_{sh} = 0.2 \left(\frac{E_{cm}}{3}\right) \varepsilon_{sh} \qquad \text{(Eq. 6.6)}$$

The free shrinkage strain, ε_{sh}, is then taken as 400-600 micro-strain, and for an elastic modulus of 41 GPa the shrinkage stress induced by external restraint is estimated in the range of 1.1-1.6 N/mm^2.

- Stress induced by internal restraint

To estimate the stress induced by differential shrinkage (or curling) the following equation is applied (although it is mentioned that quantifying curling-induced stresses has not been performed in current UK practice).

$$f_{cur} = \left(\frac{1}{2}\right) \left(\frac{E_{cm}}{3}\right)\left(\frac{\Delta\varepsilon}{1-\nu}\right) \qquad \text{(Eq. 6.7)}$$

Where, f_{cur} is the curling-induced stress, $\Delta\varepsilon$ is differential strain between top and bottom of the slab (considering a typical value of 1.5-2.0 × 10^{-6} per mm of the slab thickness), and ν is the Poisson's ratio.

Therefore, for an elastic modulus of 41 GPa and a slab thickness of 200 mm, the curling stress is estimated in the range of 2.5-3.3 N/mm^2.

This guideline apparently takes the average value of the above calculated stresses as a flexural tensile stress which should be deducted from the flexural tensile strength of concrete when calculating the negative moment capacity of the pavement in critical areas. In the case of a concrete pavement with a thickness of 200 mm and an elastic modulus of 41 GPa, the reduction in the flexural strength of concrete (in calculation of the negative moment capacity) would be in the range of 1.8-2.5 N/mm^2.

Since no cracking is permitted at the top surface, in the Concrete Society method, the calculation of the negative moment capacity is based on the uncracked cross section ($M_n =$

$f_{ct,fl}(h^2/6)$, where $f_{ct,fl}$ is the tensile flexural strength of concrete.

Assuming the range of values calculated based on Concrete Society TR34 for flexural strength reduction due to drying shrinkage (1.8-2.5 N/mm^2), and adopting this values to the SFR-RCC pavement examined in this research ($f_{ct,fl} = 7.1 \frac{N}{mm^2}$), the tensile flexural strength must be reduced by 25-35% (average 30%) to take into account the effect of drying shrinkage. It means that the stress block considered in the calculation of negative moment should be changed as shown in Figure 6.27(b), while based on FE analysis in this study the reduction in the strength due to drying shrinkage is 50% at the top surface Figure 6.27(c).

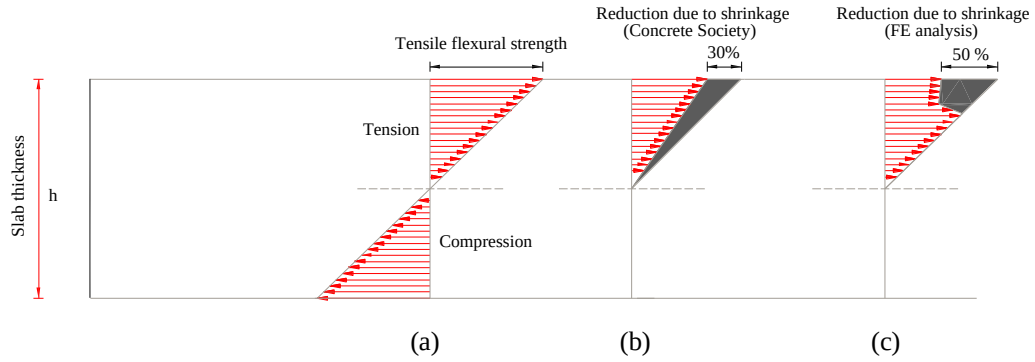

Figure 6.27 Stress block in calculation of negative moment capacity based on TR34 (a) without shrinkage; (b) reducing shrinkage stress based on TR34; (c) reducing shrinkage stress based on FE analysis

TR34 takes the average value of stress induced by the effect of internal and external restraints. However, the current study shows that the stress induced by the effect of internal restraint (or curling) is dominant, since the differential shrinkage creates an upward-curled shape slab, in which no external restraint is applied for a large part of the contact area, due to separation. If the stress induced by the effect of curling (as the dominant mechanism) is replaced by the average value, in the calculation based on TR34, the reduction in the tensile flexural strength would be in the range of 35-46% (average 40.5%). Additionally the effect of elastic creep has been ignored in the FE analysis in the current research (estimated as 7%) (see Section 6.1.4 and 6.3.2.1). Therefore, the difference between TR34 and FE in the reduction due to shrinkage can mainly be attributed to these issues.

6.3.4 Shrinkage of hardened SFR-RCC pavement

In this section, the shrinkage behaviour of a hardened SFR-RCC pavement is compared with an immature one, to evaluate the effect of any delay in drying of the concrete slab by extended curing.

TR34 reports that curing does not reduce shrinkage, although it improves the durability of concrete. A concrete slab will eventually dry and shrink by a specific amount which is nearly independent of when drying begins. Curing is not an efficient way to minimise the drying shrinkage of concrete, but the key is to design the concrete mix such that it requires the lowest possible water content (e.g. by using the minimum volume of cement paste, and largest practical aggregate size, or using water reducing admixtures) (Concrete Society TR34, 2003).

The beneficial effect of curing is increasing the tensile strain capacity of concrete during its drying period which can reduce the risk of cracking, if the order of shrinkage strains is lower than the capacity of the hardened concrete.

Since in this study it has been assumed that the "hygral contraction coefficient" is not affected by the maturity of concrete (Section 6.1.5), the state of shrinkage strains are the same for hardened and immature concrete. The only difference occurs in the state of short-term stress development (Figuren6.28).

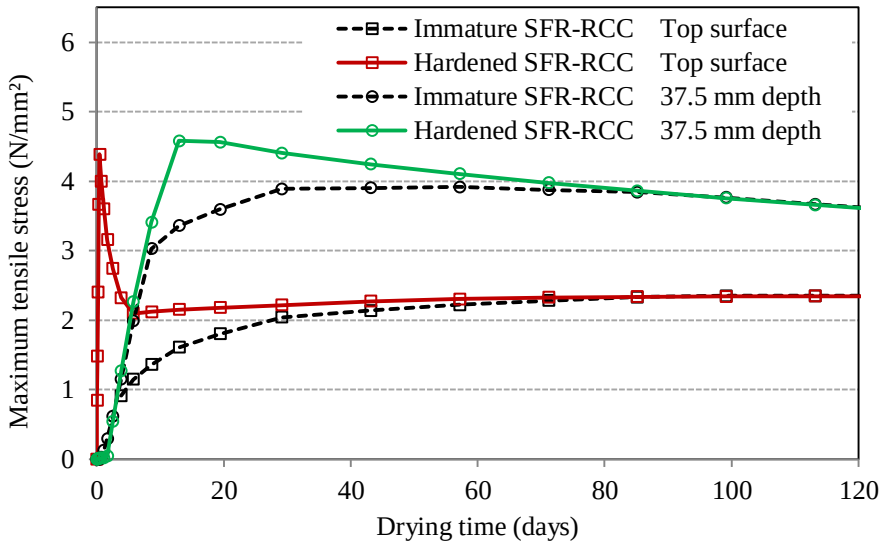

Figure 6.28 Time history of stress development in the case of a hardened SFR-RCC slab, in comparison with an immature slab

As seen in Figure 6.28, in the case of hardened concrete a high peak tensile stress is developed at the surface, before reaching the ultimate state of shrinkage stress. Since the shrinkage strains, developed in the surface of the SFR-RCC slab, are higher than the ones needed to reach the tensile strength of concrete, cracking occurs in both cases. In the short-term, the residual tensile strength of the hardened slab is higher than the immature slab, while it doesn't make any difference in the long-term when drying is continued.

6.4 Stress analysis of SFRC pavements under monotonic loading

Two conditions are analysed for this load case:

1) Distress induced by shrinkage is ignored and the pavement is analysed under monotonic wheel load and the self-weight of the slab. The load is applied in four different positions along the slab (Figure 6.29). The wheel load is increased gradually to exceed the standard axle load and subsequently continued up to failure at the ultimate limit state. Since no prescriptive mode of failure has been defined for concrete pavements (Section 6.1.6), the load carrying capacity has been evaluated for various failure modes corresponding to various levels of damage.

2) In addition to the self-weight, the effect of drying shrinkage is considered in the first year after construction and then the traffic load is applied and increased up to failure.

It is considered that the contact surface of the concrete slab to the foundation is cohesion free, and the concrete matures during the first 90 days. The analyses are performed for the SFR-RCC mix (as the critical mix), and the mean values obtained from the experiments are used for the material properties.

6.4.1 Monotonic loading only

Four load configurations are considered as shown in Figure 6.29. For corner loading, one end of the standard axle is located on the corner of the slab. For longitudinal edge loading, one end of the standard axle is located on the longitudinal edge far away from the corner. For interior loading the standard axle is located symmetrically at the middle of the slab far away

from the transversal edges. For transversal edge loading, the standard axle is located symmetrically at the transversal edge of the slab.

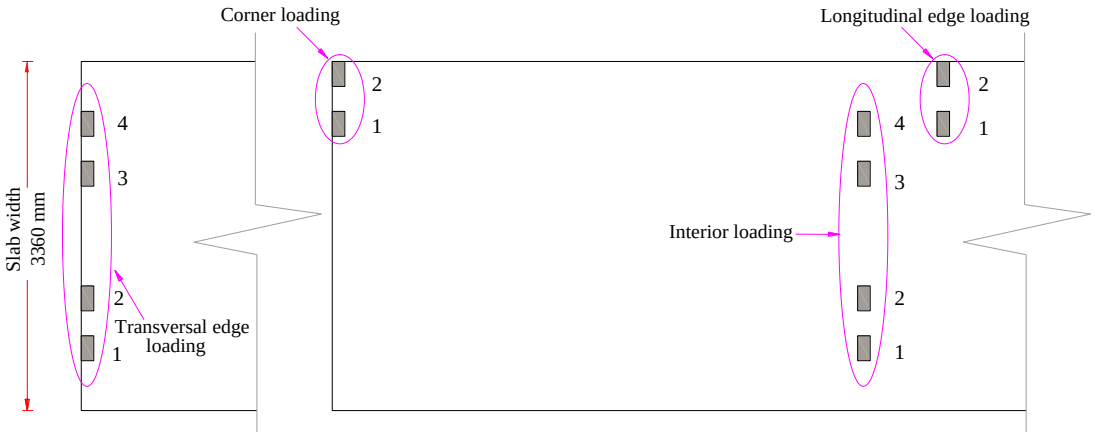

Figure 6.29 Configurations assumed for corner, edge and interior loading

Although the given slab has been designed for the equivalent standard axle load (ESAL) with a given number of repetitions (Section 6.1.2.1), the monotonic load in the analysis is increased further to investigate the ultimate state behaviour of the pavement. Since the investigations are performed in a comparative way, safety factors are not applied.

Since the repetition of the load is ignored in the case of monotonic loading, the predicted load bearing capacity of the pavement under different configurations is expected to be much higher than the standard axle load (SAL).

6.4.1.1 Corner loading

In this condition, under the corner load, the slab behaves elastically (without cracking) until the axle load reaches 4.2SAL (Figure 6.30), then cracking at the bottom surface initiates under tyre 1. Corner cracking at the top surface initiates due to negative moment, when the axle load reaches 5SAL (Figure 6.30). The corner break penetrates to half of the slab depth when the axle load reaches 8SAL. Figure 6.31 shows the development of cracking strains when the corner break penetrates to half of the slab depth at 8SAL (Only half of this load has been applied to the slab corner, since the other half is in the next segment).

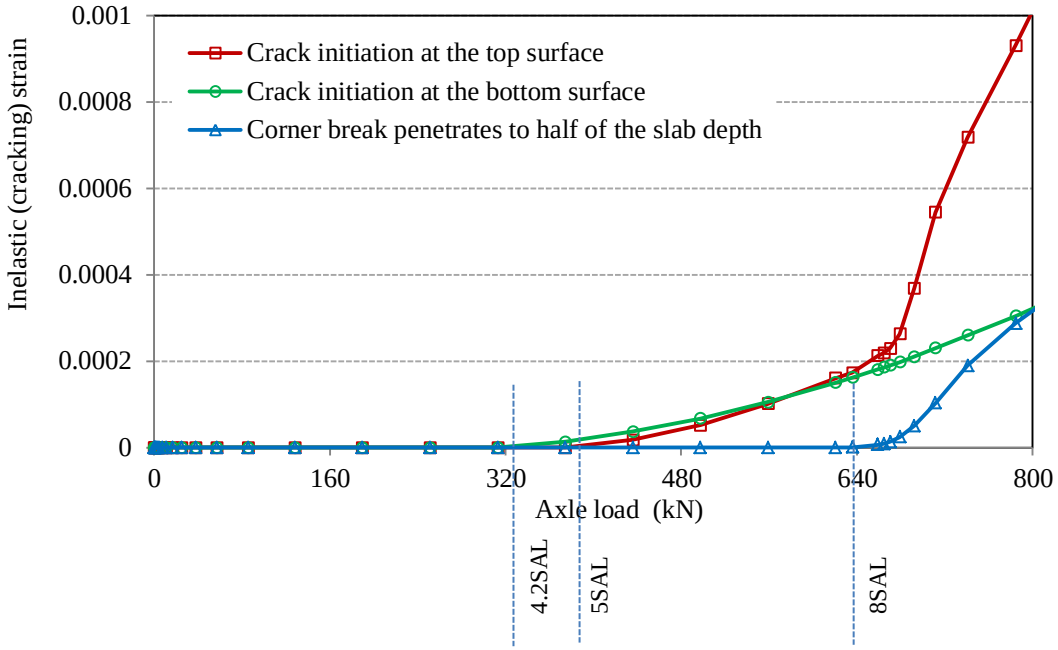

Figure 6.30 Cracking strain versus the axle load (Corner load only)

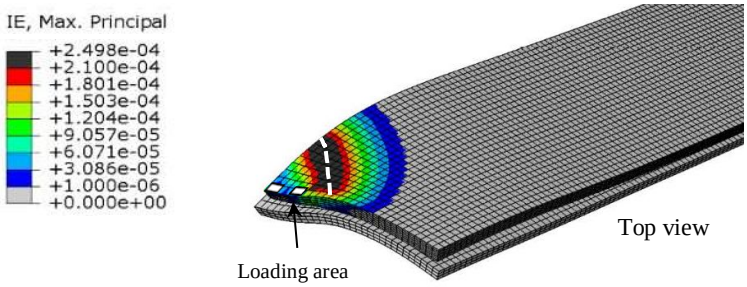

Figure 6.31 Maximum cracking strain under a total axle load = 8SAL (Corner load only; one end of the axle located at the corner)

Figure 6.32 shows the profile of the maximum cracking strain at the top surface versus the diagonal distance from the corner, "*w*", for various axle loads. Assuming that the localisation of crack opening occurs at a location which has the maximum cracking strain, the area under the curves represents the equivalent crack opening.

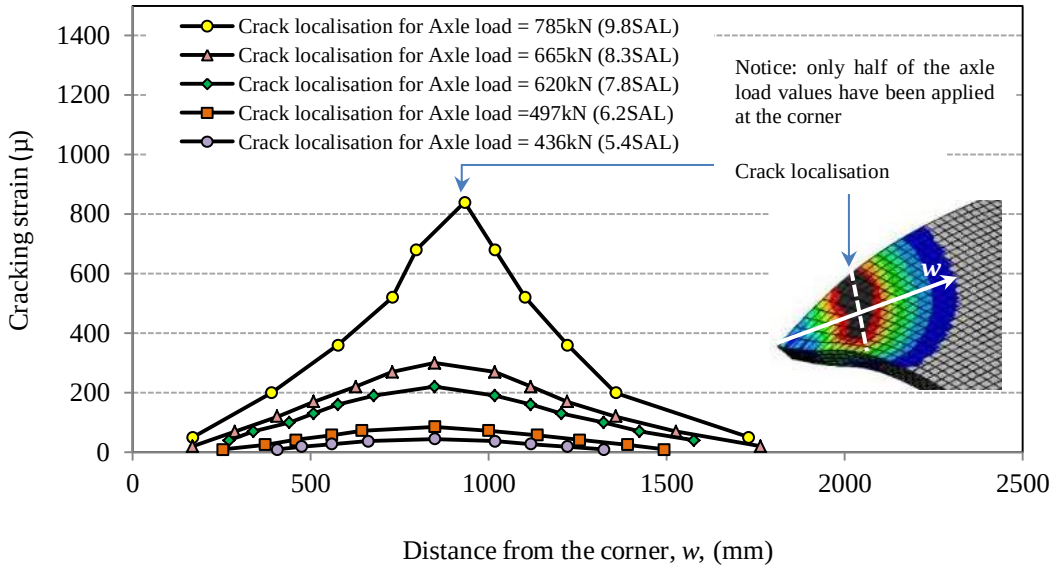

Figure 6.32 Maximum cracking strain at the top surface versus the distance from the corner, (Corner load only)

Figure 6.33 shows the variation of the equivalent crack opening versus the axle load.

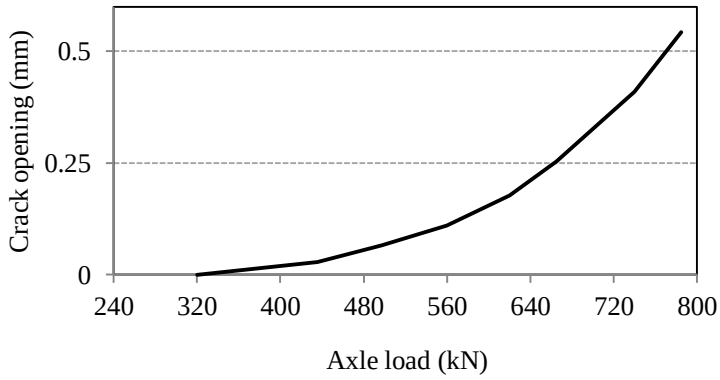

Figure 6.33 Variation of the equivalent crack opening versus the load (Corner load only)

The equivalent opening of the corner crack exceeds 0.5 mm when the axle load exceeds 9.5SAL. It should be noted that the effect of shrinkage and fatigue has not been included yet. Comparison with the case of considering shrinkage will be done in Section 6.4.2.1.

6.4.1.2 Longitudinal edge loading

Under the longitudinal edge load, the slab behaves elastically (without cracking) until the axle load reaches 3.5SAL (Figure 6.34), when cracking at the bottom surface initiates under the load. This bottom crack penetrates to half of the slab depth when the axle load exceeds

6.6SAL. Cracking at the top surface initiates (due to negative moment) when the axle load reaches 8SAL (Figure 6.34).

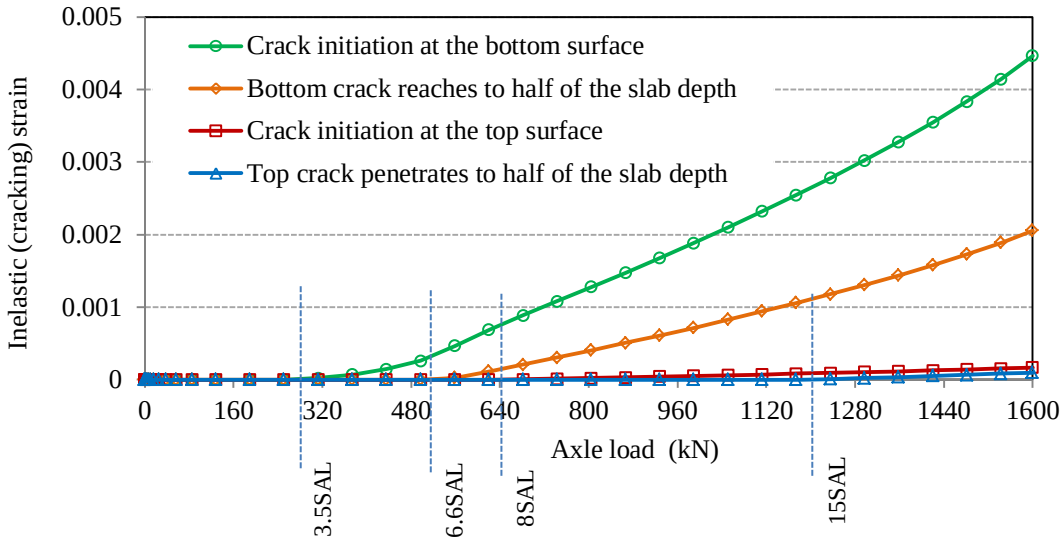

Figure 6.34 Cracking strain versus the axle load (Longitudinal edge load only)

Cracking at the top surface develops in a semi-circular shape until it reaches the edges (Figure 6.35). The top surface cracking penetrates to half of the slab depth when the axle load reaches 15SAL. Figure 6.35 shows the development of cracking strains when the top surface cracking penetrates to half of the slab depth.

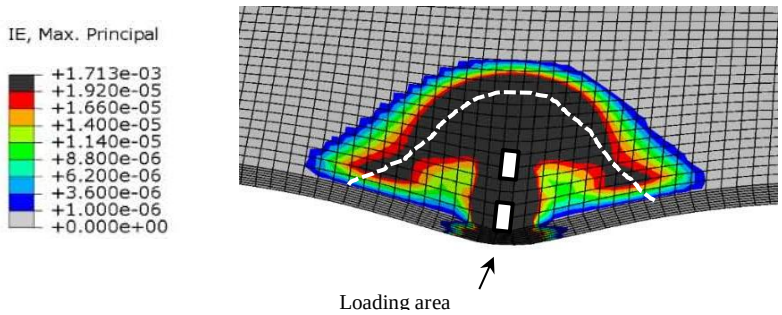

Figure 6.35 Maximum cracking strain under a total axle load =15SAL (Longitudinal edge load only; one end of the axle located at the edge)

Figure 6.36 shows the profile of the maximum cracking strain at the top surface versus the diagonal distance from the longitudinal edge, "*w*".

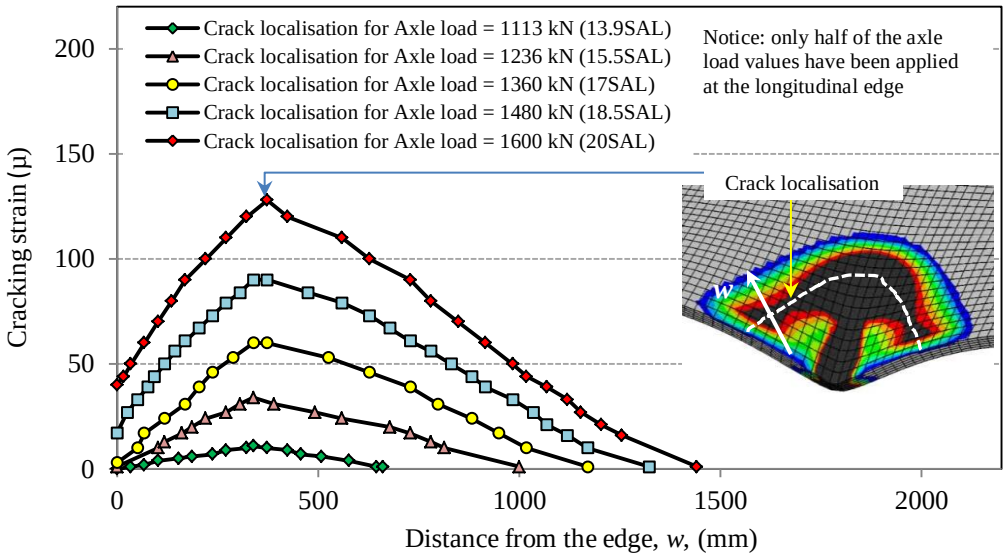

Figure 6.36 Maximum cracking strain at the top surface versus the distance from the edge, (Longitudinal edge load only)

Figure 6.37 shows the variation of the equivalent crack opening versus the axle load, based on the definition given in Section 6.4.1.1.

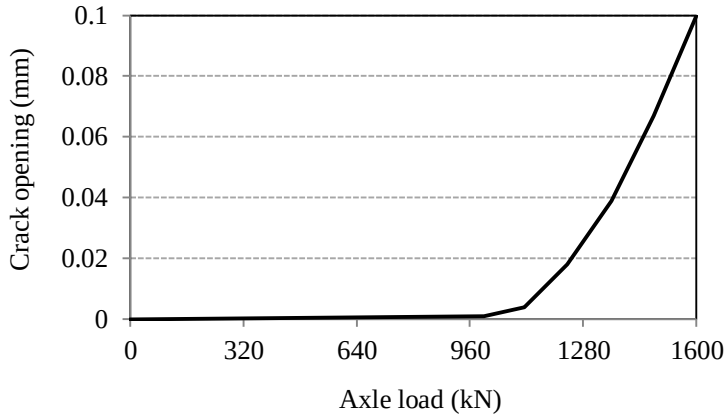

Figure 6.37 Variation of the equivalent crack opening versus the axle load (Longitudinal edge load only)

Since bottom cracking is dominant in this load configuration, no significant crack opening occurs at the top surface. The effect of shrinkage and fatigue is not included yet. Comparison with the case of considering shrinkage will be done in Section 6.4.2.2.

6.4.1.3 Transversal edge loading

Under the transversal edge load, the slab behaves elastically (without cracking) until the axle load reaches 5.8SAL (Figure 6.38), when cracking at the bottom surface initiates under the load. This bottom crack penetrates to half of the slab depth when the axle load exceeds 10.4SAL. Cracking at the top surface initiates (due to negative moment) when the axle load reaches 7.3SAL (Figure 6.38). Cracking at the top surface extends horizontally to reach the edges (Figure 6.39). The top surface cracking penetrates to half of the slab depth when the axle load reaches 12SAL. Figure 6.39 shows the development of cracking strains when the top surface cracking nearly penetrates to half of the slab depth.

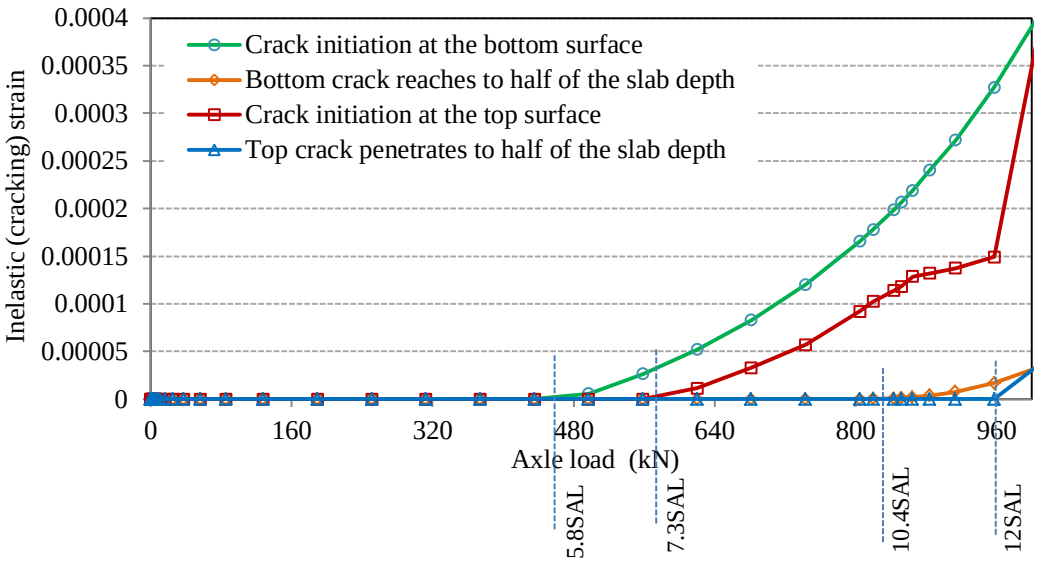

Figure 6.38 Cracking strain versus the axle load (Transversal edge load only)

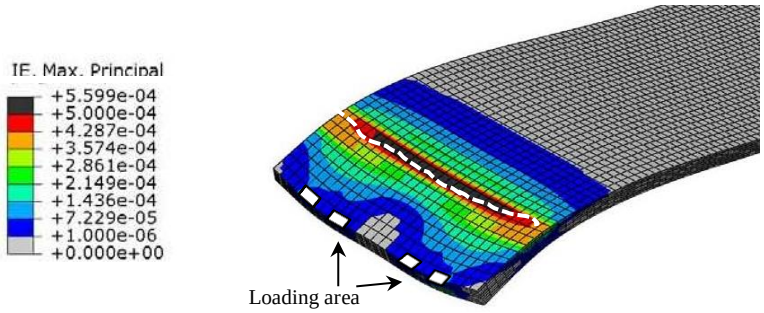

Figure 6.39 Maximum cracking strain under an axle load =12SAL (Transversal edge loading)

Figure 6.40 shows the profile of the maximum cracking strain at the top surface versus the distance, "*w*", from the edge for various axle loads.

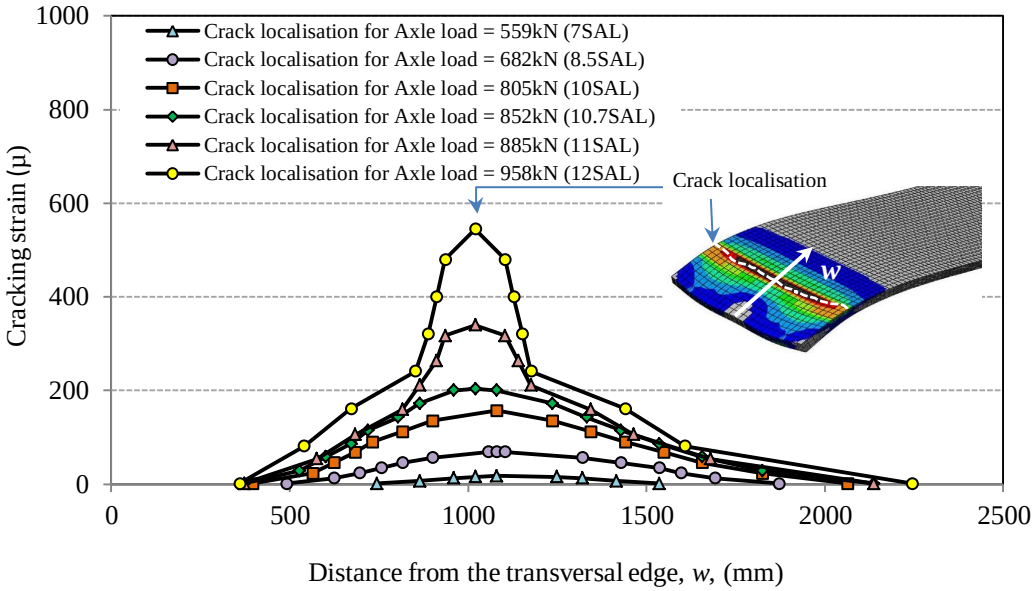

Figure 6.40 Maximum cracking strain at the top surface versus the distance from the transversal edge (Transversal edge load only)

Figure 6.41 shows the variation of the equivalent crack opening versus the load, based on the definition given in Section 6.4.1.1.

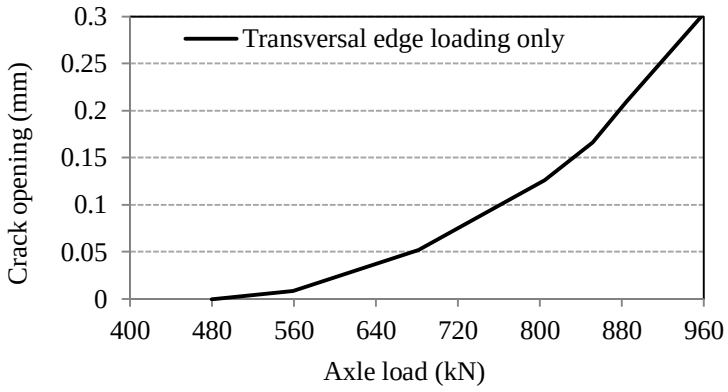

Figure 6.41 Variation of the equivalent crack opening versus the axle load (Transversal edge load only)

The effect of shrinkage and fatigue is not included yet. Comparison with the case of considering shrinkage will be done in Section 6.4.2.3.

6.4.1.4 Interior loading

Under the interior load, the slab behaves elastically (without cracking) until the axle load

reaches 5.5SAL (Figure 6.42), where cracking at the bottom surface initiates under the load. This bottom crack penetrates to half of the slab depth when the axle load exceeds 9.3SAL. Cracking at the top surface did not occur in the examined range of loading (0-20SAL).

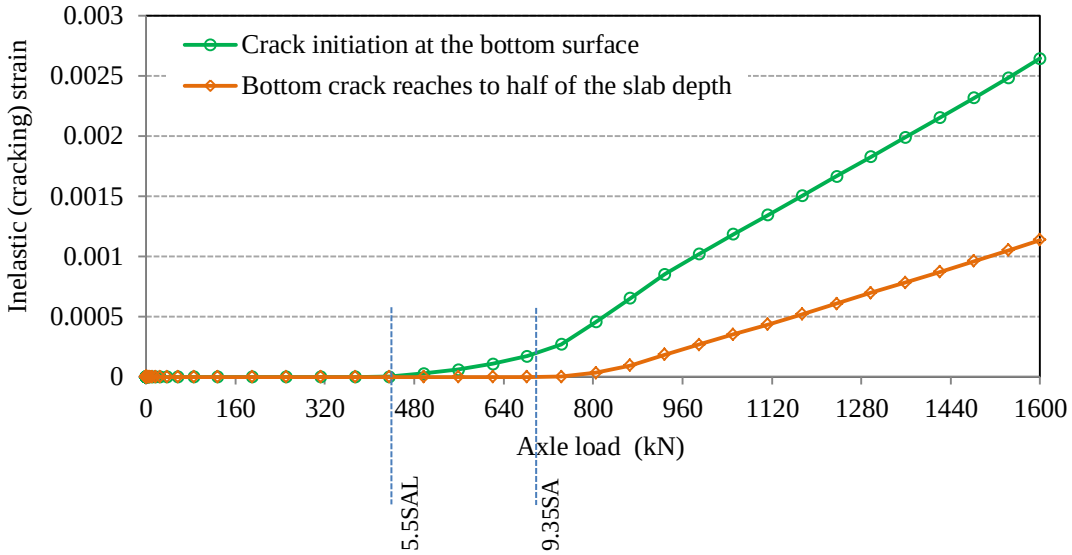

Figure 6.42 Cracking strain versus the axle load (Interior load only)

The effect of shrinkage and fatigue is not included yet. Comparison with the case of considering shrinkage will be done in Section 6.4.2.4.

6.4.2 Monotonic loading with restrained shrinkage

Under monotonic loading with restrained shrinkage, the continuous pavement initially curls upward under non-uniform drying shrinkage (Figure 6.13). Then the monotonic loading is applied according to the load configurations assumed in Section 6.4.1 (Figure 6.29). The applied load is then increased to find the maximum load that can be sustained.

6.4.2.1 Corner loading

In this condition, micro-cracks develop all over the slab surface before the traffic load is applied (Section 6.3.2). No significant increase in the cracking strains at the top surface occurs when the applied load is less than 1SAL (Figure 6.43). When the axle load exceeds the SAL, cracking strains at the top surface further develop and corner break is initiated. The corner crack penetrates to half of the slab depth when the axle load reaches 4SAL. Figure 6.44 shows the development of cracking strains when the corner break penetrates to half of the slab

depth. A bottom crack initiates under tyre 1 at 1.22SAL.

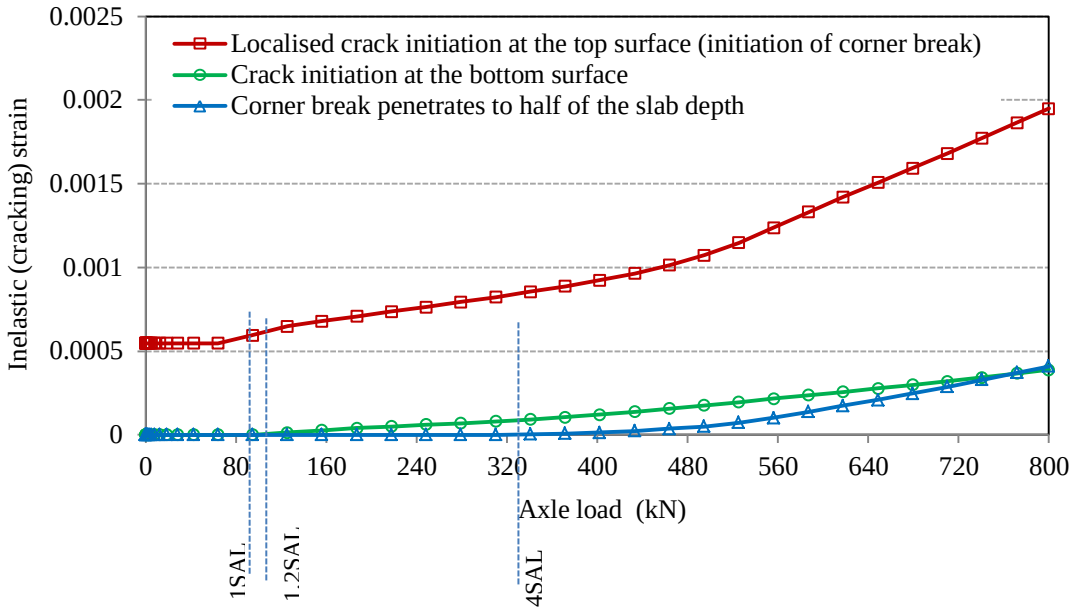

Figure 6.43 Cracking strain versus the axle load (Corner load + Drying shrinkage)

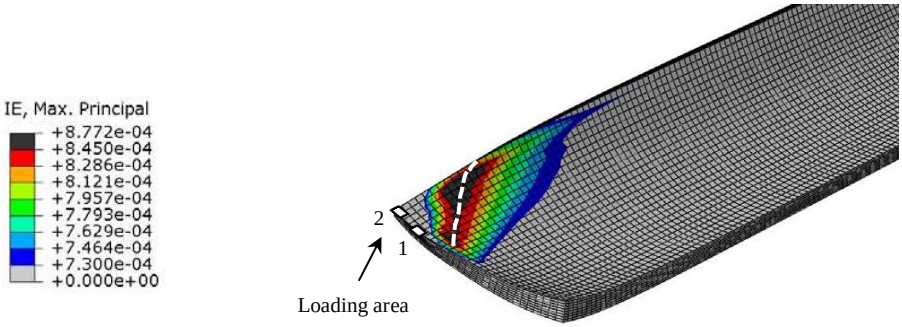

Figure 6.44 Maximum cracking strains under an axle load = 4SAL (Corner load + Drying shrinkage; one end of the axle located at the corner)

Figure 6.45 shows the profile of the maximum cracking strain at the top surface versus the distance, "*w*", from the corner for various axle loads. Assuming that the localisation of crack opening occurs at the location of the maximum cracking strain, the area under the curves represents the equivalent crack opening in excess of the initial micro-cracking. In Figure 6.45, a strain value of 450 micro-strain is developed at the corner area of the slab and at the top surface, due to drying shrinkage and prior to applying the load. This strain forms distributed micro-cracks on the surface of the slab (refer to Section 6.3.2). When the load is applied, the micro cracks initially widen and no significant localisation occurs until the load reaches 200

kN. For bigger loads, the cracking strain is localised at a specific distance from the corner and can lead to a corner break.

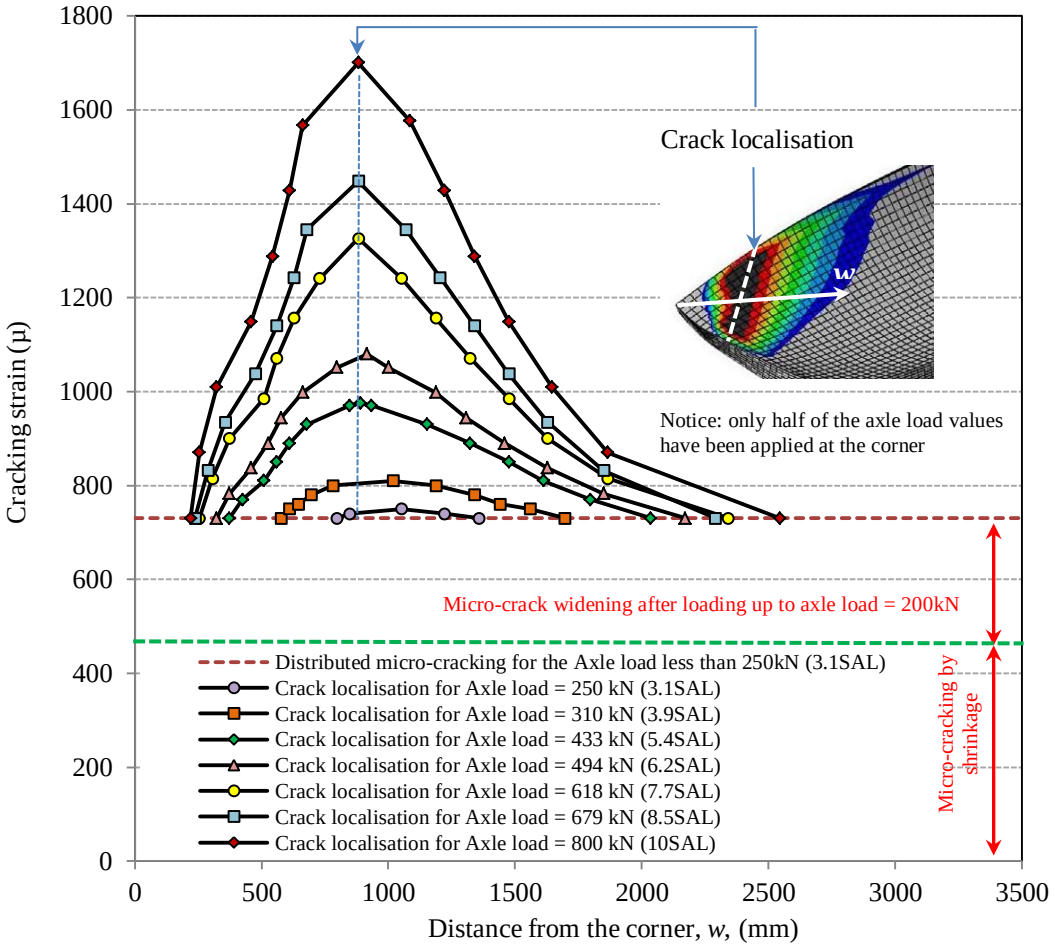

Figure 6.45 Maximum cracking strain at the top surface versus the distance from the corner (Corner load + Drying shrinkage)

Figure 6.46 shows a comparison of the equivalent crack opening versus the load, with and without shrinkage. This comparison shows that distress induced by drying shrinkage at the top surface of the slab significantly increases the crack opening developed due to loading, although the effect of shrinkage distress does not initially seem significant in terms of visible cracks. For example, the corner crack opening of 0.5 mm, which corresponds to an axle load of 765 kN in the case of corner load only, increases to 1.0 mm when considering drying shrinkage. It should be noted that the effect of fatigue is not included yet.

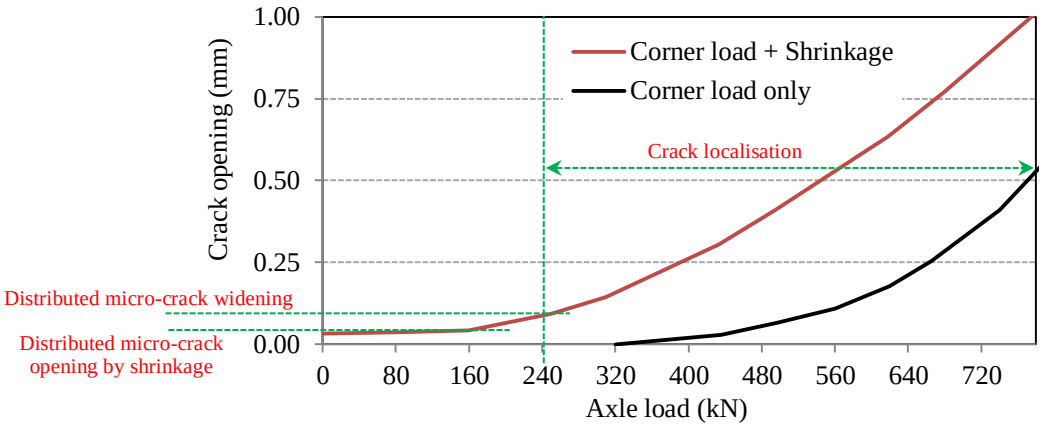

Figure 6.46 Variation of the equivalent crack opening versus the axle load (Corner load + Drying shrinkage; compared to Corner load only)

6.4.2.2 Longitudinal edge loading

On the contrary to corner loading, bottom cracking is dominant in the case of longitudinal edge loading. Bottom crack initiates when the axle load exceeds 5SAL, and it penetrates to half of the slab depth when the axle load reaches to 9SAL (Figure 6.47). Since the slab is pre-stressed due to shrinkage, and the bottom surface is under compression before applying the load, the bottom-cracking-load in this case is a bit higher than for the case of ignoring the shrinkage effects. In this case there is a slow increase in the cracking strains at the top surface, away from the applied load.

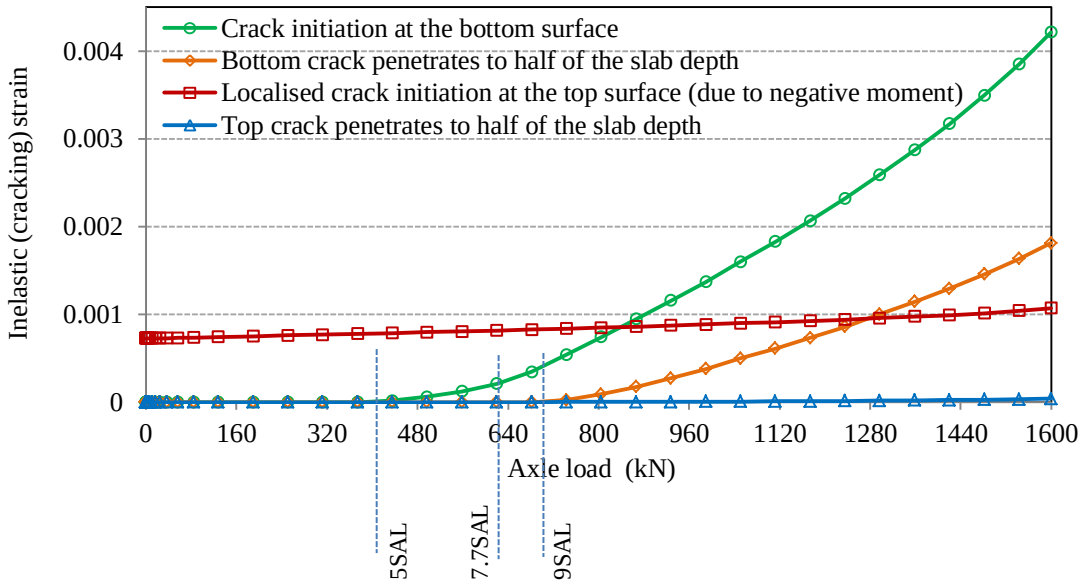

Figure 6.47 Cracking strain versus the load (Longitudinal edge load + Drying shrinkage)

The cracking strain due to negative moment reaches to half of the slab depth when the load is equal to 7.7SAL (Figure 6.47). Although the increase in cracking strain at the top surface occurs at a slow rate, it leads to crack widening as it is localised in the position of maximum negative moment. Figure 6.48 shows the development of cracking strains when the axle load is equal to 7.7SAL.

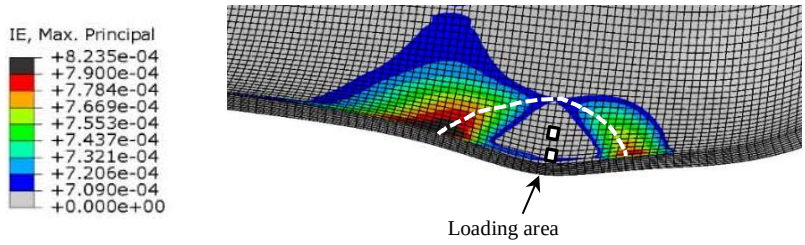

Figure 6.48 Maximum cracking strains at an axle load = 7.7SAL (Longitudinal edge load + Drying shrinkage; one end of the axle located at the edge) - plan view

Figure 6.49 shows the profile of maximum cracking strain at the top surface versus the diagonal distance "*w*", from the longitudinal edge for various axle loads.

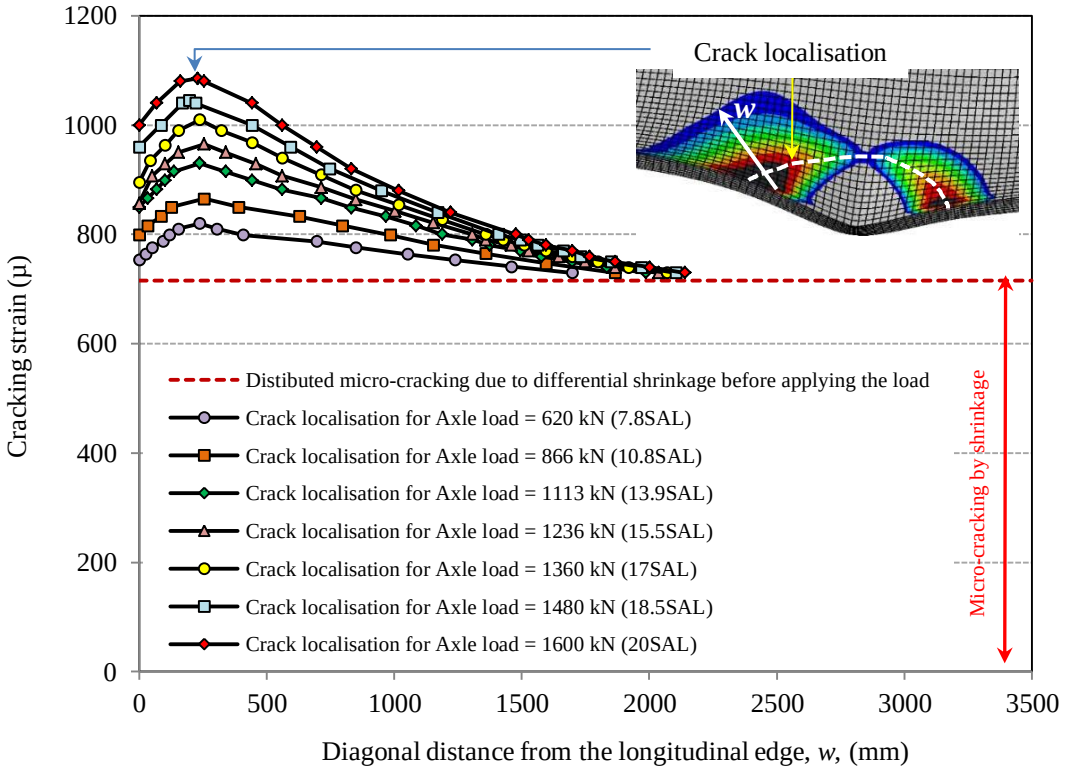

Figure 6.49 Maximum cracking strain at the top surface versus the distance from the edge (Longitudinal edge load + Drying shrinkage)

In Figure 6.49, a cracking strain value of 700 micro-strain is produced at the top surface of the slab, due to drying shrinkage and prior to applying the load. This strain forms distributed micro-cracks on the surface of the slab. When the load is applied, the micro cracks are widened locally in a semi-circular path, at a distance from the longitudinal edge load.

Figure 6.50 shows the variation of the equivalent crack opening versus the axle load, compared to when shrinkage is ignored.

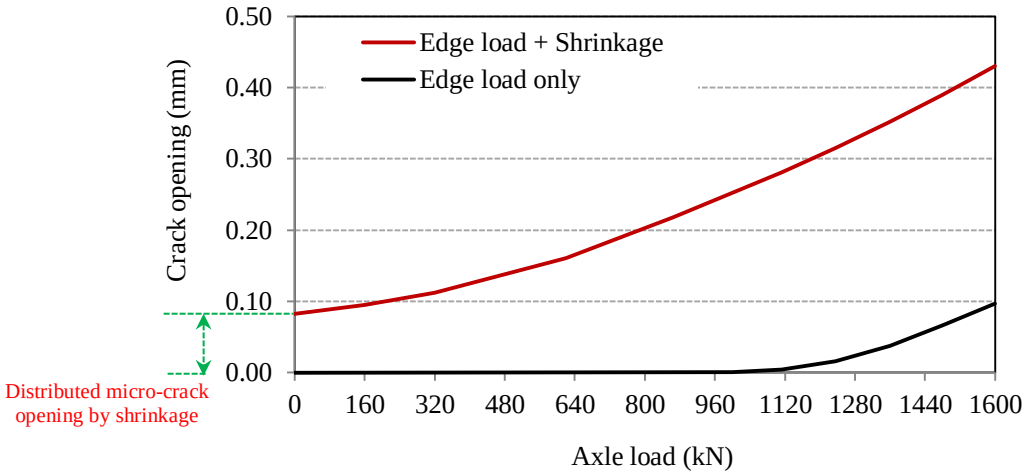

Figure 6.50 Variation of the equivalent crack opening versus the axle load (Longitudinal edge load + Drying shrinkage; compared to Longitudinal edge load only)

As shown in Figure 6.50, distress induced by drying shrinkage significantly increases the crack opening due to loading. The effect of fatigue has not been considered.

6.4.2.3 Transversal edge loading

Micro-cracks have already formed all over the slab surface before applying the traffic load due to differential shrinkage (Section 6.3.2).

No significant increase in the cracking strains at the top surface occurs when the applied load is less than the 0.5SAL (Figure 6.51). When the axle load exceeds the 0.5SAL, cracking strains at the top surface develop further and a transversal crack is initiated at a certain distance from the transversal edge. The transversal crack penetrates to half of the slab depth when the axle load reaches 6.5SAL. Figure 6.52 shows the development of cracking strains when the transversal cracking penetrates to half of the slab depth (at 6.5SAL). Bottom cracks initiate under each end of the axle when the axle load exceeds 5SAL, and it penetrates to half

of the slab depth when the axle load reaches 11SAL.

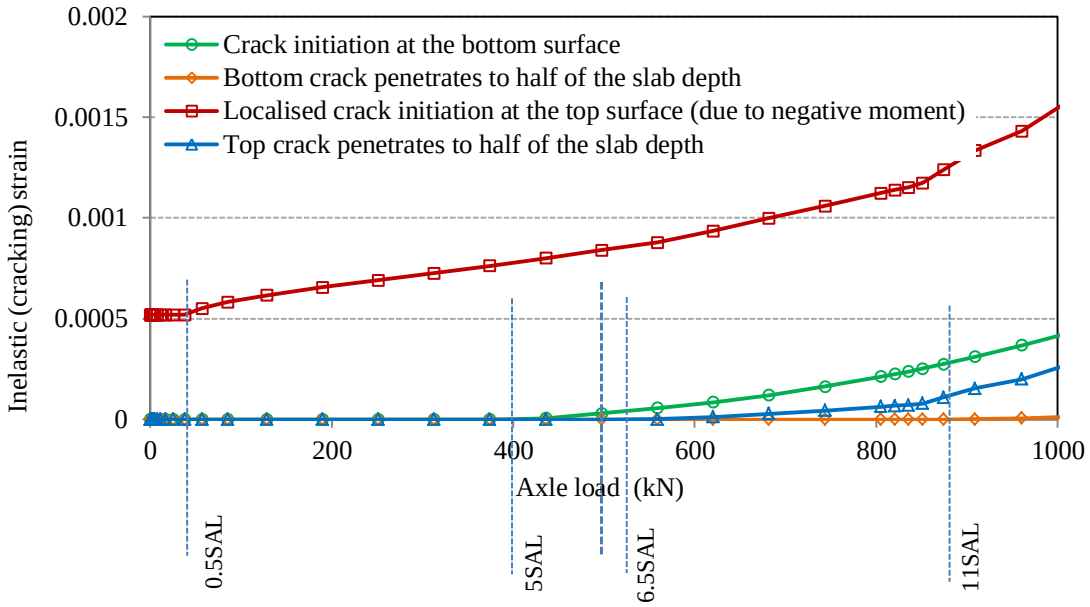

Figure 6.51 Cracking strain versus the axle load (Transversal edge load + Drying shrinkage)

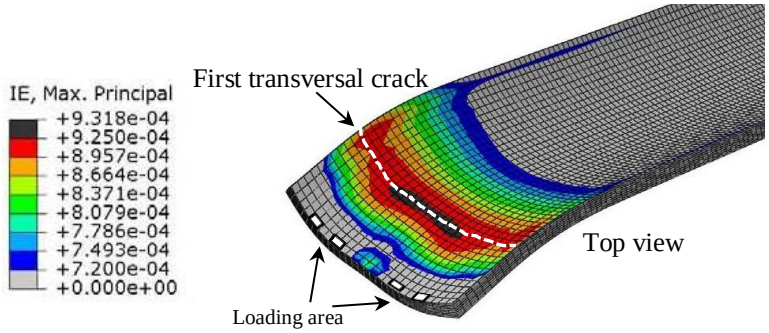

Figure 6.52 Maximum cracking strains at an axle load = 6.5SAL (Transversal edge loading + Drying shrinkage)

Figure 6.53 shows the profile of the maximum cracking strain at the top surface versus the distance from the transversal edge, *w*, for various axle loads.

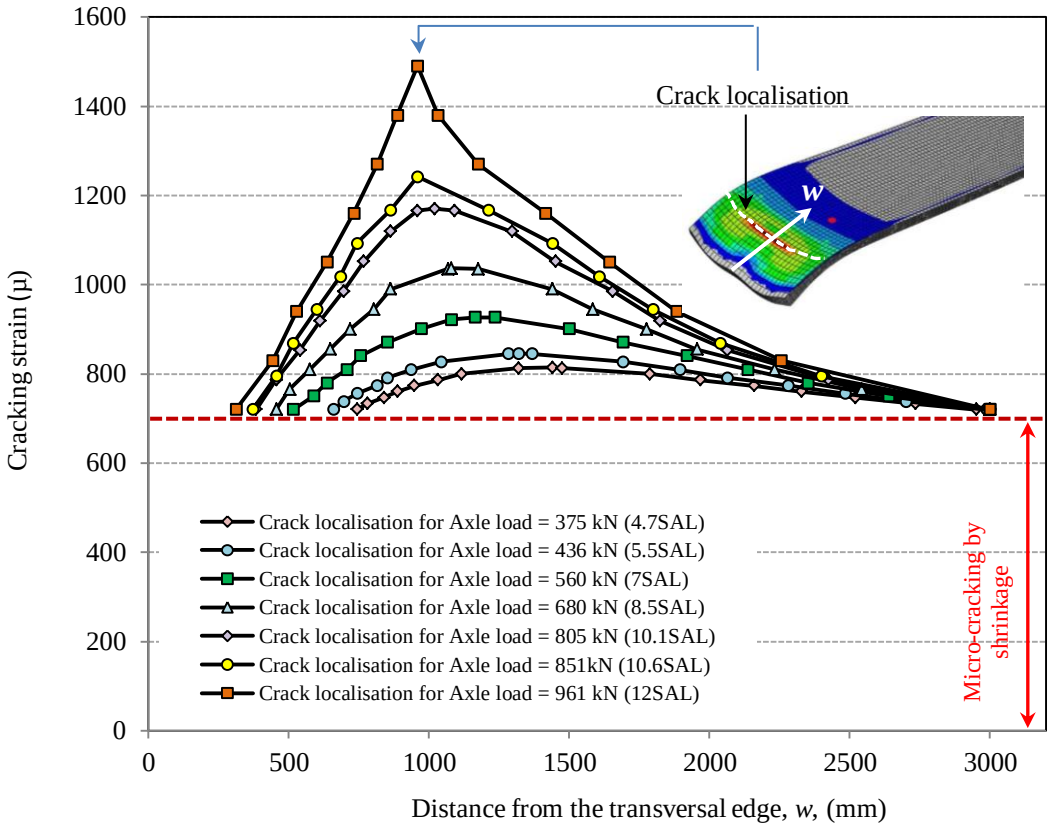

Figure 6.53 Maximum cracking strain at the top surface versus the distance from the edge (Transversal edge load + Drying shrinkage)

A cracking strain value of 550 micro-strain is produced at the top surface of the slab near to the transversal edge, and a value of 700 micro-strain is produced at the interior areas, due to drying shrinkage and prior to applying the load. This strain forms distributed micro-cracks on the surface of the slab. When the load is applied, the micro cracks widen locally forming a transversal crack, at around 1m distance from the transversal edge.

Figure 6.54 shows the variation of the equivalent crack opening versus the axle load compared to when shrinkage is ignored. This comparison shows that distress induced by drying shrinkage at the top surface of the slab significantly increases the crack opening due to loading. It should be noted that the effect of fatigue has not been considered yet.

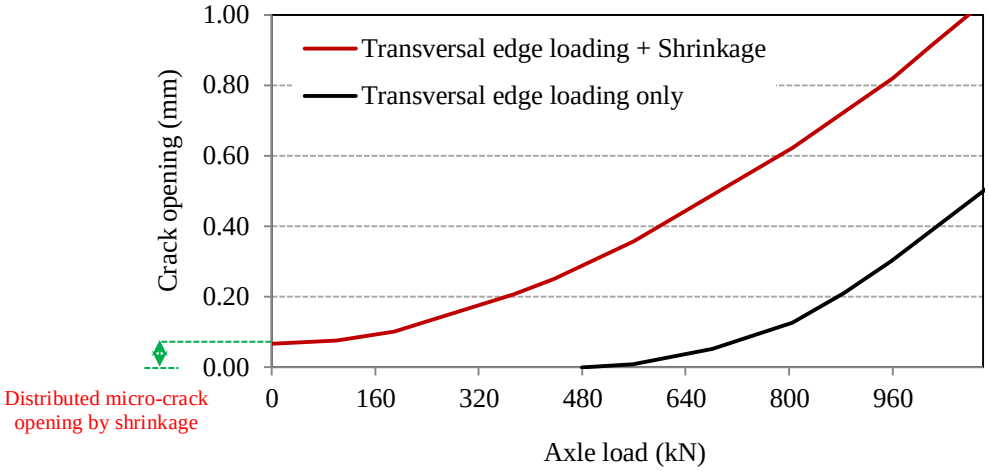

Figure 6.54 Variation of the equivalent crack opening versus the axle load (Transversal edge load + Drying shrinkage; compared to Transversal edge load only)

6.4.2.4 Interior loading

Bottom cracking is dominant for interior loading. Therefore, a slow increase in the cracking strains at the top surface occurs when the load is applied. The cracking strain due to the negative moment reaches half of the depth when the load is equal to 18.8SAL (Figure 6.55).

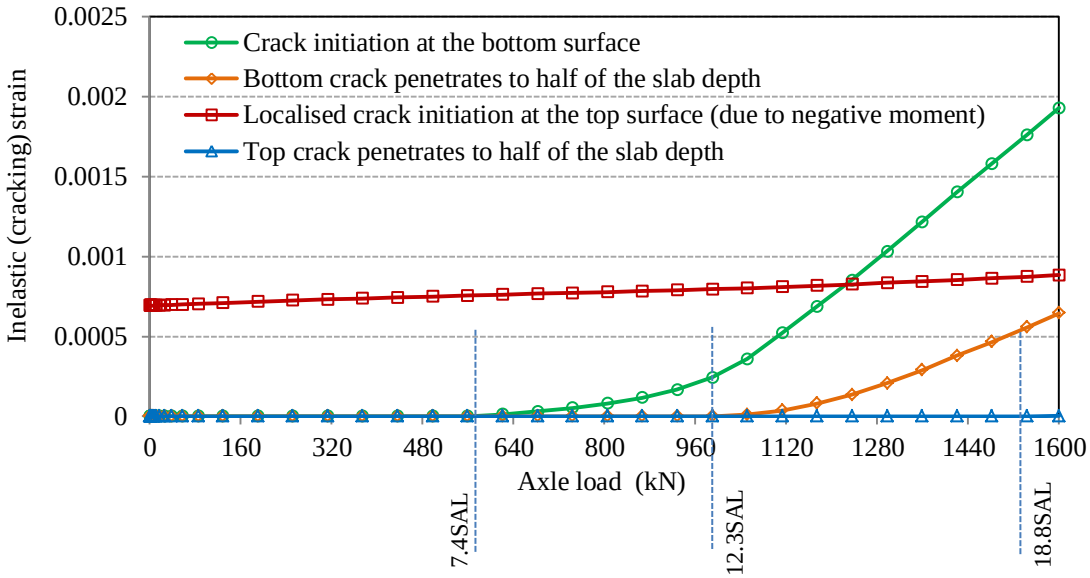

Figure 6.55 Cracking strain versus the axle load (Interior load + Drying shrinkage)

Bottom crack initiates when the axle load exceeds 7.4SAL, and it penetrates to half of the slab depth when the axle load reaches 12.3SAL. Since the slab is pre-stressed due to shrinkage,

and the bottom surface is under compression before applying the load, the bottom-cracking-load in this case in a bit higher than the case of ignoring the shrinkage effects.

Although the increase of cracking strain at the top surface occurs in a slow rate, it still leads to crack widening as it is localised in the position of maximum negative moment. Figure 6.56 shows the development of cracking strains when the axle load is equal to 18.8SAL.

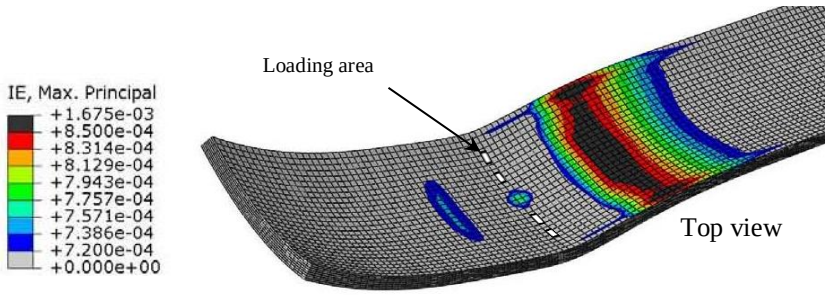

Figure 6.56 Maximum cracking strains at an axle load=18.8SAL (Interior loading + Drying Shrinkage)

Figure 6.57 shows the profile of the maximum cracking strain at the top surface versus the longitudinal distance "*w*", from the axle load.

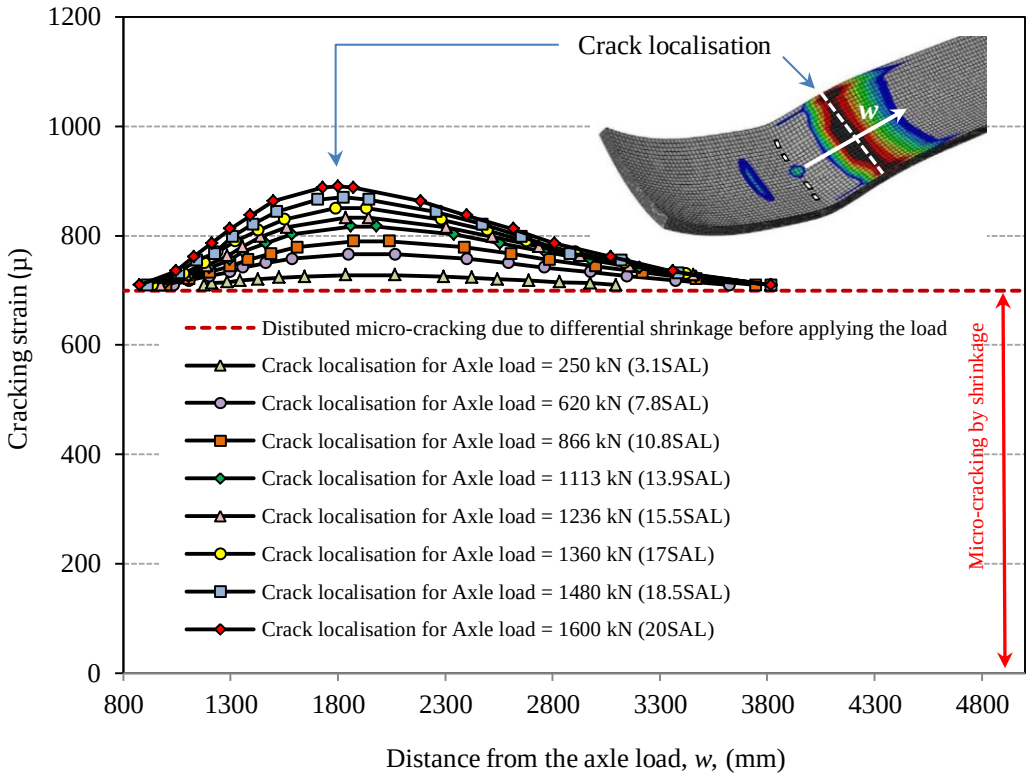

Figure 6.57 Maximum cracking strain at the top surface versus the distance from the axle load (Interior load + Drying shrinkage)

A cracking strain value of 700 micro-strain is produced at the top surface of the slab, due to drying shrinkage and prior to applying the load. This strain forms distributed micro-cracks on the surface of the slab. When the load is applied, the micro cracks widen locally at a transversal band with a distance of around 1.8m from the axle load.

Figure 6.58 shows the variation of the equivalent crack opening versus the axle load, compared to when shrinkage is ignored (no cracking at the top surface occurs when shrinkage is ignored for this load case).

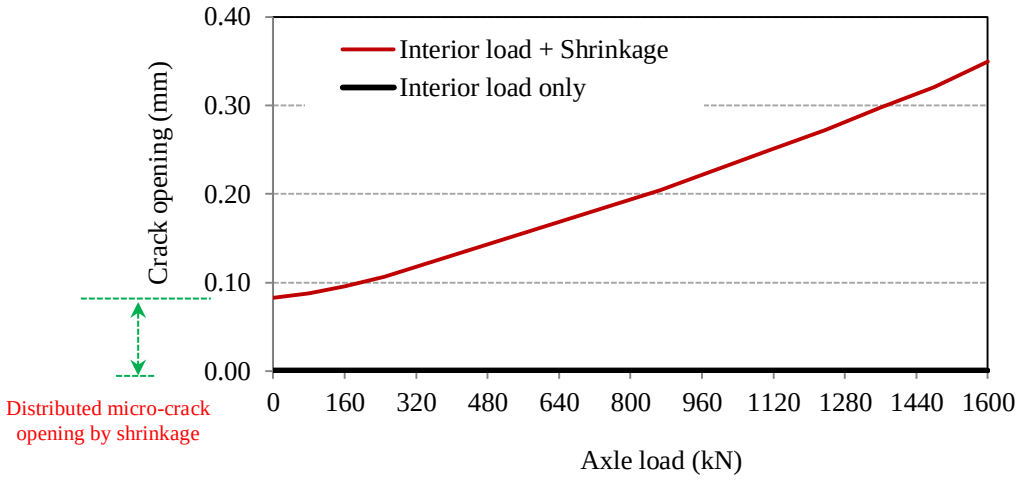

Figure 6.58 Variation of the equivalent crack opening versus the axle load (Interior load + Drying shrinkage; compared to Interior load only)

6.4.3 Summary of the results

The summary of the results for monotonic loading analysis is given in Table 6.3 in terms of the load bearing capacity for various levels of failure.

The result of monotonic loading analysis will be verified in Section 6.4.4.3, by comparing with the simplified analytical method proposed by the Concrete Society TR34 (2003), for the failure level of crack initiation at the top surface. The predicted failure loads will also be used in Chapter 7 (Section 7.3.1), in studying the long-term fatigue behaviour (to calculate the nominal stress ratio, which is defined as the ratio of the service load to the failure load).

Table 6.3 Load bearing capacities for various load cases and failure criteria

Level of failure	Load cases: Corner load only	Longitudinal edge load only	Transversal edge load only	Interior load Only
Crack initiation at the bottom surface	340 kN (4.25SAL)	280 kN (3.5SAL)	465 kN (5.8SAL)	440 kN (5.5SAL)
Crack initiation at the top surface	400 kN (5SAL)	650 kN (8.15SAL)	585 kN (7.3SAL)	> 1600 kN (>20SAL)
Top cracking reaches half of the slab depth	640 kN (8SAL)	1200 kN (15SAL)	960 kN (12.0SAL)	> 1600 kN (>20SAL)
Bottom cracking reaches half of the slab depth	-	530 kN (6.6SAL)	835 kN (10.4SAL)	745 kN (9.3SAL)
	Corner load + shrinkage	Longitudinal edge load + shrinkage	Transversal edge load + shrinkage	Interior load + shrinkage
Crack initiation at the bottom surface	95 kN (1.2SAL)	400 kN (5SAL)	400 kN (5SAL)	590 kN (7.4SAL)
Crack widening at the top surface	80 kN (1SAL)	25 kN (0.3SAL)	40 kN (0.5SAL)	25 kN (0.3SAL)
Top cracking reaches half of the slab depth	320 kN (4SAL)	620 kN (7.75SAL)	520 kN (6.5SAL)	1500 kN (18.75SAL)
Bottom cracking reaches half of the slab depth	-	720 kN (9SAL)	880 kN (11SAL)	1000 kN (12.5SAL)

6.4.4 Verifying and discussing the results

The FE model developed in this research, to investigate the behaviour of concrete pavements, is a comprehensive model considering several aspects in the behaviour of concrete pavements. These aspects consist of:

- Moisture transport mechanism in concrete pavements during drying
- Combination of drying with a cracking model to predict the micro-cracking induced by drying shrinkage
- The behaviour of a multi layered pavement under traffic load, able to mobilise the frictional resistance and cohesion between the slab and the cement-treated base.

To verify the general behaviour of such a model, field studies or a massive laboratory testing

plan, considering the above mentioned aspects, is needed, which is outside the scope of this research, in terms of both time and cost.

Instead of verifying the combination of the above-mentioned issues in the performance of the model pavement, the remaining option is verifying single issues separately. For example the accuracy of the model in the moisture transportation was verified in Section 5.1.1 in a comparison with the results of a simple-geometry experimental specimen obtained by Asad (1995). The performance of the model under traffic load is also verified in comparison with existing methods such as analytical simplified closed-form equations in the following.

6.4.4.1 Existing methods

Existing design codes and guidelines for industrial or transportation slabs, such as ACI 360R (1992), PCA (1966; 1984) and Concrete Society TR34 (2003), rely on elastic or basic elasto-plastic theories and methods of analysis. However, these methods are not perfect for general analysis and numerical methods are more flexible in the range of problems they can solve. Some of these limitations are discussed below.

- Westergaard's theory

The first complete design method for rigid pavements was developed around 1920, based on Westergaard's theory (ACI 360R, 1992). Westergaards formulation has been developed for infinite-size slabs (Figure 6.59) and assumes that the slab is a homogenous, isotropic, elastic solid domain resting on a perfect subgrade.

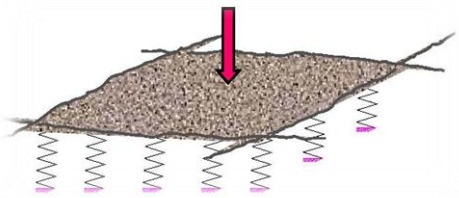

Figure 6.59 Model of the pavement considered in the Westergaard's theory

The reaction of the foundation is vertical and proportional to the deflection of the slab (Winkler foundation). Westergaards's equation does not consider a frictional resistance under the slab. A perfect contact between the slab and foundation is considered to be maintained in the case of a negative pressure (loss of support under the slab is not permitted). However, extensive investigations have shown good agreement between observed behaviour in the

elastic range and Westergaard's theory, as long as the slab remained continuously supported by the subgrade (ACI 360R, 1992). Despite the fact that the required slab thickness is overestimated by an elastic approach, Westergaard's equations are still widely used for computing stresses in pavements and verifying models developed using different techniques.

- Burmister 's theory

In 1943, Burmister et al. (1943) proposed the theory of stresses and displacements in layered systems in accordance with the methods of the mathematical theory of elasticity. Burmister et al. assumed that the pavement structure is made up of two layers, where the top layer is modelled as an elastic domain infinite in the horizontal direction only and the bottom layer is a semi-infinite solid of lower modulus of elasticity. This theory was never developed enough for engineering design practices, because it is not applicable for limited-length slabs under edge and corner loads.

- Losberg's and Meyerhof's theory

Later, in 1961 Losberg (1961) and in 1962 Meyerhof (1962) developed strength theories based on the yield line concept. However, these theories are not able to predict the deformational behaviour of the slab-foundation system.

To verify the performance of the FE model in the elastic range, Westergaard equations are used to compare with the linear part of the load-deflection curves under corner, edge and interior loading configurations. To evaluate the performance of the FE model at the ultimate limit state, the method proposed by the Concrete Society TR34 (2003), which is based on Meyerhof's elasto-plastic theory, is adopted.

6.4.4.2 Verifying the results of the FE model in the elastic range

Westergaard equations relating load to the maximum deflection, are given in Eq. 6.8, 6.9 and 6.10, for central, edge, and corner loading, respectively.

For interior loading:	$w_{max} = P/(8\,k\,l^2)$	(Eq. 6.8)
For edge loading:	$w_{max} = ((1+0.4v)P)/(6^{0.5}\,k\,l^2)$	(Eq. 6.9)
For corner loading:	$w_{max} = (1.1 - 0.88\frac{a_1}{l})\frac{P}{k\,l^2}$	(Eq. 6.10)

Where, w_{max} is the maximum deflection of the slab; P is the load; k is the modulus of subgrade reaction, v is Poisson's ratio, l is the radius of relative stiffness ($l = (D/K)^{0.25}$), D is the stiffness of the slab ($D = Eh^3/[12(1-v^2)]$), E is the elastic modulus, a_1 is the distance from the load centre to the corner, and h is the slab thickness.

Since the Westergaard's formulation is not capable of addressing the behaviour of a multi-layered foundation, to make the comparison possible the base layer is initially removed from the FE analysis. In this case, a concrete slab with a given thickness lays on a Winkler subgrade with a given modulus of reaction. The assumed properties for the slab and the subgrade are the same as assumed in FE analysis performed in Section 6.4.1, but the loads are concentrated in square shapes with a dimension of 120 mm.

There are still two differences between Wesergaard's assumptions and the FE model developed in Section 6.4.1. Westergaard assumes an infinite size slab in plan, while the FE model has limited dimensions. Furthermore, in the Winkler model adopted in the FE analysis, no resistance is mobilised against upward movement of the slab, while no upward movement is permitted in Westergaard's formulation. Based on these differences, a perfect match is not expected between Westergaard's and FE results, although the results should be expected to reasonably match each other (Figure 6.60).

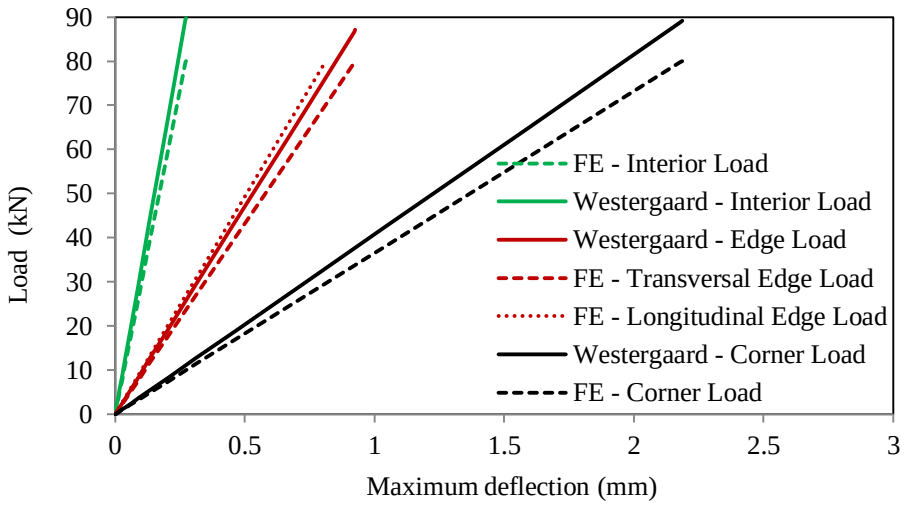

Figure 6.60 Comparison of FE results and Westergaard's analytical equations

6.4.4.3 Verifying the results of the FE model in the ultimate limit state

Most of the existing codes and guidelines for pavements (e.g. PCA, 1984; Highways Agency,

2006) do not account for the post-cracking capacity of slabs-on-ground (that can be considerable in the case of SFRC pavements).

ACI (ACI 360R, 1992; ACI 544.4R, 1999) accepts that SFRC pavements subjected to heavy traffic need a thickness of 60% to 75% of the plain slab thickness to perform as well as plain concrete pavements. This code recognises the potential benefits of fibres and the improvement in strength properties and fatigue resistance of SFRC material, but does not include practical design guidelines for SFRC slabs.

In the Concrete Society TR34 method (2003), the post-first-cracking flexural strength is taken into account in the calculation of the design positive (sagging) moment capacities. Cracking is only allowed to occur on the bottom surface of the slab but not at the top surface, and negative (hogging) moments are calculated using the uncracked strength. In fact, this guideline uses the ultimate limit state concept for fibre reinforced ground floors, but only partially. The failure load is reached immediately before the development of visible cracks on the top surface. Though this method may be more economical for SFRC slabs, the fatigue effect is not taken into account.

In this method partial safety factors are applied to the loads and to the material properties, and design controls are performed on both the strength (ultimate state) and serviceability of the slab. It is recommended to apply a partial safety factor of 1.6 to the dynamic loads. A partial material safety factor of $\gamma = 1.5$ is also applied for plain concrete and SFRC, and the design value of a concrete property is related to its characteristic value as follows:

$$Design\ value = \ characteristic\ value/\gamma$$

Formulation for dual loading centred at a relatively far distance is only given for interior load configuration (Figure 6.61) in the Concrete Society TR34 (2003), as follows:

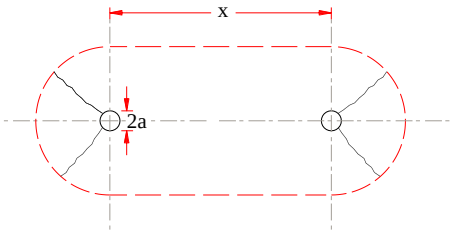

Figure 6.61 Interior dual load

For interior dual loading

$$P_u = [4\pi/(1-(a/(3l))) + 1.8x/(l-(a/2))][M_p + M_n] \quad for \;\; a/l > 0.2 \qquad \text{(Eq. 6.11)}$$

Where P_u is the collapse load; $M_p = f_{ct,fl}(R_{e,3})(h^2/6)$ is the residual positive bending moment capacity; $M_n = f_{ct,fl}(h^2/6)$ is the negative bending moment capacity; $f_{ct,fl}$ is the tensile flexural strength; a is the equivalent contact radius of the load; x is the centre-line spacing of the equivalent contact area of the load; $l = [E_{cm}h^3/12k(1-\nu^2)]^{0.25}$ is the radius of relative stiffness; E_{cm} is the modulus of elasticity of the concrete; ν is Poisson's ration; k is the modulus of subgrade reaction; h is the slab thickness; $R_{e,3}$ is the equivalent flexural strength measured using the Japanese Standard test method (JSCE-SF4, 1984).

For edge dual loading centred at a relatively far distance, it is roughly recommended to apply a factor of 0.5 to the interior loading capacity.

For a single load applied at the corner the following equation is used:

$$P_u = \; 4M_n/[1-a/l] \qquad for \;\; a/l > 0.2 \qquad \text{(Eq. 6.12)}$$

The only property of the foundation, which is used in the Concrete Society equations, is the modulus of subgrade reaction, and there is no possibility to consider the effect of the stabilised base layer, separately. For a stabilised base of a thickness of 150 mm and an elastic modulus of 8 GPa, placed on the top of a subgrade with an elastic reaction modulus of 0.06 MPa/mm (as assumed in the FE analysis), the composite modulus of reaction is estimated equal to 0.15 MPa/mm based on the graphs provided by US Army corps of engineers (EM 1110-3-142, 1984).

For the geometry, the material properties and the load configurations examined in Section 6.4.1, the ultimate load bearing capacity for interior, edge and corner load is calculated as presented in Table 6.4, based on Concrete Society TR34 (2003) and the failure criterion of crack initiation at the top surface. For corner loading, half of the axle load is applied at a single area to use the Eq. 6.12. The results are compared with the results obtained in this research for the same failure criterion. For SFR-RCC, the value of $R_{e,3}$ is calculated as 0.47, based on the load-deflection curves from tests of SFRC (Chapter 4).

Table 6.4 Load bearing capacity of the SFR-RCC Pavement (comparison with TR34)

		Failure criterion : crack initiation at the top surface **		
		Current research	Concrete Society method	
		Ultimate load bearing capacity	Ultimate load bearing capacity	With partial safety factors
Axle* Load (kN)	Interior	>1600 (>20SAL)	1390 (17.4SAL)	579 (7.2SAL)
	Edge	650 (8.15SAL)	695 (8.7SAL)	290 (3.6SAL)
	Corner	400 (5SAL)	475 (6SAL)	199 (2.5SAL)

*only half of the axle load is applied at the edge and corner

**without considering the effect of shrinkage

Considering the simplifications made in the Concrete Society method (such as concentrating the loads in circular shapes), the predictions from the current research match well with the Concrete Society results. The results presented above (Table 6.4) are for maximum load bearing without considering the load repetition and the effect of shrinkage. With applying the partial safety factors provided in TR34, the load bearing capacity which is controlled by the corner loading configuration reduces from 6 to 2.5 times the standard axle load for which the slab has been designed for a high repetition in a highly trafficked road. The experimental mean values have been adopted for strength properties of concrete. By applying the characteristic values the estimated load bearing capacity would be even less.

6.4.4.4 Discussion of results

The top-surface crack initiation level, although useful in comparing the FE result with the Concrete Society method for the case of no shrinkage, is not a suitable definition of failure when shrinkage distress is taken into account. In the FE analysis, when shrinkage is considered, the top surface of the slab is cracked at the micro scale before applying the load. Therefore, there is not a clear threshold of crack initiation at the top surface due to loading. Additionally, initiation of cracks at the top surface is not really a collapse or ultimate state in the behaviour of the slab.

Penetration of the top surface cracking to the bottom is also not a good failure criterion, since the corresponding failure load is too high (due to the stiff reaction of the pavement and the cement treated base).

A middle level failure criterion adopted in this study is the penetration of top surface cracking to half of the slab depth. Top surface cracking is dominant in the case of corner loading. The results presented in Table 6.3 shows that, for the top surface cracking criterion, the "failure" load when shrinkage is ignored is twice that of the "failure" load when shrinkage is considered, for corner and edge loading (Table 6.3).

In the case of interior loading, bottom surface cracking is dominant. Since the slab is pre-stressed due to shrinkage and the bottom surface is under compression before applying the load, the bottom-cracking-load for interior loading plus shrinkage is higher when ignoring shrinkage. This study showed that for bottom surface cracking criteria (crack initiation at the bottom surface, and penetration of bottom surface cracking to half depth), the failure load when shrinkage is ignored is 70% of the failure load corresponding to when shrinkage is considered, both for interior loading and longitudinal edge loading (Table 6.3).

The predicted monotonic failure loads for various load cases are useful in studying the long-term fatigue behaviour of the pavement. This issue will be discussed in Chapter 7; Section 7.1.1.3, and the idea will be adopted in Section 7.3.1.

The results obtained in this chapter are valid under the assumed environmental conditions and for the given concrete compositions reinforced with 2.5% recycled steel fibres of the mentioned characteristics, which have been chosen based on the optimisation studies carried out during the Ecolanes project. For other concrete compositions, with various fibre contents and types, and under different environmental conditions different results are expectable. The relative humidity of 40% assumed in this study is a medium to low value for outdoor conditions. In practice a wide range of environmental relative humidity is likely to occur depending to the climate conditions of the construction site. Lower environmental relative humidity can accelerate drying and shrinkage of the specimens. Higher environmental relative humidity may also affect the results inversely by delaying drying and shrinkage of the specimens.

Chapter 7

7 Long-term fatigue analysis

Long-term fatigue analysis is performed in this chapter, to investigate how initial distress due to shrinkage can affect the fatigue performance of SFRC pavements. For this aim, the results obtained in Chapter 6 are used in addition to the experimental fatigue test results obtained by Graeff (2011), for the Ecolanes project. Two different approaches are used to evaluate the fatigue performance of the SFRC pavement. These approaches and the way of adopting them for pavements are discussed in Section 7.1. The fatigue test results for SFR-RCC are presented and processed in Section 7.2. Investigating the effect of shrinkage distress on the fatigue performance, based on the data provided, is performed in Section 7.3.

7.1 Experimental approaches

Two experimental approaches are usually followed in studying the effect of cyclic loads on the fatigue behaviour of structural members. In the first approach the number of load cycles up to failure is obtained for various stress ratios (Fatigue endurance curves). In the second approach, the variation of a progressive damage factor (such as strain or displacement in a critical zone) is recorded during the fatigue life of the structure, which represents the evolution of damage due to fatigue.

7.1.1 Traditional methods to obtain fatigue endurance curves for concrete pavements

The fatigue endurance curve for concrete pavements can be obtained via the three following methods:

7.1.1.1 Concrete beam fatigue equations

Traditionally, the number of cycles until initial cracking in beams is assumed to represent the

concrete's fatigue life. Darter (1977) compiled 140 fatigue beam results from three published research projects into one least square regression equation (Eq. 7.1), in order to develop a design procedure for jointed plain concrete pavements (cited in Roesler et al., 2005).

$$\mathrm{Log}\,(N_f) = 17.61 - 17.61\left(\frac{\sigma}{MOR}\right) \qquad \text{(Eq. 7.1)}$$

Where, N_f is the number of load application until failure, σ is the applied maximum stress level, and MOR is the modulus of rupture.

For indeterminate structures such as ground-supported slabs, the first crack does not necessarily represent the end of fatigue life (Roesler et al., 2005), particularly in the case of steel fibre reinforced concrete. Altoubat et al. (2008) believe that the benefits imparted by fibres to the fatigue resistance of concrete pavements, if they are based on fatigue curves obtained from beam tests, will not be rewarded in structural design. In other words, beam testing does not always predict the fatigue resistance of ground-supported slabs.

7.1.1.2 Field-calibrated fatigue equations for concrete slabs

Rollings (1988; et al., 1990) studied the field response of airfield pavements and published concrete fatigue equations based on layered elastic analysis and the Structural Condition Index (SCI, which drops with increase of the distress level). These developed equations are as follows (cited in Roesler et al., 2005):

$$DF_{first\ crack} = 0.5234 + 0.3920 \times \log\,(C_{100}) \qquad \text{(Eq. 7.2)}$$

$$DF_{shattered\ slab} = 0.2967 + 0.3881 \times \log\,(C_0) \qquad \text{(Eq. 7.3)}$$

Where, DF is the inverse of stress ratio (MOR/σ, also defined as the design factor); C_{100} is defined as the number of load cycles for the SCI to drop below 100%, C_0 is the number of load cycles required to reduce the SCI of the pavement to zero. For intermediate SCI values interpolation can be performed.

The first equation is representative of the "first crack", while the second equation is representative of the "shattered slab". Figure 7.1 shows a comparison between the Rollings's equations and Darter's equation.

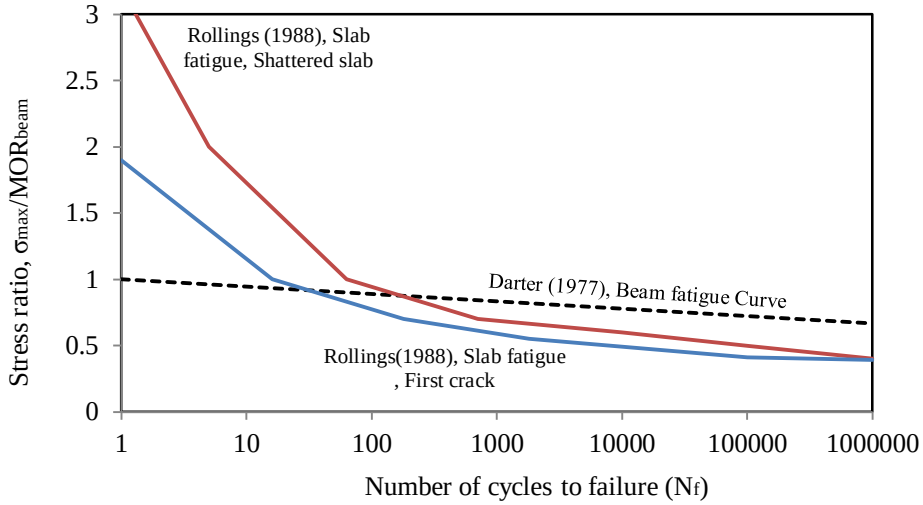

Figure 7.1 Comparison of Rollings's field-calibrated fatigue curves with Darter's beam fatigue curve (Roesler et al., 2005)

7.1.1.3 Laboratory fatigue equations for concrete slabs

The main factor causing differences in the fatigue behaviour of concrete slabs and beams is the definition of the failure condition. Particularly in the case of SFRC slabs, where a high amount of loading capacity is utilized in the post-cracking phase, relying directly on the results of beam fatigue tests could be misleading.

Roesler (1998) experimentally examined the effect of boundary and support conditions on the fatigue response of beams and slabs. Fatigue tests on fully-supported slabs showed that concrete ground slabs have a higher fatigue life than predicted by beam fatigue equations. The inconsistency in defining the peak stress ratio in beam and slab equations was found as the cause of shifting the fatigue curves for concrete slabs higher than that of beams.

Roesler (1998) developed the following regression equation for the ground-slabs fatigue life, for 50% probability of failure:

$$N_f = [1.3/(\frac{\sigma}{MOR_{beam}})]^{32.57} \qquad \text{(Eq. 7.4)}$$

In the above equation, for the first cycle of loading, the peak stress ratio defined for the slab fatigue equation, (σ/MOR_{beam}), would be equal to 1.3. It means that in Roesler's study (1998), for a non-repetitive loading, the flexural strength of the slab has been predicted to be 1.3 times of the modulus of rupture of the beam. As a comparison with beam fatigue equation

proposed by Darter (1977), for the first cycle of loading the peak stress ratio defined for the beam fatigue equation, $\frac{\sigma}{MOR}$, equates to unity.

Roesler et al., (2005) revealed that if the ultimate flexural strength of the slab could be measured and be replaced with the modulus of rupture of the beam in fatigue equations (e.g. in Darter's equation), then all specimen geometries and boundary conditions (e.g. simply-supported beam, fully-supported beam, and fully supported slab) produce similar fatigue curves.

A monotonic test is required to obtain the flexural strength of the slab, (MOR_{slab}). Roesler et al. (2005) conducted monotonic and cyclic edge loading on sixteen fully-supported slabs. The monotonic testing was performed to characterise the flexural strength of the ground supported slab relative to the standard simply-supported beam. The load cycle relevant to the appearance of the initial crack (a hairline crack or a change in strain behaviour) was recorded, but to achieve the flexural failure of the slab the test was continued. The point when the concrete slab fully-hinged along one axis was defined as the flexural failure of the slab. Therefore the main difference between beam and slab fatigue test is the additional cycles needed to extend an initial crack through the slab depth or across the slab length, whereas a beam could fail without the appearance of a visual crack.

Roesler et al. (2005) compared the fatigue life of concrete fully-supported slabs with previous predictions by Darter (1977) and Roesler (1998) (Figure 7.2).

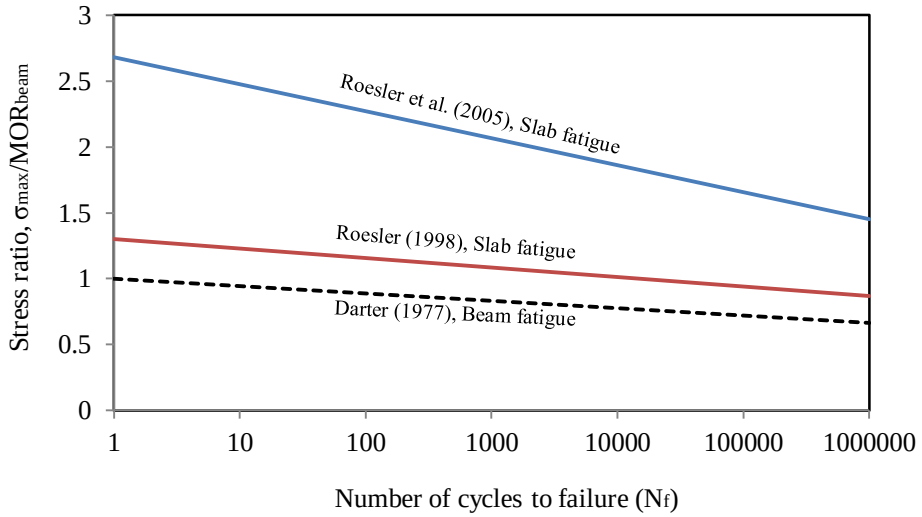

Figure 7.2 Comparison of Roesler's (2005 and 1998) slab fatigue curves based on beam-rupture-modulus, MOR_{beam}, with the beam fatigue curve (Roesler et al., 2005)

In this study, Roesler et al. predicted the monotonic flexural strength of the slab to be on average 2.8 times the monotonic strength of the simply-supported beam, against the 1.3 times value predicted by Roesler (1998). Based on the considerable difference between the results of two studies, it was concluded that the slab to beam strength ratio depends on many factors such as the thickness of the specimen, geometry of the slab, boundary conditions and loading configuration (Roesler et al., 2005).

Both studies carried out by Roesler (1998) and Roesler et al. (2005) show that the S-N fatigue curves for concrete slabs were shifted higher than beam fatigue curves, due to considerably higher monotonic flexural strength of concrete slabs compared to beams. In both curves, when the modulus of rupture of the beam is replaced by the monotonic flexural strength of the slab (MOR_{slab}), the fatigue results show similar behaviour with the Darter (1977) curve (Figure 7.3).

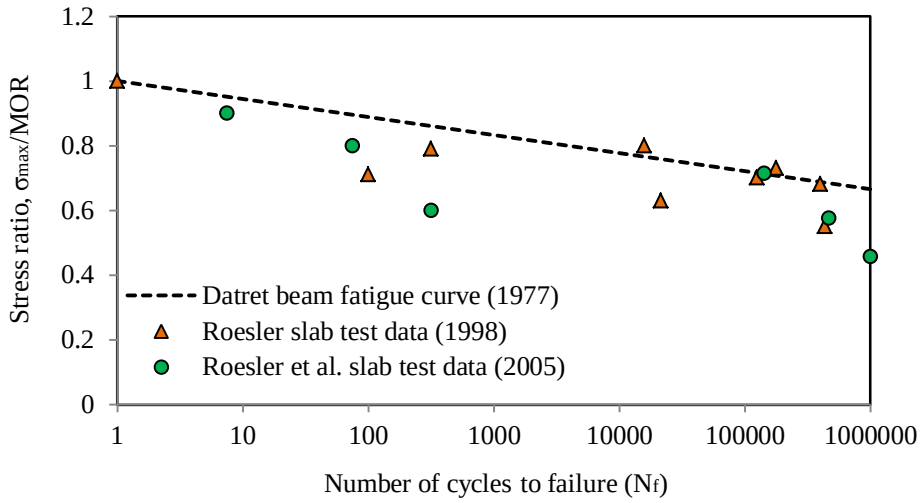

Figure 7.3 Comparison of Roesler's (2005 and 1998) slab fatigue curves based on slab-rupture-modulus, MOR_{slab}, with the beam fatigue curve (Roesler et al., 2005)

Therefore to accurately predict the fatigue life of a concrete slab, the flexural strength of the concrete slab for a given geometry and boundary conditions must be known. This is to take into account the different failure behaviour of ground-supported slabs and simply supported beams, in the fatigue behaviour (Roesler et al., 2005). In the current study the numerically obtained monotonic flexural strength of the slab is used in the experimentally obtained endurance curve (Section 7.2).

7.1.2 Evolution of damage due to fatigue

When the pavement operates under normal service conditions, damage gradually occurs in the pavement from repetitive load. Fatigue failure is caused at stress levels lower than the monotonic strength (Jiang et al., 1998).

Miner's fatigue damage hypothesis gives a method for defining different levels of damage in the life time of the pavement. This hypothesis states that any structure has a finite fatigue life (defined by the allowed number of load cycles prior to failure) and the fatigue damage to the structure is cumulative. Each load cycle consumes a fraction of fatigue life and when the fatigue life is exceeded the fatigue damage is 1.0 or 100% (Jiang et al., 1998). In Miner's hypothesis, a fatigue damage factor, D_f, is defined which varies for different numbers of load cycles (Jiang et al., 1998). The accumulation of fatigue damage for a constant rate of load repetition is non-linear over the life time of the pavement.

To determine the damage curve, Molinas-Vega et al. (1995) suggested to adopt the evolution of some internal variables as characteristics of the process. These variables must represent the evolution of damage under the imposed conditions (e.g. evolution of maximum strain or maximum deflection, which follows the same trend as damage propagation). This fatigue representing variable must be recorded for a range of stress ratios, and then must be presented versus the number of cycles normalised to the maximum number of cycles at failure.

Molinas-Vega et al (1995), by investigating different techniques and experimental works, presented three stages for damage evolution (Figure 7.4). Stage 1 consists of about 20% of the fatigue life and in which fatigue damage is accumulated relatively fast due to propagation of microcracks located at the interface between the aggregates and the cement paste. Stage 2 occurs roughly between 20% and 80% of the fatigue life, in which the rate of damage evolution is almost constant. In this stage microcracking accumulates inside the cement paste. Stage 3, which is characterised as the fast period of damage accumulation, normally consists of the last 20% of the fatigue life. In this stage macrocracks are formed leading to failure (Molinas-Vega et al., 1995).

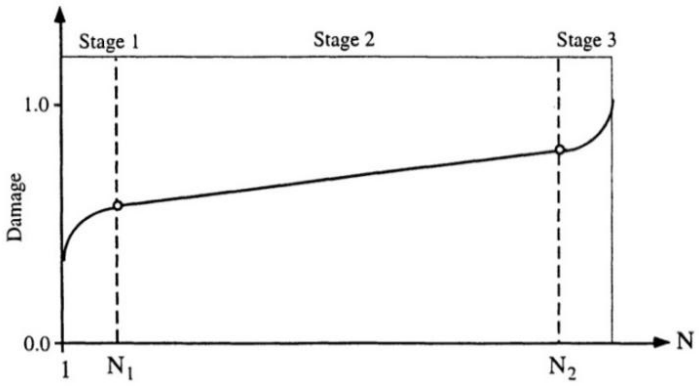

Figure 7.4 Damage evolution (Molinas-Vega et al., 1995)

A semi-empirical damage curve obtained by Molinas-Vega et al. (1995) for a specific stress ratio, 0.8, (Figure 7.5) was used by Bhatti et al. (1998) to study the fatigue behaviour of jointed concrete pavements.

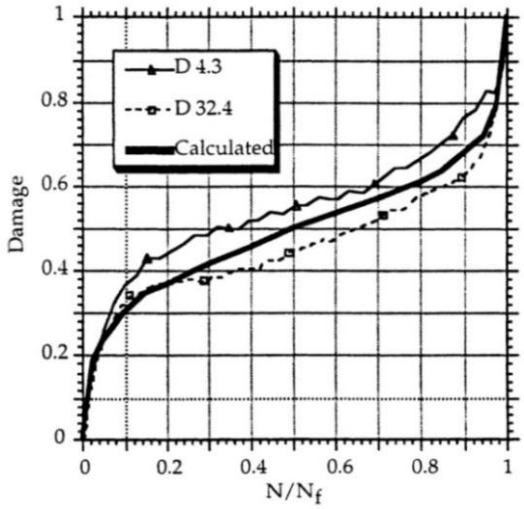

Figure 7.5 A semi-empirical damage evolution curve for s=0.8 (Molinas-Vega et al., 1995)

In that study the total number of load repetitions was divided into a reasonable number of steps, and the material properties were reduced at the end of each step by a factor D.

To evaluate the damage evolution function in the current research experimental data are required (Section 7.2).

7.2 Experimental test results for evaluation of fatigue parameters for SFR-RCC

To estimate fatigue parameters (endurance curve and damage evolution function) for the SFR-RCC mix adopted in the current research, the experimental results obtained by Graeff (2011) will be used. Graeff (2011) studied the fatigue resistance of SFR-RCC, for the same concrete mixes as developed in the current research (in the scope of Ecolanes project). In that study the effect of cyclic loads on flexural beams was experimentally evaluated by two approaches:

1) Obtaining the number of cycles up to failure, *N*, for various stress ratios (Fatigue endurance curves)

2) Vertical displacement analysis; from this approach, the history of vertical displacement, u, at the mid-span of prisms were obtained for given stress ratios, versus the number of load cycles. After processing the results for various mixes, the following pattern (Figure 7.6) was identified for displacement versus number of cycles.

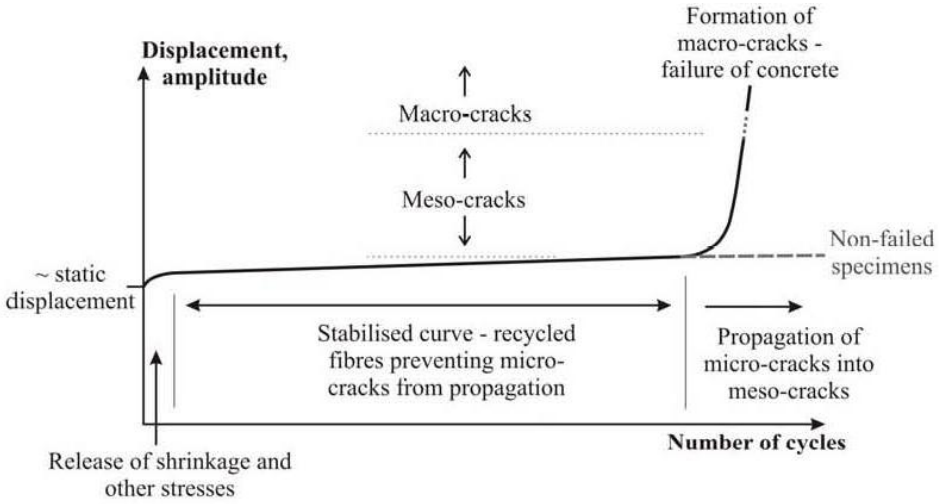

Figure 7.6 Pattern for variation of mid-span displacement versus the number of cycles, for beam fatigue tests (Graeff, 2011)

For SFR-RCC (containing 2% recycled fibres), the results of fatigue testing are presented in Figure 7.7 and 7.8.

Figure 7.7 shows the logarithmic values of number of load cycles up to failure, log (N), versus the stress level, s. This experimental endurance curve, obtained for SFR-RCC beams,

will be used in Section 7.1.1.3 to estimate the endurance curve suitable for the concrete pavement studied in the current research.

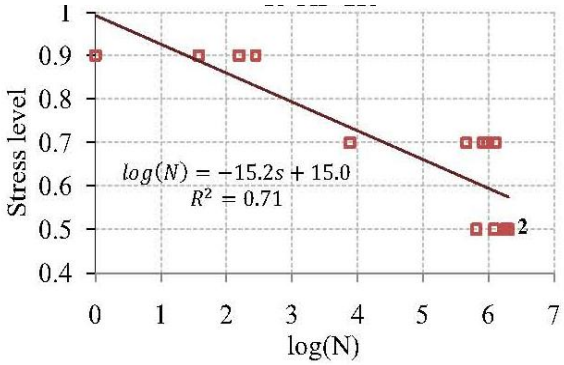

Figure 7.7 Experimental fatigue test results for SFR-RCC (containing 2% recycled fibres), endurance curve (Graeff, 2011)

In Figure 7.8, vertical displacement at the mid-span is plotted versus the number of load cycles during the fatigue life, for several specimens under the stress ratio of 0.5.

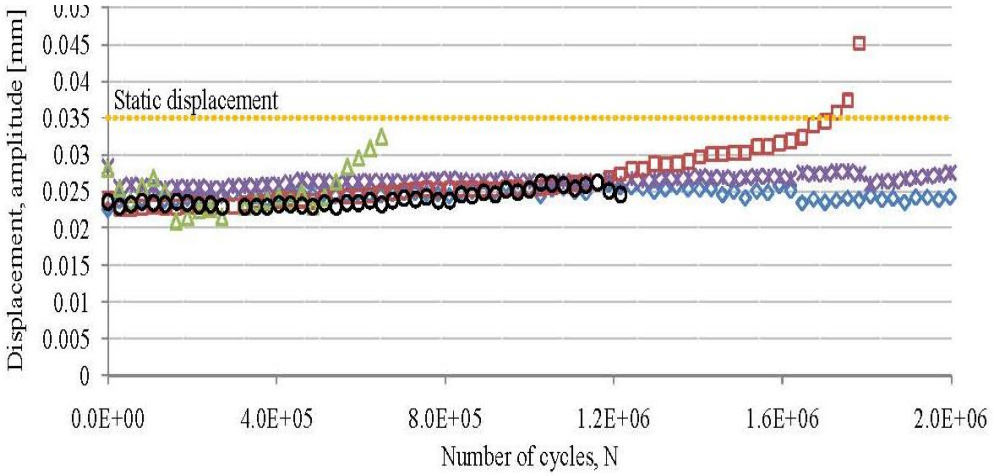

Figure 7.8 Experimental fatigue test results for SFR-RCC (containing 2% recycled fibres), mid-span deflection versus the number of load cycles (Graeff, 2011)

After processing the data given in Figure 7.8, the average curve is calculated (Figure 7.9). Figure 7.9, is an appropriate fatigue parameter to estimate the damage evolution function. For this aim, the linear transformation defining the accumulation of damage is applied (Eq. 7.5).

$$D_i = (u_i - u_0)/(u_{ult} - u_0) \qquad \text{(Eq. 7.5)}$$

Where, D_i is damage at a given value of N/N_f; u_i is the value of vertical displacement at a given value of N/N_f; u_0 is the value of vertical displacement at the first load application; u_{ult} is the value of vertical displacement at the last load application when $N/N_f = 1$.

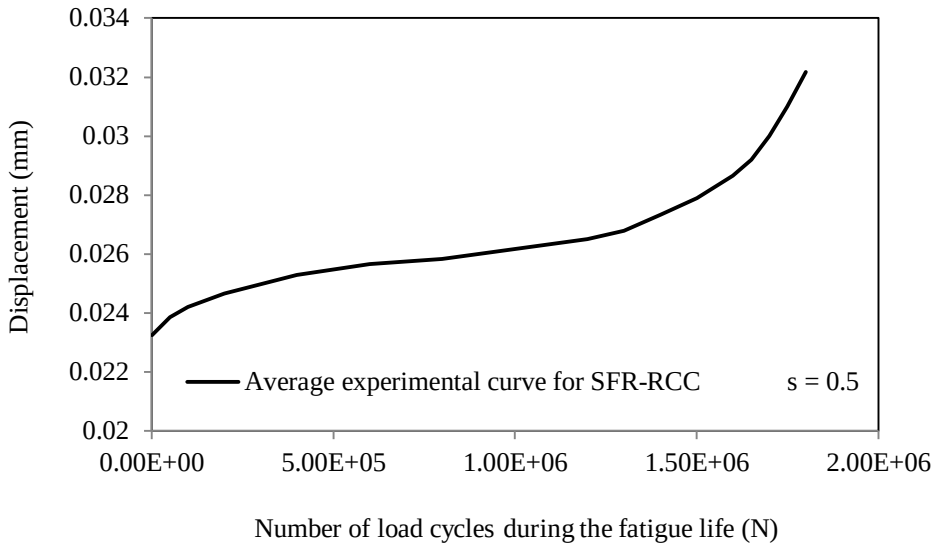

Figure 7.9 The average experimental curve for mid-span deflection versus the number of load cycles, for SFR-RCC (containing 2% recycled fibres)

The fatigue damage factor has been calculated as shown in Figure 7.10.

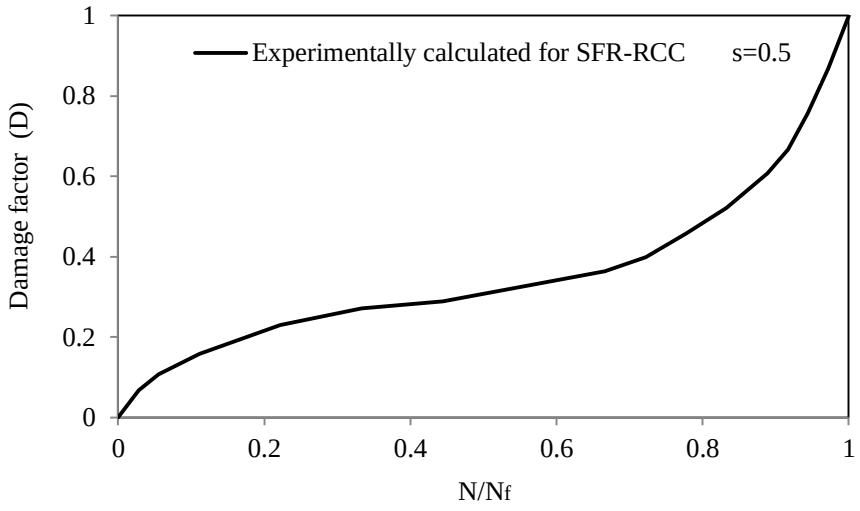

Figure 7.10 Fatigue damage factor for SFR-RCC (containing 2% recycled fibres), calculated from experimental results

7.3 Investigating the effect of shrinkage distress on fatigue performance

This section investigates how the initial distress due to shrinkage can affect the fatigue performance of the SFRC pavements.

7.3.1 Using the experimental fatigue endurance curve

The modulus of rupture (also called flexural tensile strength, refer to Section 4.2.2.4; BS EN 14651, 2005 and BS EN 14488-3, 2006) for experimental beams under third-point loading is defined as a fictitious stress at the tip of the notch (or at the constant moment zone of an un-notched prism, at the bottom surface) with linear stress distribution, which is assumed to act in an uncracked mid-span section of a prism subjected to a load F_L. F_L is the maximum load carried by the beam before failure (or before the descending part of the load-deflection curve initiates). In a similar way, the flexural strength or the modulus of rupture for pavements is defined as the fictitious maximum tensile stress at the critical zone (under the given load case), with linear stress distribution, corresponding to the failure load.

Therefore, due to the linearity used in defining the MOR, the stress ratio is proportional to the ratio of the applied load to the failure load.

The slab failure load can be obtained via experimental monotonic loading (Section 7.1.1.3) or can be estimated by FE analysis, as performed in the current research (Chapter 6, Table 6.3). The slab modulus of rupture is used to replace the beam modulus of rupture in the experimental fatigue endurance curve to make it suitable for use in the case of concrete pavements (Section 7.1.1.3).

7.3.1.1 Number of load cycles at edges and corners

As observed in the FE analysis results (Section 6.4), the placement of the wheels along the edge of the slab, produces higher stress than that at the interior locations. Although the frequency of loads passing through the edge is much lower than that of the interior areas, studies have shown that the fatigue life of the pavement is usually controlled by the few axle

loads passing along the slab edge (Jiang et al., 1998; Huang, 2004).

To correlate the fatigue life at the pavement edges to the interior areas, the distribution of load placement across the traffic lane must be known, theoretically. This issue has been studied by PCA (1984), and it was found that the same fatigue damage can be obtained by considering the edge loading only, and locating 6% of the total number of cycles at the edge of the pavement. If the total number of cycles is adopted, the edge stress must be reduced by a specific factor to result to the same fatigue damage. For 6% frequency of the load passing through the edge, the adjustment factor to reduce the stress is 0.894.

The studied pavement in the current research has been designed for 300 million standard axle load (Section 6.1.2.1). Assuming that 6% of this traffic passes through the longitudinal edges, the pavement should be able to pass 18 msa through the edges during the service life.

7.3.1.2 Provided safety factors

Since the pavement has been studied based on the ultimate limit state, a safety factor should be provided (after considering every distress factor).

Using the experimental fatigue endurance curve (obtained by Graeff, 2011), the stress ratios are calculated for 300 million and 18 million load repetitions (Table 7.1).

Table 7.1 Provided safety factors in the long-term

	Corner load	Longitudinal edge load	Interior load	Transversal edge load
Required number of cycles	18 msa	18 msa	300 msa	300 msa
Stress ratio based on the endurance curve	0.516	0.516	0.434	0.434
Service load (Axle* Load, kN)	80	80	80	80
Minimum required load bearing capacity based on the stress ratio(Axle* Load, kN)	155	155	184	184
Ignoring shrinkage distress				
Failure load based on FE analysis (Axle* load, kN)	640	1,200	1,850	960
Safety factor	4.1	7.7	10.0	5.2
Considering shrinkage distress				
Failure load based on FE analysis (Axle* load, kN)	320	620	1,500	520
Safety factor	2.1	4.0	8.1	2.8

*only half of the axle load is applied at the edge and corner

For ground-slabs the stress ratio is equal to the service load over the ultimate load bearing capacity of the slab. Assuming 80 kN standard axle as the service load, the minimum required load bearing capacities are calculated for interior areas and edges, as given in Table 7.1.

Comparing with the existing load bearing capacity of the designed pavement, obtained by FE analysis (Section 6.4), the provided safety factors are calculated with and without considering shrinkage (Table 7.1). The minimum provided safety factor in the case of considering shrinkage distress is 2.1, which is a reasonable value. The safety factor in the case of ignoring shrinkage is increased to a minimum of 4.1. It shows that the overall long-term load bearing capacity of the pavement could be overestimated by twice, if shrinkage distress is ignored.

7.3.1.3 Allowable stress ratios

To deal with the issue in another way, the reduction in the allowable stress ratio, due to considering shrinkage distress, is examined. From the experimental fatigue endurance curve (Figure 7.7), for 300 million load repetition the stress ratio should be less than 0.435, and for 18 million cycles, the stress ratio should be less than 0.516. Considering shrinkage distress, the permitted stress ratios are reduced further, depending on the reduction in the failure loads corresponding to various load configurations.

Based on the values given in Table 6.3, the monotonic failure load in the case of considering shrinkage distress is reduced by the factors given in Table 7.2, compared to when shrinkage distress is ignored (failure defined as top cracks propagates to half of the slab depth). Therefore, the MOR of the slab is reduced with the same factor, for any given load configuration. If this reduction is applied in the experimental fatigue endurance curve (see Section 7.1.1.3), the relation between the stress ratio and the allowable number of load cycles changes as shown in Figure 7.11.

Table 7.2 Failure load reduction factors when shrinkage distress is considered

Load configuration	Corner loading	Longitudinal edge loading	Transversal edge loading	Interior loading
Failure load reduction factor	0.50	0.52	0.54	0.8

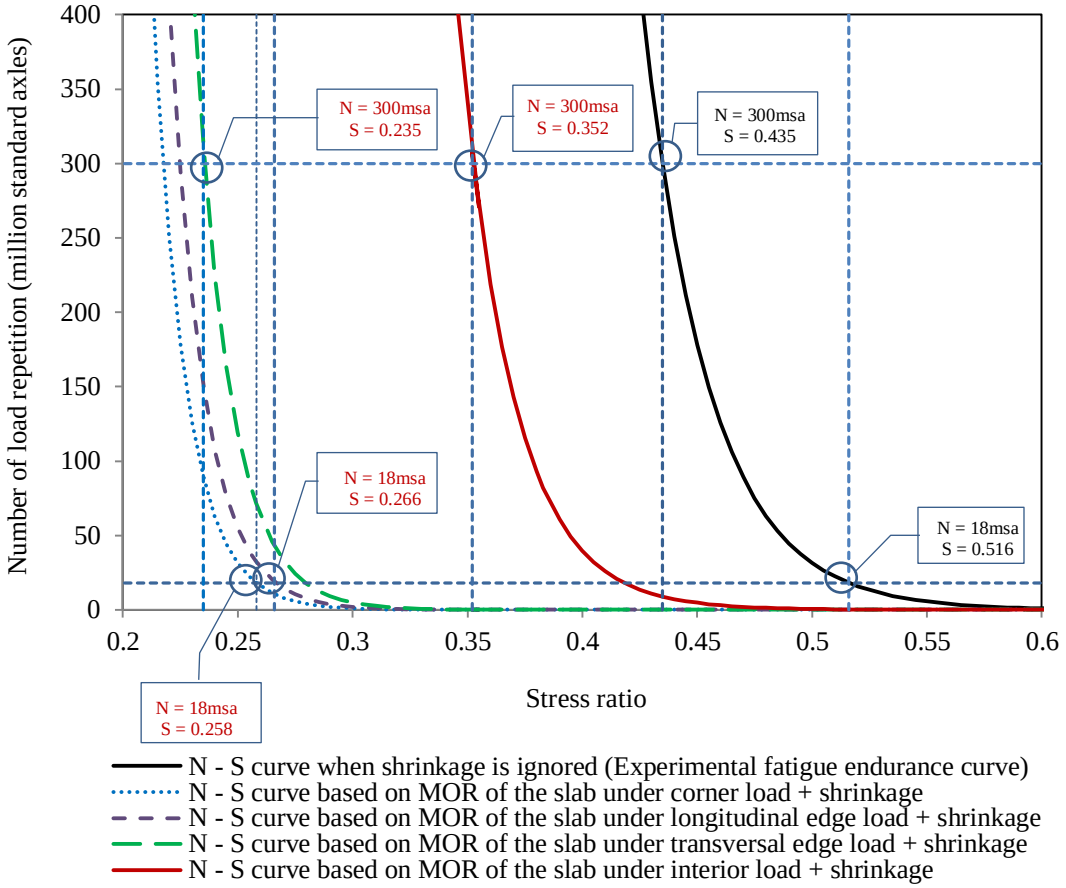

Figure 7.11 Comparison of N-S curves when shrinkage distress is considered or ignored

Figure 7.11 shows that considering shrinkage distress, to pass 300 msa the stress ratio should be reduced from 0.435 to 0.352 in the interior areas and to 0.235 in transversal edges (the transversal edge is dominant). To pass 18 msa (6% of the total number of cycles), the stress ratio should also be reduced from 0.516 to 0.266 in the longitudinal edges and to 0.258 in corners (corner is dominant). Therefore, considering shrinkage the overall long-term load bearing capacity of the pavement is reduced by a factor of 2.0.

7.3.2 Using the experimental fatigue damage evolution

Fatigue causes strength loss. For example, ACI 544.4R (1999) states that the fatigue strength of SFRC is 65% to 95% of the static strength, at one to two million cycles of non-reversed loads. These values are compared to typical values of 50% to 55% for slabs without fibres. This code implies that for properly proportioned high-quality SFRC, a fatigue value of 85% is often used in pavement design. ACI 215R (1992) also states that the fatigue strength of plain

concrete for a life of 10 million cycles in compression, tension or flexure is roughly about 55% of the static strength with a probability of exceedance of 50 %.

In the numerical analysis, the loss of strength due to fatigue can be simulated by considering different concrete strengths, representing different levels of strength loss at different number of load cycles (Channakeshava et al., 1993). In this approach, the fatigue strength of concrete is defined as a fraction of its static strength. This fraction is a function of magnitude and number of cycles (ACI 215R, 1992).

In this section, the FE model accounts for the behaviour of concrete pavement under cyclic loading by considering the nonlinear fatigue damage accumulation in concrete. Since the tensile strength of concrete is dominant in the behaviour of concrete pavements, fatigue for concrete in tension is considered and fatigue in compression is ignored. The experimental failure damage evolution factor for SFR-RCC (containing 2% recycled fibres), obtained in Section 7.2 (Figure 7.10), is adopted for this purpose.

Since the corner loading is the critical load case (according to Table 6.3 and Table 7.1), only this load case is examined in this section. The constant standard axle load (80 kN) is assumed as the cyclic load. As shown in Section 7.3.1.2, for the designed slab there is a safety factor of 2 against ultimate failure, considering the combined effect of fatigue and shrinkage. The factor of safety is increased to 4.0 when the effect of shrinkage is ignored.

In the fatigue damage evolution approach, in order to observe the behaviour of the pavement in terms of life span before reaching the failure threshold, the safety factors are initially applied as load factors. The pavement is analysed with and without considering shrinkage distress, and the slab is assumed to reach the end of its life span when the top surface cracking penetrates to half of the slab depth. In this analysis, the time and the number of load cycles have the same magnitude in the loading step.

Figure 7.12 shows cracking strain versus N/N_f (the ratio of the number of load cycles to the designed number of load cycles at failure) at the top surface and at half depth, when shrinkage is ignored and a load factor 4.0 is applied. This figure shows that crack initiation at the top surface occurs at 22% of the designed life span and the top crack penetrates to the half depth at 91% of the designed life span, when a load factor 4.0 is applied.

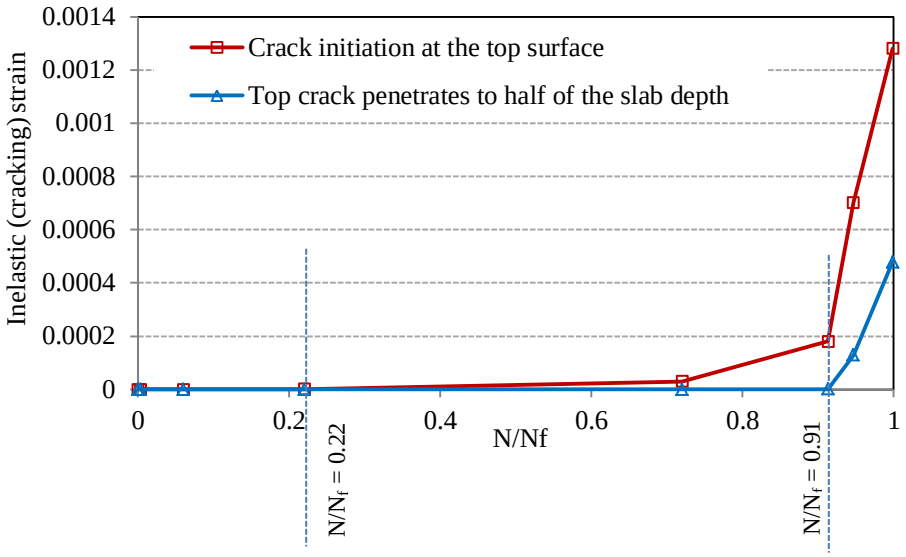

Figure 7.12 Crack initiation versus N/N_f, when shrinkage is ignored and a load factor 4.0 is applied

Figure 7.13 shows cracking strain versus N/N_f at the top surface and at half depth, when shrinkage is considered and a load factor 2.0 is applied. This figure shows that sudden crack widening occurs at the top surface when the first cycles are applied. The cracking strain then remains nearly constant till 70% of the fatigue life span is reached, and crack widening accelerates again afterwards (This behaviour is compatible with predictions previously performed in the literature (Chapter 2, Section 2.2)). The top surface crack penetrates to half depth at 91% of the designed life span, when a load factor 2.0 is applied.

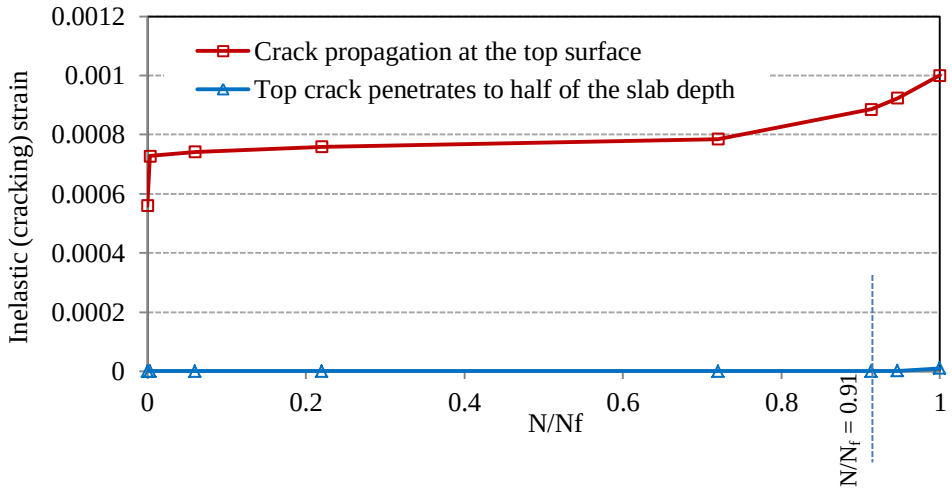

Figure 7.13 Crack propagation versus N/N_f, when shrinkage is considered and a load factor 2.0 is applied

This analysis showed that adopting the experimental fatigue damage evolution curve, the failure occurs at 91% of the designed fatigue life, when a load factor 4.0 and 2.0 is applied, with and without considering shrinkage, respectively. Although, to meet the 100% of the designed fatigue life (instead of 91%) the safety factors should be a bit lower than the assumed values, this analysis shows that the reduction in the load bearing capacity by around 50% due to shrinkage distress is confirmed again via this approach.

7.4 Conclusion

The effect of shrinkage distress on the fatigue performance was investigated via two approaches: Using the experimental fatigue endurance curve; and using the experimental fatigue damage evolution. Although, these two approaches are based on quite different concepts, both of them showed that the overall long-term load bearing capacity of the pavement can be overestimated by twice, if shrinkage distress is ignored. In other words, considering shrinkage the overall long-term load bearing capacity of the pavement is reduced by 50%.

The results of this chapter are valid for the given concrete compositions and under the assumed environmental conditions. For other concrete compositions, with various fibre contents and types, and under different environmental conditions different results are expectable.

Chapter 8

8 Discussion, conclusion and recommendations for future work

This chapter discusses the main results obtained in this thesis, and summarises the conclusions. Limitations of the work done are also identified and recommendations are given for future work.

8.1 Discussion and concluding remarks

This thesis aimed at understanding shrinkage behaviour of SFRC (CC and RCC) pavements incorporating recycled fibres in the way of developing design rules. R-SFR-RCC has been the main focus of this thesis to understand the restrained shrinkage behaviour of continuous pavements and its consequent effect on monotonic and cyclic load bearing capacity. Nevertheless, the results are adjustable to R-SFR-CC pavements and pavements using industrial fibres, if accounting for the difference in moisture transport, shrinkage properties and mechanical properties of concrete mixes. These differences were investigated experimentally for R-SFR-RCC and R-SFR-CC mixes and were compared with plain RCC and plain CC as reference mixes.

The experimental results, analyses and conclusions drawn from this study are valid under the assumed environmental conditions. The relative humidity of 40% assumed in this study is a medium to low value, while a wide range of environmental relative humidity is likely to occur in practice depending to the climate conditions of the construction site. The main conclusions drawn from this thesis are presented below.

8.1.1 Moisture transport mechanism and drying shrinkage properties (Chapter 3)

The flow of moisture in concrete subjected to drying is assumed to obey the diffusion equation especially when the moisture content decreases below 70 to 80% of initial saturation. The equation of moisture diffusion in concrete is equivalent to the equation of heat conduction, but the order of magnitude of corresponding coefficients is entirely different. Hence, FE modelling of moisture transport in concrete is usually performed by using heat transfer analysis code with modified coefficients. The corresponding coefficients (the diffusion coefficient and the surface factor) can be determined from experimental moisture measurements combined with inverse analysis. A modified gravimetric method was developed and adopted in the current research, for moisture measurement.

The relationship between moisture loss and free shrinkage strain ("hygral contraction coefficient") is required to determine drying shrinkage in concrete based on moisture transport. Once this material property is obtained it is applicable to any shape of concrete member and with any type of restraint. This coefficient can also be obtained through experimental measurements on free shrinkage specimens combined with inverse analysis.

8.1.2 Experimental studies (Chapter 4)

In terms of compressive strength and elastic modulus the following can be concluded:

- The compressive strength of CC mixes is a bit higher than RCC mixes, and the compressive strength of SFRC mixes is slightly higher than plain mixes. For SFR-RCC, the mean 28-days compressive strength obtained from cubes is 52 MPa and the mean 90-day compressive strength obtained from cylinders is 56 MPa. The compressive elastic modulus of RCC is 17% lower than that of CC.

In terms of flexural behaviour, and bending elastic modulus the following can be concluded:

- The LOP for SFR-RCC specimens is slightly higher than for SFR-CC specimens (by less than 10%). The LOP for plain RCC specimens is also higher than for plain CC specimens by 15-20%. The LOP for SFRC specimens is slightly higher than for plain specimens. The increase in the LOP as a result of adding fibres is bigger for CC mixes

compared with RCC mixes.

- For SFRC mixes, as expected, the residual flexural strengths are considerably higher than for plain mixes. The residual flexural strengths of SFR-RCC specimens are also higher than for SFR-CC specimens. For example $f_{R,2}$ for SFR-RCC is around 30% higher than for SFR-CC.

- The average bending elastic modulus is nearly the same for SFRC and plain mixes. The average bending elastic modulus of RCC mixes is slightly lower than CC mixes (less than 5%). The elastic modulus obtained from the bending tests for CC mixes are very close to the values obtained from the compressive tests on cylinders. However, the compressive elastic modulus of RCC mixes is considerably (16%) lower than the elastic modulus obtained from the bending tests. This was attributed to the effect of the mould boundaries on the compaction of RCC cylinders. Therefore, the analyses performed based on the bending elastic modulus.

In terms of moisture transport and shrinkage properties the following can be concluded:

- Concrete drying is shown to be a very slow process. After 85 days of drying at 40% relative humidity, the moisture content drops to the range of 65% to 70% at a depth of 10 mm from the drying surface for various mixes, while at a depth of 60 mm it only drops to around 99%, at the same time. The slow penetration of the drying front is attributed to the dense pore system of concrete.

- Drying in RCC mixes is faster than in CC mixes, due to the higher porosity of RCC. Drying in SFRC mixes is also faster than plain mixes, for the same reason. The rate of drying is relatively faster at the early stages and decreases with concrete aging.

- Free shrinkage of CC mixes at early ages occurs at a fast rate and then the rate considerably decreases, while for RCC mixes shrinkage occurs at a more uniform rate. This could be the reason for the lower short-term shrinkage for RCC reported in the literature compared to CC. In the current research, at the end of the experimental time period, shrinkage of the RCC mixes reached the value of shrinkage obtained for CC mixes and it is predicted to exceed it beyond that time.

- Free shrinkage of plain mixes is higher than that of SFRC mixes, at any time during the experimental measurements. This is attributed to the restraining effect of fibres. In the current research, this difference approaches zero at the end of the experimental time period. This means that the restraining effect of fibres is not high enough to cope with high shrinkage values.

8.1.3 Data processing analysis (Chapter 5)

In terms of moisture diffusivity, "hygral contraction coefficient" and surface factor obtained from inverse analysis of the experimental results the following can be concluded:

- Moisture diffusivity curves contain a nearly-horizontal branch, varying in the range of 0-5 mm^2/day, followed by a sharp increase. There are only small differences in moisture diffusivity of the various concrete mixes. The moisture diffusivity of RCC mixes is slightly higher than for CC mixes, and for SFRC mixes is slightly higher than for plain mixes, due to the higher porosity.

- The use of the diffusion theory as the single moisture transfer mechanism in concrete gives good accuracy at moisture contents lower than 75-80%. This reveals that for nearly saturated conditions bulk water flux also participates in moisture transport, although diffusion in the form of vapour flux is the governing mechanism in unsaturated concrete.

- The "hygral contraction coefficient" of CC mixes is higher than for RCC mixes for moisture contents higher than 80%, for both SFRC and plain mixes. This effect can be attributed to the higher restraining effect of crushed aggregates in RCC mixes. For moisture contents lower than 80% the "hygral contraction coefficient" of CC reaches that of RCC. The "hygral contraction coefficient" of SFRC mixes is generally lower than for plain mixes (RCC and CC). This effect is a result of the restraining effect of fibres.

- Surface factor can significantly affect the moisture profiles near the drying surface. Away from the drying surface, the effect of the surface factor on the moisture profiles is quickly diminished. To improve the accuracy of the back-calculated surface factors, the experimental values of the moisture variations at very close distance from the drying surface are required (which are not always possible to be measured). This issue was not dealt with in this study. However, the order of accuracy for the surface factor, in the

calculated range, does not have a significant effect on the final results, especially at the end of the drying period.

In terms of tension stiffening properties of SFRC (σ-ε models), obtained from inverse analysis of the flexural test results: the following can be concluded:

- Inverse analysis was performed via three numerical approaches (section analysis, FE analysis using CSC material model, and FE analysis using CDP material model) for the un-notched prisms. These approaches match very well after sufficient mesh refinement in the FE models.

- Mesh sensitivity is found when concentrated cracking occurs and the element size is larger than the size of the cracking zone. Therefore, mesh sensitivity also depends on the amount of reinforcement. The mesh sensitivity issue can be resolved by choosing element sizes smaller than the length of the cracking zone.

8.1.4 Pavement analysis under restrained shrinkage and monotonic loading (Chapter 6)

In terms of stress analysis of SFRC pavements under restrained shrinkage the following can be concluded:

- Surface micro-cracks are formed predominantly due to the curling of the slab. A nearly uniform cracking strain is produced in the middle part (along the length) of the slab decreasing towards the transversal free edge. Regarding the dominant direction of micro-cracks, the primary cracks include: 1) transversal surface cracks all over the slab; 2) diagonal surface cracks near the corner; and 3) longitudinal surface cracks near the middle of the transversal edge. Longitudinal surface cracks spread along the slab length as secondary cracks.

- The closely-spaced transversal micro-cracks in the middle part of the slab have an average opening density of 0.69 mm/m at the surface, which decreases to 0.5 mm/m at a depth of 25 mm and 0.19 mm/m at a depth of 50 mm from the surface. These cracking strains diminish gradually at bigger depths. The secondary longitudinal micro-cracks also

have an average opening density of 0.5 mm/m at the surface.

- Cracking at the top surface initiates from the beginning of drying, while at a depth of 37.5 mm, crack initiation occurs after 7 days of drying. The crack penetration reaches the depth of 62.5 mm after 225 days of drying. It is also observed that the cracking strain at the top surface approaches a constant value after 180 days of drying. This means that the shrinkage cracks at the surface stabilise after that time period.

- To estimate the order of neglected intrinsic creep, a comparison is made between the magnitude of cracking strain and elastic strain versus time. This comparison shows that intrinsic creep does not affect the strain results at the top surface by more than 7%. The dominant component of creep, which is micro-cracking creep, is automatically taken into account in the cracking model adopted for FE analysis. `

- Based on a hypothesis given by Bazant et al. (1982, 1979) and confirmed by Granger (1997, cited in Bisschop, 2002), the crack spacing in the studied SFR-RCC pavement is estimated in the range of 14 mm- 56 mm, with an opening in the range of 0.01 mm- 0.04 mm at the stabilised state of drying.

- A comparison between SFR-RCC and SFR-CC pavements shows that although cracking due to drying shrinkage in SFR-RCC is less than in SFR-CC at early days, it gets worse after a couple of months of drying. Therefore, the stress analysis under traffic load was focused on SFR-RCC, since the stabilised value of cracking strain for SFR-RCC is higher than that of SFR-CC.

- For the studied SFR-RCC pavement, the analysis shows that after drying shrinkage the tensile strength at the top surface reaches around 50% of the maximum tensile strength capacity of concrete. As a Comparison, using the estimation based on Concrete Society TR34 (2003) the tensile flexural strength must be reduced by around 30% to take into account the effect of drying shrinkage. The reduction of tensile flexural strength capacity in TR34 is applied proportional to the distance from the neutral axis (at half of the slab depth), whereas FE analysis shows that the strength loss mainly occurs in the top quarter of the slab depth.

- TR34 uses the average value of stress induced by internal and external restraints. However, the current study shows that the stress induced by the internal restraint (or

curling) is dominant, since the differential shrinkage creates an upward-curled shape slab, in which no external restraint is applied for a large part of the contact area due to separation. If the stress induced by curling (as the dominant mechanism) is replaced by the average value in TR34, the reduction in the tensile flexural strength would be in the range of 35-46% (average 40.5%). Further, the effect of the intrinsic creep was ignored in the FE analysis in the current research (estimated as 7%). Therefore, the differences in the reduction due to shrinkage between FE and TR34 can be mainly attributed to these issues.

- To evaluate the effect of any delay in drying of the concrete slab by extended curing, a comparison was made between the shrinkage behaviour of a hardened SFR-RCC pavement with an immature one. It was found that shrinkage strains are the same for hardened and immature concrete, since the "hygral contraction coefficient" has been assumed independent of concrete maturity. However, there is a difference in short-term stress development. In the short-term, the residual tensile strength of the hardened slab is higher than that of the immature slab. Cracking occurs in both cases, since the shrinkage stresses exceed the tensile strength of the concrete.

In terms of stress analysis of SFRC pavements under monotonic loading the following can be concluded:

- Top surface cracking is dominant in the case of corner loading. For the top surface, the "failure" load when shrinkage is ignored is twice of the "failure" load when shrinkage is included, for corner and edge loading.

- In the case of interior loading, bottom surface cracking becomes dominant. Since the slab is pre-stressed due to shrinkage and the bottom surface is under compression, the cracking load for interior loading only is lower than for interior loading plus shrinkage (the former one is 70% of the later one).

- Distress induced by drying shrinkage significantly increases the crack opening developed due to loading, although the effect of shrinkage distress does not initially seem significant in terms of visible cracks. For example, for corner loading the "equivalent crack opening" of 0.5 mm increases to 1.0 mm when drying shrinkage is considered, under the same load. For transversal edge loading, the "equivalent crack opening" of 0.1

mm, increases to 0.6 mm when considering drying shrinkage, under the same load.

8.1.5 Long-term fatigue analysis (Chapter 7)

In terms of investigating the effect of shrinkage distress on the long-term fatigue behaviour, using the experimental fatigue endurance curve, the following can be concluded:

- The minimum provided safety factor in the case of including shrinkage distress was 2.1, while it increased to a minimum of 4.1 when shrinkage was ignored. This shows that the overall long-term load bearing capacity of pavements can be overestimated by twice, if shrinkage distress is ignored.

- Examining allowable stress ratios for the studied pavement shows that the stress ratio should be kept below 0.44 for interior and transversal edge loading, and less than 0.52 for corner and longitudinal edge loading. Considering shrinkage distress, the permitted stress ratios are reduced further from 0.44 to 0.35 in the interior areas and to 0.24 in transversal edges (the transversal edge is dominant). The stress ratio should also be reduced from 0.52 to 0.27 for longitudinal edges and to 0.26 for corners (corner is dominant). Therefore, considering shrinkage in design of the pavement, the allowable stress ratio is reduced by around 50%.

In terms of investigating the effect of shrinkage distress on the long-term fatigue behaviour, using the experimental fatigue damage evolution:

- It was found that the failure occurs at 91% of the design fatigue life, when a load factor 2.0 and 4.0 is applied with and without considering shrinkage, respectively. Although to meet 100% of the design fatigue life (instead of 91%) the safety factors need to be slightly lower than the assumed values, the ratio of these safety factors shows that a reduction in the load bearing capacity by around 50% occurs due to shrinkage distress.

8.2 Limitations of the current research and suggestions for development of the work in the future

8.2.1 On the research approach

- Due to limitations in terms of time limit to complete the study and the absence of financial sources to conduct expensive experiments, it was not possible to undertake field studies or laboratory testing on pavements. However, as a suggestion for future development of the work, it would be quite useful to conduct large-scale tests to investigate restrained shrinkage and possibly its consequent effect on the fatigue deterioration, to verify the results obtained in the current research.

- In the current research the effect of autogenous shrinkage was not considered, due to its minor effect compared with drying shrinkage. However, for a more complete consideration, the effect of autogenous shrinkage can also be incorporated for further development of this work.

- In terms of drying creep, the micro-cracking component of drying creep was included in the current research, while the intrinsic component of creep was ignored. Based on the estimation made, the intrinsic drying creep was small compared with micro-cracking creep. The accumulation of shrinkage strain over time also curtails the time-dependant influence of intrinsic creep. Furthermore, the occurrence of intrinsic creep can only be significant prior to the formation of shrinkage micro-cracks, since after cracking deformation is released mainly through widening of micro-cracks. However, for more confidence, it is worth to take an approach for a reliable consideration of intrinsic creep.

- The other source of volumetric movement in concrete pavements is thermal variation inside the concrete slab. Thermal variation occurs as the result of heat generation due to hydration and being exposed to environmental conditions. Concrete initial temperature can also affect the maximum temperature reached inside the concrete pavement. Temperature is released in the same way as moisture, but at a faster rate. Thermal movement of the concrete slab can be minimised by controlling the maximum peak temperature reached, by using low heat cement and reducing the initial temperature. Volumetric movement due to temperature variation was not incorporated in the current

research, however it is recommended for future studies.

- Drying shrinkage investigated in the current research is relevant to the initial drying of concrete from saturation condition after casting, in which all pores and voids inside the concrete are filled with water, until concrete reaches a relative equilibrium with the environmental humidity. Seasonal rewetting and drying of the concrete was not accounted for in the current research. Previous studies (Pickett, 1956; Helmuth et al., 1967, Bisschop, 2002) have also shown that in the first time of drying the shrinkage strains are much bigger than when it is rewetted and dries for the second time. A large amount (as large as 60%) of the first time drying shrinkage cannot be recovered upon rewetting. However, for a more complete investigation of the effect of environmental factors on the behaviour of concrete pavements, seasonal rewetting and drying of the concrete slab can also be included.

- There is evidence in the literature showing that the flow of moisture in concrete subjected to drying mostly obeys the diffusion equation, based on vapour flux. However, the mechanisms of bulk water flux and vapour flux can more-or-less be coupled through the moisture transport in concrete, especially in highly saturated conditions. Therefore, to develop the current study in the future more precisely, it is worth considering bulk water flux as another mechanism of moisture transport in concrete.

8.2.2 On the assumptions

- In terms of hygral boundary conditions, in the current research the surrounding environment was assumed to have a constant relative humidity (40%). The top surface of the slab was considered to be exposed to the environment and other surfaces were assumed not to have any moisture interaction with the neighbouring domains. Although, the assumed environmental humidity is a medium value, a range of environmental relative humidity can be studied for a more complete investigation. More possible scenarios can also be considered for hygral boundary conditions. For example, moisture conduction through the bottom surface of the slab can also be modelled. Hygral interaction of the concrete slab with the foundation can be considered, in the case that the foundation material has the ability of absorbing water from the concrete slab.

- In this study, the shrinkage behaviour of continuous pavement (continuity in length) was

investigated. As a comparative study, the behaviour of short-length slabs can be evaluated. The effect of partial-depth joints (sawn or freshly-cut) can also be investigated, although it is predicted that the effect of partial-depth joints is quite local, and not significant in altering severity or distribution of uniformly-distributed shrinkage microcracks along the slab. However, the effect of these joints can be considerable in controlling irregular widening of shrinkage microcracks after loading, especially in the case of uniformly-spaced transversal cracks through the length of the pavement.

8.2.3 Suggestions for development of design guidelines

Comprehensive investigations in this research showed that the short-term and the long-term load bearing capacity of SFRC pavements can be overestimated by twice, when the effect of drying shrinkage on the performance of the pavement is ignored. To include this effect, a more sophisticated approach should be adopted in the design guidelines. This approach can be based on a combination of empirical studies and FE modelling, as followed in the current research, to cover a variety of pavement geometries, environmental conditions and material properties (e.g. for inclusion of industrial or recycled fibres with various percentage in RCC or CC mixes). Parametric studies can be performed consequently to develop appropriate design charts. The variable parameters can be defined in terms of geometry data (thickness, plan dimensions), moisture transport properties, shrinkage properties, tensile strength properties and foundation stiffness.

References

AASHTO (1986), “Guide for Design of Pavement Structures”, American Association of State Highway and Transportation Officials, Washington D.C.

ABAQUS (2010), Version 6.10, Dassault Systèmes Simulia Corp., Providence, RI, USA.

ACI 209R (1992), “Prediction of Creep, Shrinkage, and Temperature Effects in Concrete Structures”, American Concrete Institute, Detroit, USA.

ACI 215R (1992), “Considerations for Design of Concrete Structures Subjected to Fatigue Loading”, American Concrete Institute, Detroit, USA.

ACI 360R (1992), “Design of Slabs on Grade”, American Concrete Institute, Detroit, USA.

ACI 544.1R (1996), “State-of-the-Art Report on Fibre-Reinforced Concrete”, American Concrete Institute, Detroit, USA.

ACI 544.4R (1999), “Design Considerations for Steel Fibre Reinforced Concrete”, American Concrete Institute, Detroit, USA.

ACPA (2007), "Green Highways: Environmentally and Economically Sustainable Concrete Pavements", American Concrete Pavement Association; Concrete Pavement Research and Technology Special Report, Washington, USA.

ACPA (2002), "Stabilised Subbases and Airfield Concrete Pavement Cracking", American Concrete Pavement Association; Concrete Pavement Research and Technology Update, Washington, USA.

ACPA (2000), "A Comparison of Pavement Performance and Costs, Interstate 40, Tennessee", American Concrete Pavement Association; Report No. SR991P, Washington, USA.

Akita H., Fujiwara T., Ozaka Y. (1997). “A practical procedure for the analysis of moisture transfer within concrete due to drying”, Magazine of Concrete Research 49 (179): 129-137.

Alexander M.G. (1982), “A Simple Bending Test for Elastic and Rupture Moduli for Plain Concrete and Mortar”, Concrete/ Beton, South Africa 92(27): 18-24.

Altoubat S.A., Roesler J.R., Lange D.A., Rieder K. (2008), "Simplified Method for Concrete Pavement Design with Discrete Structural Fibres", Construction and Building Materials 22(3): 384-393.

Altoubat S.A., Lange D.A. (2003), "A New Look at Tensile Creep of Fibre Reinforced Concrete", ACI Special Publications (216): 143-160.

Altoubat S.A., Lange D.A. (2001), "Creep, Shrinkage and Cracking of Restrained Concrete at Early Age", ACI Materials Journal 98(4): 323–331.

Aly T., Sanjayan J.G., Collins F. (2008), "Effect of Polypropylene Fibres on Shrinkage and Cracking of Concretes", Materials and Structures 41 (10): 1741-1753.

Andrei R., Taranu N., Zarojanu H. Gh., Vlad N. V., Boboc V, Vrancianu I. D. and Nerges M. (2007), "State-of-the-Art Report on Design and Construction of Long Lasting Rigid Pavements-LLRP: WP3 (Pavement Testing, Analysis and Design)" Deliverable Report 3.1, FP6 EU STREP Project EcoLanes (031530), Ref. ECO/D3.1.

Graeff A. (2011), "Long-Term Performance of Recycled Steel Fibre Reinforced Concrete for Pavement Applications", PhD Thesis, University of Sheffield, UK.

Angelakopoulos H. (2012), "Steel-Fibre-Reinforced-Roller-Compacted-Concrete", PhD Thesis, University of Sheffield, UK.

Angelakopoulos H., Neocleous K. and Pilakoutas K. (2008[a]), "Wet Concrete Mix Optimisation for Selected Fibres", Deliverable Report 2.3b, FP6 EU STREP Project EcoLanes (031530), Ref. ECO/D2.3b.

Angelakopoulos H., Neocleous K. and Pilakoutas K. (2008[b]), "Concrete Mix Optimisation for Roller Compacted Concrete", Deliverable Report 2.4, FP6 EU STREP Project EcoLanes (031530), Ref. ECO/D2.4.

Angelakopoulos H., Neocleous K. and Pilakoutas K. (2008[c]), "Flexural testing of SFR-RCC and SFRC for all different types of fibres supplied", Deliverable Report 2.5, FP6 EU STREP Project EcoLanes (031530), Ref. ECO/D2.5.

Asad M., Baluch M.H., Al-Gadhib A.H. (1997), "Drying Shrinkage Stresses in Concrete Patch Repair Systems", Magazine of Concrete Research 49(181): 283-293.

Asad M. (1995), "Computational Modelling of Shrinkage in Repaired Concrete", A Thesis Submitted for Mater of Science, King Fahad University of Petroleum and Minerals,

Dhahran, Saudi Arabia.

ASTM C 1018 (1997), "Standard Test Method for Flexural Toughness and First-Crack Strength of Fibre-Reinforced Concrete (Using Beam with Third-Point Loading)", American Standards, USA.

ASTM C 157 (2008), "Standard Test Method for Length Change of Hardened Hydraulic Cement Mortar and Concrete", American Standards, USA.

Ayano T., Wittmann F.H. (2002), "Drying, Moisture Distribution, and Shrinkage of Cement-Base Materials", Materials and Structures 35(April): 134-140.

Balaguru P., Ramesh N., Patel M. (1992), "Flexural Toughness of Steel Fibre Reinforced Concrete", ACI Material Journal 89(6): 541-546.

Balaguru P., Ramakrishnan V. (1988), "Properties of Fibre Reinforced Concrete: Workability, Behaviour under Long-Term Loading, and Air-Void Characteristics", ACI Material Journal (May-June): 189-196.

Barros J.A.O., Gouveia A.V., Cruz J.M.S. Antunes J.A.B, Azevedo A.F.M. (2005), "Design Methods for Steel Fibre Reinforced Concrete Industrial Floors", International Conference on Construction Materials 3, Vancouver, Canada.

Barros J.A.O., Figueiras J.A. (2001), "Model for the Analysis of Steel Fibre Reinforced Concrete on Grade", Computers and Structures 79: 97-106.

Barros J.A.O. (1999), "Analysis of Concrete Slabs Supported on Soil", MĖTODOS NUMĖRICOS EN INGENIERĬA, R. Abascal, J. Dominguez y G, Bugeda (Eds.), SEMNI, Espaňa.

Barros J.A.O., Figueiras J.A. (1999), "Flexural Behaviour of SFRC: Testing and Modelling", Journal of Materials in Civil Engineering, ASCE 11(4): 331-339.

Barros J.A.O., Figueiras J.A. (1997), "Experimental Analysis of Fibre Reinforced Concrete Slabs", International Conference New Technologies in Structural Engineering (IABSE, FIP and LNEC), LNEC, Lisbon: 271-278.

Bazant Z. P., Raftshol W. J. (1982), "Effect of Cracking in Drying and Shrinkage Specimens", Cement and Concrete Research 12: 209-226.

Bazant Z.P., Ohtsubo H. (1979), "Stability and Post-Critical Growth of a System of Cooling or Shrinkage Cracks", International Journal of Fracture 15: 443-456.

Bazant Z.P., Najjar L.J. (1972), "Nonlinear Water Diffusion in Nonsaturated Concrete", Materials and Structures 5(25): 3-20.

Bazant Z.P., Najjar L.J. (1971), "Drying of Concrete as a Nonlinear Diffusion Problem", Cement and Concrete Research 1(5): 461-473.

Beckett D. (1999), "A Comparison of Thickness Design Methods for Concrete Industrial Ground Floors", 4th International Colloquium on Industrial Floor.

Beushausen H., Alexander M.G. (2006), "Failure Mechanisms and Tensile Relaxation of Bonded Concrete Overlays Subjected to Differential Shrinkage", Cement and Concrete Research 36: 1908-1914.

Bhatti M.A., Molinas-Vega I. Stoner J.W. (1998), "Nonlinear Analysis of Jointed Concrete Pavements", Transportation Research Record 1629, TRB: 50-57.

Bischoff P.H., Valsangkar A. J., Irving J. (2003), "Use of Fibres and Welded-Wire Reinforcement in Construction of Slabs on Ground", Practice Periodical on Structural Design and Construction, ASCE 8(1): 41-46.

Bischoff P.H., Valsangkar A. J., Irving J. (1998), "Concrete Slab-on-Grade Construction: To Reinforce or not", Proc., Canadian Society of Civil Engineering Annual Conf., Montreal ,Vol. IIIa: 309-318.

Bischoff P.H., Valsangkar A. J., Irving J. (1996), "Experimental Study of Concrete Floor Slabs on Grade", Proc., Canadian Society of Civil Engineering Annual Conf., Montreal, Vol. IIa: 273-282.

Bisschop J. (2002), "Drying Shribkage Micro-Cracking in Cement-Based Materials", PhD Thesis, Delft university of technology, ISBN 90-407-2341-9.

Bolander J.E, Berton S. (2004), "Simulation of Shrinkage Induced Cracking in Cement Composite Overlays", Cement & Concrete Composites 26(7): 861-871.

Boltzmann L. (1974), "Theoretical Physics and Philosophical Problems: Selected Writings". Reidel Pub. Co., Boston.

Bordelon A., Roesler J. (2009), "Fibre-Reinforced Concrete Pavement Design and Material Requirements", Proceedings of the 8th International Conference on the Bearing Capacity of Roads, Railways and Airfields (BCR2A'09), University of Illinois at Urbana Champaign, Illinois, USA, 717-727.

Bradbury R.D. (1938), "Reinforced Concrete Pavements", Wire Reinforcement Institute, Washington, D.C.

BS EN 12617-4 (2002), "Products and Systems for the Protection and Repair of Concrete Structures -Test Methods - Part 4: Determination of Shrinkage and Expansion", British Standards Institution, London, UK.

BS EN 12812 (2008), "Falsework-Performance Requirements and General Design", British Standards Institution, London, UK.

BS EN 12350-2 (2009), "Testing Fresh Concrete – Part 2: Slump Test", British Standards Institution, London, UK.

BS EN 12350-7 (2000), "Testing Fresh Concrete – Part 7: Air Content – Pressure Methods", British Standards Institution, London, UK.

BS EN 12390-3 (2009), "Testing of Hardened Concrete – Part 3: Compressive Strength of Test Specimens", British Standards Institution, London, UK.

BS EN 14488-3 (2006), "Testing Sprayed Concrete – Part 3: Flexural Strengths (First Peak, Ultimate and Residual) of Fibre Reinforced Beam Specimens", British Standards Institution, London, UK.

BS EN 14651 (2005), "Test Method for Metallic Fibered Concrete - Measuring the Flexural Tensile Strength (Limit of Proportionality (LOP), Residual", British Standards Institution, London, UK.

BS EN 1992-1-1 (2004), "Eurocode 2: Design of Concrete Structures, Part 1-1: General Rules and Rules for Buildings", British Standards Institution, London, UK.

BS ISO 1920-10 (2009), "Testing of Concrete, Part 10: Determination of Static Modulus of Elasticity in Compression", British Standards Institution, London, UK.

Burmister D.M, Palmer L.A., Barber E.S. (1943), "The Theory of Stress and Displacement in Layered Systems and Applications to the Design of Airport Runways", Highway Research Board Proceeding 23: 126-148, Washington DC.

Byfors J. (1980), "Plain Concrete at Early Ages", Research 3:80, Swedish Cement and Concrete Research Institute, Cement och Betong Institutet, Stockholm, Sweden.

Carlson R.W. (1937), "Drying Shrinkage of Large Concrete Members", ACI Journal 33(Jan.-Feb): 327-336.

Carlswärd J. (2006), "Shrinkage Cracking of Steel Fibre Reinforced Self Compacting Concrete Overlays", Doctoral Thesis, Luleå University of Technology, Department of Civil and Environmental Engineering, Sweden.

Casanova P., Rossi P. (1997), "Analysis and design of steel fibre reinforced concrete beams", ACI Structural Journal 94 (5): 595 – 602.

CEB-FIP Model Code (2010), "Design Code for Concrete Structures", First complete draft – Volume 1, International Federation for Structural Concrete (fib), Lausanne.

CEB-FIP ('90) Model Code (1993), "Design Code for Concrete Structures", Comite Euro-International Du Beton, Thomas Telford Services Ltd.

Channakeshava C., Barzegar F., and Voyiadjis G.Z. (1993), "Nonlinear FE Analysis of Plain Concrete Pavements with Doweled Joints", Journal of Transportation Engineering, ASCE 119(5): 763-781.

Chen D., Mahadevan S. (2007), "Cracking Analysis of Plain Concrete under Coupled Heat Transfer and Moisture Transport Process", Journal of Structural Engineering, ASCE 133(3): 400-410.

Chen S. (2004), "Strength of Steel Fibre Reinforced Concrete Ground Slabs", Proceeding of the Institution of Civil Engineering, Structures & Buildings I57, Issue SB2: 157-163.

Chern J.C, Young C.H. (1989), "Compressive Creep and Shrinkage of Steel Fibre Reinforced Concrete", The International Journal of Cement Composites and Lightweight Concrete 11(4): 205-214.

Clarke C. (2009), "Concrete Shrinkage Prediction Using Maturity and Activation Energy", Thesis Submitted for Master of Science, University of Maryland, College Park.

Concrete Society TR34 (2003), "Concrete Industrial Ground Floors; A Guide to Their Design and Construction", Technical Report No. 34, UK.

Cope R.J., Roa P.V., Clark L.A., Norris P. (1980), "Modelling of Reinforced Concrete Behaviour for Finite Element Analysis of Bridge Slabs", Numerical Methods for Nonlinear Problems, 1st Edition, Pineridge Press, Swansea 1: 457-470.

CORD (1992), "Catalogue of Road Defects", Highways Department: the Government of the Hong Kong Special Administrative Region, Publication No. RD/GN/015.

Cornelissen. (1984[a]), "Fatigue Failure of Concrete in Tension", Heron, Delft University of

Technology, The Netherlands.

Cornelissen. (1984[b]), "Constant-Amplitude Tests on Plain Concrete in Uniaxial Tension and Tension-Compression", Technical Report No. 5-84-1, Delft University of Technology, Stevin Laboratory, The Netherlands.

Darter M.I. (1977), "Design of Zero-Maintenance Plain Jointed Concrete Pavement", Federal Highway Administration, Report No. FHWA-RD-77-III, Vol. 1: Development of Design Procedures.

de Borst R., Nauta P. (1985), "Non-Orthogonal Cracks in Smeared Finite Element Model", Engineering Computations Journal 2: 35-46.

Delatte N.J. (2008), "Concrete Pavement Design, Construction, and Performance", Taylor & Francis, ISBN 0-203-96108-0.

Delatte N. (2004), "Simplified Design of Roller-Compacted Concrete Composite Pavement", Transportation Research Record: Journal of the Transportation Research Board (1896): 57-65.

Ecolanes (2006-2009), "Economical and Sustainable Pavement Infrastructure for Surface Transport", EU FP6 STREP project, Contract 031530, ecolanes.shef.ac.uk.

Elshaigh W.A. (2007), "Modelling the Behaviour of Steel Fibre Reinforced Concrete Pavements", Ph.D. Thesis, University of Pretoria.

EM 1110-3-142. (1984), "Engineering and Design: Airfield Rigid Pavement", U.S. Army Corps of Engineers, Engineer Manual. No . 1110-.3-142, DAEN-ECE-G. Washington D.C.

Embacher R.A. and Snyder M.B. (2001), "Life-Cycle Cost Comparison of Asphalt and Concrete Pavements on Low-Volume Roads Case Study Comparisons", Transportation Research Record (1749): 28-37.

Eyre J.R. (2006), "Membrane Action in Ground-Bearing Concrete Slabs", Proceeding of the Institution of Civil Engineering, Structures & Buildings 159(SB3): 153-163.

Fernandez-Gomez J., Landsberger G.A. (2007), "Evaluation of Shrinkage Prediction Models for Self-Consolidating Concrete", ACI Material Journal 104(5): 464-473.

FHWA (1993), "U.S. Tour of European Concrete Highways", Federal Highway Administration, Publication No. FHWA-SA-93-012, Washington, D.C.

Graeff A.G., Pilakoutas K., Neocleous K., Peres M.V. (2012), "Fatigue Resistance and Cracking Mechanism of Concrete Pavements Reinforced with Recycled Steel Fibres Recovered from Post-Consumer Tyres", Engineering Structures 45: 385-395.

Graeff A. (2011), "Long-Term Performance of Recycled Steel Fibre Reinforced Concrete for Pavement Applications", PhD Thesis, University of Sheffield, UK.

Granger L. (1997), "Thoughts about Drying Shrinkage: Experimental Results and Quantification of Structural Drying Creep", Materials and Structures 30: 588-598.

Granju J.L. (1996), "Thin Bonded Overlays: About the Role of Fibre Reinforcement on the Limitation of Their Debonding", Advanced Cement Based Materials 4: 21-27.

Grasley Z.C, Lange D.A. (2004), "Modeling Drying Shrinkage Stress Gradients in Concrete", Cement, Concrete, and Aggregates 26(2): 115-122.

Gribniak V., Kaklauskas G., Bacinskas D. (2008), "Shrinkage in Reinforced Concrete Structures: A Computational Aspect", Journal of Civil Engineering and Management, 14(1): 49-60.

Grzybowski M., Shah S.P. (1990), "Model to Predict Cracking in Fibre Reinforced Concrete due to Restrained Shrinkage", Magazine of Concrete Research 41(148): 125-135.

Hassan K.E., Chandler J.W.E., Harding H.M. and Dudgeon R.P. (2005), "New Continuously Reinforced Concrete Pavement Designs", Highways Agency: TRL Report TRL630, UK.

Helmuth R.A., Turk D.H. (1967), "The Reversible and Rrreversible Drying Shrinkage of Hardened Portland Cement and Tricalcium Silicate Paste", J PCA Res. Dev. Lab, 9 (2): 8-21.

Highways Agency (2006), "Design Manual for Roads and Bridges, Volume 7 –Pavement Design and Maintanance, Section 2 – Pavement Design and Construction, Part 3 – Pavement Design", HD 26/06, London, UK.

Hoff G. (1987), "Durability of Fibre Reinforced Concrete in a Severe Marine Environment", Fibre Reinforced Concrete Properties and Applications, SP-105, American Concrete Institute, Detroit, 997-1041.

Huang Y.H (2004), "Pavement Analysis and Design", University of Kentucky, ISEN 0-13-142473-4, Pearson Education, Inc.

Huang Y.H. (1993), "Pavement Analysis and Design", Prentice Hall, Englewood Cliffs, NJ.

Hughes B.P. (2003), "A New Look at Rigid Concrete Pavement Design", Proceeding of the Institution of Civil Engineers, Transport I56, Issue 1: 29-36.

Hveen F.N., Tremper B. (1957), "Some Factors Influencing Shrinkage of Concrete Pavements", Journal of ACI 53(2): 781-789.

Hwang C. L. and Young J. F. (1984), "Drying Shrinkage of Portland Cement Pastes. I. Microcracking during Drying", Cement and Concrete Research 14: 585-594.

JCI-S-001 (2003), "Method of Test for Fracture Energy of Concrete by Use of Notched Beam", Japan Concrete Institute Standard.

JCI-S-003 (2007), "Method of Test for Bending Moment–Curvature Curve of Fiber-Reinforced Cementitious Composites", Japan Concrete Institute Standard.

Jeong J.H. and Zollinger D.G. (2005), "Environmental Effects on the Behaviour of Jointed Plain Concrete Pavements", Journal of Transportation Engineering, ASCE 131(2): 140-148.

Jiang Y.J., Tayabji S.D. (1998), "Mechanistic Evaluation of Test Data from Long-Term Pavement Performance Jointed Plain Concrete Pavement Test Sections", Transportation Research Record 1629: 32-40, Washington D.C.

JSCE-SF1 (1984), "Recommendation for design and construction steel fibre reinforced concrete", Japan Society of Civil Engineers, Concrete Library.

JSCE-SF4 (1984), "Methods of Tests for Flexural Strength and Flexural Toughness of Steel Fibre Reinforced Concrete", Japan Society of Civil Engineers, Concrete Library.

Kim S.M., Won M.C., McCullough B.F. (1998), "Numerical Modelling of Continuously Reinforced Concrete Pavement Subjected to Environmental Loads", Transportation Research Record 1629: 76–89, Washington D.C.

Kodikara J., Chakrabarti S. (2005), "Modelling of Moisture Loss in Cementitiously Stabilised Pavement Materials", International Journal of Geomechanics, ASCE 5(4): 295-303.

Kupfer H., Hilsdrof H. K., Rusch H. (1973), "Behaviour of Concrete under Biaxial Stress", ACI 99(98): 656-666.

Kwon S.H., Shah S.P. (2008), "Prediction of Early-Age Cracking of Fibre-Reinforced Concrete due to Restrained Shrinkage", ACI Material Journal 105(4): 381-389.

Lee C.J., Lange D.A., Liu Y. (2010), "Prediction of Moisture Curling of Concrete Slab",

Materials and Structures 44 (4): 787-803.

Li C., Li K., Chen Z. (2008), "Numerical Analysis of Moisture Influential Depth in Concrete and Its Application in Durability Design", Tsinghua Science & Technology 13(S1): 7-12.

Li Z., Lara M.A.P., Bolander J.E. (2006), "Restraining Effects of Fibres during Non-Uniform Drying of Cement Composites", Cement and Concrete Research 36: 1643-1652.

Lim D.H., Nawy E.G. (2005), "Behaviour of Plain and Steel-Fibre-Reinforced High-Strength Concrete Under Uniaxial and Biaxial Compression", Magazine of Concrete Research 57(10): 603-610.

Liu J., Zollinger D.G. (2005). "Shrinkage Effect on the Stress Intensity Factors of Concrete Pavements at an Early Age", Proceeding the 8th Int'l Conference on Concrete Pavements, Colorado, USA.

Losberg A. (1961), "Design Methods for Structurally Reinforced Concrete Pavements", Transactions of Chalmers University of Technology Gothenburg, Sweden.

Luhr, D. R. (2004). "Design and Construction of Roller-Compacted Concrete Pavements for Container Terminals." Proc., Ports 2004: Port Development in the Changing World, S. A. Curtis, eds., ASCE, Reston, Va., 1–10.

Mangat P.S., Azari M.M, (1984), "A Theory for the Free Shrinkage of Steel Fibre Reinforced Cement Matrices", Journal of Material Science 19 (7): 2183-2194

Mayhew H.C., Harding H.M. (1987),"Thickness Design of Concrete Roads", Transport and Road Research Laboratory (TRRL): RR87, ISSN 0266-5247, UK.

McCullough B.F., Dossey T., Zollinger D. (2000), "Evaluation of the Performance of Texas Pavements Made with Different Coarse Aggregates", Texas Department of Transportation, Report No. TX-01/7-3925-1.

McCullough B.F., Rasmussen R.O. (1998), "Fast-Track Paving: Concrete Temperature Control and Traffic Opening Criteria for Bonded Concrete Overlays, Volume I: Final Report", FHWA-RD-98-167, Office of Infrastructure R&D, Federal Highway Administration.

McCullough B.F., Abou-Ayyash A., Hudson W.R., Randall J.P. (1975), "Design of Continuously Reinforced Concrete Pavements for Highways", Research Project NCHRP 1-15, Centre for Highway Research, The University of Texas at Austin, Austin, TX.

Meda A., Plizzari G. A. (2004[a]), "New Design Approach for Steel Fibre-Reinforced Concrete Slabs-on-Ground Based on Fracture Mechanics", ACI Structural Journal 101(3): 298-303.

Meda A., Plizzari G. A., Riva P. (2004[b]), "Fracture Behaviour of SFRC Slabs on Grade", Materials and Structures 37(6): 405-411.

Mensi R., Acker P., Attolou A. (1988), "Séchage du Béton: Analyse et Modélisation", Materials and Structures 21: 3-12.

Meyerhof G.G. (1962), "Load Carrying Capacity of Concrete Pavements", Journal of Soil Mechanics and Foundation Division, Proceeding of the American Society of Civil Engineers, 89-116.

Molinas-Vega I., Bhatti M.A, Nixon W.A. (1995), "A Non-Linear Fatigue Damage Model for Concrete in Tension", International Journal of Damage Mechanics 4: 362-379.

Musacchi E., Pierfelice M. (2008), "A Prototype Attachment for Producing Fibres Suitable for Concrete", Deliverable Report 1.4, FP6 EU STREP Project EcoLanes (031530), Ref. ECO/D1.4.

Musacchi E., Iacobucci P., Neocleous K., Angelakopoulos H., Pilakoutas K. (2007), "Classification of Fibres from Different Mechanical Treatments and the Reasons for Fibre Balling", Deliverable Report 1.2, FP6 EU STREP Project EcoLanes (031530), Ref. ECO/D1.2.

Nanni A, Johari A. (1989), "RCC Pavement Reinforced with Steel Fibres", Concrete International 64-69.

Nam J.H., Kim S.M., Won M.C. (2006), "Measurement and Analysis of Early-Age Concrete Strains and Stresses: Continuously Reinforced Concrete Pavement under Environmental Loading", Journal of Transportation Research Board (1947): 79-90.

NCHRP Report 372 (1995), "Support under Portland Cement Concrete Pavements", Transportation Research Board, Washington, D.C.

Neocleous K., Angelakopoulos H., Pilakoutas K. (2007), "Methodology for Statistical Analysis of the Length of Steel Tyre-Cord Fibres", Technical Report TR1.1, FP6 EU STREP Project EcoLanes (031530), Ref. REPORT ECO/ TR1.1.

Neocleous K., Tlemat H., Pilakoutas K. (2006), "Design Issues for Concrete Reinforced with

Steel Fibres, Including Fibres Recovered from Used Tires", Journal of Materials in Civil Engineering, ASCE 18(5): 677-685.

Oh B.H. (1991), "Cumulative Damage Theory of Concrete under Variable-Amplitude Fatigue Loadings", ACI Material Journal 88(1): 41-48.

Paskova T. and Meyer C. (1997), "Low-Cycle Fatigue of Plain and Fibre-Reinforced Concrete", ACI Material Journal 94(4): 273-285.

PCA (2006), "Roller-Compacted Concrete (RCC) Pavements", Portland Cement Association, http://www.cement.org/pavements/pv_rcc.asp.

PCA (1984), "Thickness Design for Concrete Highway and Street Pavements", Packard, P. E. (author) Skokie, Portland Cement Association.

PCA (1966), "Thickness Design for Concrete Pavements", Portland Cement Association, Publication No. IS010P.

Penev D., Kawamura M. (1991), "Moisture Diffusion in Soil-Cement Mixtures", Cement and Concrete Research 21(1); 137-146.

Pickett G. (1956), "Effect of Aggregates on Shrinkage of Concrete and a Hypothesis Concerning Shrinkage", Journal of ACI 52(5): 581-590.

Pickett G. (1946), "Shrinkage Stresses in Concrete", Journal of ACI 17 (3): 165-204.

Pickett G. (1942), "The Effect of Change in Moisture Content on the Creep of Concrete under a Sustained Load ", Journal of ACI 38: 333-356.

Pihlajavaara S.E. (1965), "On the Main Features and Methods of Investigation of Drying and Related Phenomena in Concrete", PhD Thesis, Publ. No. 100, State Institute for Technical Research, Helsinki.

Pihlajavaara S.E., Vaisanen J. (1965), "Numerical Solution of Diffusion Equation with Diffusivity Concentration Dependent", Publ. No. 87, State Institute for Technical Research, Helsinki.

Pilakoutas K., Neocleous K., Tlemat H. (2004), "Reuse of Tyre Steel Fibres as Concrete Reinforcement", Proceedings of the Institution of Civil Engineers, Engineering Sustainability 157, Issue ES3: 131-138.

Pilakoutas K., Strube R. (2001), "Reuse of Tyre Fibres in Concrete", Procs International Symposium Recycling and Re-use of Used Tyres, Dundee (Thomas Tleford, London):

225-236.

Pittman D.W. and Steven A.R. (1998), "Drying Shrinkage of Roller-Compacted Concrete for Pavement Applications", ACI Materials Journal 95(1): 19-26.

Pittman D.W. (1996), "Load Transfer Characteristics of Roller-Compacted Concrete Pavement Joints and Cracks", Transportation Research Board 1525.

Poblete M., Salsilli R., Valenzuela R., Bull A. and Spratz P., (1989), "Field Evaluation of Thermal Deformations in Undowelled PCC Pavement Slabs", Transportation Research Record 1207.

Rahman M.K., Baluch M.H., Al-Gadhib A.H. (2000), "Simulation of Shrinkage Distress and Creep Relief in Concrete Repair", Composites: Part B, 31: 541-553.

Rahman M.K., Baluch M.H., Al-Gadhib A.H. (1999), "Modeling of Shrinkage and Creep Stresses in Concrete Repair", ACI Material Journal 96(5): 542-551.

RILEM TC 162 TDF (2002), "Test and Design Method for Steel Fibre Reinforced Concrete-Final Recommendations: Bending Test", Materials and Structures 35(253): 579-582.

RILEM TC 162-TDF (2000), "Test and Design Methods for Steel Fibre Reinforced Concrete: σ-ε Design Method", Materials and Structures 33(225): 75-81.

Roa K.S.S., Singh S. (1986), "Concentrated Load Carrying Capacity of Concrete Slabs on Ground", Journal of Structural Engineering, ASCE 112(12): 2628-2645.

Roesler J.R., Hiller J.E., Littleton P.C. (2005), "Large-Scale Airfield Concrete Slab Fatigue Tests", International Journal of Concrete Pavements (IJCP) 1(1): 66-87.

Roesler J. R., Lang D. A., Altoubat S. A., Rieder K.A., Ulreich G. R. (2004), "Fracture of Plain and Fibre-Reinforced Concrete Slabs under Monotonic Loading", Journal of Material in Civil Engineering, ASCE 16(5): 452-460.

Roesler J.R. (1998), "Fatigue of Concrete Beams and Slabs", Ph.D. Thesis, University of Illinois, Urbana, Illinoise.

Rogers M. (2003), "Highway Engineering", ISBN 0-632-05993-1, Blackwell Publishing Ltd, Oxford.

Rollings R.S. (2005), " Why Do Our Concrete Pavements Still Fail?", Proceedings of the 8th International Conference on Concrete Pavements, Volume I, Colorado Springs,

CO: International Society for Concrete Pavements, 167–180.

Rollings R.S. (1993), "Curling Failures of Steel-Fiber-Reinforced Concrete Slabs", Journal of Performance of Constructed Facilities 7(1): 3-19.

Rollings R.S. and Witczak M. (1990), "Structural Deterioration Model for Rigid Airfield Pavements", Journal of Transportation Engineering, ASCE 116(4): 479-491.

Rollings R.S. (1988), "Design of Overlays for Rigid Airfield Pavements": Final Report, DOT/FAA/PM-87/19, Federal Aviation Administration, Washington, D.C.

Romualdi J.P., and Batson G.B. (1963), "Mechanics of Crack Arrest in Concrete", Proceedings, ASCE 89(EM3): 147-18.

Rots J.G. (1988), "Computational Modelling of Concrete Fracture", PhD Thesis, Delft University of Technology, Netherlands.

Ruiz M., Rasmussen R.O., Chang G.K., Dick J.C., Nelson P.K. (2006), "Computer-Based Guidelines for Concrete Pavements; Volume III: Technical Appendices", US Department of Transportation, Federal Highway Administration, Publication No. FHWA-HRT-04-127.

Ruiz M., Rasmussen R.O., Chang G.K., Dick J.C., Nelson P.K. (2005[a]), "Computer-Based Guidelines for Concrete Pavements; Volume I: Project Summary", US Department of Transportation, Federal Highway Administration, Publication No. FHWA-HRT-04-121.

Ruiz M., Rasmussen R.O., Chang G.K., Dick J.C., Nelson P.K. (2005[b]), "Computer-Based Guidelines for Concrete Pavements; Volume II: Design and Construction Guidelines and HIPERPAVE II User's Manual", US Department of Transportation, Federal Highway Administration, Publication No. FHWA-HRT-04-122.

Sa C., Benboudjema F., Thiery M., Sicard J. (2008), "Analysis of Microcracking Induced by Differential Drying Shrinkage", Cement & Concrete Composites 30: 947-956.

Sakata K., Shimomura T. (2004), "Recent Progress in Research on and Evaluation of Concrete Creep and Shrinkage in Japan", Journal of Advanced Concrete Technology 2(2): 133-140.

Sakata K. (1983), "A Study on Moisture Diffusion in Drying and Drying Shrinkage of Concrete", Cement and Concrete Research 13(2): 216-224.

Selih J., Sousa A.C.M., Bremner T.W. (1996), "Moisture Transport in Initially Fully

Saturated Concrete During Drying", Transport in Porous Media 24: 81-106.

Seow P.E.C, Swaddiwudhipong S. (2005), "Failure Surface for Plain Concrete and SFRC under Multiaxial Load-a Unified Approach", ASCE, J. Mater. Civ. Eng. 17(2): 219-228.

Shaw Q.H.W. (2010), "The Early Behaviour of RCC in Large Dams", International Journal of Hydropower and Dams 17(2): 83-90.

Silliman K.R, Newtson C. (2006), "Effect of Misting Rate on Concrete Shrinkage", Proc. of HPC: Build Fast, Build to Last, Concrete Bridge Conference, Reno, Nevada, PCA.

Smith K.D., Peshkin D.G. Darter M.I, Mueller A.L., Carpenter S.H. (1990), "Performance of Jointed Concrete Pavements, Volume V- Appendix B: Data Collection and Analysis Procedures", FHWA-RD-89-140, Federal Highway Administration, Washington, DC.

Sorelli L.G., Meda A., Plizzari G.A. (2006), "New Design Approach for Steel Fibre-Reinforced Concrete Slabs-on-Ground Based on Fracture Mechanics", ACI Structural Journal 103(4): 551-558.

Suh Y.C., Hankins K., McCullough B.F. (1992), "Early-age Behaviour of Continuously Reinforced Concrete Pavement and Calibration of the Failure Prediction Model in the CRCP-7 Program", Research Report 1244-3, Centre for Transportation Research, The University of Texas at Austin, Austin, TX.

Swaddiwudhipong S., Seow P.E.C (2006), "Modelling of Steel Fibre-Reinforced Concrete Under Multi-Axial Loads", Cement and Concrete Research 36: 1354-1361.

Swamy R.N., Stavrides V. (1979), "Influence of Fibre Reinforcement on Restrained Shrinkage and Cracking", ACI Journal 76(3): 443-460.

Tan K.H., Paramasivam P.,Tan K.C. (1994), "Creep and Shrinkage Deflections of RC Beams with Steel Fibres", Journal of Materials in Civil Engineering, ASCE 6(4): 474-494.

Tatnall P.C., Kuitenbrouwer L. (1992), "Steel Fibre Reinforced Concrete in Industrial Floors", Concrete Int: 43-47.

Thom N. H., Thompson I., Peaston, C. H. (2000), "Use of Steel Fibre Reinforcement in Cement Treated Base", 4th International RILEM Conference on Reflective Cracking in Pavements, Ottawa, U.S.A., 413-422.

Timoshenko, S.P. and Goodier, J.N. (1970), "Theory of Elasticity", 3rd Edition, McGraw Hill, New York.

Titus-Glover L., Owusu-Antwi E.B., Hoener T., Darter M.I. (1998), "Design and Construction of PCC Pavements, Volume II: Design Features and Practices that Influence Performance of Pavements", FHWA-RD-98-127, Federal Highway Administration, Washington, DC.

Tlemat, H., Pilakoutas, K & Neocleous, K. (2006), "Stress-Strain Characteristic of SFRC Using Recycled Fibres", Materials and Structures 39(3): 365-377.

Tlemat H. (2004), "Steel Fibres from Waste Tyres to Concrete: Testing, Modelling and Design", Ph.D. Thesis, Department of Civil and Structural Engineering, University of Sheffield, UK.

Tlemat, H., Pilakoutas, K. & Neocleous, K. (2003[a]), "Flexural Toughness of SFRC Made with Fibres Extracted from Tyres", Recycling and Reuse of Waste Materials: Proceedings of International Symposium on Advances in Waste Management and Recycling, Dundee (Thomas Telford Ltd, London), 365–374.

Tlemat, H., Pilakoutas, K. & Neocleous, K. (2003[b]), "Pull-out Behaviour of Steel Fibres Recycled from Used Tyres", Role of Concrete in Sustainable Development, Proceedings of International Symposia on Celebrating Concrete: People and Practice, Dundee (Thomas Telford Ltd, London), 175–184.

UFC (2004) (Unified Facilities Criteria, UFC 3-250-01FA), "Pavement Design for Roads, Streets, Walks, and Open Storage Areas", U.S. Army Corps of Engineers, TM 5-822-5/AFM 88-7, Chapter 1, Department of the Army and the Air Force, Washington, DC.

USFD (2001). "Thin Wire Reinforcement for Concrete". British Patent Application No 0130852.7 and 0511012.7 (filed by the University of Sheffield on 24/12/01 and published on 9/11/2005), Sheffield, UK.

Vondran G.L. (1991), "Application of Steel Fibre Reinforced Concrete", Concrete International 13(11): 44-49.

Walker D. (2002), "Concrete Roads", Wisconsin Transportation Information Centre, Madison.

Wang K., Shah S.P., Phuaksuk P. (2001) "Plastic Shrinkage Cracking in Concrete Materials-Influence of Fly Ash and Fibres", ACI Material Journal 98(6): 458-464.

Westergaard H.M. (1948), "New Formulas for Stresses in Concrete Pavements of Airfield",

Trans ASCE 113(2340): 425-444.

Westergaard H.M. (1926), "Stresses in Concrete Pavements Computed by Theoretical Analysis", Journal of Public Roads 7(2): 25-35.

Westergaard H.M. (1925), "Theory of Stresses in Road Slabs", Proceeding, Fourth Annual Meeting of the Highway Research Board.

Wilson G.W., Fredlund D.G., Barbour S.L. (1994), "Coupled Soil-atmosphere modelling for soil evaporation", Canadian Geotechnical Journal 31(2): 151-161.

Winkler E. (1867), "Die Hehre von der Elastizitat und Festigkeit" (The Theory of Elasticity and Stiffness), H.Dominicus, Prague.

Wittmann F.H. (2001), "Mechanisms and Mechanics of Shrinkage", In Proc. of the 6th Int. Conf. of Creep, Shrinkage and Durability Mechanics of Concrete and Other Quasi-Brittle Materials, Boston, USA, 3-12.

Wittmann X., Sadouki H., Wittmann F.H. (1989), "Numerical Evaluation of Drying Test Data", Transaction 10th Int. Conf. on Struct. Mech. in Reactor Techn., Vol Q, 71-79.

Wong S.F., Wee T.H., Swaddiwudhipong S., Lee S.L. (2001), "Study of Water Movement in Concrete", Magazine of Concrete Research 53(3): 205-220.

Xi Y., Bazant Z.P., Jennings H.M. (1994), "Moisture Diffusion in Cementitious Materials-Moisture Capacity and Diffusivity", Advanced Cement Based Materials 1(6): 258-266.

Xin D., Zollinger D,G, Allent G.D. (1995), "An Approach to Determine Diffusivity in Hardened Concrete Based on Measured Humidity Profiles", Advanced Cement Based Materials 2: 138-144.

Ye D., Zollinger D.G., Morian D.A. (2007), "Characterisation and Aanalysis of Early Age Concrete Pavement Behaviour at the National Airport Pavement Test Facility (NAPTF)", IPRF Research Report, Innovative Pavement Research Foundation, Report IPRF 01-G-002-04-2(s), Texas Transportation Institute.

Yin W.S., Su E.C.M., Mansour M.A., Hsu T.T.C. (1989), "Biaxial Tests of Plain and Fibre Concrete" ACI Material Journal 86(3): 236-243.

Yuan Y., Wan Z.L. (2002), "Prediction of Cracking within Early-Age Concrete due to Thermal, Drying and Creep Behaviour" Cement and Concrete Research 32: 1053-1059.

Zhang J., Leng B. (2004), "Analysis of Shrinkage-Induced Stresses in Concrete Pavements",

Magazine of Concrete Research 56(10): 585-595.

Zhang J., Li V.C. (2001[1]), "Influence of Supporting Base Characteristics on Shrinkage-Induced Stresses in Concrete Pavements", Journal of Transportation Engineering, ASCE 127(6): 455-462.

Zhang J., Li V.C. (2001[2]), "Influence of Fibres on Drying Shrinkage of Fibre-Reinforced Cementitious Composite", Journal of Engineering Mechanics, ASCE 127(1): 37-44.

SHRINKAGE BEHAVIOUR OF STEEL-FIBRE-REINFORCED-CONCRETE PAVEMENTS

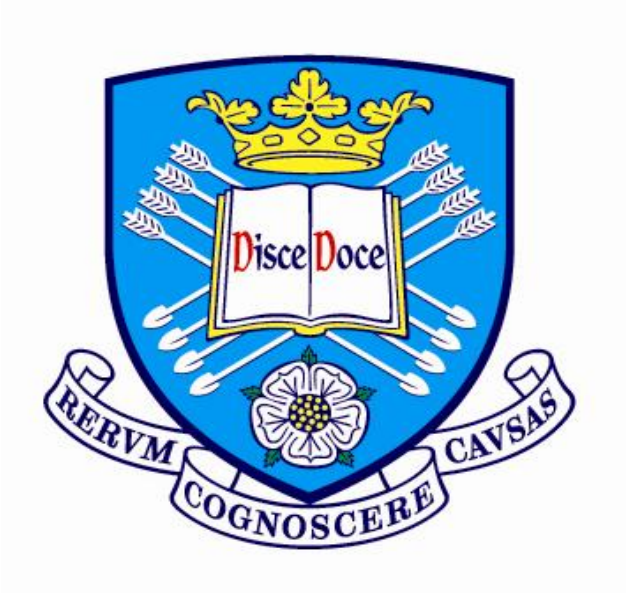

A thesis submitted for the degree of Doctor of Philosophy

By

Naeimeh Jafarifar

(BSc, MSc)

Department of Civil and Structural Engineering

The University of Sheffield

Sheffield

November, 2012

APPENDICES

Appendix A: Analytical solution for 1D moisture diffusivity equation

Assuming a one-dimensional moisture transport, the non-linear moisture diffusion equation is as follows:

$$\frac{\partial C}{\partial t} = \frac{\partial}{\partial x}[K_c(C)\frac{\partial C}{\partial x}] \qquad \text{(Eq. A.1)}$$

The parameters are as defined in Chapter 3. By introducing a single variable $(x,t) = x/\sqrt{t}$, called Boltzmann's transformation (1974), the above differential equation is reduced to an ordinary differential equation in τ as follows (Asad et al., 1997; Sakata, 1983; Penev et al., 1991):

$$-\frac{1}{2}\tau\frac{\partial C}{\partial \tau} = \frac{\partial}{\partial \tau}[K_c(C)\frac{\partial C}{\partial \tau}] \qquad \text{(Eq. A.2)}$$

Assuming the following initial and boundary conditions:

Initial condition: $C = 1 \qquad for \quad x > 0\,, \;\; t = 0$

Boundary condition: $C = C_1 \qquad for \quad x = 0\,, \;\; t > 0$

For any moisture content C_1, moisture diffusivity, K_c, is given as follows:

$$K_c]_{C=C_1} = \frac{-\frac{1}{2}\int_1^{C_1}\tau.dc}{\frac{dC}{d\tau}]_{C=C_1}} \qquad \text{(Eq. A.3)}$$

Having the above equation and the moisture content profiles, $C(x,t)$, the moisture diffusivity is determined as a function of the moisture content. From the experimental results, for any given *x* and *t*, τ is calculated and is plotted in a diagram versus the relevant value of C, and closed-form functions can be fitted to this diagram.

Some of these typical functions presented by Penev et al. (1991) (Eq. A.4 and Eq. A.5), Sakata (1983) (Eq. A.6) and Akita et al. (1997) (Eq. A.7) are as follows:

$$c(\tau) = [1 - \frac{p^2}{p^2+\tau^2}] \qquad \text{(Eq. A.4)}$$

$$c(\tau) = [1 - \exp(a\tau^b)] \qquad \text{(Eq. A.5)}$$

$$c(\tau) = [1 - (\frac{a-\tau}{b})n] \qquad \text{(Eq. A.6)}$$

$$c\ \tau\ = [a - \frac{b}{(\tau+n)^2}] \qquad \text{(Eq. A.7)}$$

Where p is the value of τ at 50% moisture loss; a, b and n are regression coefficients.

Using each of these equations to find the best regression with experimental data or using numerical integration it is possible to obtain the required variables and substitute them in the Eq. A3 to calculate the diffusivity factor, K_c, as a function of the moisture content C.

Additionally, some other investigators have proposed different forms of analytically or empirically estimated functions defining dependency of K_c on C. Those functions are as follow:

- The S-shaped function proposed by Bazant et al. (1971) (Eq. A.8):

$$K_C(C) = p_1 + \frac{p_2 - p_1}{1 + (\frac{1-C}{1-p_3})^{p_4}} \qquad \text{(Eq. A.8)}$$

Where p_1 is the diffusion coefficient in oven-dried condition ($C = 0$), p_2 is the diffusion coefficient in saturated condition (C = 100%), p_3 is the moisture content at inflection point of the curve (where the curve K_C drops, Bazant et al. found for most concretes this parameter is notably about *p3=0.75)*, and p_4 is a fitting parameter which is usually in the range of 6 to 16.

This function has been widely used afterwards. In CEB-FIP ('90) model code (1993) this function has been proposed for evaluation of moisture diffusion coefficient in isothermal conditions.

- The hyperbolic function proposed by Penev et al. (1991) (Eq. A.9):

$$K_C(C) = p_1 + a(\frac{C}{1-C})^b \qquad \text{(Eq. A.9)}$$

Where a and b are fitting parameters.

- The power function proposed by Pihlajavaara et al. (1965) (cited in Wittmann et al., 1989) (Eq. A.10) and Xi et al. (1994) (cited in Kwon et al. (2008)) (Eq. A.11):

$$K_C(C) = p_1 + p_2 C^{p_3} \qquad \text{(Eq. A.10)}$$

$$K_C(C) = p_1 + p_2[1 - 2^{-10^{p_3(c-1)}}] \qquad \text{(Eq. A.11)}$$

- The exponential function proposed by Li et al. (2006) and Mensi et al.(1988) (cited in Wittmann et al., 1989) (Eq. A.12), Penev et al. (1991) (Eq. A.13) and Ayano et al. (2002) (Eq. A.14):

$$K_C(C) = p_1 \exp(p_2 C) \qquad \text{(Eq. A.12)}$$

$$K_C(C) = p_1 \exp(p_2 C^b) \qquad \text{(Eq. A.13)}$$

$$K_C(C) = p_1 \exp(p_2 (1 - C)) \qquad \text{(Eq. A.14)}$$

- The trigonometric function proposed by Rahman et al., 2000 (Eq. A.15):

$$K_C(C) = a.\tan(b.C^n) \qquad \text{(Eq. A.15)}$$

Maybe it is not generally decidable that which of the above mentioned equations or any new one is the most appropriate. Although a common property of all of those is that the function $K_C = K_C(C, p_1, p_2, \ldots, p_k)$ is differentiable until the 2nd order with respect to C and parameters $p_1, p_2, \ldots, p_k$ (Wittmann et al. 1989).

Appendix B: Derivation of equation for moisture content in the gravimetric method

For this purpose the concrete specimen *i* of the height h_i is assumed (Figure B1 (a)).

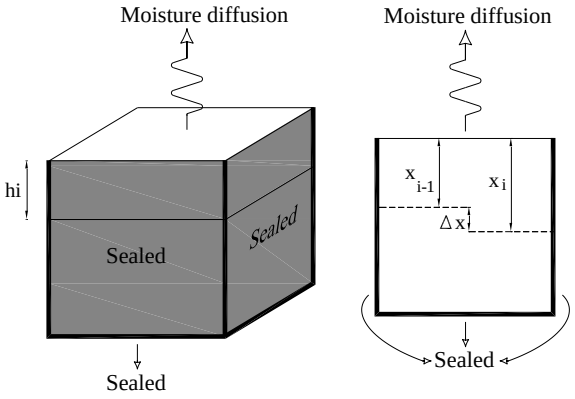

Figure B1 (a) Concrete specimen *i* in formulation of the moisture content; (b) Variable depth *x* in formulation of the moisture content

Diffusible moisture per unit volume for the specimen *i* is calculated as follows:

$$\gamma_{0i} = \frac{W_{0i} - W_{fi}}{h_i . S} \qquad \text{(Eq. B.1)}$$

Where h_i is the height of the specimen; W_{0i} is the weight of the specimen at the beginning of drying; W_{fi} is the weight of the specimen finally after drying in the oven; and S is the area of the drying surface.

Theoretically, diffusible moisture per unit volume should be the same for different height specimens (γ_0).

The moisture loss in the body of the specimen *i* up to time *t*, M_{ti}, is as Eq. B.2, and the moisture flux (remained moisture that can be potentially lost) in the specimen *i* at time *t*, q_{ti}, is as Eq. B.3.

$$M_{ti} = W_{0i} - W_{ti} \qquad \text{(Eq. B.2)}$$

$$q_{ti} = \gamma_0 . h_i . S - M_{ti} \qquad \text{(Eq. B.3)}$$

Where, W_{ti} is the weight of the specimen at time *t*.

Assuming the above notations, the moisture content, $C(x,t)$, as the percentage of initial diffusible moisture, at any depth x_i (Figure B1 (b)) and at time *t* is formulated as Eq. B.4:

$$C(x_i,t) = \frac{q_{ti} - q_{t(i-1)}}{\gamma_0.S.(x_i - x_{i-1})} \times 100 = \frac{(\gamma_0.h_i.S - M_{ti}) - (\gamma_0.h_{i-1}.S - M_{t(i-1)})}{\gamma_0.S.(h_i - h_{i-1})} \times 100$$

$$= \left[1 - \frac{(M_{ti} - M_{t(i-1)})}{\gamma_0.S.(h_i - h_{i-1})}\right] \times 100 \qquad \text{(Eq. B.4)}$$

Using the above formulation and measuring the weights of the various length specimens at frequent time steps it is possible to extract the time history of moisture profiles for any given concrete mix. The next step is to determine the nonlinear moisture diffusivity using these profiles.

Appendix C: Experimental test results

C.1. Compressive strength test results

C.1.1 Cubes

Table C.1 Compressive strength test results: Cubes

Mix type	Specimen No.	Ultimate load (kN)	Ultimate pressure (MPa)
SFR-RCC (2.5% recycled steel fibres)	1	1184.2	52.6
	2	1133.1	50.4
	3	1175.1	52.2
	Average	1164.1	51.7
SFR-CC (2.5% recycled steel fibres)	1 (Rejected)	1153.0	51.2
	2	1362.1	60.5
	3	1362.9	60.6
	Average	1362.5	60.6
Plain RCC	1	1045.4	46.5
	2	1130.4	50.2
	3	1121.5	49.8
	Average	1099.1	48.9
Plain CC	1	1320.0	58.7
	2	1258.4	55.9
	3	1341.9	59.6
	Average	1306.8	58.1

(Loading rate = 0.25MPa/s; Loading area = 22500 mm^2; Loading age = 28 days)

C.1.2 Cylinders

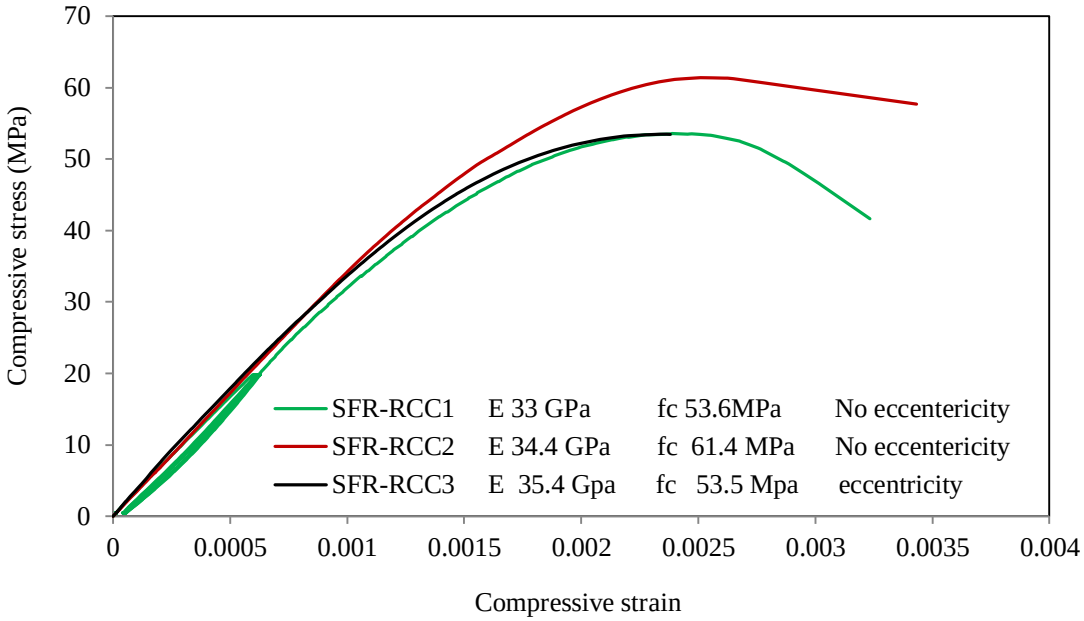

Figure C1 Compressive strength test results: Cylinders, SFR-RCC (2.5% recycled fibres)

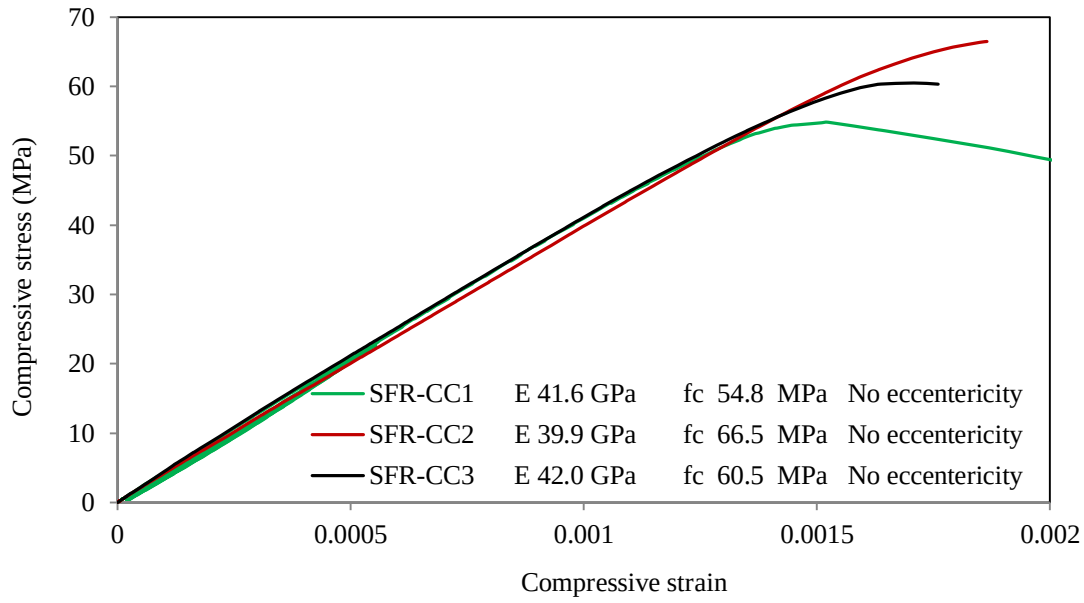

Figure C2 Compressive strength test results: Cylinders, SFR-CC (2.5% recycled fibres)

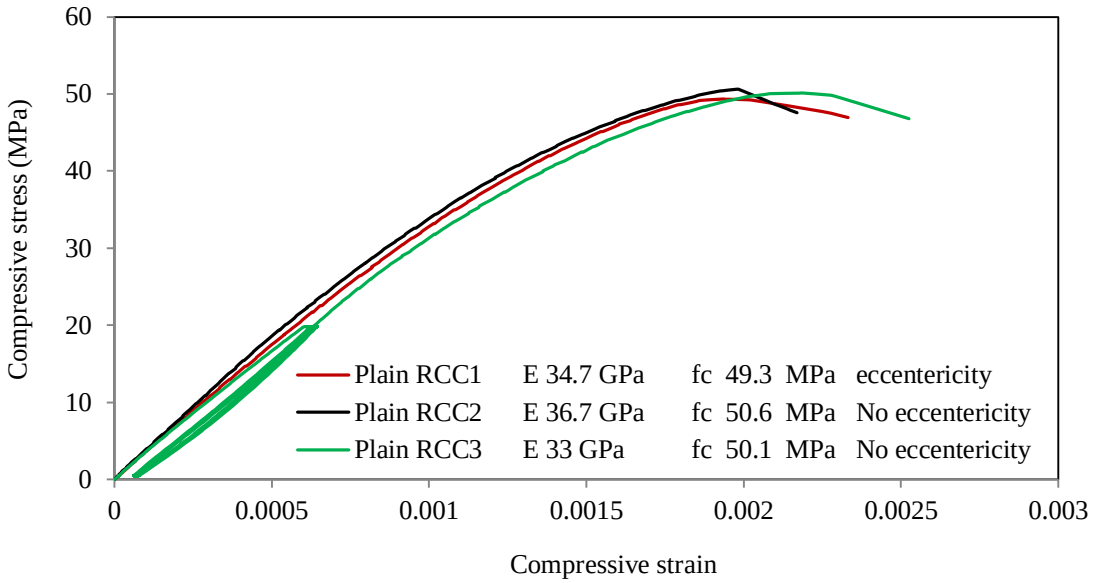

Figure C3 Compressive strength test results: Cylinders, Plain RCC

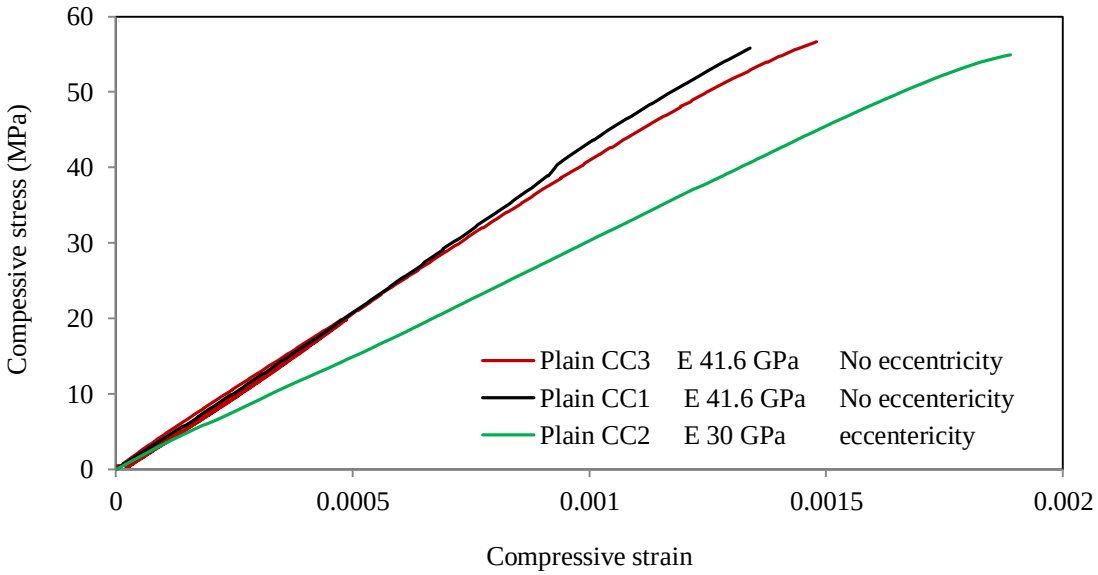

Figure C4 Compressive strength test results: Cylinders, Plain CC

C.2. Bending test results

C.2.1 Notched prisms

The experimental load-deflection curves and the calculated flexural modulus of elasticity curves for the notched prisms are shown in Figure C5 to C8, for different concrete mixes.

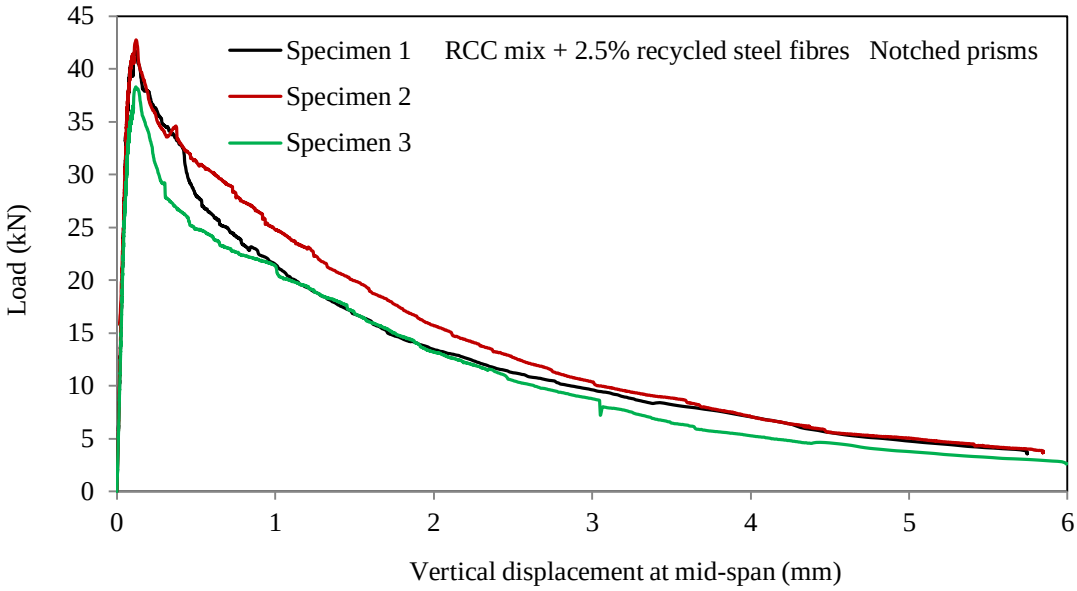

(a)

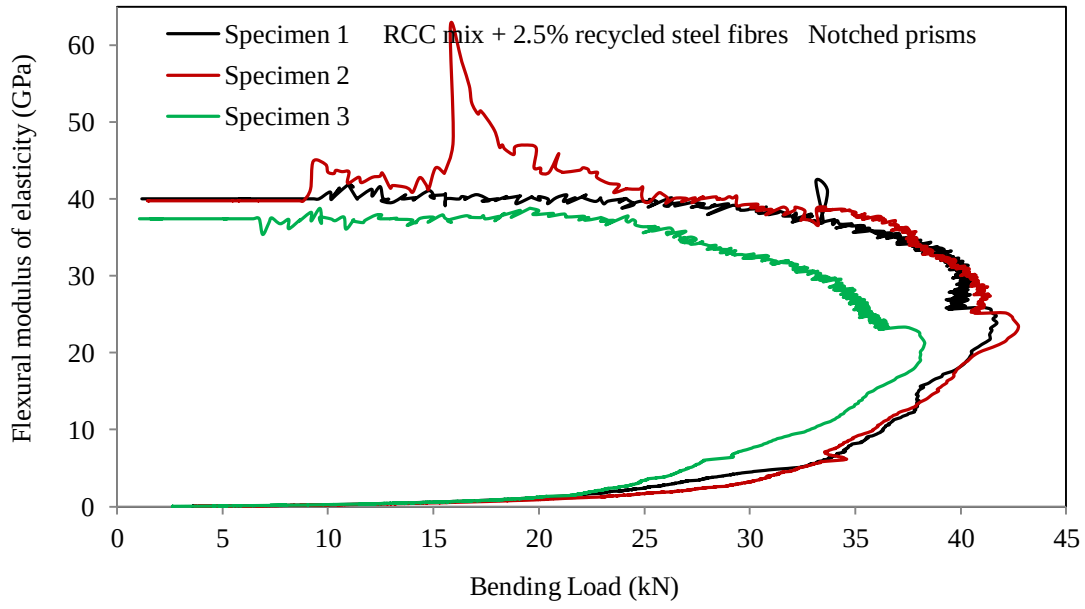

(b)

Figure C5 (a) Load-vertical deflection; (b) Flexural modulus of elasticity for SFR-RCC notched prisms

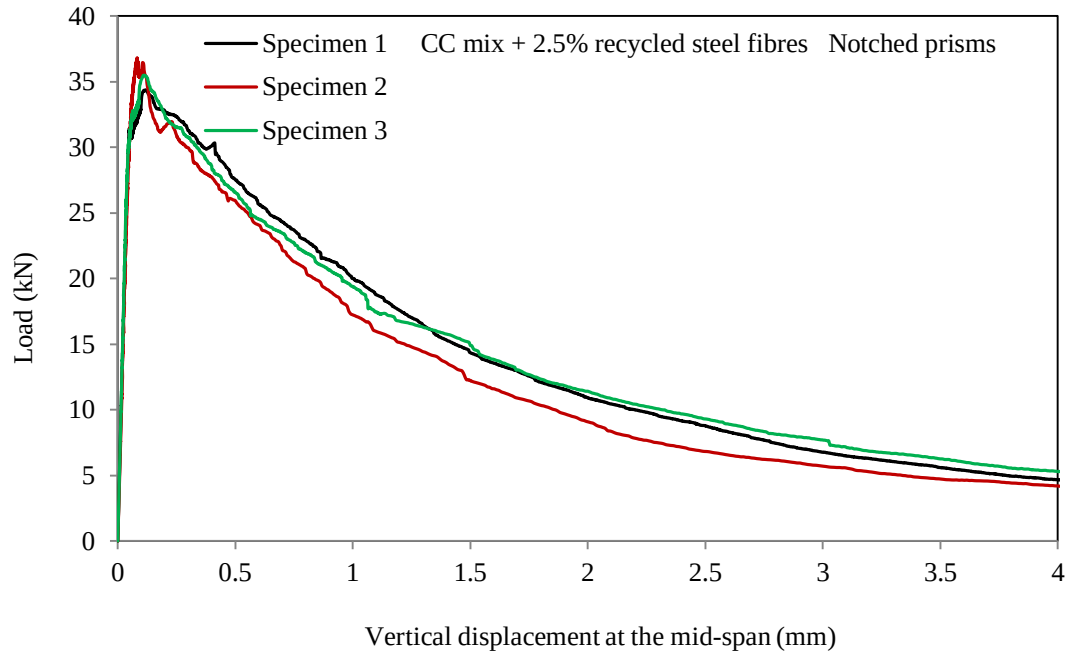

(a)

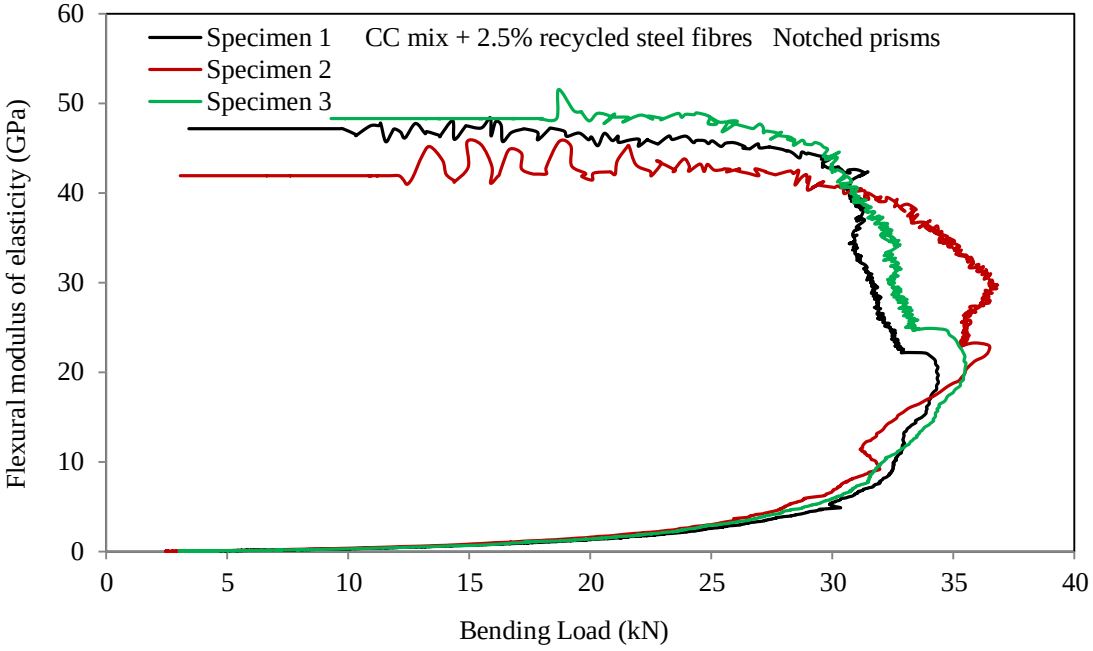

(b)

Figure C6 (a) Load-vertical deflection; (b) Flexural modulus of elasticity for SFR-CC notched prisms

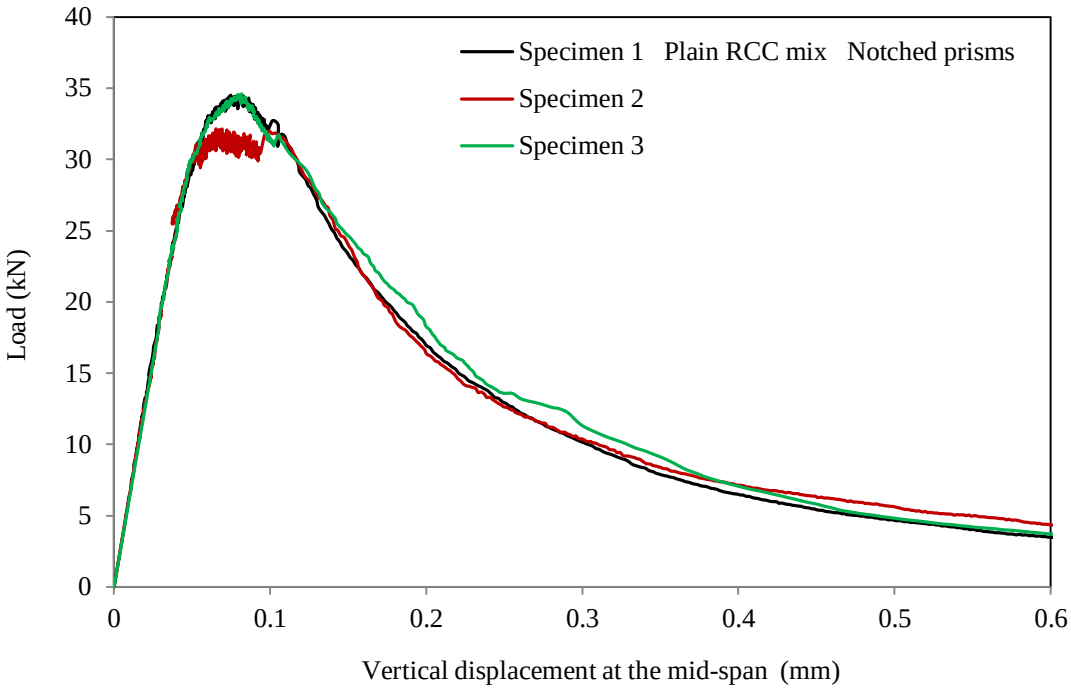

(a)

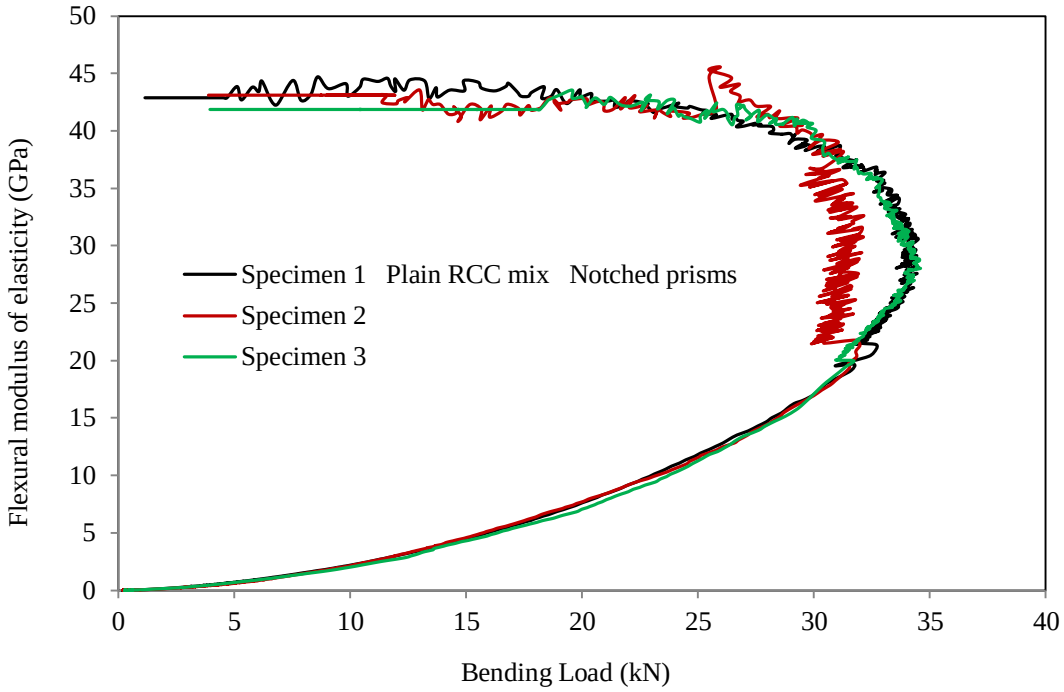

(b)

Figure C7 (a) Load-vertical deflection; (b) Flexural modulus of elasticity for plain RCC mix notched prisms

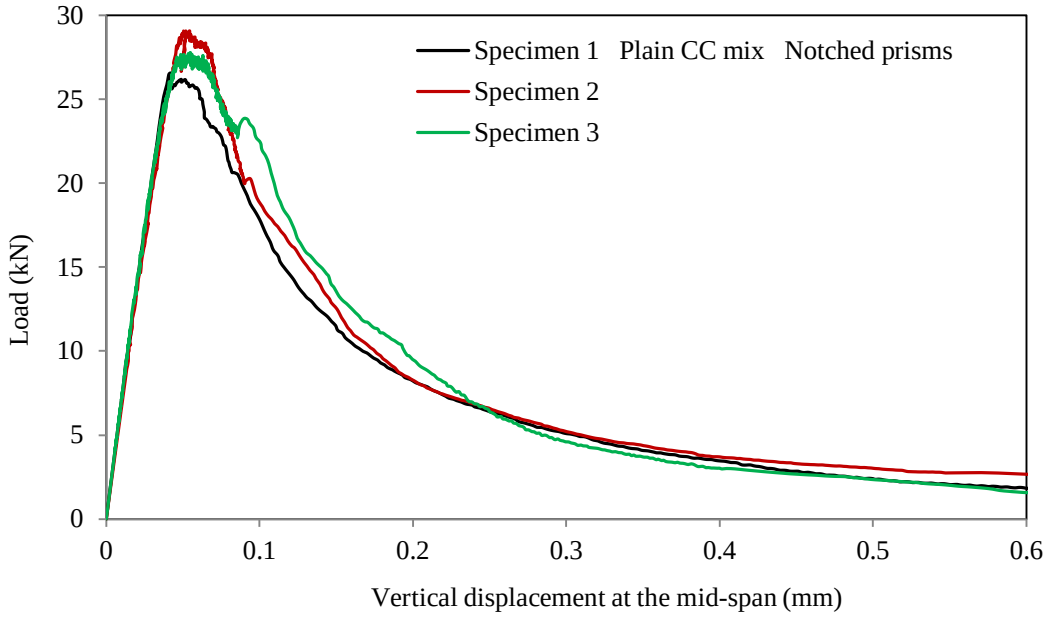

(a)

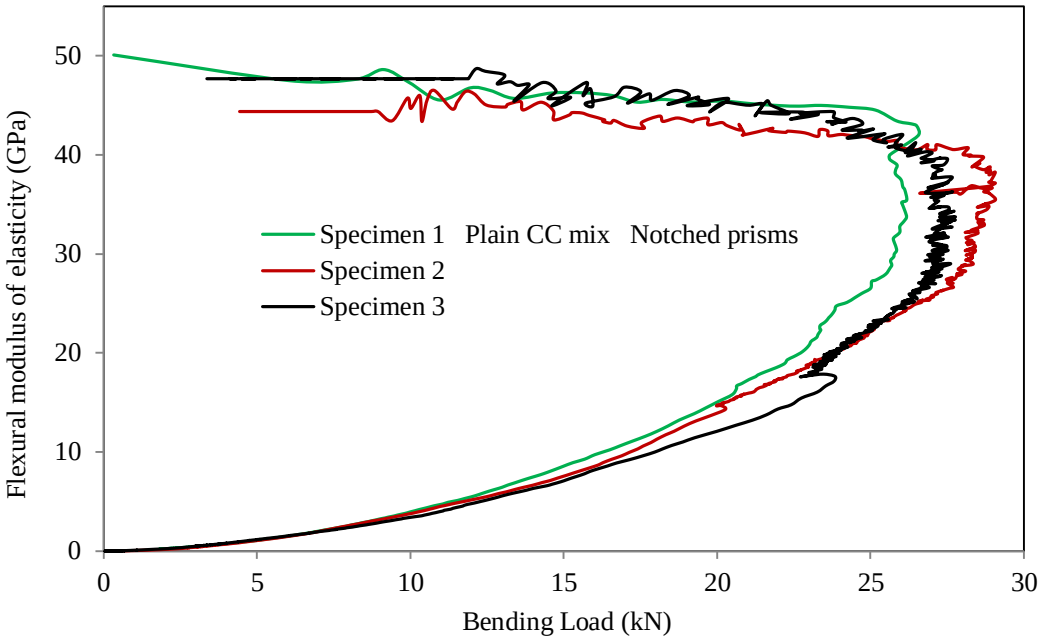

(b)

Figure C8 (a) Load-vertical deflection; (b) Flexural modulus of elasticity for plain CC mix notched prisms

C.2.2 Unnotched prisms

The experimental load-deflection curves, the calculated flexural modulus of elasticity curves and pictures showing cracking positions for the unnotched prisms are shown in Figure C9 to C12, for different concrete mixes.

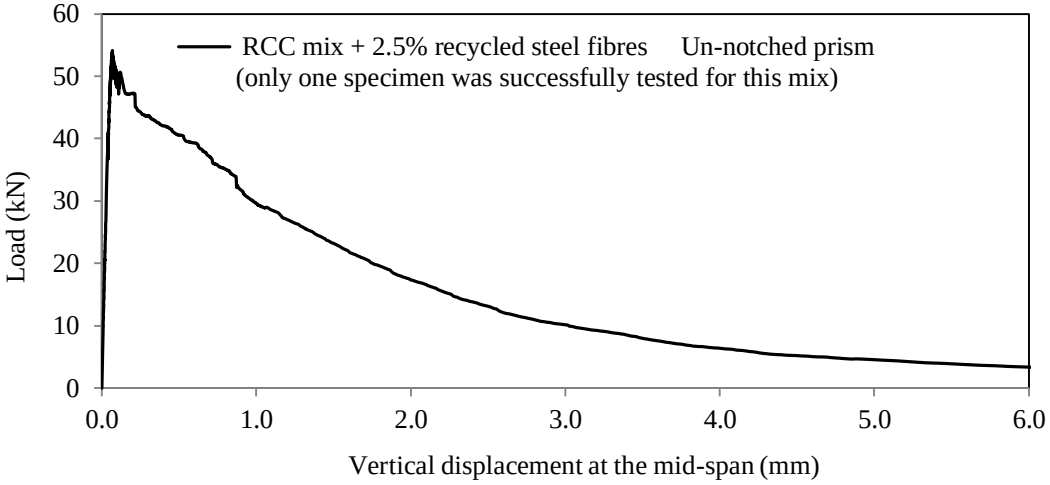

(a)

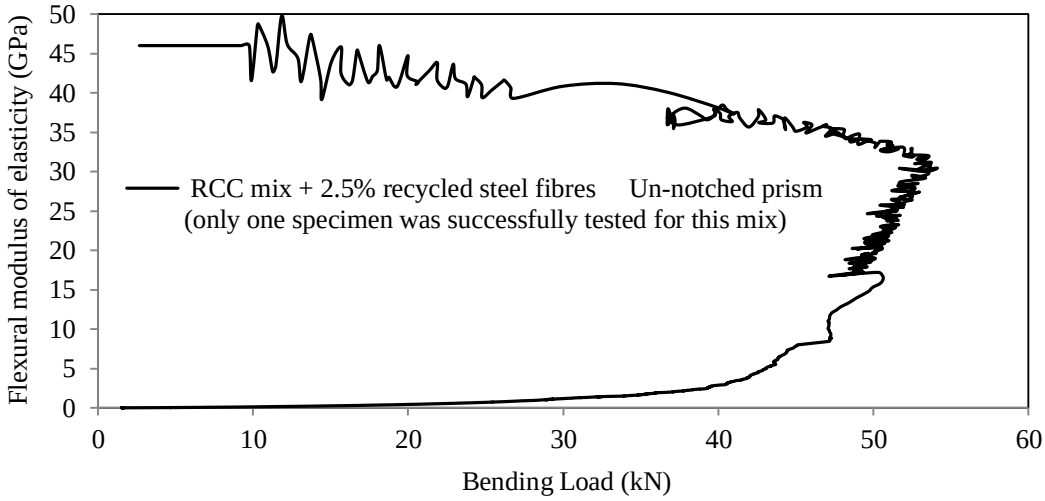

(b)

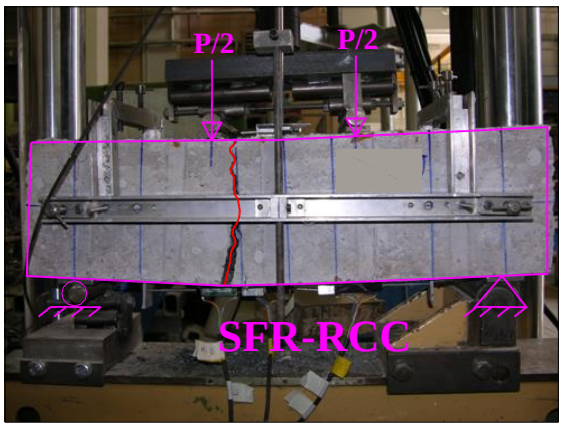

(c)

Figure C9 (a) Load-vertical deflection; (b) Flexural modulus of elasticity for SFR-RCC mix un-notched prisms (c) Cracked specimen

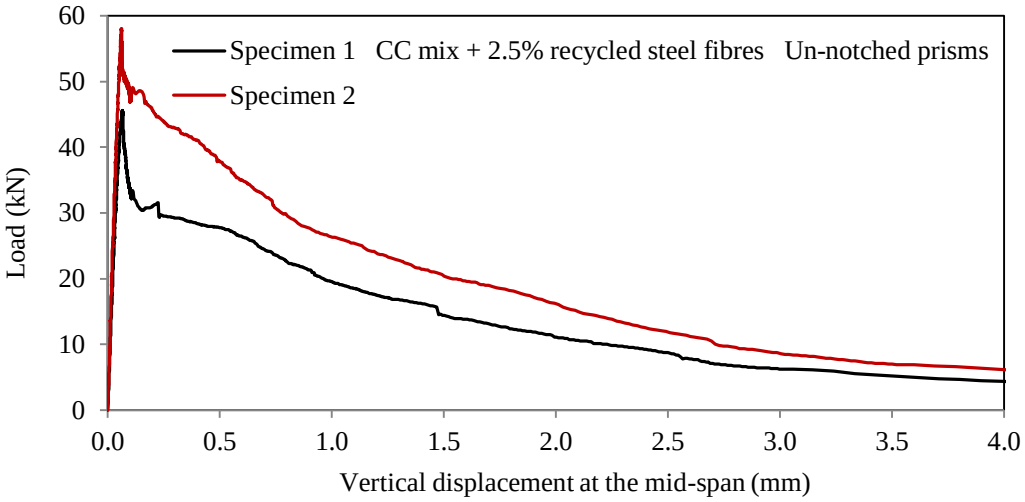

(a)

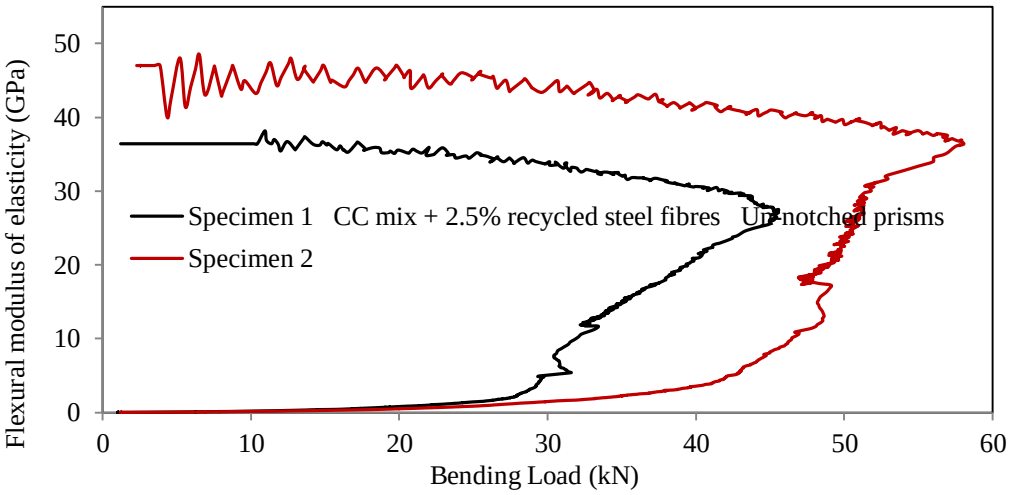

(b)

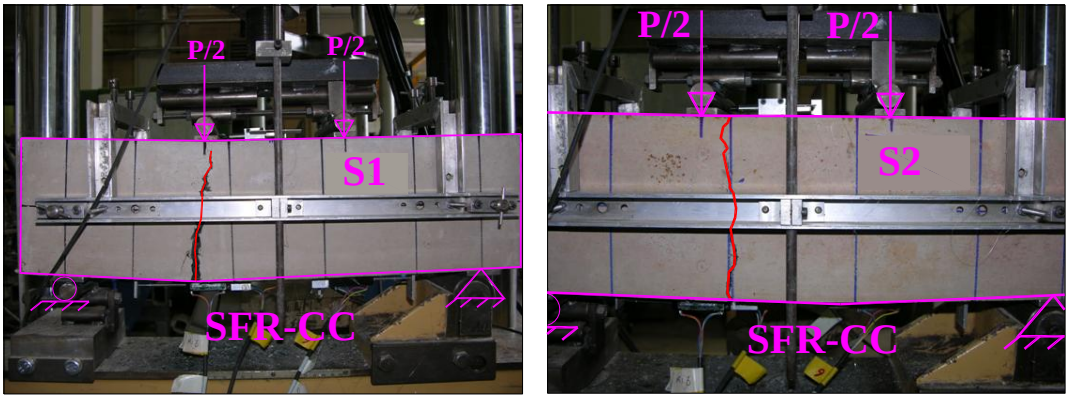

(c)

Figure C10 (a) Load-vertical deflection; (b) Flexural modulus of elasticity for SFR-CC mix un-notched prisms; (c) Cracked specimens

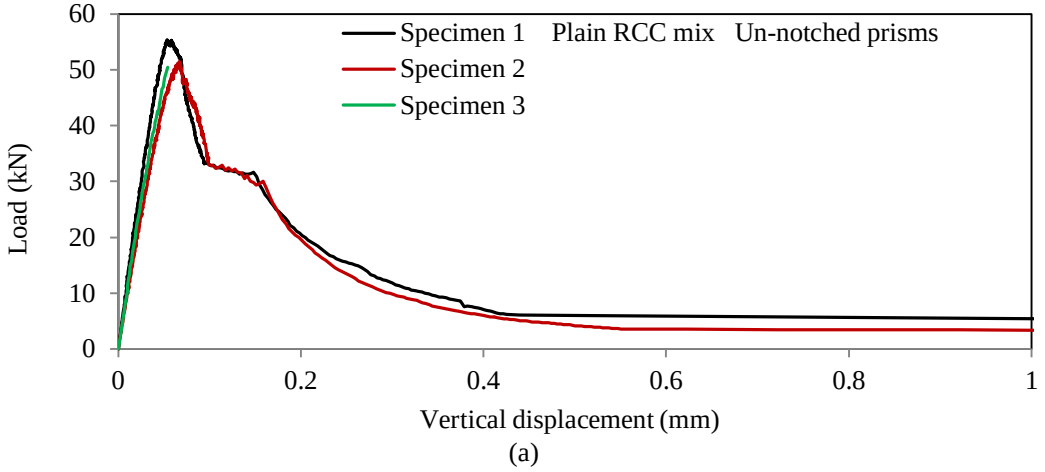

(a)

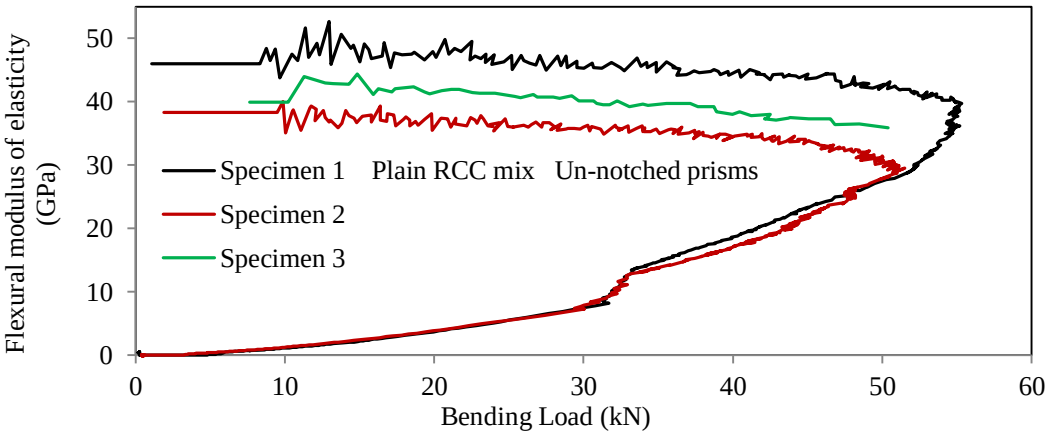

(b)

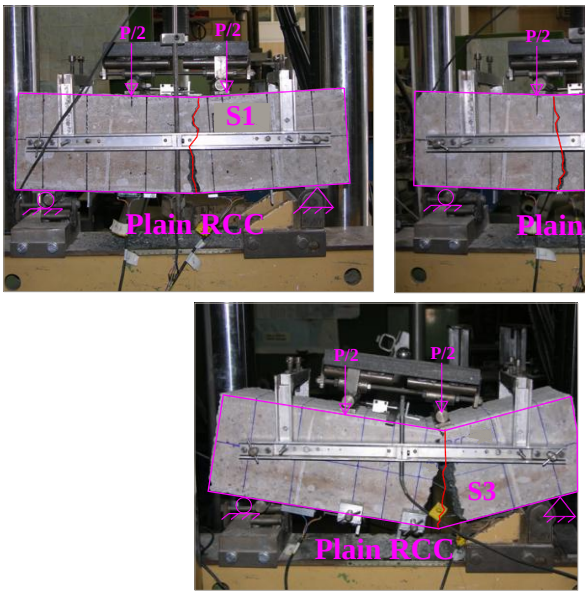

(c)

Figure C11 (a) Load-vertical deflection; (b) Flexural modulus of elasticity for plain RCC mix un-notched prisms; (c) Cracked specimens

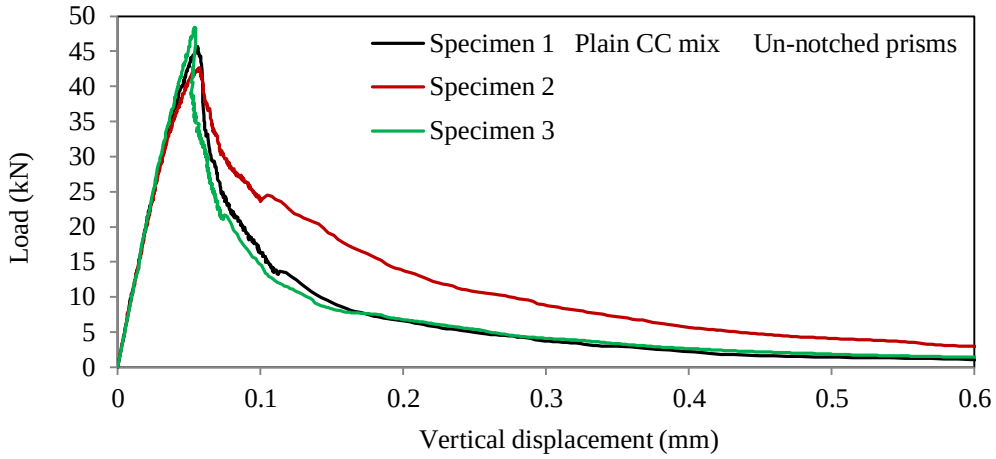

(a)

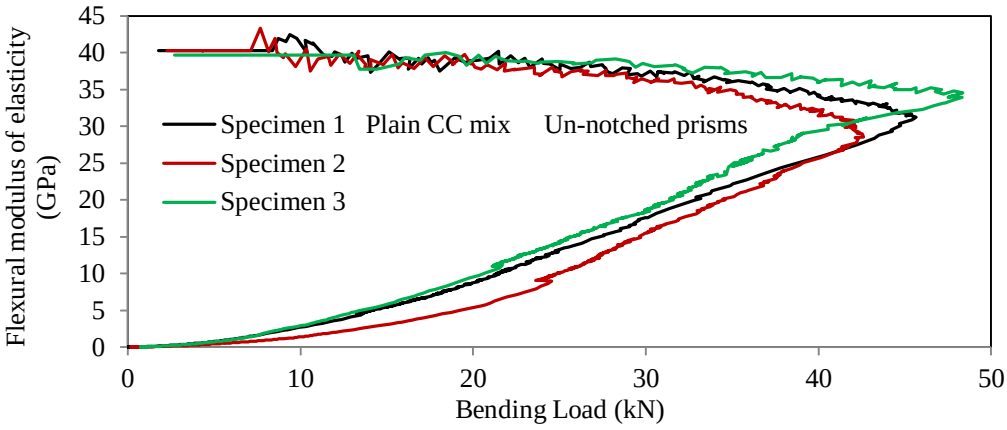

(b)

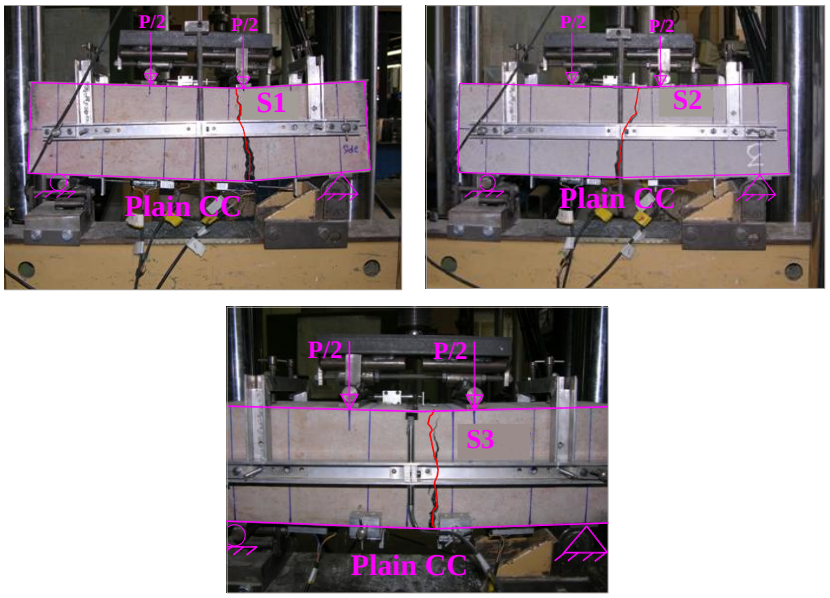

(c)

Figure C12 (a) Load-vertical deflection; (b) Flexural modulus of elasticity for plain CC mix un-notched prisms; (c) Cracked specimens

C.3. Moisture measurement test results

C.3.1 Weight measurements

Table C.2 Moisture measurement test results for SFR-RCC mix

Mix	Specimen No.	Height (mm)	Density (gr/mm^3)	Initial weight (unsealed) (gr)	Weight of the sealed specimen (gr) during drying*										83 days (unsealed) (gr)	After unsealing and drying in the oven** (gr)
					Drying time (days)											
					0	1	2	3	7	14	29	42	56	70	83	
SFR-RCC (2.5% recycled steel fibres)	1-1	13.63	0.0022	821.9	828.3	824.3	821.2	821.2	820.4	818.8	817.1	815.6	814.5	813.4	812.6	805.7	776.4
	1-2	11.88	0.0023	751.0	755.4	752.1	749.4	748.9	748.5	747.3	745.7	744.4	743.3	742.6	741.7	736.7	710.6
	1-3	12.0	0.0024	766.0	772.3	767.8	765.4	765.0	764.5	763.1	761.0	759.7	758.5	757.6	756.9	750.0	725.1
	Ave	12.5	0.0023	779.6	785.3	781.4	778.9	778.4	777.8	776.4	774.6	773.2	772.1	771.2	770.4	764.1	743.6
	2-1	21.6	0.0025	1470.3	1480.6	1473.9	1470.6	1469.7	1468.6	1466	1463.1	1460.9	1459.2	1457.4	1456.1	1444.7	1382.3
	2-2	20.1	0.0025	1382.6	1391.1	1387.3	1384.3	1383.6	1383.0	1381.4	1379.0	1377.1	1375.7	1374.2	1373.0	1363.4	1307.1
	2-3	21.4	0.0025	1452.9	1462.5	1458.9	1456.6	1455.8	1455.1	1453.5	1451.3	1449.5	1448.2	1446.7	1445.7	1435.8	1376.7
	Ave	21.0	0.0025	1435.3	1444.7	1440.0	1437.2	1436.4	1435.6	1433.6	1431.1	1429.2	1427.7	1426.1	1424.9	1414.6	1365.7
	3-1	36.3	0.0024	2370.7	2383.7	2379.0	2376.0	2375.0	2373.9	2371.1	2367.7	2365.3	2363.2	2361.2	2359.7	2345.6	2240.2
	3-2	35.5	0.0024	2315.0	2326.7	2321.8	2317.9	2316.9	2316.1	2313.7	2310.4	2307.8	2305.5	2303.5	2301.8	2289.5	2187.9
	3-3	36.3	0.0024	2404.3	2420.4	2415.3	2412.5	2411.7	2410.8	2408.4	2405.1	2402.6	2400.2	2398.0	2396.5	2378.7	2276.3
	Ave	36.0	0.0024	2363.3	2376.9	2372.0	2368.8	2367.9	2366.9	2364.4	2361.1	2358.6	2356.3	2354.2	2352.7	2337.9	2234.8
Ave Density			0.0024														

*the specimens were sealed on all surfaces except the top surface (1D drying)
**Drying in the oven last for 7 days at 120°C

Table C.3 Moisture measurement test results for SFR-CC mix

Mix	Specimen No.	Height (mm)	Density (gr/mm^3)	Initial weight (unsealed) (gr)	Weight of the sealed specimen (gr) during drying*										85 days (unsealed) (gr)	After unsealing and drying in the oven** (gr)
					Drying time (days)											
					0	1	2	3	7	14	29	42	56	70	85	
SFR-CC (2.5% recycled steel fibres)	1-1	8.8	0.0022	514.4	516.9	514.6	512.7	511.2	510.9	510.3	509.4	508.3	507.8	507	506.3	502.9	482.9
	1-2	11.38	0.0020	610.6	616.2	613.5	613.1	610.6	610.3	609.3	608.2	606.8	606.0	605.0	604.3	598.1	569.7
	1-3	11.38	0.0021	631.2	634.6	632.4	631.4	630.1	629.4	628.4	627.3	625.9	625.3	624.2	623.6	620.0	593.2
	Ave	10.5	0.0021	585.4	589.2	586.8	585.7	584.0	583.5	582.7	581.6	580.3	579.7	578.7	578.1	573.7	548.6
	2-1	20.5	0.0021	1180.4	1188.0	1185.5	1183.5	1181.3	1180.7	1179.5	1178	1176.5	1175.5	1174.2	1173.2	1164.7	1114.5
	2-2	18.8	0.0023	1148.4	1153.9	1150.6	1150.1	1147	1146.6	1145.3	1143.8	1142.1	1141	1139.7	1138.5	1132.0	1079.9
	2-3	19.9	0.0022	1211.6	1218.2	1216.3	1215.1	1213.6	1212.9	1211.5	1210.1	1208.3	1207.3	1206.1	1204.8	1197.9	1144.0
	Ave	19.7	0.0022	1180.1	1186.7	1184.1	1182.9	1180.6	1180.1	1178.8	1177.3	1175.6	1174.6	1173.3	1172.2	1164.9	1112.8
	3-1	35.1	0.0022	2062.1	2073.7	2070.6	2068.8	2066.4	2065.6	2064.1	2062.3	2060.4	2059.1	2057.4	2056.0	2043.6	1950.9
	3-2	34.4	0.0023	2151.3	2162.6	2159.4	2158.6	2156.2	2155.6	2154	2152.2	2150.3	2148.7	2147.4	2145.9	2134.2	2041.7
	3-3	35.3	0.0023	2194.5	2206.5	2204.7	2203.6	2202.0	2201.1	2199.8	2198.1	2196.2	2195.0	2193.6	2192.4	2179.6	2083.6
	Ave	34.5	0.0023	2136.0	2147.6	2144.9	2143.7	2141.5	2140.8	2139.3	2137.5	2135.6	2134.3	2132.8	2131.4	2119.1	2025.4
Ave Density			0.0022														

*the specimens were sealed on all surfaces except the top surface (1D drying)
**Drying in the oven last for 7 days at 120°C

Table C.4 Moisture measurement test results for Plain RCC mix

Mix	Specimen No.	Height (mm)	Density (gr/mm^3)	Initial weight (unsealed) (gr)	Weight of the sealed specimen (gr) during drying*										85 days (unsealed) (gr)	After unsealing and drying in the oven** (gr)
					Drying time (days)											
					0	1	2	3	7	14	29	42	56	70	85	
Plain RCC	1-1	11.5	0.0025	764.7	769.7	763.8	762.5	761.8	760.4	758.6	757.3	755.3	754.0	753.0	751.8	745.4	719.4
	1-2	10.25	0.0022	616.7	619.8	613.9	612.9	612.2	610.8	609.8	608.3	607.0	605.9	605.1	604.1	600.3	518.6
	1-3	10.75	0.0026	740.7	746.4	741.7	741.3	740.7	739.3	737.7	736.1	734.5	733.4	732.6	731.3	724.3	698.4
	Ave	10.8	0.0024	707.4	712.0	706.5	705.6	704.9	703.5	702.0	700.6	698.9	697.8	696.9	695.7	690.0	645.5
	2-1	19.9	0.0025	1327.2	1336.0	1329.9	1328.8	1328.4	1326.5	1324.3	1322.5	1320.4	1318.7	1317.1	1315.4	1306.1	1249.6
	2-2	20.1	0.0024	1303.5	1309.1	1302.4	1301.4	1300.5	1298.9	1296.9	1294.9	1292.7	1290.9	1289.5	1288.0	1281.3	1229.6
	2-3	19.8	0.0025	1340.5	1347.3	1341.9	1341.6	1340.2	1338.3	1336.2	1333.8	1331.9	1330.1	1328.6	1326.9	1319.2	1193.4
	Ave	19.9	0.0025	1323.7	1330.8	1324.7	1323.9	1323.0	1321.2	1319.1	1317.1	1315.0	1313.2	1311.7	1310.1	1302.2	1224.2
	3-1	35.1	0.0023	2220.8	2231.8	2224.8	2223.5	2222.8	2220.7	2217.8	2215.8	2213.1	2210.9	2209.2	2207.1	2194.9	2194.9
	3-2	35.8	0.0024	2337.2	2347.6	2340.9	2339.6	2338.9	2337.3	2334.9	2332.2	2329.8	2327.7	2326.1	2324.1	2312.9	2203.9
	3-3	36.6	0.0024	2359.6	2372.5	2366.8	2366.5	2365.7	2363.9	2361.3	2358.2	2355.7	2353.4	2351.3	2349.1	2334.1	2219.5
	Ave	35.8	0.0024	2305.9	2317.3	2310.8	2309.9	2309.1	2307.3	2304.7	2302.1	2299.5	2297.3	2295.5	2293.4	2280.6	2206.1
Ave Density			0.0024														

*the specimens were sealed on all surfaces except the top surface (1D drying)
**Drying in the oven last for 7 days at 120°C

Table C.5 Moisture measurement test results for Plain CC mix

Mix	Specimen No.	Height (mm)	Density (gr/mm^3)	Initial weight (unsealed) (gr)	Weight of the sealed specimen (gr) during drying*									80.5days (unsealed) (gr)	After unsealing and drying in the oven** (gr)
					Drying time (days)										
					0	1	2	3	9.5	23.5	37.5	51.5	65.5	80.5	
Plain CC	1-1	8.2	0.0023	516.4	517.4	517.5	516.7	516.1	514.2	512.5	511.8	510.5	509.2	508.4	503.6	482.2
	1-2	10.1	0.0022	600.3	602.6	601.6	600.7	599.9	598.3	596.7	595.9	594.4	593.6	592.9	589.9	567.2
	1-3	11.87	0.0021	685.8	689.4	688.2	687.2	687.0	685.1	683.2	682.3	681.1	680.7	679.7	675.0	648.9
	Ave	10.1	0.0022	633.8	603.1	602.4	601.5	601.0	599.2	597.5	596.7	595.3	594.4	593.7	589.5	566.1
	2-1	19.3	0.0022	1145.1	1151.4	1151.0	1150.1	1149.8	1146.7	1144.5	1143.2	1140.9	1139.5	1138.3	1130.1	1082.6
	2-2	19.9	0.0023	1254.2	1260.7	1260.2	1259.1	1258.2	1256.2	1253.8	1252.6	1250.6	1249.5	1248.4	1241.2	1191.6
	2-3	20.3	0.0022	1214.0	1220.0	1219.2	1218.2	1217.8	1216.0	1213.4	1212.3	1210.8	1209.9	1208.7	1201.7	1150.0
	Ave	19.8	0.0022	1204.4	1210.7	1210.1	1209.1	1208.6	1206.3	1203.9	1202.7	1200.8	1199.6	1198.5	1191.0	1141.4
	3-1	33.5	0.0023	2042.4	2053.3	2053.2	2052.0	2050.9	2047.9	2045.1	2043.5	2040.7	2038.8	2037.3	2024.3	1934.9
	3-2	35.9	0.0023	2212.4	2224.1	2224.7	2223.5	2222.6	2220.4	2217.9	2216.3	2214.1	2212.8	2211.5	2197.1	2109.4
	3-3	35.0	0.0023	2158.1	2168.0	2168.4	2167.2	2167.0	2164.5	2161.6	2160.3	2158.5	2157.4	2155.9	2143.9	2049.2
	Ave	34.8	0.0023	2137.6	2148.5	2148.8	2147.6	2146.8	2144.3	2141.5	2140.0	2137.8	2136.3	2134.9	2121.8	2031.2
Ave Density			0.0022													

*the specimens were sealed on all surfaces except the top surface (1D drying)
**Drying in the oven last for 7 days at 120°C

C.3.2 Moisture contents

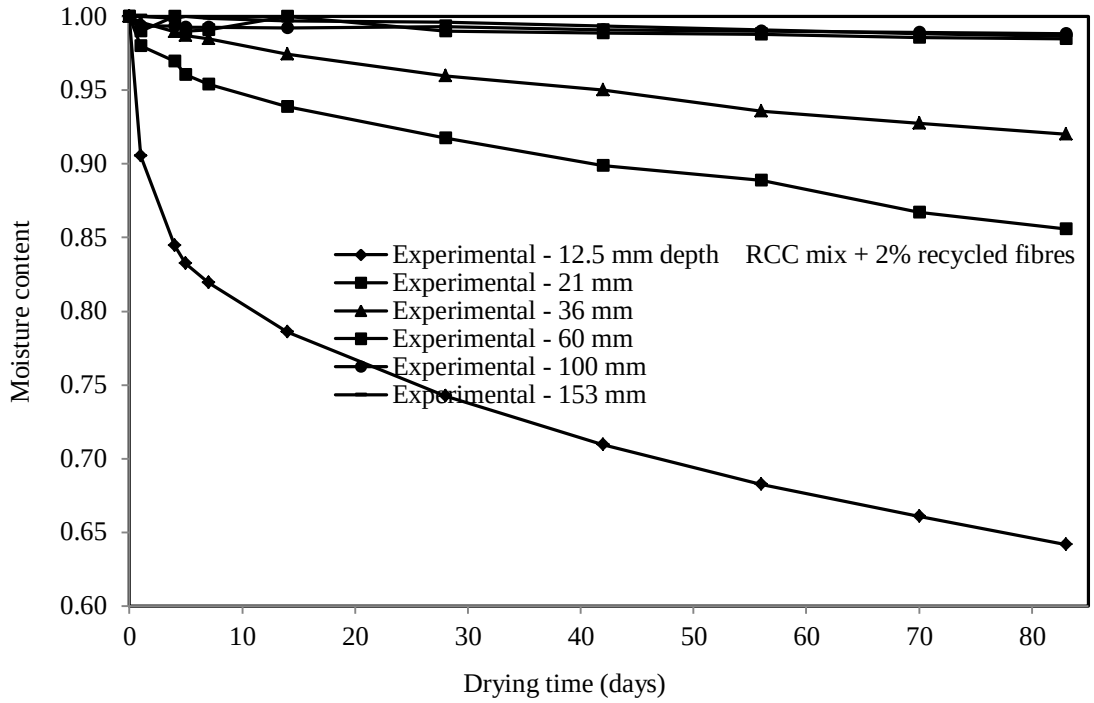

Figure C13 Experimental moisture profiles, SFR-RCC mix (2.5% recycled steel fibres)

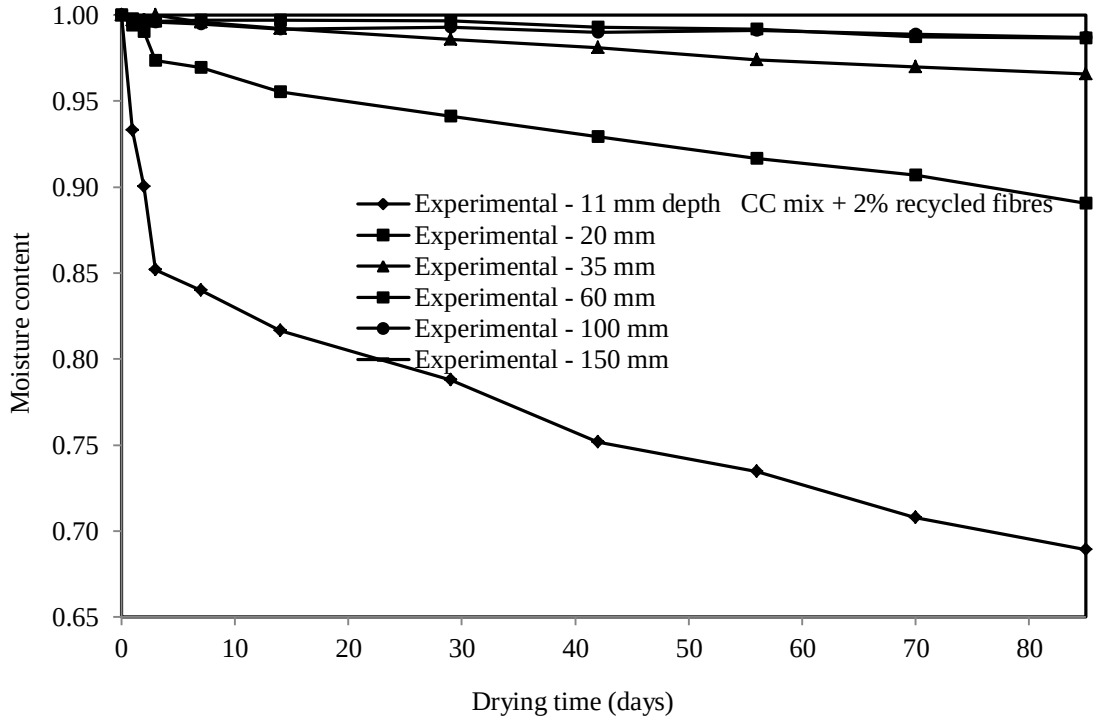

Figure C14 Experimental moisture profiles, SFR-CC mix (2.5% recycled steel fibres)

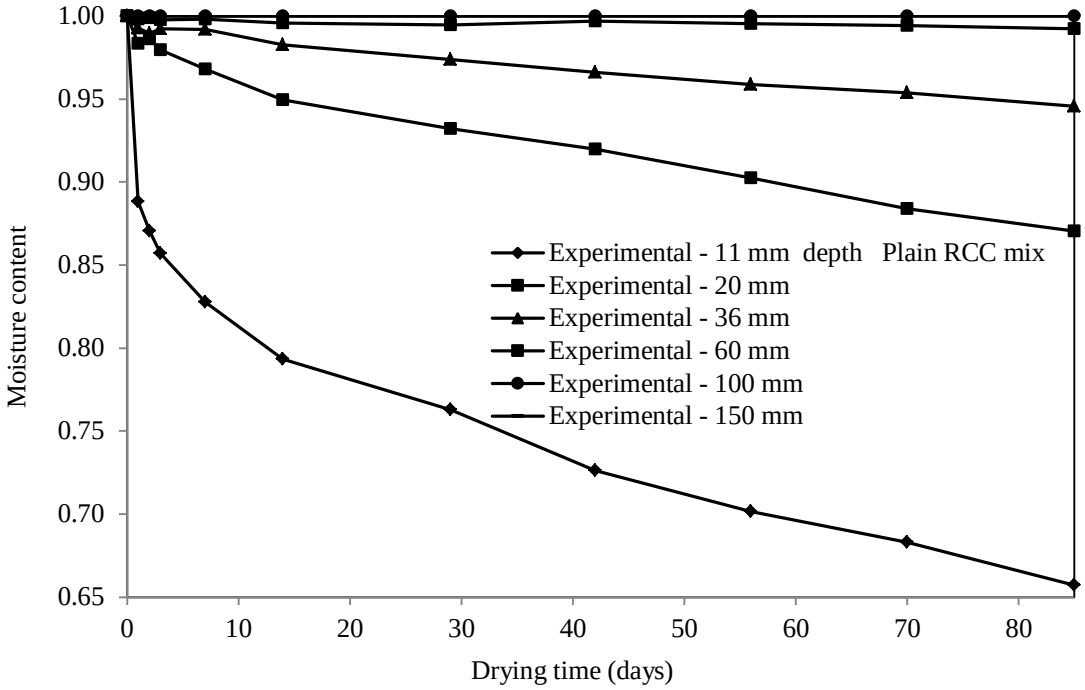

Figure C15 Experimental moisture profiles, Plain RCC mix

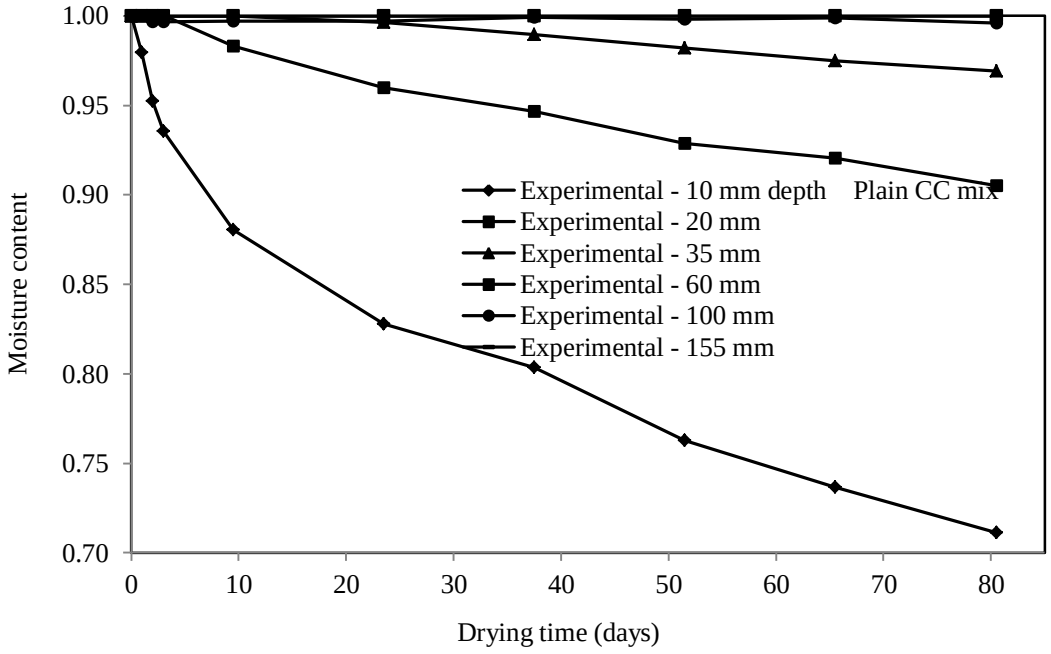

Figure C16 Experimental moisture profiles, Plain CC mix

C.4. Free shrinkage test results

Table C.6 Free shrinkage measurement test results for SFR-RCC mix

Mix	Specimen No.	Length, L_0 (mm)	Length changes during drying, L_t-L_0										
			Drying time (days)										
			0	1	4	5	7	14	28	42	56	70	83
SFR-RCC (2.5% recycled steel fibres)	1	547	0	-0.010	-0.039	-0.052	-0.057	-0.061	-0.100	-0.118	-0.176	-0.208	-0.266
	2	549	0	-0.009	-0.035	-0.036	-0.037	-0.042	-0.091	-0.113	-0.155	-0.177	-0.232
	3	552	0	-0.008	-0.015	-0.022	-0.024	-0.028	-0.065	-0.093	-0.131	-0.155	-0.195
	Ave.	549	0	-0.009	-0.029	-0.037	-0.039	-0.044	-0.085	-0.108	-0.154	-0.180	-0.231

Table C.7 Free shrinkage measurement test results for SFR-CC mix

Mix	Specimen No.	Length, L_0 (mm)	Length change during drying, L_t-L_0									
			Drying time (days)									
			0	2	3	7	14	28	42	56	70	83
SFR-CC (2.5% recycled steel fibres)	1	550	0	-0.076	-0.103	-0.119	-0.142	-0.166	-0.185	-0.204	-0.219	-0.245
	2	551	0	-0.076	-0.103	-0.117	-0.131	-0.153	-0.179	-0.176	-0.198	-0.217
	Ave.	551	0	-0.076	-0.103	-0.118	-0.136	-0.159	-0.182	-0.190	-0.209	-0.231

Table C.8 Free shrinkage measurement test results for Plain RCC mix

Mix	Specimen No.	Length, L_0 (mm)	Length change during drying, L_t-L_0										
			Drying time (days)										
			0	1	2	3	7	14	29	42	56	70	85
Plain RCC	1	551	0	-0.029	-0.046	-0.052	-0.077	-0.095	-0.120	-0.158	-0.186	-0.208	-0.235
	2	551	0	-0.023	-0.048	-0.047	-0.079	-0.094	-0.122	-0.159	-0.187	-0.206	-0.230
	3	550	0	-0.023	-0.048	-0.061	-0.067	-0.076	-0.133	-0.169	-0.193	-0.215	-0.226
	Ave.	551	0	-0.025	-0.047	-0.053	-0.074	-0.088	-0.125	-0.162	-0.189	-0.210	-0.230

Table C.9 Free shrinkage measurement test results for Plain CC mix

Mix	Specimen No.	Length, L_0 (mm)	Length change during drying, L_t-L_0								
			Drying time (days)								
			0	3	4	8.5	22.5	36.5	50.5	65.5	80.5
Plain CC	1		0	-0.116	-0.141	-.0159	-.0141	-0.199	-0.194	-0.208	-0.206
	2		0	-0.116	-0.166	-0.176	-0.175	-0.219	-0.220	-0.229	-0.231
	3		0	-0.116	-0.156	-0.167	-0.160	-0.207	-0.209	-0.218	-0.219
	Ave.		0	-0.116	-0.154	-0.167	-0.159	-0.208	-0.207	-0.218	-0.218

Appendix D: Numerical Repetitive Section Analysis

By section analysis, an individual section is analysed using tensile and compressive stress-strain curves assumed for the SFRC section. As a simulation of the bending test, the load is started from zero and is increased gradually to pass the pre-cracking, cracking and post-cracking modes of strength (Figure D1). The key factor is that the linear variation of strain is assumed through the section for entire load steps until complete collapse. Initially the neutral axis depth is assumed equal to half of the depth of the SFRC prism. The concrete compressive and tensile forces are calculated at each step. Then the neutral axis depth is iteratively modified and two forces are re-evaluated until force equilibrium is achieved. The areas of the compressive stress block and tensile stress block can be determined by using the trapezoidal rule for numerical integration. Once the force equilibrium is achieved, the bending moment resistance capacity is calculated. The crack finally is developed through the whole section and the section collapses.

Four phases could be distinguished in the tensile zone of the cross section, according to Figure D1 (Tlemat, 2004). In Phase 1, the concrete behaves elastically and there is no crack in the tensile zone. In Phase 2 cracking is started in the concrete accompanying with a sharp descent in the stress-strain behaviour of SFRC. The beginning of this phase corresponds with the first deviation from linearity in the load-deflection curve. In Phase 3 the main cracking in the concrete has formed and the tensile stress in the section is carried mostly by the fibres pulling out. In phase 4 part of the concrete in the tensile zone is no more carrying any tensile stress and the neutral axis moves closer to the top of the prism.

The main output of section analysis, disregarding the length of the beam and the boundary conditions, is the moment-strain curve of the individual section. At this stage, the theoretical load resistance and deflection of the SFRC prism can be evaluated regarding the geometry and the boundary conditions.

In this analysis the extended part of the tension softening diagram is assumed so that the analytical load-displacement curve fits the experimental one. This assumption is getting precise during a repetitive procedure. Section analysis can be used to verify FE results.

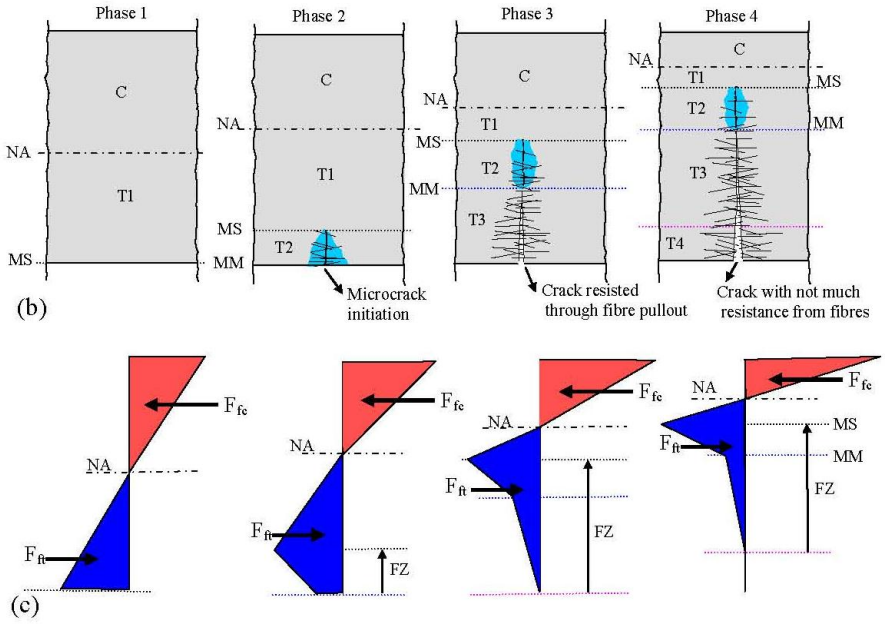

C: Compressive zone
T1: Uncracked tensile zone
T2: Aggregate and fibre bond bridging zone
T3: Fibre pull-out zone
T4: No resistance from fibres

NA: Position of the neutral axis
MS: Max. tensile stress in concrete
MM: Micro-Macro zone axis
FZ: Failure zone

Figure D1 Modes of strength in SFRC sections (Tlemat, 2004).

The equations for calculating the theoretical load resistance, P_{th}, and deflection, δ_{th}, of the SFRC prism are as follows (Figure D2).

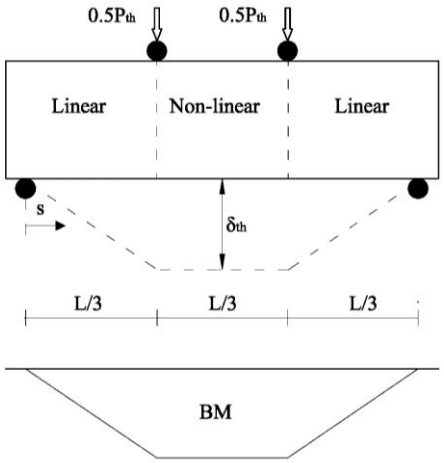

Figure D2 Third-point loading on prisms

$$P_{th} = \frac{6M}{L} \qquad \text{(Eq. D.1)}$$

Where, M is the bending moment resistance capacity, and L is the length of the prism

between supports.

When the prism is cracked, the deflection is calculated by assuming that the prism consists of a non-linear hinge of length *L/3*, in which the smeared crack is considered to be formed, and of two linear-elastically behaving blocks. Based on this assumption, the following expression has been determined for the mid-span deflection (Casanova et al., 1997):

$$\delta_{th} = \frac{L^2}{9}\left(\frac{M}{3E_c I} + \frac{5\varepsilon_c}{8x}\right) \qquad \text{(Eq. D.2)}$$

Where, E_c is the elastic modulus of concrete; I is the moment of inertia; ε_c is the compressive strain of concrete at the extreme fibre, and x is the neutral axis depth from the compressive surface .

Appendix E: Constitutive material models used in FE analysis

E.1. "Concrete Smeared Cracking" model (CSC)

CSC material model in Abaqus comprises an isotropically, hardening "compressive" yield/flow surface in dominantly compressive state of stress combined with an independent "crack detection failure surface". The term "crack", in this model, means an orientation in which cracking has been detected at a specific calculation point. It can be physically interpreted that a continuum of micro-cracks exists at the point, oriented as predicted by the model. The concept of oriented damaged elasticity is used for defining the response of material after cracking, in the sense that the crack affects the calculations by damaging the elasticity. When a crack is detected, the orientation of the crack stored for subsequent calculations. Since stress components of an open crack are neglected in detecting the additional cracks, secondary cracks at the same point can only occur in orthogonal direction to the first crack. Additionally, in a 3D model a maximum of three cracks can occur at any point (two cracks in 2D and one crack in 1D). Cracks are irrecoverable but can open and close. (ABAQUS, 2010).

The required parameters for stress analysis in "Concrete Smeared Cracking" material model are as follow:

- Uniaxial tension

Under uniaxial tension, concrete behaves elastically until cracks form. After cracking, concrete loses strength through a softening mechanism. The tension softening diagram is the relationship between tensile stress and tensile strain in the fracture zone (Figure E1). In CSC softening mechanism is a damage effect in which open cracks are represented by loss of elastic stiffness with no permanent strain associated with cracking. In this definition cracks are allowed to close completely if the stress across them becomes compressive (ABAQUS Documentation, 2010).

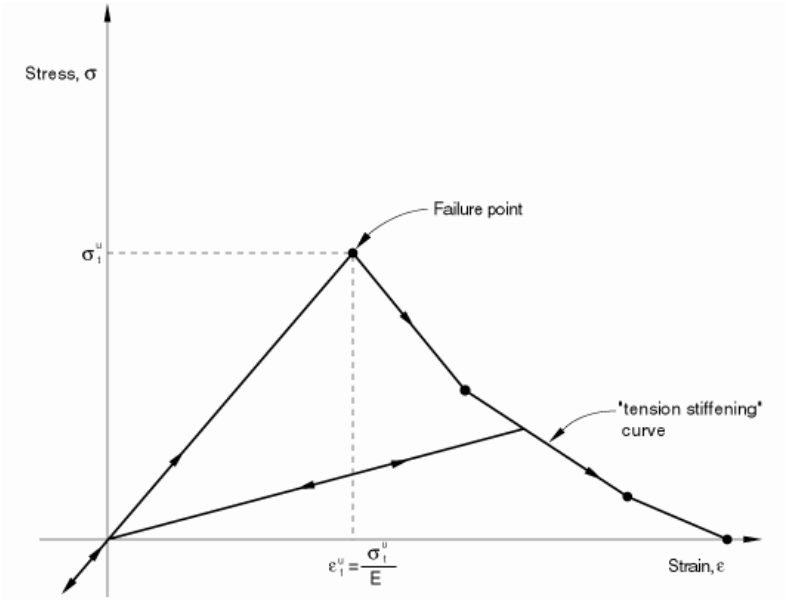

Figure E1 Tension stiffening behaviour of concrete in CSC model (ABAQUS, 2010)

- Uniaxial compression

The elastic-plastic theory is used to model the response of the concrete, when the principal stress components are dominantly compressive. In uniaxial compressive stress states concrete initially exhibits an elastic response when loaded. Inelastic straining occurs when the stress is increased, and then the response of the material can be defined into the softening regime beyond the ultimate stress (Figure E2).

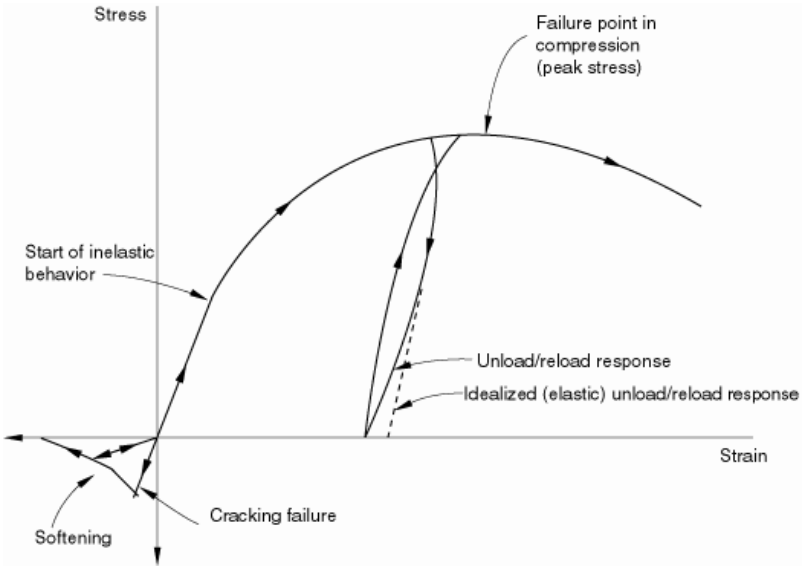

Figure E2 Uniaxial behaviour of concrete in CSC model (ABAQUS, 2010)

- Multiaxial yield and flow

In multiaxial stress states, the yield criterion is defined through the concept of surfaces of failure in stress space. The assumed failure criteria are linear functions of p, the equivalent pressure or hydrostatic stress invariant and, q, the Mises equivalent deviatoric stress invariant (Figure E3). The crack detection surface in Figure E3 is a simple Coulomb line and the compression surface is derived based on associated flow and isotropic hardening assumptions.

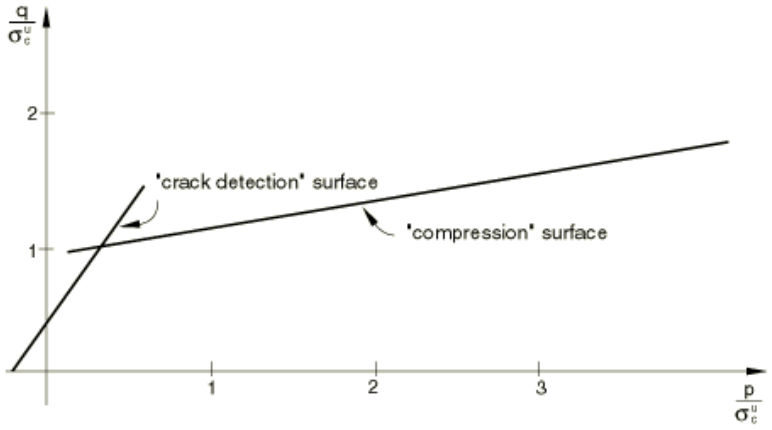

Figure E3 Yield and failure surfaces in the (p–q) plane (ABAQUS, 2010)

Yield and failure surfaces in plane stress are also shown in Figure E4. In ABAQUS, the reasonability of the predictions made by this model has been compared with the experimental results of Kupfer et al. (1973).

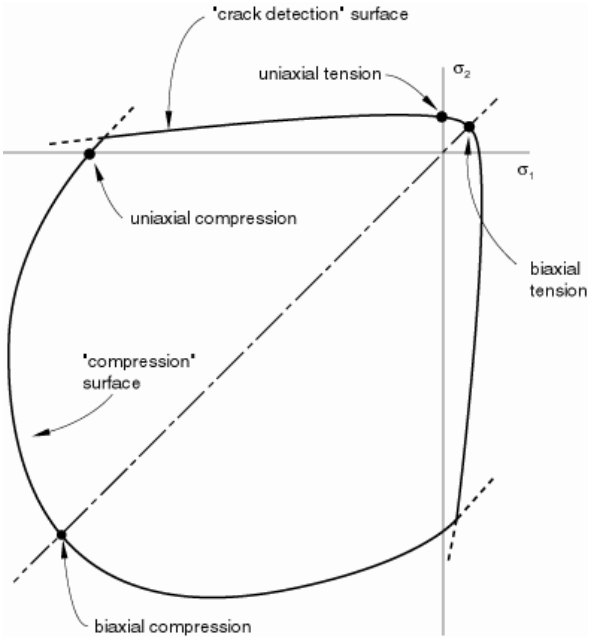

Figure E4 Yield surfaces in plane stress in CSC model (ABAQUS, 2010)

To define the shape of the failure surface for a specific concrete, failure ratios are specified. These ratios are as follow:

1. FR1: "The ratio of the ultimate biaxial compressive stress to the ultimate uniaxial compressive stress". This ratio typically is about 1.15 for plain concrete (ABAQUS, 2010).

2. FR2: "The absolute value of the ratio of the uniaxial tensile stress at failure to the ultimate uniaxial compressive stress".

3. FR3: "The ratio of the magnitude of a principal component of plastic strain at ultimate stress in biaxial compression to the plastic strain at ultimate stress in uniaxial compression". This ratio typically is about 1.28 for plain concrete (ABAQUS, 2010).

4. FR4: "The ratio of the tensile principal stress at cracking, in plane stress, when the other principal stress is at the ultimate compressive value, to the tensile cracking stress under uniaxial tension". This ratio typically is about 0.33 for plain concrete (ABAQUS, 2010).

These ratios must be determined such that failure surfaces fit biaxial experimental data. When biaxial experiments, required to specify the failure ratios, are not available, the typical values are used for the failure ratios.

The biaxial compressive strength of SFRC is increased by the addition of fibres (Yin et al., 1989). The effect of adding fibres on increasing the biaxial compressive strength of concrete is similar to the addition of a small amount of confinement pressure in the unloaded directions, which can significantly increase the ultimate strength by changing the failure modes (Yin et al., 1989; Lim et al., 2005). The confinement effect of fibres is due to their pull-out resistance (Lim et al., 2005). Yin et al. (1989) showed that the increase in the biaxial compressive strength could be as high as 35% in the case of 2% (volumetric ratio) of steel fibres and a stress ratio of $\sigma1/\sigma2=0.2$. Lim et al. (2005) found that the maximum increase of biaxial compressive strength compared to uniaxial strength occurs at a stress ratio of 0.5 for all cases of plain and SFRC, and the amount of increase is about 30% over that of the specimens under uniaxial compression.

Swaddiwudhipong and Seow (2006 & 2005) developed analytically a failure surface for SFRC under multi-axial compression, and verified it by a significant number of biaxial experiments on plate specimens (Figure E5). In Figure E5, dashed-line curves numbered 1-4

illustrate analytical-numerical failure surfaces developed using FE method, and continuous lines represent the experimental failure surfaces (Swaddiwudhipong et al., 2006).

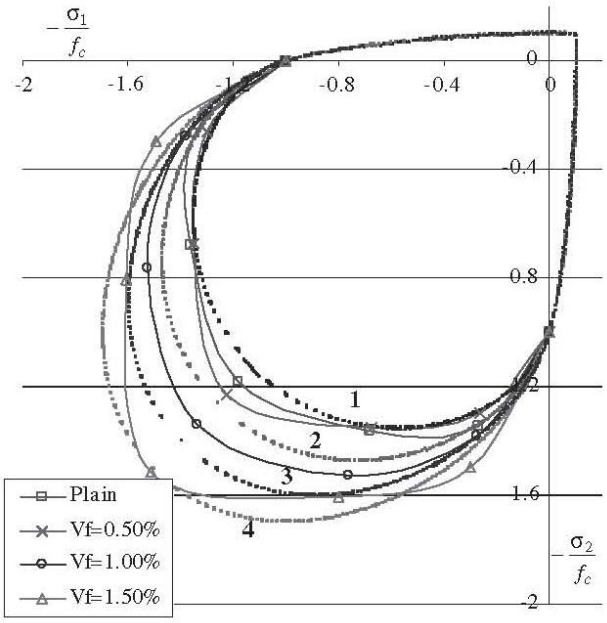

Figure E5 Experimental and predicted biaxial curves (Swaddiwudhipong et al., 2006)

This figure shows that, for a ratio of 0.5% (by volume) steel fibres (that is comparable to the experimental fibre content in the current research), FR1 increases by 5% compared to plain concrete. Other failure ratios do not differ for SFRC and plain concrete. Therefore, the typical value of 1.15 for FR1 relevant to plain concrete is increased to 1.20 for SFRC in this study.

- Shear retention factors

When concrete cracks, its shear stiffness is reduced. This effect can be considered in ABAQUS by defining the reduction in the shear modulus as a function of the opening strain across the crack. The reduction in the shear modulus for closed cracks can also be specified. In this way, degradation of shear stiffness due to cracking is taken into account. The default option in ABAQUS is to assume that the shear behaviour is not affected by cracking (full shear retention). Since the overall response of the concrete member is rarely strongly dependent on the amount of shear retention, this could be a reasonable assumption. (ABAQUS, 2010). Another option is to assume that the shear stiffness linearly reaches zero at the same strain as the maximum value assigned in the tension stiffening model. In the current research, in the absence of the experimental post-cracking shear behaviour of SFRC material, full shear retention is assumed.

E.2. “Concrete Damaged Plasticity” model (CDP)

“Concrete Damaged Plasticity” is a plasticity–based damage model for concrete that assumes the main failure mechanisms are tensile cracking and compressive crushing. The evolution of the failure surface is controlled by two hardening plasticity variables termed tensile and compressive equivalent plastic strains. These two variables, combined with scalar (isotropic) damaged elasticity, describe the irreversible damage that occurs in the fracturing process. Damage or degradation of the elastic stiffness is induced by plastic straining (ABAQUS, 2010).

The required parameters for stress analysis in “Concrete Damaged Plasticity” material model are as follow:

- Uniaxial tension

Under uniaxial tension, concrete behaves in a linear elastic form until the failure stress, σ_{t0}, is reached. The failure stress corresponds to the initiation of micro-cracks in concrete and follows by a softening response (Figure E6) (ABAQUS, 2010).

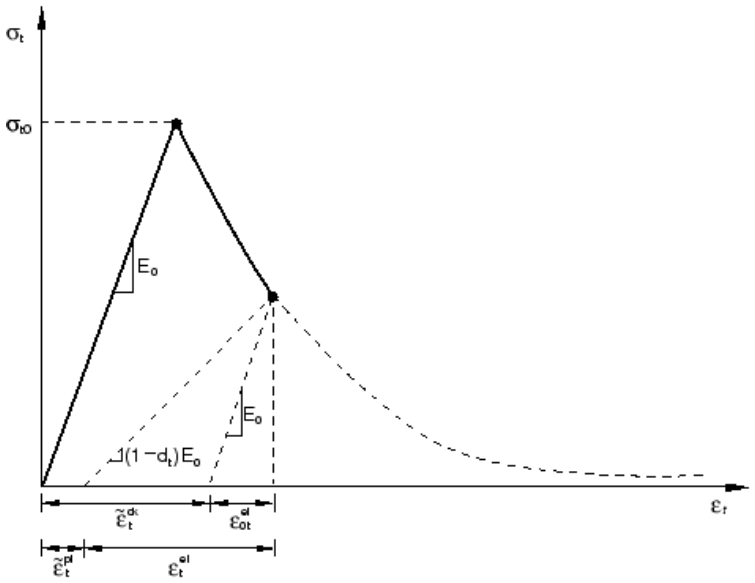

Figure E6 Uniaxial tensile behaviour of concrete in CDP model (ABAQUS, 2010)

- Uniaxial compression

The uniaxial compressive behaviour of concrete in CDP model is assumed the same as in CSC. As shown in Figure E7, it is linear until the value of initial yield, σ_{c0}. In the plastic regime, the behaviour is characterised by stress hardening to the ultimate value of σ_{cu},

followed by strain softening.

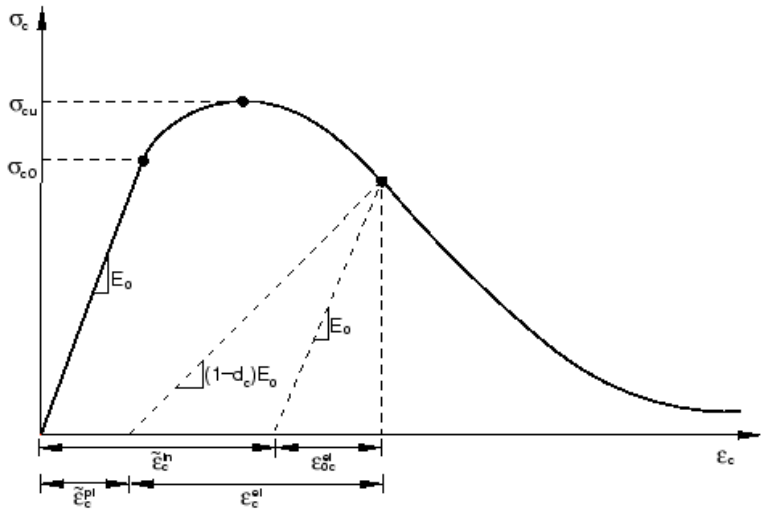

Figure E7 Uniaxial compressive behaviour of concrete in CDP model (ABAQUS, 2010)

- Damage factors and post-failure stress-strain relation

When the concrete is unloaded from any point on the strain softening branch, the unloaded response is weakened such that the elastic stiffness of the material seems to be damaged. This degradation in the elastic stiffness is characterised by two scalar variables, d_t and d_c. The stress-strain relations under uniaxial loading are then calculated as follows:

$$\sigma_t = (1 - d_t)E_0(\varepsilon_t - \tilde{\varepsilon}_t^{pl}) \qquad \text{(Eq. E.1)}$$

$$\sigma_c = (1 - d_c)E_0(\varepsilon_c - \tilde{\varepsilon}_c^{pl}) \qquad \text{(Eq. E.2)}$$

Where E_0 is the initial undamaged elastic stiffness, the subscripts t and c refer to tension and compression, respectively, and $\tilde{\varepsilon}_t^{pl}$ and $\tilde{\varepsilon}_c^{pl}$ are the equivalent plastic strains.

These damage variables are functions of plastic strains and can take values from zero, representing the undamaged material, to one, representing total strength loss.

Specifying the post-failure behaviour in tension generally means to give the relation between the post-failure stress and cracking strain, $\tilde{\varepsilon}_t^{ck}$. Cracking strain is defined as the total strain minus the undamaged elastic strain, $\tilde{\varepsilon}_t^{ck} = \varepsilon_t - \varepsilon_{0t}^{el}$, and $\varepsilon_{0t}^{el} = \frac{\sigma_t}{E_0}$ (Figure E7). The relationship between the equivalent plastic tensile strain and the cracking strain is as Equation E.3.

$$\tilde{\varepsilon}_t^{pl} = \tilde{\varepsilon}_t^{ck} - \frac{d_t}{(1-d_t)}\frac{\sigma_t}{E_0} \qquad \text{(Eq. E.3)}$$

The tensile plastic strain will be equivalent to the cracking strain in the absence of tensile damage factor; $\tilde{\varepsilon}_t^{pl} = \tilde{\varepsilon}_t^{ck}$ for $d_t = 0$.

In the current research, the coefficient of tensile damage, $1 - d_t$, is applied at the same rate as the tension stiffening behaviour of concrete, in the sense that for any given $\varepsilon_t \geq \varepsilon_{t0}$ the factor $1 - d_t$ is equated to σ_t/σ_{t0}, where ε_{t0} and σ_{t0} are the cracking strain and stress, respectively.

The post-elastic compressive behaviour of concrete is also provided in the form of stress versus inelastic (or crushing strain). In the hardening regime, the post-elastic data are assumed in terms of inelastic strain, $\tilde{\varepsilon}_c^{in} = \varepsilon_c - \varepsilon_{0c}^{el}$, instead of plastic strain, $\tilde{\varepsilon}_c^{pl}$, where $\varepsilon_{0c}^{el} = \frac{\sigma_c}{E_0}$ (Figure E7). The compressive damage factor is only specified beyond the ultimate stress, and in the strain-softening regime. The relationship between the equivalent plastic compressive strain and the inelastic (crushing) strain is as Equation E.4.

$$\tilde{\varepsilon}_c^{pl} = \tilde{\varepsilon}_c^{in} - \frac{d_c}{(1-d_c)}\frac{\sigma_c}{E_0} \qquad \text{(Eq. E.4)}$$

The compressive plastic strain will be equivalent to the inelastic (crushing) strain in the absence of compressive damage factor; $\tilde{\varepsilon}_c^{pl} = \tilde{\varepsilon}_c^{in}$ for $\mathrm{d_c} = 0$.

In the current research the compressive stresses are not dominant and the compressive strain-softening regime will never be suffered by the structure. Therefore applying the compressive damage factor is not required for this research.

- Multiaxial yield and flow

The flow potential used in CDP model is a plastic flow named the Drucker-Prager hyperbolic function as given by Equation E.5 (Figure E8).

$$G=((\epsilon\sigma_{t_0}\tan\psi)^2 + \overline{q}^2)^{0.5} - \overline{p}\tan\psi \qquad \text{(Eq. E.5)}$$

Where, ψ is the dilation angle at high confining pressure that is measured in the $p-q$ plane; σ_{t_0} is the uniaxial tensile stress at failure ($\sigma_{t_0} = \sigma_t|_{\tilde{\varepsilon}_t^{pl}=0,\ \tilde{\varepsilon}_t^{pl}=0}$); ϵ is eccentricity or a small positive number standing for the rate at which the hyperbolic flow potential approaches its asymptote (when the eccentricity tends to zero, the flow potential tends to a straight line); and

$\overline{p}$ and $\overline{q}$ are two stress invariants of the effective stress tensor ($\overline{p}$ is the hydrostatic pressure stress and $\overline{q}$ is the Mises equivalent effective stress) (ABAQUS, 2010).

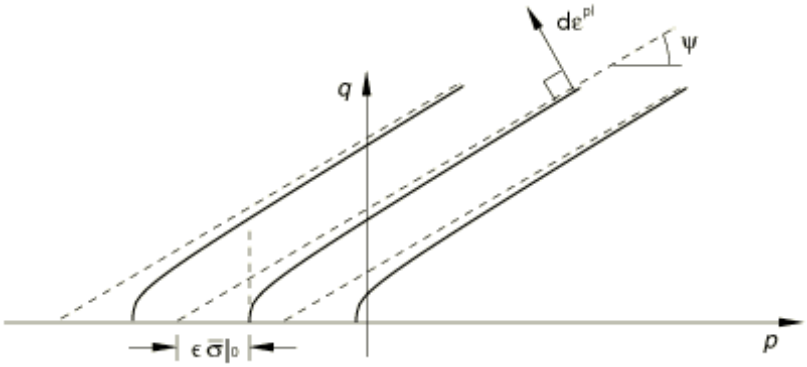

Figure E8 Hyperbolic flow potentials in the *p*–*q* plane (ABAQUS, 2010)

The CDP model uses the yield function of Lubliner et al. (1989) modified by Lee et al. (1998) (ABAQUS, 2010). The yield function generalises the concept of yield stress to multi-axial stress states, while the flow rule determines the connection between the yield surface and the stress-strain relationship (Malm, 2009). The following parameters are required to assign yield and flow relations.

1. Dilation Angle, ψ. Dilation is referred to a significant volume change in the concrete subjected to severe inelastic states (Malm, 2009). Malm (2009) showed that the difference in the behaviour of concrete in four-point bending is only marginal when the dilation angle varies between 30º and 40º, and the best agreement with the experiments is reached in that range. In the verification of the material model performed by Lee et al. (1998), to describe both uniaxial tensile and compressive failure, the best dilation angle was found as 31º. Jankowiak et al. (2005), in a parametric study of the dilation angle, determined the dilation angle as 38º to minimise the error of Kupfer (1969) biaxial failure envelope and the yield surface developed for damaged plasticity model in ABAQUS (cited in Malm, 2006). In the current study the dilation angle of 31º is used as found by Lee et al. (1998).
2. Eccentricity, ϵ, which is a small positive number standing for the rate at which the hyperbolic flow potential approaches its asymptote (ABAQUS, 2010). The default is $\epsilon = 0.1$.
3. The ratio of biaxial compressive strength to uniaxial compressive strength, $\sigma_{b_0}/\sigma_{c_0}$ (Figure E9). The typical value of this ratio is about 1.15 for plain concrete. For the SFRC mixes studied in the current research, as explained for CSC model, this ratio is increased to 1.2.

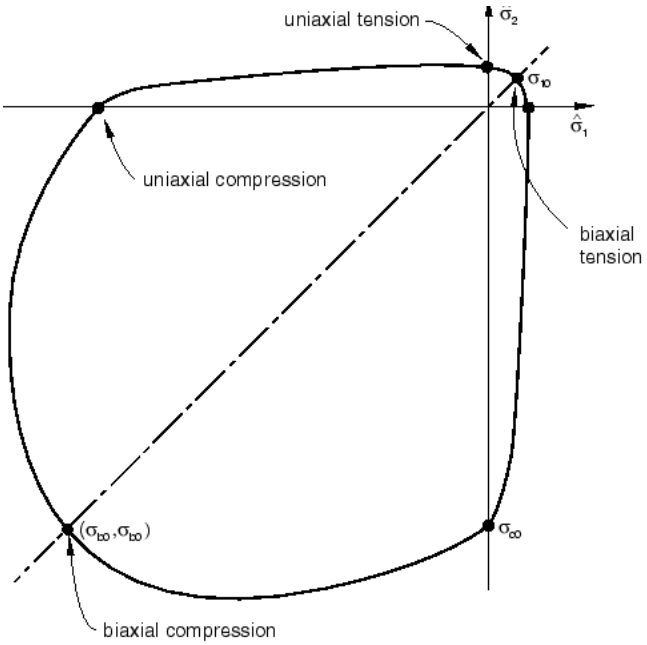

Figure E9 Yield surfaces in plane stress in CDP model (ABAQUS, 2010)

4. K_c, which is "the ratio of the second stress invariant on the tensile meridian, $q_{(TM)}$, to that on the compressive meridian, $q_{(CM)}$, at initial yield for any given value of the pressure invariant p such that the maximum principal stress is negative, $\hat{\sigma}_{max} < 0$" (Figure E10). K_c can be in the range of 0.5 to 1.0, with a default value of 2/3 assumed in ABAQUS (ABAQUS, 2010). The default value is maintained in the current study.

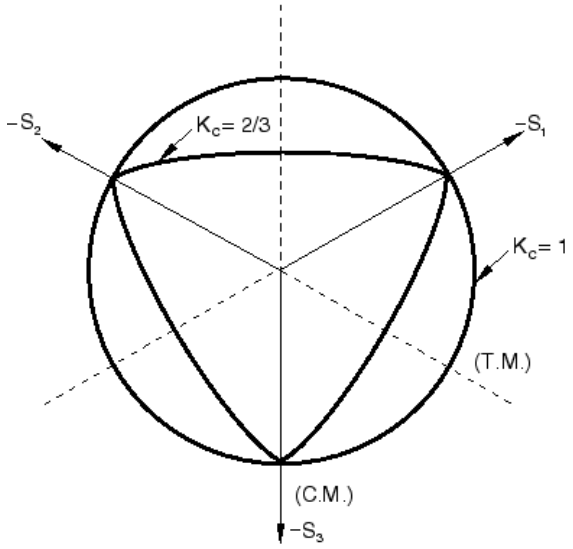

Figure E10 Yield surfaces in the deviatoric plane, for different values of K_c (ABAQUS, 2010)

The assumption made for biaxial compressive strength of SFRC is the same as in CSC model.

Appendix F: Mesh sensitivity issue in the smeared cracking model

When concentrated cracking occurs, if the element size is bigger than the size of the cracking zone, sensitivity to the element size exists in the FE model. This is because in that case the fracture energy is absorbed by the whole length of the element in the FE model, while cracking occurs only in part of the element length (Figure F1 (a)). In another description, the crack band in FE model is calculated wider than reality. By mesh refinement, as soon as the element size is modelled smaller than the size of the cracking zone (Figure F1 (b)), sensitivity to the element size is diminished. That is because the fracture energy is distributed in the element length which fully contributes in cracking, and since the elements located in the fracture zone share the fracture energy, the resultant energy per element length remains constant for further refinement (Figure F1 (c) and (d)). Finally, It can be concluded that the element size for which (and for smaller sizes) the mesh sensitivity is diminished depends to the level of reinforcement.

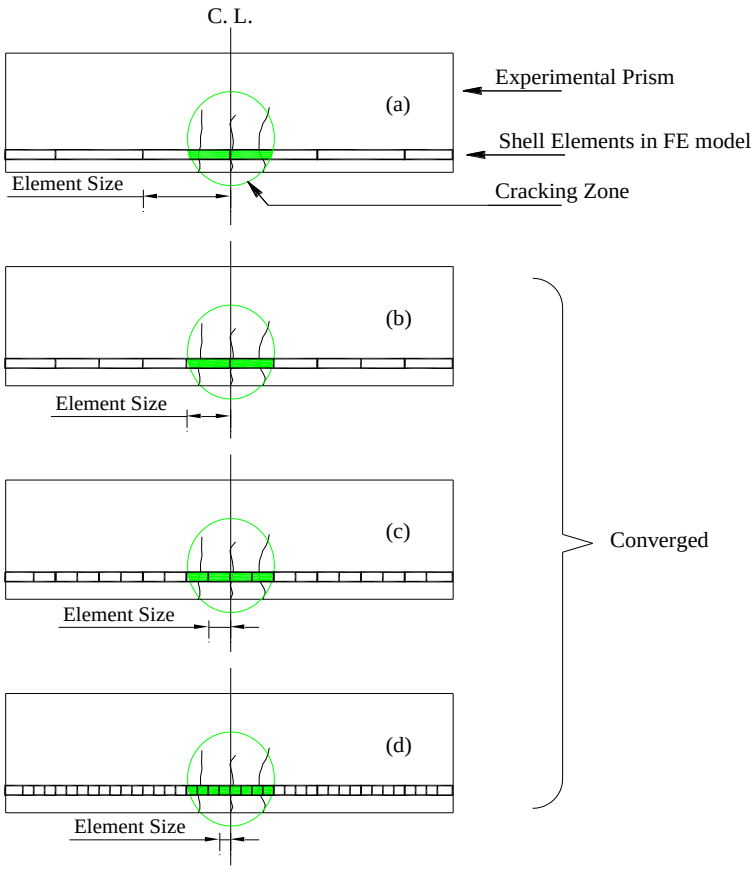

Figure F1 Effect of element size, relative to the crack band width, on analysis convergence

Appendix G: FE analysis input files

G.1. Data processing analysis

G.1.1 Diffusivity inverse analysis

File name: FRCC

```
*HEADING
*PREPRINT, echo=YES, model=YES, history=YES, contact=YES
**----------------------------------------
*Node
      1,          0.,          0.,           0.
      2,         30.,          0.,           0.
      3,         60.,          0.,           0.
      4,         90.,          0.,           0.
      5,        120.,          0.,           0.
      6,        150.,          0.,           0.
     31,          0.,        150.,           0.
     32,         30.,        150.,           0.
     33,         60.,        150.,           0.
     34,         90.,        150.,           0.
     35,        120.,        150.,           0.
     36,        150.,        150.,           0.
   1101,          0.,          0.,          52.
   1102,         30.,          0.,          52.
   1103,         60.,          0.,          52.
   1104,         90.,          0.,          52.
   1105,        120.,          0.,          52
   1106,        150.,          0.,          52.
   1131,          0.,        150.,          52.
   1132,         30.,        150.,          52.
   1133,         60.,        150.,          52.
   1134,         90.,        150.,          52.
   1135,        120.,        150.,          52.
   1136,        150.,        150.,          52.
   1901,          0.,          0.,          93.
   1902,         30.,          0.,          93
   1903,         60.,          0.,          93
   1904,         90.,          0.,          93
   1905,        120.,          0.,          93
   1906,        150.,          0.,          93
   1931,          0.,        150.,          93
   1932,         30.,        150.,          93
   1933,         60.,        150.,          93
   1934,         90.,        150.,          93
   1935,        120.,        150.,          93
   1936,        150.,        150.,          93
   2401,          0.,          0.,         117
   2402,         30.,          0.,         117
   2403,         60.,          0.,         117
```

```
    2404,         90.,          0.,           117
    2405,        120.,          0.,           117
    2406,        150.,          0.,           117
    2431,          0.,        150.,           117
    2432,         30.,        150.,           117
    2433,         60.,        150.,           117
    2434,         90.,        150.,           117
    2435,        120.,        150.,           117
    2436,        150.,        150.,           117
    2701,          0.,          0.,           132
    2702,         30.,          0.,           132
    2703,         60.,          0.,           132
    2704,         90.,          0.,           132
    2705,        120.,          0.,           132
    2706,        150.,          0.,           132
    2731,          0.,        150.,           132
    2732,         30.,        150.,           132
    2733,         60.,        150.,           132
    2734,         90.,        150.,           132
    2735,        120.,        150.,           132
    2736,        150.,        150.,           132
    2901,          0.,          0.,           140.5
    2902,         30.,          0.,           140.5
    2903,         60.,          0.,           140.5
    2904,         90.,          0.,           140.5
    2905,        120.,          0.,           140.5
    2906,        150.,          0.,           140.5
    2931,          0.,        150.,           140.5
    2932,         30.,        150.,           140.5
    2933,         60.,        150.,           140.5
    2934,         90.,        150.,           140.5
    2935,        120.,        150.,           140.5
    2936,        150.,        150.,           140.5
   3101,          0.,          0.,           153.
   3102,         30.,          0.,           153.
   3103,         60.,          0.,           153.
   3104,         90.,          0.,           153.
   3105,        120.,          0.,           153.
   3106,        150.,          0.,           153.
   3131,          0.,        150.,           153.
   3132,         30.,        150.,           153.
   3133,         60.,        150.,           153.
   3134,         90.,        150.,           153.
   3135,        120.,        150.,           153.
   3136,        150.,        150.,           153.
*NGEN,NSET=L1
  1,6,1
*NGEN,NSET=L1101
 1101,1106,1
*NGEN,NSET=L1901
 1901,1906,1
*NGEN,NSET=L2401
  2401,2406,1
*NGEN,NSET=L2701
  2701,2706,1
*NGEN,NSET=L2901
  2901,2906,1
*NGEN,NSET=L3101
 3101,3106,1
*NGEN,NSET=L3
```

```
 31,36,1
*NGEN,NSET=L1103
 1131,1136,1
*NGEN,NSET=L1903
 1931,1936,1
*NGEN,NSET=L2403
 2431,2436,1
*NGEN,NSET=L2703
 2731,2736,1
*NGEN,NSET=L2903
 2931,2936,1
*NGEN,NSET=L3103
 3131,3136,1
*NFIL,NSET=SURFB
  L1, L3, 5,6
*NFIL,NSET=SURFB1100
  L1101, L1103, 5,6
*NFIL,NSET=SURFB1900
  L1901, L1903, 5,6
*NFIL,NSET=SURFB2400
  L2401, L2403, 5,6
*NFIL,NSET=SURFB2700
  L2701, L2703, 5,6
*NFIL,NSET=SURFB2900
  L2901, L2903, 5,6
*NFIL,NSET=SURFT
  L3101, L3103, 5,6
*NFIL,NSET=ALLN1
  SURFB, SURFB1100, 11,100
*NFIL,NSET=ALLN2
  SURFB1100, SURFB1900, 8,100
*NFIL,NSET=ALLN3
  SURFB1900, SURFB2400, 5,100
*NFIL,NSET=ALLN4
  SURFB2400, SURFB2700, 3,100
*NFIL,NSET=ALLN5
  SURFB2700, SURFB2900, 2,100
*NFIL,NSET=ALLN6
  SURFB2900, SURFT, 2,100
*Nset, nset=DEPTH
6,1106, 1906, 2406, 2706, 2906
*Nset, nset=ALLN
ALLN1,ALLN2, ALLN3, ALLN4, ALLN5, ALLN6
**-------------------------------------
*Element, type=DC3D8, ELSET=E1
   1,  1,  2,  8,  7,    101,    102,   108,   107
*ELGEN,ELSET=ALLE
1,5,1,1,5,6,5,31,100,25
*Elset, elset=CENT, generate
13,763,25
*Elset, elset=TOPL, generate
751,775,1
**-----------------------------------------------------------------
*Surface, type=ELEMENT, name=TOPS
TOPL, S2
**-----------------------------------------------
*Solid Section, elset=ALLE, material="THERMAL"
*Material, name="THERMAL"
*Conductivity
 4.1, 0.001
```

```
 4.75, 0.8
 4.9, 0.83
 5, 0.86
 5.2, 0.87
 5.4, 0.88
 6, 0.89
 15, 0.925
 25, 0.96
 27, 0.97
 28, 0.98
 30, 0.999
*Density
 1,
*Specific Heat
 1,
** ----------------------------------------------------------
*Initial Conditions, type=TEMPERATURE
ALLN, 1.0
** ----------------------------------------------------------------
*Restart, write, frequency=10
*Step, name=THERML, INC=1000
*HEAT TRANSFER,DELTMX=0.1, EN=SS
.005,85, 0.00001,1,.0001
*Sfilm
TOPS, F, 0.4, 5
*NODE PRINT,FREQUENCY=50
NT,
*PRINT,FREQUENCY=10
*NODE FILE
NT,
*OUTPUT,FIELD
*NODE OUTPUT
NT,
*OUTPUT,HISTORY, FREQUENCY=1
*NODE OUTPUT, NSET=DEPTH0
NT,
*OUTPUT,HISTORY, FREQUENCY=1
*NODE OUTPUT, NSET=DEPTH1
NT,
*OUTPUT,HISTORY, FREQUENCY=1
*NODE OUTPUT, NSET=DEPTH3
NT,
*OUTPUT,HISTORY, FREQUENCY=1
*NODE OUTPUT, NSET=DEPTH5
NT,
*OUTPUT,HISTORY, FREQUENCY=1
*NODE OUTPUT, NSET=DEPTH7
NT,
*OUTPUT,HISTORY, FREQUENCY=1
*NODE OUTPUT, NSET=DEPTH9
NT,
*OUTPUT,HISTORY, FREQUENCY=1
*NODE OUTPUT, NSET=DEPTH10
NT,
**********
*Output, field, variable=ALL, FREQUENCY=100
*Node Output, nset=ALLN
*****************
*End Step
```

G.1.2 Free shrinkage inverse analysis

File name: FS-STR-THRM-FRCC-PLAS

```
*HEADING
JOB NAME: MODELILING NAEIMEH'S FREE SHRINKAGE TEST SPECIMENS
*PREPRINT, echo=YES, model=YES, history=YES, contact=YES
**----------------------------------------
*Node, NSET=ALLN
      1,          0.,         0.,           0.
     16,        150.,         0.,           0.
    241,          0.,       150.,           0.
    256,        150.,       150.,           0.
  11001,          0.,         0.,         275.
  11016,        150.,         0.,         275.
  11241,          0.,       150.,         275.
  11256,        150.,       150.,         275.
*NGEN,NSET=L1
  1,16,1
*NGEN,NSET=L3
 241,256,1
*NFIL,NSET=SURFB
  L1, L3,15,16
*NGEN,NSET=L9
11001,11016,1
*NGEN,NSET=L11
11241,11256,1
*NFIL,NSET=SURFT
  L9, L11, 15,16
*NFIL,NSET=ALLN
  SURFB, SURFT, 11,1000
*NSET, NSET=C1
 8
*NSET, NSET=C2
 24
*NSET, NSET=C3
 40
*NSET, NSET=C4
 56
*NSET, NSET=C5
 72
*NSET, NSET=C6
 88
*NSET, NSET=C7
104
*NSET, NSET=C8
120
*NSET, NSET=CC
31
*NSET, NSET=BOTL, generate
1,256,1
*NSET, NSET=DEPTH, generate
120,11120,1000
**----------------------------------------
*Element, type=C3D8, ELSET=E1
   1,  1,  2,  18,  17,    1001,    1002,   1018,   1017
*ELGEN,ELSET=ALLE
1,15,1,1,15,16,15,11,1000,225
```

```
*Elset, elset=TOPL, generate
2251,2475,1
*Elset, elset=SIDE1, generate
1,15,1
226,240,1
451,465,1
676,690,1
901,915,1
1126,1140,1
1351,1365,1
1576,1590,1
1801,1815,1
2026,2040,1
2251,2265,1
*Elset, elset=SIDE2, generate
15,225,15
240,450,15
465,675,15
690,900,15
915,1125,15
1140,1350,15
1365,1575,15
1590,1800,15
1815,2025,15
2040,2250,15
2265,2475,15
*Elset, elset=SIDE3, generate
211,225,1
436,450,1
661,675,1
886,900,1
1111,1125,1
1336,1350,1
1561,1575,1
1786,1800,1
2011,2025,1
2236,2250,1
2461,2475,1
*Elset, elset=SIDE4, generate
1,211,15
226,436,15
451,661,15
676,886,15
901,1111,15
1126,1336,15
1351,1561,15
1576,1786,15
1801,2011,15
2026,2236,15
2251,2461,15
**----------------------------------------
*Surface, type=ELEMENT, name=S1
SIDE1, S3
*Surface, type=ELEMENT, name=S2
SIDE2, S4
*Surface, type=ELEMENT, name=S3
SIDE3, S5
*Surface, type=ELEMENT, name=S4
SIDE4, S6
**----------------------------------------------
```

```
**-----------------------------------------------------------
*Solid Section, elset=ALLE, material="CDP"
*Material, name="CDP"
*Elastic
 41000., 0.18
*Concrete Damaged Plasticity
31.,0.,1.2,0.,0.
*Concrete Compression Hardening
  7.0,      0.
 13.8,   6e-05
 20.8,   9e-05
 34.0, 0.00017
 41.9, 0.00028
 48.2, 0.00042
 54.0, 0.00068
 56.1, 0.00107
*Concrete Tension Stiffening
 4.7,     0
 2.3, 0.0005
 2.0, 0.0020
 1.4, 0.0073
 0.0, 0.0300
 *Concrete Tension Damage
 0.0,     0
 0.5, 0.0005
 0.6, 0.0020
 0.7, 0.0073
 0.95, 0.030
**Density
**1,
*Expansion, zero=1.
 0.002000, 0.4
 0.002036, 0.5
 0.002082, 0.6
 0.002143, 0.7
 0.002232, 0.8
 0.002392, 0.9
 0.002446, 0.92
 0.002517, 0.94
 0.002621, 0.96
 0.002810, 0.98
 0.003011, 0.99
 0.003791, 0.999
** -----------------------------------------------------------
** -----------------------------------------------------------
*Boundary
BOTL, 3, 6
120, 1,2
121, 1,2
136, 1,2
137, 1,2
** -----------------------------------------------------------
*Initial Conditions, type=TEMPERATURE
ALLN, 1.0
** -----------------------------------------------------------
*Step, name=STRUCTURAL, amplitude=STEP, INC=1000
*STATIC
.005,85, 0.00001,5,.0001
*TEMPERATURE,FILE=FS-THRM-FRCC.odb
*Restart, write, frequency=1
```

```
*Output, field, variable=ALL, frequency=1
*End Step
**------------------------------------------------------------
```

G.1.2.1 Moisture transport analysis for free shrinkage specimens (referred in the above input file in Section G.1.2)

File name: FS-THRM-FRCC

```
*HEADING
*PREPRINT, echo=YES, model=YES, history=YES, contact=YES
**--------------------------------------
*Node, NSET=ALLN
      1,          0.,         0.,           0.
     16,        150,          0.,           0.
    241,          0.,       150,            0.
    256,        150,        150,            0.
  11001,          0.,         0.,         275
  11016,        150,          0.,         275
  11241,          0.,       150,          275
  11256,        150,        150,          275
*NGEN,NSET=L1
  1,16,1
*NGEN,NSET=L3
 241,256,1
*NFIL,NSET=SURFB
  L1, L3,15,16
*NGEN,NSET=L9
11001,11016,1
*NGEN,NSET=L11
11241,11256,1
*NFIL,NSET=SURFT
  L9, L11, 15,16
*NFIL,NSET=ALLN
  SURFB, SURFT, 11,1000
*NSET, NSET=C1
 8
*NSET, NSET=C2
 24
*NSET, NSET=C3
 40
*NSET, NSET=C4
 56
*NSET, NSET=C5
 72
*NSET, NSET=C6
 88
*NSET, NSET=C7
104
*NSET, NSET=C8
120
*NSET, NSET=CC
31
**--------------------------------------
*Element, type=DC3D8, ELSET=E1
   1,  1,  2,  18,  17,    1001,    1002,   1018,   1017
```

```
*ELGEN,ELSET=ALLE
1,15,1,1,15,16,15,11,1000,225
*Elset, elset=TOPL, generate
2251,2475,1
*Elset, elset=SIDE1, generate
1,15,1
226,240,1
451,465,1
676,690,1
901,915,1
1126,1140,1
1351,1365,1
1576,1590,1
1801,1815,1
2026,2040,1
2251,2265,1
*Elset, elset=SIDE2, generate
15,225,15
240,450,15
465,675,15
690,900,15
915,1125,15
1140,1350,15
1365,1575,15
1590,1800,15
1815,2025,15
2040,2250,15
2265,2475,15
*Elset, elset=SIDE3, generate
211,225,1
436,450,1
661,675,1
886,900,1
1111,1125,1
1336,1350,1
1561,1575,1
1786,1800,1
2011,2025,1
2236,2250,1
2461,2475,1
*Elset, elset=SIDE4, generate
1,211,15
226,436,15
451,661,15
676,886,15
901,1111,15
1126,1336,15
1351,1561,15
1576,1786,15
1801,2011,15
2026,2236,15
2251,2461,15
**--------------------------------------
*Surface, type=ELEMENT, name=S1
SIDE1, S3
*Surface, type=ELEMENT, name=S2
SIDE2, S4
*Surface, type=ELEMENT, name=S3
SIDE3, S5
*Surface, type=ELEMENT, name=S4
```

```
SIDE4, S6
**-----------------------------------------------
**-----------------------------------------------
*Solid Section, elset=ALLE, material="THERMAL"
*Material, name="THERMAL"
*Conductivity
  4.1, 0.001
 4.75,   0.8
  4.9,  0.83
   5.,  0.86
  5.2,  0.87
  5.4,  0.88
   6.,  0.89
  15., 0.925
  25.,  0.96
  27.,  0.97
  28.,  0.98
  30., 0.999
*Density
 1,
*Specific Heat
 1,
** ----------------------------------------------------------
*Initial Conditions, type=TEMPERATURE
ALLN, 1.0
**----------------------------------------------------------
*Restart, write, frequency=10
*Step, name=THERML, INC=1000
*HEAT TRANSFER, END=PERIOD, DELTMX=0.1
.005,85, 0.00001,5
*Sfilm
S1, F, 0.4, 5
S2, F, 0.4, 5
S3, F, 0.4, 5
S4, F, 0.4, 5
*NODE PRINT,FREQUENCY=50
NT,
*PRINT,FREQUENCY=10
*NODE FILE
NT,
*OUTPUT,FIELD
*NODE OUTPUT
NT,
**********
*Output, field, variable=ALL, FREQUENCY=100
*Node Output, nset=ALLN
*****************
*End Step
```

G.2. Pavement analysis

G.2.1 Moisture transport analysis of the SFR-RCC pavement

Only half of the pavement is modelled in the transversal direction (due to symmetry).

File name: PAV-FRCC-THRM-25-120-HALF-8N

```
*HEADING
*PREPRINT, echo=YES, model=YES, history=YES, contact=YES
*NODE
**SLAB NODES
    1,        0,           0,       0
   85,    10080,           0,       0
 1191,        0,        1680,       0
 1275,    10080,        1680,       0
10201,        0,           0,       200
10285,    10080,           0,       200
11391,        0,        1680,       200
11475,    10080,        1680,       200
*NGEN,NSET=EDGE1
 1,85,1
*NGEN,NSET=EDGE2
 1191,1275,1
*NFILL,NSET=SURFB
 EDGE1, EDGE2 ,14,85
*NGEN,NSET=EDGE3
 10201,10285,1
*NGEN,NSET=EDGE4
 11391,11475,1
*NFILL,NSET=SURFT
 EDGE3, EDGE4,14,85
*NFIL,NSET=SLABN
 SURFB, SURFT, 8,1275
*Element, type=DC3D8
 1, 1,2,87,86,1276,1277,1362,1361
*ELGEN, ELSET=SLABE
 1, 84, 1, 1, 14, 85, 84, 8, 1275, 1176
*Elset, elset=BOTE, generate
 1,  1176,      1
*Elset, elset=TOPE, generate
 8233,  9408,      1
**------------------------------------------------------------------
**------------------------------------------------------------------
*Surface, type=ELEMENT, name=TOPS
 TOPE, S2
**-----------------------------------------------------------
** -----------------------------------------------------------
*Solid Section, elset=SLABE, material=THERMAL-FRCC
**-----------------------------------------------------------
*Material, name=THERMAL-FRCC
*Conductivity
  4.1, 0.001
 4.75,   0.8
  4.9,  0.83
```

```
   5.,  0.86
  5.2,  0.87
  5.4,  0.88
   6.,  0.89
  15., 0.925
  25.,  0.96
  27.,  0.97
  28.,  0.98
  30., 0.999
*Density
 1.,
*Specific Heat
 1.,
** ----------------------------------------------------------------
*Initial Conditions, type=TEMPERATURE
 SLABN, 1.
** ----------------------------------------------------------------
*Step, name=THERML, inc=10000
*Heat Transfer, end=PERIOD, deltmx=0.1
 0.05, 364., 1e-05, 14
*Sfilm
TOPS, F, 0.4, 5
*Restart, write, frequency=10
*Print, frequency=10
*Output, field
*Node Output
 NT,
*Output, field, variable=ALL, frequency=10
*Output, history, frequency=0
*End Step
```

G.2.2 Restrained shrinkage analysis of the SFR-RCC pavement

Only half of the pavement is modelled in the transversal direction (due to symmetry).

G.2.2.1 Immature concrete

File name: PAV-FRCC-STR-THRM-25-120-HALF-8NF-SHRKONLY-PLASFREESH

```
*HEADING
*PREPRINT, echo=YES, model=YES, history=YES, contact=YES
*NODE
**SLAB NODES
  1,          0,           0,       0
 85,      10080,           0,       0
 1191,        0,        1680,       0
 1275,    10080,        1680,       0
10201,        0,           0,       200
10285,    10080,           0,       200
11391,        0,        1680,       200
11475,    10080,        1680,       200
*NGEN,NSET=EDGE1
 1,85,1
*NGEN,NSET=EDGE2
 1191,1275,1
*NFILL,NSET=SURFB
```

```
 EDGE1, EDGE2 ,14,85
*NGEN,NSET=EDGE3
 10201,10285,1
*NGEN,NSET=EDGE4
 11391,11475,1
*NFILL,NSET=SURFT
  EDGE3, EDGE4,14,85
*NFIL,NSET=SLABN
  SURFB, SURFT, 8,1275
*Element, type=C3D8
  1, 1,2,87,86,1276,1277,1362,1361
*ELGEN, ELSET=SLABE
   1, 84, 1, 1, 14, 85, 84, 8, 1275, 1176
*Elset, elset=BOTE, generate
 1,  1176,      1
*Elset, elset=TOPE, generate
 8233,  9408,      1
**------------------------------------------------------------
*Nset, nset=ENDS, GENERATE
85,1275,85
1360,2550,85
2635,3825,85
3910,5100,85
5185,6375,85
6460,7650,85
7735,8925,85
9010,10200,85
10285,11475,85
**------------------------------------------------------------
*Nset, nset=MIDS, GENERATE
1,85,1
1276,1360,1
2551,2635,1
3826,3910,1
5101,5185,1
6376,6460,1
7651,7735,1
8926,9010,1
10201,10285,1
**-----------------------------------------------------------
*Nset, nset=LOADNODES
10541, 10542, 10626, 10627, 10711, 10712, 10881, 10882, 10966, 10967,
11051, 11052
**------------------------------------------------------------
*Surface, type=ELEMENT, name=BOTS
BOTE, S1
*Surface, type=ELEMENT, name=TOPS
TOPE, S2
**-----------------------------------------------------------
*Node
**BASE NODES
 200001,       -120,             0,       -150
 200086,      10080,             0,       -150
 201291,       -120,          1800,           -150
 201376,      10080,          1800,       -150
 204129,       -120,             0,          0
 204214,      10080,             0,          0
 205419,       -120,          1800,              0
 205504,      10080,          1800,          0
*NGEN,NSET=BEDGE1
```

```
 200001,200086,1
*NGEN,NSET=BEDGE2
 201291,201376,1
*NFILL,NSET=BSURFB
  BEDGE1, BEDGE2 ,15,86
*NGEN,NSET=BEDGE3
 204129,204214,1
*NGEN,NSET=BEDGE4
 205419,205504,1
*NFILL,NSET=BSURFT
  BEDGE3, BEDGE4,15,86
*NFIL,NSET=BASEN
  BSURFB, BSURFT, 3,1376
*Element, type=C3D8
  160001, 200001,200002,200088,200087,201377,201378,201464,201463
*ELGEN, ELSET=BASEE
   160001, 85, 1, 1, 15, 86, 85, 3, 1376, 1275
**-----------------------------------------------------------
*Nset, nset=BTOPN, GENERATE
204129, 205504, 1
**-----------------------------------------------------------
*Nset, nset=ENDB, GENERATE
 200086, 201376, 86
 201462, 202752, 86
 202838, 204128, 86
 204214, 205504, 86
*Nset, nset=STAB, GENERATE
 200001, 201291, 86
 201377, 202667, 86
 202753, 204043, 86
 204129, 205419, 86
*Nset, nset=RIGB, GENERATE
 200001, 200086, 1
 201377, 201462, 1
 202753, 202838, 1
 204129, 204214, 1
*Nset, nset=LEFB, GENERATE
 201291, 201376, 1
 202667, 202752, 1
 204043, 204128, 1
 205419, 205504, 1
**-----------------------------------------------------------
*Elset, elset=BBOTE, generate
 160001,  161275,      1
*Elset, elset=BTOPE, generate
 162551,  163825,      1
**-------------------------------------------------------------
*Surface, type=ELEMENT, name=BTOPS
BTOPE, S2
**-----------------------------------------------------------
*Solid Section, elset=SLABE, material="CDP"
*Material, name="CDP"
*Elastic, dependencies=1
 23901., 0.18, ,1
 30842., 0.18, ,3
 33361., 0.18, ,5
 34784., 0.18, ,7
 37186., 0.18, ,14
 38984., 0.18, ,28
 40308., 0.18, ,56
```

```
 41000., 0.18, ,90
 41000., 0.18, ,366
*Concrete Damaged Plasticity
31.,0.,1.2,0.,0.
*Concrete Compression Hardening, DEPENDENCIES=1
  1.2,      0. , , ,1
  2.3,   6e-05 , , ,1
  3.4,   9e-05 , , ,1
  5.6, 0.00017 , , ,1
  6.9, 0.00028 , , ,1
  8.0, 0.00042 , , ,1
  8.9, 0.00068 , , ,1
  9.3, 0.00107 , , ,1
  2.7,      0. , , ,3
  5.3,   6e-05 , , ,3
  8.1,   9e-05 , , ,3
 13.2, 0.00017 , , ,3
 16.2, 0.00028 , , ,3
 18.7, 0.00042 , , ,3
 20.9, 0.00068 , , ,3
 21.7, 0.00107 , , ,3
  3.5,      0. , , ,5
  6.9,   6e-05 , , ,5
 10.5,   9e-05 , , ,5
 17.1, 0.00017 , , ,5
 21.1, 0.00028 , , ,5
 24.2, 0.00042 , , ,5
 27.1, 0.00068 , , ,5
 28.2, 0.00107 , , ,5
  4.0,      0. , , ,7
  8.0,   6e-05 , , ,7
 12.0,   9e-05 , , ,7
 19.7, 0.00017 , , ,7
 24.2, 0.00028 , , ,7
 27.9, 0.00042 , , ,7
 31.2, 0.00068 , , ,7
 32.4, 0.00107 , , ,7
  5.0,      0. , , ,14
 10.0,   6e-05 , , ,14
 15.0,   9e-05 , , ,14
 24.6, 0.00017 , , ,14
 30.3, 0.00028 , , ,14
 34.8, 0.00042 , , ,14
 39.0, 0.00068 , , ,14
 40.5, 0.00107 , , ,14
  5.9,      0. , , ,28
 11.7,   6e-05 , , ,28
 17.6,   9e-05 , , ,28
 28.7, 0.00017 , , ,28
 35.4, 0.00028 , , ,28
 40.7, 0.00042 , , ,28
 45.6, 0.00068 , , ,28
 47.4, 0.00107 , , ,28
  6.6,      0. , , ,56
 13.0,   6e-05 , , ,56
 19.7,   9e-05 , , ,56
 32.1, 0.00017 , , ,56
 39.6, 0.00028 , , ,56
 45.5, 0.00042 , , ,56
 51.0, 0.00068 , , ,56
```

```
 53.0, 0.00107 , , ,56
  7.0,      0. , , ,90
 13.8,   6e-05 , , ,90
 20.8,   9e-05 , , ,90
 34.0, 0.00017 , , ,90
 41.9, 0.00028 , , ,90
 48.2, 0.00042 , , ,90
 54.0, 0.00068 , , ,90
 56.1, 0.00107 , , ,90
  7.0,      0. , , ,366
 13.8,   6e-05 , , ,366
 20.8,   9e-05 , , ,366
 34.0, 0.00017 , , ,366
 41.9, 0.00028 , , ,366
 48.2, 0.00042 , , ,366
 54.0, 0.00068 , , ,366
 56.1, 0.00107 , , ,366
*Concrete Tension Stiffening, DEPENDENCIES=1
 0.8,     0., , ,1
 0.4, 0.0002, , ,1
 0.4, 0.0006, , ,1
 0.2, 0.0023, , ,1
 0.02, 0.0094, , ,1
 1.9,     0., , ,3
 0.9, 0.0003, , ,3
 0.8, 0.0011, , ,3
 0.6, 0.0041, , ,3
 0.02, 0.0170, , ,3
 2.5,     0., , ,5
 1.2, 0.0004, , ,5
 1.1, 0.0013, , ,5
 0.7, 0.0050, , ,5
 0.05, 0.0204, , ,5
 2.9,     0., , ,7
 1.4, 0.0004, , ,7
 1.2, 0.0015, , ,7
 0.9, 0.0055, , ,7
 0.05, 0.0225, , ,7
 3.6,     0., , ,14
 1.8, 0.0005, , ,14
 1.5, 0.0017, , ,14
 1.1, 0.0064, , ,14
 0.05, 0.0263, , ,14
 4.2,     0., , ,28
 2.1, 0.0005, , ,28
 1.8, 0.0019, , ,28
 1.3, 0.0071, , ,28
 0.05, 0.0294, , ,28
 4.5,     0., , ,56
 2.2, 0.0005, , ,56
 1.9, 0.0020, , ,56
 1.3, 0.0073, , ,56
 0.05, 0.0300, , ,56
 4.7,     0., , ,90
 2.3, 0.0005, , ,90
 2.0, 0.0020, , ,90
 1.4, 0.0073, , ,90
 0.05, 0.0300, , ,90
 4.7,     0., , ,366
 2.3, 0.0005, , ,366
```

```
  2., 0.0020, , ,366
 1.4, 0.0073, , ,366
 0.05, 0.0300, , ,366
 *Concrete Tension Damage, DEPENDENCIES=1
 0.0,     0.,  ,1
 0.5, 0.0002,  ,1
 0.6, 0.0006,  ,1
 0.7, 0.0023,  ,1
 0.95, 0.0094,  ,1
 0.0,     0.,  ,3
 0.5, 0.0003,  ,3
 0.6, 0.0011,  ,3
 0.7, 0.0041,  ,3
 0.95, 0.0170,  ,3
 0.0,     0.,  ,5
 0.5, 0.0004,  ,5
 0.6, 0.0013,  ,5
 0.7, 0.0050,  ,5
 0.95, 0.0204,  ,5
 0.0,     0.,  ,7
 0.5, 0.0004,  ,7
 0.6, 0.0015,  ,7
 0.7, 0.0055,  ,7
 0.95, 0.0225,  ,7
 0.0,     0.,  ,14
 0.5, 0.0005,  ,14
 0.6, 0.0017,  ,14
 0.7, 0.0064,  ,14
 0.95, 0.0263,  ,14
 0.0,     0.,  ,28
 0.5, 0.0005,  ,28
 0.6, 0.0019,  ,28
 0.7, 0.0071,  ,28
 0.95, 0.0294,  ,28
 0.0,     0.,  ,56
 0.5, 0.0005,  ,56
 0.6, 0.0020,  ,56
 0.7, 0.0073,  ,56
 0.95, 0.0300,  ,56
 0.0,     0.,  ,90
 0.5, 0.0005,  ,90
 0.6, 0.0020,  ,90
 0.7, 0.0073,  ,90
 0.95, 0.0300,  ,90
 0.0,     0.,  ,366
 0.5, 0.0005,  ,366
 0.6, 0.0020,  ,366
 0.7, 0.0073,  ,366
 0.95, 0.0300,  ,366
**Density
**1,
*Expansion, zero=1.
 0.002000, 0.4
 0.002036, 0.5
 0.002082, 0.6
 0.002143, 0.7
 0.002232, 0.8
 0.002392, 0.9
 0.002446, 0.92
 0.002517, 0.94
```

```
 0.002621, 0.96
 0.002810, 0.98
 0.003011, 0.99
 0.003791, 0.999
** ----------------------------------------------------------
** ----------------------------------------------------------
*Solid Section, elset=BASEE, material="ELASTIC B"
*Material, name="ELASTIC B"
*Elastic
 8000., 0.3
** ----------------------------------------------------------
*Surface Interaction, name=CONTPROP
*Friction, slip tolerance=0.005, taumax=0.1
0.5,
*Surface Behavior, pressure-overclosure=HARD
** ----------------------------------------------------------
*Boundary
ENDS, 1, 1
*Boundary
MIDS, 2, 2
*Boundary
ENDB, 1, 1
*Boundary
RIGB, 2, 2
** ----------------------------------------------------------
*AMPLITUDE, NAME=TFUNC, TIME=TOTAL TIME, DEFINITION=TABULAR,
VALUE=ABSOLUTE
0, 0, 400, 400
*Initial Conditions, type=TEMPERATURE
SLABN, 1.0
*Initial Conditions, type=FIELD, VARIABLE=1
SLABN, 0.001
*Foundation
BBOTE, F1, 0.06
*Contact Pair, interaction=CONTPROP, TYPE=SURFACE TO SURFACE
BOTS, BTOPS
** ----------------------------------------------------------
*Step, name=STRUCTURAL, amplitude=STEP, INC=10000, NLGEOM=YES
*STATIC
0.05, 364., 1e-05, 14
**CONTACT CONTROLS, SLAVE=BOTS, MASTER=BTOPS, MAXCHP=50000,
PERRMX=1.0
*Dload
SLABE, BZ, -2.5432e-05
*TEMPERATURE,FILE=PAV-FRCC-THRM-25-120-HALF-8N.odb
*FIELD, VARIABLE=1, AMPLITUDE=TFUNC
SLABN, 364
*Restart, write, frequency=1
*Output, field, variable=ALL, frequency=1
*End Step
```

G.2.2.2 Hardened concrete

File name: PAV-FRCC-STR-THRM-25-120-HALF-8NF-SHRKONLY-PLASFREESH-HARDENED

```
*HEADING
*PREPRINT, echo=YES, model=YES, history=YES, contact=YES
```

```
*NODE
**SLAB NODES
  1,          0,           0,       0
 85,      10080,           0,       0
 1191,        0,        1680,       0
 1275,    10080,        1680,       0
10201,        0,           0,       200
10285,    10080,           0,       200
11391,        0,        1680,       200
11475,    10080,        1680,       200
*NGEN,NSET=EDGE1
 1,85,1
*NGEN,NSET=EDGE2
 1191,1275,1
*NFILL,NSET=SURFB
 EDGE1, EDGE2 ,14,85
*NGEN,NSET=EDGE3
 10201,10285,1
*NGEN,NSET=EDGE4
 11391,11475,1
*NFILL,NSET=SURFT
  EDGE3, EDGE4,14,85
*NFIL,NSET=SLABN
  SURFB, SURFT, 8,1275
*Element, type=C3D8
  1, 1,2,87,86,1276,1277,1362,1361
*ELGEN, ELSET=SLABE
   1, 84, 1, 1, 14, 85, 84, 8, 1275, 1176
*Elset, elset=BOTE, generate
 1,  1176,      1
*Elset, elset=TOPE, generate
 8233,  9408,      1
**-----------------------------------------------------------------
*Nset, nset=ENDS, GENERATE
85,1275,85
1360,2550,85
2635,3825,85
3910,5100,85
5185,6375,85
6460,7650,85
7735,8925,85
9010,10200,85
10285,11475,85
**-----------------------------------------------------------------
*Nset, nset=MIDS, GENERATE
1,85,1
1276,1360,1
2551,2635,1
3826,3910,1
5101,5185,1
6376,6460,1
7651,7735,1
8926,9010,1
10201,10285,1
**-----------------------------------------------------------
*Nset, nset=LOADNODES
10541, 10542, 10626, 10627, 10711, 10712, 10881, 10882, 10966, 10967,
11051, 11052
**-----------------------------------------------------------------
*Surface, type=ELEMENT, name=BOTS
```

```
BOTE, S1
*Surface, type=ELEMENT, name=TOPS
TOPE, S2
**-----------------------------------------------------
*Node
**BASE NODES
 200001,       -120,             0,       -150
 200086,      10080,             0,       -150
 201291,       -120,          1800,           -150
 201376,      10080,          1800,       -150
 204129,       -120,             0,          0
 204214,      10080,             0,          0
 205419,       -120,          1800,              0
 205504,      10080,          1800,          0
*NGEN,NSET=BEDGE1
 200001,200086,1
*NGEN,NSET=BEDGE2
 201291,201376,1
*NFILL,NSET=BSURFB
  BEDGE1, BEDGE2 ,15,86
*NGEN,NSET=BEDGE3
 204129,204214,1
*NGEN,NSET=BEDGE4
 205419,205504,1
*NFILL,NSET=BSURFT
  BEDGE3, BEDGE4,15,86
*NFIL,NSET=BASEN
  BSURFB, BSURFT, 3,1376
*Element, type=C3D8
  160001, 200001,200002,200088,200087,201377,201378,201464,201463
*ELGEN, ELSET=BASEE
   160001, 85, 1, 1, 15, 86, 85, 3, 1376, 1275
**-----------------------------------------------------------
*Nset, nset=BTOPN, GENERATE
204129, 205504, 1
**-----------------------------------------------------------
*Nset, nset=ENDB, GENERATE
 200086, 201376, 86
 201462, 202752, 86
 202838, 204128, 86
 204214, 205504, 86
*Nset, nset=STAB, GENERATE
 200001, 201291, 86
 201377, 202667, 86
 202753, 204043, 86
 204129, 205419, 86
*Nset, nset=RIGB, GENERATE
 200001, 200086, 1
 201377, 201462, 1
 202753, 202838, 1
 204129, 204214, 1
*Nset, nset=LEFB, GENERATE
 201291, 201376, 1
 202667, 202752, 1
 204043, 204128, 1
 205419, 205504, 1
**-----------------------------------------------------------
*Elset, elset=BBOTE, generate
 160001,  161275,      1
*Elset, elset=BTOPE, generate
```

```
 162551,  163825,      1
**-----------------------------------------------------------------
*Surface, type=ELEMENT, name=BTOPS
BTOPE, S2
**-----------------------------------------------------------
*Solid Section, elset=SLABE, material="CDP"
*Material, name="CDP"
*Elastic
 41000., 0.18
*Concrete Damaged Plasticity
31.,0.,1.2,0.,0.
*Concrete Compression Hardening
  7.0,      0.
 13.8,   6e-05
 20.8,   9e-05
 34.0, 0.00017
 41.9, 0.00028
 48.2, 0.00042
 54.0, 0.00068
 56.1, 0.00107
*Concrete Tension Stiffening
 4.7,     0
 2.3, 0.0005
 2.0, 0.0020
 1.4, 0.0073
 0.05, 0.0300
 *Concrete Tension Damage
 0.0,     0
 0.5, 0.0005
 0.6, 0.0020
 0.7, 0.0073
 0.95, 0.0300
**Density
**1,
*Expansion, zero=1.
 0.002000, 0.4
 0.002036, 0.5
 0.002082, 0.6
 0.002143, 0.7
 0.002232, 0.8
 0.002392, 0.9
 0.002446, 0.92
 0.002517, 0.94
 0.002621, 0.96
 0.002810, 0.98
 0.003011, 0.99
 0.003791, 0.999
** -----------------------------------------------------------
** -----------------------------------------------------------
*Solid Section, elset=BASEE, material="ELASTIC B"
*Material, name="ELASTIC B"
*Elastic
 8000., 0.3
** -----------------------------------------------------------
*Surface Interaction, name=CONTPROP
*Friction, slip tolerance=0.005, taumax=0.1
0.5,
*Surface Behavior, pressure-overclosure=HARD
** -----------------------------------------------------------
*Boundary
```

```
ENDS, 1, 1
*Boundary
MIDS, 2, 2
*Boundary
ENDB, 1, 1
*Boundary
RIGB, 2, 2
** ----------------------------------------------------------
*Initial Conditions, type=TEMPERATURE
SLABN, 1.0
*Initial Conditions, type=FIELD, VARIABLE=1
SLABN, 0.001
*Foundation
BBOTE, F1, 0.06
*Contact Pair, interaction=CONTPROP, TYPE=SURFACE TO SURFACE
BOTS, BTOPS
** ----------------------------------------------------------
*Step, name=STRUCTURAL, amplitude=STEP, INC=10000, NLGEOM=YES
*STATIC
0.05, 364., 1e-05, 14
**CONTACT CONTROLS, SLAVE=BOTS, MASTER=BTOPS, MAXCHP=50000,
PERRMX=1.0
*Dload
SLABE, BZ, -2.5432e-05
*TEMPERATURE,FILE=PAV-FRCC-THRM-25-120-HALF-8N.odb
*Restart, write, frequency=1
*Output, field, variable=ALL, frequency=1
*End Step
**-------------------------------------------------------------
```

G.2.3 Analysis of the SFR-RCC pavement under monotonic loading only

The full pavement is modelled in transversal direction, since the load is not applied symmetrically.

G.2.3.1 Corner loading

File name: PAV-FRCC-STR-THRM-25-120-FULL-8NF-MONOONLY-CORNER

```
*HEADING
*PREPRINT, echo=YES, model=YES, history=YES, contact=YES
*NODE
**SLAB NODES
    1,          0,         0,         0
  169,      20160,         0,         0
 4733,          0,      3360,         0
 4901,      20160,      3360,         0
39209,          0,         0,       200
39377,      20160,         0,       200
43941,          0,      3360,       200
44109,      20160,      3360,       200
```

```
*NGEN,NSET=EDGE1
 1,169,1
*NGEN,NSET=EDGE2
 4733,4901,1
*NFILL,NSET=SURFB
 EDGE1, EDGE2 ,28,169
*NGEN,NSET=EDGE3
 39209,39377,1
*NGEN,NSET=EDGE4
 43941,44109,1
*NFILL,NSET=SURFT
  EDGE3, EDGE4,28,169
*NFIL,NSET=SLABN
  SURFB, SURFT, 8,4901
*Element, type=C3D8
  1, 1,2,171,170,4902,4903,5072,5071
*ELGEN, ELSET=SLABE
   1, 168, 1, 1, 28, 169, 168, 8, 4901, 4704
*Elset, elset=BOTE, generate
 1,  4704,      1
*Elset, elset=TOPE, generate
 32929,  37632,      1
**-----------------------------------------------------------------
*Nset, nset=ENDS, GENERATE
169,4901,169
5070,9802,169
9971,14703,169
14872,19604,169
19773,24505,169
24674,29406,169
29575,34307,169
34476,39208,169
39377,44109,169
**-----------------------------------------------------------
*Nset, nset=MIDS, GENERATE
1,169,1
4902,5070,1
9803,9971,1
14704,14872,1
19605,19773,1
24506,24674,1
29407,29575,1
34308,34476,1
39209,39377,1
**-----------------------------------------------------------
*Nset, nset=LOADNODES
42927, 42928, 43096, 43097, 43265, 43266, 43603, 43604, 43772,
43773, 43941, 43942,
**-----------------------------------------------------------------
*Nset, nset=N1
2282, 2451, 2620
*Nset, nset=N2
2450, 2451, 2452
*Nset, nset=NB1
202480, 202651, 202822
*Nset, nset=NB2
202650, 202651, 202652
**-------------------------------------------------------------
*Surface, type=ELEMENT, name=BOTS
BOTE, S1
```

```
*Surface, type=ELEMENT, name=TOPS
TOPE, S2
**-----------------------------------------------------
*Node
**BASE NODES
 200001,       -120,          -120,       -150
 200171,      20280,          -120,       -150
 205131,       -120,          3480,       -150
 205301,      20280,          3480,       -150
 215904,       -120,          -120,          0
 216074,      20280,          -120,          0
 221034,       -120,          3480,          0
 221204,      20280,          3480,          0
*NGEN,NSET=BEDGE1
 200001,200171,1
*NGEN,NSET=BEDGE2
 205131,205301,1
*NFILL,NSET=BSURFB
  BEDGE1, BEDGE2 ,30,171
*NGEN,NSET=BEDGE3
 215904,216074,1
*NGEN,NSET=BEDGE4
 221034,221204,1
*NFILL,NSET=BSURFT
  BEDGE3, BEDGE4,30,171
*NFIL,NSET=BASEN
  BSURFB, BSURFT, 3,5301
*Element, type=C3D8
  160001, 200001,200002,200173,200172,205302,205303,205474,205473
*ELGEN, ELSET=BASEE
   160001, 170, 1, 1, 30, 171, 170, 3,5301, 5100
**-----------------------------------------------------------
*Nset, nset=BTOPN, GENERATE
215904, 221204, 1
**-----------------------------------------------------------
**-----------------------------------------------------------
*Elset, elset=BBOTE, generate
 160001,  165100,      1
*Elset, elset=BTOPE, generate
 170201,  175300,      1
**-------------------------------------------------------------
*Surface, type=ELEMENT, name=BTOPS
BTOPE, S2
**-----------------------------------------------------------
**-----------------------------------------------------------
*Solid Section, elset=SLABE, material="CDP"
*Material, name="CDP"
*Elastic
 41000., 0.18
*Concrete Damaged Plasticity
31.,0.,1.2,0.,0.
*Concrete Compression Hardening
  7.0,      0.
 13.8,   6e-05
 20.8,   9e-05
 34.0, 0.00017
 41.9, 0.00028
 48.2, 0.00042
 54.0, 0.00068
 56.1, 0.00107
```

```
*Concrete Tension Stiffening
 4.7,      0
 2.3, 0.0005
 2.0, 0.0020
 1.4, 0.0073
 0.05, 0.0300
 *Concrete Tension Damage
 0.0,      0
 0.5, 0.0005
 0.6, 0.0020
 0.7, 0.0073
 0.95, 0.0300
** ----------------------------------------------------------
** ----------------------------------------------------------
*Solid Section, elset=BASEE, material="ELASTIC B"
*Material, name="ELASTIC B"
*Elastic
 8000., 0.3
** ----------------------------------------------------------
*Surface Interaction, name=CONTPROP
*Friction, slip tolerance=0.005, taumax=0.1
0.5,
*Surface Behavior, pressure-overclosure=HARD
** ----------------------------------------------------------
*Boundary
N1, 1, 1
*Boundary
N2, 2, 2
*Boundary
NB1, 1, 1
*Boundary
NB2, 2, 2
** ----------------------------------------------------------
*Initial Conditions, type=TEMPERATURE
SLABN, 1.0
*Foundation
BBOTE, F1, 0.06
*Contact Pair, interaction=CONTPROP, TYPE=SURFACE TO SURFACE
BOTS, BTOPS
** ----------------------------------------------------------
*Step, name=STRUCTURAL, amplitude=STEP, INC=10000
*STATIC
0.2, 364., 1e-05,100
**CONTACT CONTROLS, SLAVE=BOTS, MASTER=BTOPS, MAXCHP=50000,
PERRMX=1.0
*Dload
SLABE, BZ, -2.5432e-05
*Restart, write, frequency=1
*Output, field, variable=ALL, frequency=1
*End Step
**-----------------------------------------------------------------
**-----------------------------------------------------------------
*Step, name=LOADING, inc=10000
*Static
0.05, 364., 1e-06, 14
*Cload
** 20TIMES OF THE ONE CYCLE SERVICE LOAD
LOADNODES, 3, -66666.6
*Restart, write, frequency=1
*Output, field, variable=ALL, frequency=1
```

```
*End Step
```

G.2.4 Analysis of the SFR-RCC pavement under monotonic loading plus shrinkage

G.2.4.1 Corner loading and shrinkage

File name: PAV-FRCC-STR-THRM-25-120-FULL-8NF-MONOLOPSHRK-CORNER

```
*HEADING
*PREPRINT, echo=YES, model=YES, history=YES, contact=YES
*NODE
**SLAB NODES
    1,          0,         0,         0
  169,      20160,         0,         0
 4733,          0,      3360,         0
 4901,      20160,      3360,         0
39209,          0,         0,       200
39377,      20160,         0,       200
43941,          0,      3360,       200
44109,      20160,      3360,       200
*NGEN,NSET=EDGE1
 1,169,1
*NGEN,NSET=EDGE2
 4733,4901,1
*NFILL,NSET=SURFB
 EDGE1, EDGE2 ,28,169
*NGEN,NSET=EDGE3
 39209,39377,1
*NGEN,NSET=EDGE4
 43941,44109,1
*NFILL,NSET=SURFT
  EDGE3, EDGE4,28,169
*NFIL,NSET=SLABN
  SURFB, SURFT, 8,4901
*Element, type=C3D8
  1, 1,2,171,170,4902,4903,5072,5071
*ELGEN, ELSET=SLABE
   1, 168, 1, 1, 28, 169, 168, 8, 4901, 4704
*Elset, elset=BOTE, generate
 1,  4704,      1
*Elset, elset=TOPE, generate
 32929,  37632,      1
**----------------------------------------------------------------
*Nset, nset=ENDS, GENERATE
169,4901,169
5070,9802,169
9971,14703,169
14872,19604,169
19773,24505,169
24674,29406,169
29575,34307,169
34476,39208,169
39377,44109,169
```

```
**-------------------------------------------------------
*Nset, nset=MIDS, GENERATE
1,169,1
4902,5070,1
9803,9971,1
14704,14872,1
19605,19773,1
24506,24674,1
29407,29575,1
34308,34476,1
39209,39377,1
**-------------------------------------------------------
*Nset, nset=LOADNODES
39376,  39377, 39545, 39546, 39714, 39715, 40052, 40053, 40221,
40222, 40390, 40391
**-------------------------------------------------------------
*Surface, type=ELEMENT, name=BOTS
BOTE, S1
*Surface, type=ELEMENT, name=TOPS
TOPE, S2
**-------------------------------------------------------
*Node
**BASE NODES
 200001,       -120,          -120,       -150
 200171,      20280,          -120,       -150
 205131,       -120,          3480,       -150
 205301,      20280,          3480,       -150
 215904,       -120,          -120,          0
 216074,      20280,          -120,          0
 221034,       -120,          3480,          0
 221204,      20280,          3480,          0
*NGEN,NSET=BEDGE1
 200001,200171,1
*NGEN,NSET=BEDGE2
 205131,205301,1
*NFILL,NSET=BSURFB
  BEDGE1, BEDGE2 ,30,171
*NGEN,NSET=BEDGE3
 215904,216074,1
*NGEN,NSET=BEDGE4
 221034,221204,1
*NFILL,NSET=BSURFT
  BEDGE3, BEDGE4,30,171
*NFIL,NSET=BASEN
  BSURFB, BSURFT, 3,5301
*Element, type=C3D8
  160001, 200001,200002,200173,200172,205302,205303,205474,205473
*ELGEN, ELSET=BASEE
   160001, 170, 1, 1, 30, 171, 170, 3,5301, 5100
**-------------------------------------------------------
*Nset, nset=BTOPN, GENERATE
215904, 221204, 1
**-------------------------------------------------------
**-------------------------------------------------------
*Elset, elset=BBOTE, generate
 160001,  165100,      1
*Elset, elset=BTOPE, generate
 170201,  175300,      1
**-------------------------------------------------------------
*Surface, type=ELEMENT, name=BTOPS
```

```
BTOPE, S2
**-----------------------------------------------------------
**-----------------------------------------------------------
*Solid Section, elset=SLABE, material="CDP"
*Material, name="CDP"
*Elastic, dependencies=1
 23901., 0.18, ,1
 30842., 0.18, ,3
 33361., 0.18, ,5
 34784., 0.18, ,7
 37186., 0.18, ,14
 38984., 0.18, ,28
 40308., 0.18, ,56
 41000., 0.18, ,90
 41000., 0.18, ,366
*Concrete Damaged Plasticity
31.,0.,1.2,0.,0.
*Concrete Compression Hardening, DEPENDENCIES=1
  1.2,      0. , , ,1
  2.3,   6e-05 , , ,1
  3.4,   9e-05 , , ,1
  5.6, 0.00017 , , ,1
  6.9, 0.00028 , , ,1
  8.0, 0.00042 , , ,1
  8.9, 0.00068 , , ,1
  9.3, 0.00107 , , ,1
  2.7,      0. , , ,3
  5.3,   6e-05 , , ,3
  8.1,   9e-05 , , ,3
 13.2, 0.00017 , , ,3
 16.2, 0.00028 , , ,3
 18.7, 0.00042 , , ,3
 20.9, 0.00068 , , ,3
 21.7, 0.00107 , , ,3
  3.5,      0. , , ,5
  6.9,   6e-05 , , ,5
 10.5,   9e-05 , , ,5
 17.1, 0.00017 , , ,5
 21.1, 0.00028 , , ,5
 24.2, 0.00042 , , ,5
 27.1, 0.00068 , , ,5
 28.2, 0.00107 , , ,5
  4.0,      0. , , ,7
  8.0,   6e-05 , , ,7
 12.0,   9e-05 , , ,7
 19.7, 0.00017 , , ,7
 24.2, 0.00028 , , ,7
 27.9, 0.00042 , , ,7
 31.2, 0.00068 , , ,7
 32.4, 0.00107 , , ,7
  5.0,      0. , , ,14
 10.0,   6e-05 , , ,14
 15.0,   9e-05 , , ,14
 24.6, 0.00017 , , ,14
 30.3, 0.00028 , , ,14
 34.8, 0.00042 , , ,14
 39.0, 0.00068 , , ,14
 40.5, 0.00107 , , ,14
  5.9,      0. , , ,28
 11.7,   6e-05 , , ,28
```

```
 17.6,    9e-05 , , ,28
 28.7, 0.00017 , , ,28
 35.4, 0.00028 , , ,28
 40.7, 0.00042 , , ,28
 45.6, 0.00068 , , ,28
 47.4, 0.00107 , , ,28
  6.6,       0. , , ,56
 13.0,    6e-05 , , ,56
 19.7,    9e-05 , , ,56
 32.1, 0.00017 , , ,56
 39.6, 0.00028 , , ,56
 45.5, 0.00042 , , ,56
 51.0, 0.00068 , , ,56
 53.0, 0.00107 , , ,56
  7.0,       0. , , ,90
 13.8,    6e-05 , , ,90
 20.8,    9e-05 , , ,90
 34.0, 0.00017 , , ,90
 41.9, 0.00028 , , ,90
 48.2, 0.00042 , , ,90
 54.0, 0.00068 , , ,90
 56.1, 0.00107 , , ,90
  7.0,       0. , , ,366
 13.8,    6e-05 , , ,366
 20.8,    9e-05 , , ,366
 34.0, 0.00017 , , ,366
 41.9, 0.00028 , , ,366
 48.2, 0.00042 , , ,366
 54.0, 0.00068 , , ,366
 56.1, 0.00107 , , ,366
*Concrete Tension Stiffening, DEPENDENCIES=1
 0.8,      0., , ,1
 0.4, 0.0002, , ,1
 0.4, 0.0006, , ,1
 0.2, 0.0023, , ,1
 0.02, 0.0094, , ,1
 1.9,      0., , ,3
 0.9, 0.0003, , ,3
 0.8, 0.0011, , ,3
 0.6, 0.0041, , ,3
 0.02, 0.0170, , ,3
 2.5,      0., , ,5
 1.2, 0.0004, , ,5
 1.1, 0.0013, , ,5
 0.7, 0.0050, , ,5
 0.05, 0.0204, , ,5
 2.9,      0., , ,7
 1.4, 0.0004, , ,7
 1.2, 0.0015, , ,7
 0.9, 0.0055, , ,7
 0.05, 0.0225, , ,7
 3.6,      0., , ,14
 1.8, 0.0005, , ,14
 1.5, 0.0017, , ,14
 1.1, 0.0064, , ,14
 0.05, 0.0263, , ,14
 4.2,      0., , ,28
 2.1, 0.0005, , ,28
 1.8, 0.0019, , ,28
 1.3, 0.0071, , ,28
```

```
0.05, 0.0294, , ,28
4.5,     0., , ,56
2.2, 0.0005, , ,56
1.9, 0.0020, , ,56
1.3, 0.0073, , ,56
0.05, 0.0300, , ,56
4.7,     0., , ,90
2.3, 0.0005, , ,90
2.0, 0.0020, , ,90
1.4, 0.0073, , ,90
0.05, 0.0300, , ,90
4.7,     0., , ,366
2.3, 0.0005, , ,366
 2., 0.0020, , ,366
1.4, 0.0073, , ,366
0.05, 0.0300, , ,366
*Concrete Tension Damage, DEPENDENCIES=1
0.0,     0.,  ,1
0.5, 0.0002,  ,1
0.6, 0.0006,  ,1
0.7, 0.0023,  ,1
0.95, 0.0094,  ,1
0.0,     0.,  ,3
0.5, 0.0003,  ,3
0.6, 0.0011,  ,3
0.7, 0.0041,  ,3
0.95, 0.0170,  ,3
0.0,     0.,  ,5
0.5, 0.0004,  ,5
0.6, 0.0013,  ,5
0.7, 0.0050,  ,5
0.95, 0.0204,  ,5
0.0,     0.,  ,7
0.5, 0.0004,  ,7
0.6, 0.0015,  ,7
0.7, 0.0055,  ,7
0.95, 0.0225,  ,7
0.0,     0.,  ,14
0.5, 0.0005,  ,14
0.6, 0.0017,  ,14
0.7, 0.0064,  ,14
0.95, 0.0263,  ,14
0.0,     0.,  ,28
0.5, 0.0005,  ,28
0.6, 0.0019,  ,28
0.7, 0.0071,  ,28
0.95, 0.0294,  ,28
0.0,     0.,  ,56
0.5, 0.0005,  ,56
0.6, 0.0020,  ,56
0.7, 0.0073,  ,56
0.95, 0.0300,  ,56
0.0,     0.,  ,90
0.5, 0.0005,  ,90
0.6, 0.0020,  ,90
0.7, 0.0073,  ,90
0.95, 0.0300,  ,90
0.0,     0.,  ,366
0.5, 0.0005,  ,366
0.6, 0.0020,  ,366
```

```
 0.7, 0.0073,  ,366
 0.95, 0.0300,  ,366
**Density
**1,
*Expansion, zero=1.
 0.002000, 0.4
 0.002036, 0.5
 0.002082, 0.6
 0.002143, 0.7
 0.002232, 0.8
 0.002392, 0.9
 0.002446, 0.92
 0.002517, 0.94
 0.002621, 0.96
 0.002810, 0.98
 0.003011, 0.99
 0.003791, 0.999
** ----------------------------------------------------------
** ----------------------------------------------------------
*Solid Section, elset=BASEE, material="ELASTIC B"
*Material, name="ELASTIC B"
*Elastic
 8000., 0.3
** ----------------------------------------------------------
*Surface Interaction, name=CONTPROP
*Friction, slip tolerance=0.005, taumax=0.1
0.5,
*Surface Behavior, pressure-overclosure=HARD
** ----------------------------------------------------------
*Boundary
2282, 1, 1
*Boundary
2451, 1, 1
*Boundary
2620, 1, 1
*Boundary
2450, 2, 2
*Boundary
2451, 2, 2
*Boundary
2452, 2, 2
*Boundary
202480, 1, 1
*Boundary
202651, 1, 1
*Boundary
202822, 1, 1
*Boundary
202650, 2, 2
*Boundary
202651, 2, 2
*Boundary
202652, 2, 2
** ----------------------------------------------------------
*AMPLITUDE, NAME=TFUNC, TIME=TOTAL TIME, DEFINITION=TABULAR,
VALUE=ABSOLUTE
0, 0, 800, 800
*Initial Conditions, type=TEMPERATURE
SLABN, 1.0
*Initial Conditions, type=FIELD, VARIABLE=1
```

```
SLABN, 0.001
*Foundation
BBOTE, F1, 0.06
*Contact Pair, interaction=CONTPROP, TYPE=SURFACE TO SURFACE
BOTS, BTOPS
** ----------------------------------------------------------
*Step, name=STRUCTURAL, amplitude=STEP, INC=10000
*STATIC
0.2, 364., 1e-05,14
**CONTACT CONTROLS, SLAVE=BOTS, MASTER=BTOPS, MAXCHP=50000,
PERRMX=1.0
*Dload
SLABE, BZ, -2.5432e-05
*TEMPERATURE,FILE=PAV-FRCC-THRM-25-120-FULL-8N.odb
*FIELD, VARIABLE=1, AMPLITUDE=TFUNC
SLABN, 364
*Restart, write, frequency=1
*Output, field, variable=ALL, frequency=1
*End Step
**-------------------------------------------------------------
**-----------------------------------------------------------------
*Step, name=LOADING, inc=10000
*Static
0.05, 364., 1e-06, 14
*Cload
** 10TIMES OF THE ONE CYCLE SERVICE LOAD
LOADNODES, 3, -33333.3
*Restart, write, frequency=1
*Output, field, variable=ALL, frequency=1
*End Step
```

G.2.4.2 Moisture transport analysis for full width slab (referred in the above input files in Section, G.2.4.1)

File name: PAV-FRCC-THRM-25-120-FULL-8N

```
*HEADING
*PREPRINT, echo=YES, model=YES, history=YES, contact=YES
*NODE
**SLAB NODES
    1,          0,         0,         0
  169,      20160,         0,         0
 4733,          0,      3360,         0
 4901,      20160,      3360,         0
39209,          0,         0,       200
39377,      20160,         0,       200
43941,          0,      3360,       200
44109,      20160,      3360,       200
*NGEN,NSET=EDGE1
 1,169,1
*NGEN,NSET=EDGE2
 4733,4901,1
*NFILL,NSET=SURFB
 EDGE1, EDGE2 ,28,169
*NGEN,NSET=EDGE3
```

```
 39209,39377,1
*NGEN,NSET=EDGE4
 43941,44109,1
*NFILL,NSET=SURFT
  EDGE3, EDGE4,28,169
*NFIL,NSET=SLABN
  SURFB, SURFT, 8,4901
*Element, type=DC3D8
  1, 1,2,171,170,4902,4903,5072,5071
*ELGEN, ELSET=SLABE
   1, 168, 1, 1, 28, 169, 168, 8, 4901, 4704
*Elset, elset=BOTE, generate
 1,  4704,      1
*Elset, elset=TOPE, generate
 32929,  37632,      1
**------------------------------------------------------------
*Surface, type=ELEMENT, name=TOPS
TOPE, S2
** ----------------------------------------------------------
*Solid Section, elset=SLABE, material=THERMAL-FRCC
**----------------------------------------------------------
*Material, name=THERMAL-FRCC
*Conductivity
 4.1, 0.001
 4.75, 0.8
 4.9, 0.83
 5, 0.86
 5.2, 0.87
 5.4, 0.88
 6, 0.89
 15, 0.925
 25, 0.96
 27, 0.97
 28, 0.98
 30, 0.999
*Density
1.,
*Specific Heat
1.,
** ----------------------------------------------------------------
*Initial Conditions, type=TEMPERATURE
SLABN, 1.
** ----------------------------------------------------------------
*Step, name=THERML, inc=10000
*Heat Transfer, end=PERIOD, deltmx=0.1
0.05, 364., 1e-05, 14
*Sfilm
TOPS, F, 0.4, 5
*Restart, write, frequency=10
*Print, frequency=10
*Output, field
*Node Output
NT,
*Output, field, variable=ALL, frequency=10
*Output, history, frequency=0
*End Step
```